Physics of the Solid State, Vol. 43, No. 12, 2001, pp. 2205–2208. Translated from Fizika Tverdogo Tela, Vol. 43, No. 12, 2001, pp. 2113–2116.
Original Russian Text Copyright © 2001 by Veksler, Gavriliuk, Morozov, Semenov.

METALS AND SUPERCONDUCTORS

Specific Features of Exoelectronic Emission in Amorphous Metal Alloys

A. S. Veksler, A. A. Gavriliuk, I. L. Morozov, and A. L. Semenov
Irkutsk State University, bul'v. Gagarina 20, Irkutsk, 664003 Russia
e-mail: zubr@api.isu.runnet.ru

Received March 5, 2001; in final form, May 18, 2001

Abstract—This paper reports on a study of the specific features of photo- and thermostimulated exoelectronic emission in amorphous metal alloys of $Fe_{64}Co_{21}B_{15}$ composition. The temperature dependences of the exoelectronic emission spectrum were established to adequately reflect the two-stage nature of the transition of an amorphous alloy to the crystalline state. The exoelectronic emission spectrum is sensitive to variations in the thermal treatment to which the alloy is subjected. Thermal treatment of an amorphous metal alloy gives rise to an increase in the exoelectron emission intensity. The growth in the exoelectron emission intensity was found to be the highest for alloys in the initial stage of crystallization. *© 2001 MAIK "Nauka/Interperiodica".*

Photo- and thermostimulated exoelectronic emission (PTSEE) is one of the most sensitive methods of reliable identification of the initial stages in the structural modification of a solid undergoing a phase transition [1, 2]. The small escape depth of exoelectrons makes the PTSEE method sensitive even to very slight changes in the surface structure of a solid. Although many aspects of the mechanisms of PTSEE in solids are presently well understood, information on its features upon the transition of a solid from a structurally disordered to an ordered state is scarce. Amorphous metal alloys (AMAs) are the most convenient model subjects for studying this transition [3, 4]. This paper investigates various features of PTSEE in AMAs of $Fe_{64}Co_{21}B_{15}$ composition obtained through rapid quenching from melt that have considerable application potential [5, 6].

To properly understand the mechanisms underlying the PTSEE in the samples under study and to correctly interpret the results obtained, measurement of the exoelectronic emission spectra should be complemented by simultaneous study of the AMA structure using other appropriate methods. Therefore, spectral studies of the PTSEE were run in parallel with x-ray diffractometry and differential thermal analysis (DTA) of the structure, as well as with monitoring the variation in electrical resistance in the course of phase transformations in the solid sample.

The PTSEE was studied on samples 25–30 μm thick and 10 mm wide. In the initial stage, the alloys were diffractometrically amorphous. The samples were heated in a chamber in a vacuum of 10^{-4} Pa. Photostimulation was effected by an optical arrangement based on a MUM-4 monochromator. The wavelength of the exciting radiation was chosen equal to 310 nm. The sample temperature could be varied from 290 to 1000 K. The PTSEE spectra were measured at constant heating rates ranging from 5 to 60 K/min. The DTA was carried out in air on a Paulik derivatograph at constant heating rates ranging from 2 to 20 K/min. The crystalline phases formed during alloy heating were analyzed with FeK_α radiation on a DRON-3.0 diffractometer. The variation of the sample resistance under heating was monitored with a digital voltmeter using a four-point method with simultaneous PTSEE spectral measurements.

For the chosen photostimulation conditions and constant heating rates ranging from 5 to 20–25 K/min, the temperature dependences of the PTSEE response exhibited two characteristic peaks. The first peak obtained on the $Fe_{64}Co_{21}B_{15}$ alloy at these heating rates is positioned in the temperature range from 670 to 820 K; the second peak, in the range from 850 to 900 K. Figure 1 displays the characteristic dependence of the ratio of the exoelectronic emission photocurrent I to its maximum value I_{max} on the heating rate for the alloy under study. The position of the second peak corresponds to the onset of an irreversible drop in alloy electrical resistance, which, after heating of the samples to 1000 K and subsequent cooling to room temperature, decreases by a factor of 2 to 2.5. The drop in electrical resistance during heating from 800 to 850 K indicates the irreversibility of the crystallization process taking place throughout the alloy volume [7].

The presence of two maxima in the temperature response of the PTSEE may be connected with different crystallization stages of the alloys under study. As follows from x-ray diffraction measurements, the first maximum in the PTSEE response is due to the formation of the α-Fe, α-Co, and β-Co crystalline phases [4]. The second maximum in the PTSEE response corresponds to the completion of the α-Fe crystallization and

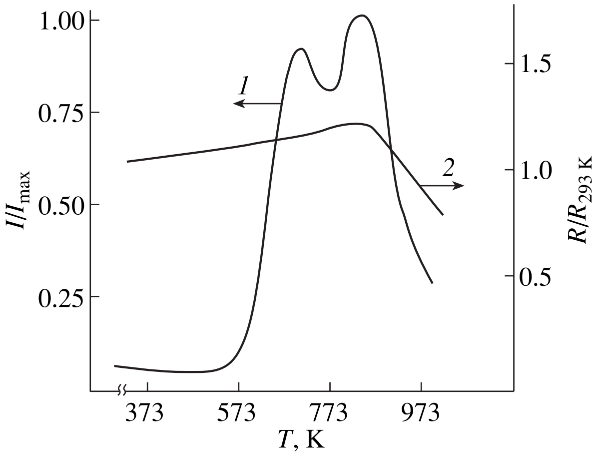

Fig. 1. Temperature dependences of (*1*) the ratio of the exoelectron emission photocurrent I to its maximum value I_{max} and (*2*) the reduced electrical resistance of an $Fe_{64}Co_{21}B_{15}$ amorphous metal alloy.

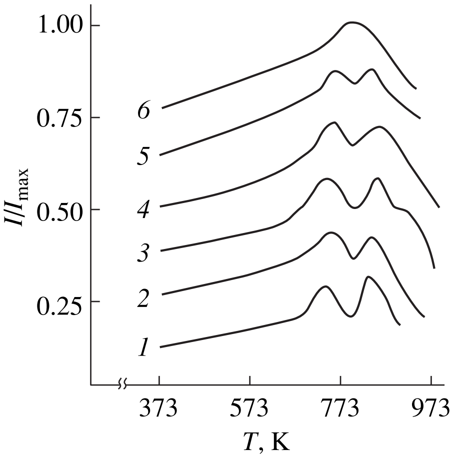

Fig. 2. Temperature dependences of the ratio of the exoelectron emission photocurrent I to its maximum value I_{max} for an $Fe_{64}Co_{21}B_{15}$ alloy obtained at various constant heating rates: (*1*) 5, (*2*) 10, (*3*) 15, (*4*) 20, (*5*) 40, and (*6*) 60 K/min.

to the formation of new phases, namely, iron and cobalt compounds with other components (Fe_2B, Fe_3B, CoB). The DTA data for the $Fe_{64}Co_{21}B_{15}$ alloy exhibit four exothermic peaks at 653, 753, 853, and 973 K, appearing as the alloy is heated to 1000 K. The first two peaks can be assigned to the crystallization of the alloy, and the last two are shown by thermogravimetric measurements to be due to oxidation processes occurring on the sample surface [4].

As the heating rate is increased, the temperature interval between the two maxima in the PTSEE response of the alloys under study decreases until, at heating rates above 60 K/min, the two maxima merge (Fig. 2). This permits one to conclude that the temperature interval separating the two stages of alloy crystallization becomes narrower for sample heating at a higher constant rate.

An interesting feature in the PTSEE of the $Fe_{64}Co_{21}B_{15}$ alloy is that repeated heating (within the temperature range studied) of samples in which the crystallization has come to an end does not produce any maxima in the PTSEE curves. This suggests that the structure of the alloy under study has practically completely changed in the given temperature range, with no noticeable structural changes occurring during a repeated heating run.

The PTSEE data were used to estimate the activation energy of exoelectronic emission under the assumption that the intensity of the escaping exoelectron flux is proportional to the rate of variation of the emitting-center concentration. The exoelectron emission activation energy was estimated using chemical kinetic equations [8]. The calculations yield 1–1.5 eV for the activation energy of our alloy in the first crystallization stage and 2.6–3.0 eV for the second stage. The experiment shows the reaction to be first-order, which agrees with the results of investigating AMA crystallization obtained in [3].

To find how the PTSEE features are related to the crystallization processes, we measured PTSEE spectra of the alloys at a constant heating rate at positions both below and above the position of the first peak and studied the temperature dependence of the PTSEE intensity under various sample heating conditions (Fig. 3). The PTSEE intensity of the alloy samples subjected to isothermal treatment at a temperature below the position of the first peak increases. If we assume that when the heating time is increased the PTSEE intensity is deter-

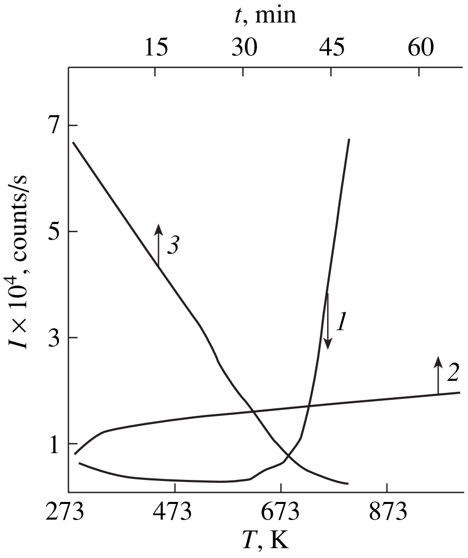

Fig. 3. Kinetic and isothermal dependences of the PTSEE spectra of an $Fe_{64}Co_{21}B_{15}$ alloy: (*1*) for a sample heated from 293 to 623 K at a rate of 20 K/min and (*2*, *3*) under isothermal sample treatment at 623 and 823 K, respectively.

mined by the rate of crystallization, this intensity, as follows from the rate equation for a first-order reaction, should decrease at a fixed temperature. The experimentally observed growth in the PTSEE intensity with increasing isothermal heating time is characteristic of topochemical reactions [9]. The rate of a topochemical reaction first increases with increasing isothermal heating time because of the initial growth of crystal nuclei and subsequently decreases when the nuclei start to coalesce.

To better understand the specific features of exoelectronic emission in the alloys under study, we measured the PTSEE response as a function of the wavelength of stimulating radiation both before thermal treatment of the $Fe_{64}Co_{21}B_{15}$ alloy and after it. The thermal treatment was carried out in the following regimes:

(1) The sample was heated in vacuum to a temperature of 970 K, which is in considerable excess of its crystallization temperature. After subsequent cooling to room temperature, the PTSEE spectrum was measured as a function of the stimulating radiation wavelength (Fig. 4).

(2) The sample was heated in vacuum to 690 K, which corresponds to the initial stage of alloy crystallization; it was then cooled to room temperature. After cooling, the PTSEE response was measured as a function of the stimulating radiation wavelength (Fig. 5).

(3) The alloy was subjected to isothermal heating in air at 470 K for 100 and 200 h, after which it was cooled to room temperature. As in the first two cases, a PTSEE spectrum was obtained after sample cooling (Fig. 5). In all three cases, after thermal treatment, the samples were maintained isothermally at room temperature for 24 h and then a PTSEE spectrum was again measured.

After thermal treatment of the alloy, the exoelectron emission intensity increased in comparison to that for the original sample throughout the radiation wavelength range studied, irrespective of the actual treatment conditions chosen. The growth in the exoelectron emission intensity was larger, the longer the alloy isothermal heating time. The increase in the exoelectron emission intensity induced by the thermal treatment was the largest in the second regime, i.e., after the alloy passed through the initial crystallization stage. After the sample had been kept at room temperature for 24 h, the exoelectron emission intensity decreased, irrespective of the thermal treatment regime it had been subjected to.

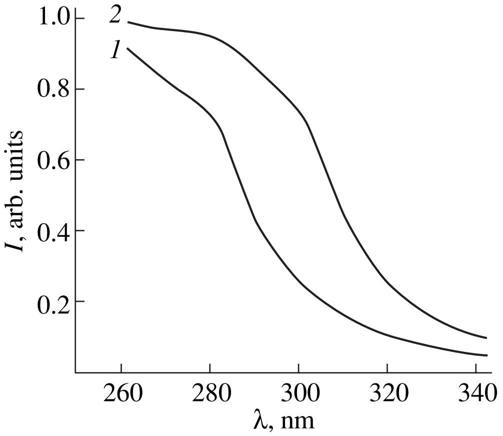

Fig. 4. Spectral response of the exoelectron emission photocurrent I of an $Fe_{64}Co_{21}B_{15}$ alloy: (*1*) starting sample and (*2*) a sample subjected to thermal treatment in vacuum at 970 K.

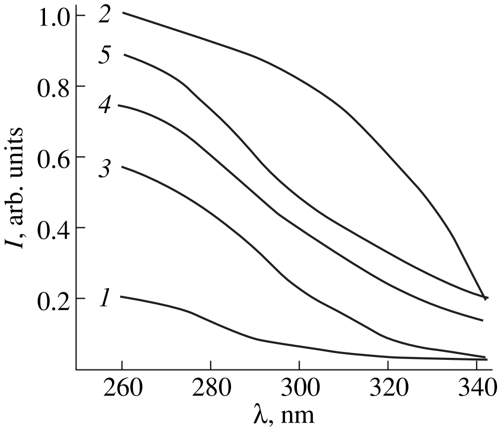

Fig. 5. Spectral response of the exoelectron emission photocurrent I of an $Fe_{64}Co_{21}B_{15}$ alloy: (*1*) starting sample; (*2*) a sample subjected to thermal treatment in vacuum at 690 K; (*3*) a sample subjected to further isothermal treatment at room temperature for 24 h; and (*4*, *5*) samples subjected to isothermal treatment at 473 K in air for 100 and 200 h, respectively.

These results can be interpreted as follows. The growth in the exoelectron emission intensity is caused by a change in the alloy surface work function. It may be conjectured that the change in the exoelectron work function observed in the first two regimes of the alloy thermal treatment can be caused by the increased internal stresses due to crystallization in the sample. A decrease in the exoelectron work function with increasing internal stresses in a metal was observed earlier in [1]. The growth in the exoelectron emission intensity after isothermal treatment at 470 K in air may be caused by surface oxidation. When a sample is kept at room temperature, the internal stresses created in the course of crystallization relax and, as a consequence, the PTSEE intensity decreases. The change ΔE in the exoelectron work function can be estimated from the relation

$$\Delta E = (\hbar c/\lambda_m^2)\Delta\lambda,$$

where c is the velocity of light and λ_m is the mean wavelength of the stimulating radiation at the same exoelectron emission intensity for the original and thermally treated samples. When a $Fe_{64}Co_{21}B_{15}$ sample is heated to 970 K at $\lambda_m = 300$ nm, the change $\Delta\lambda$ is equal to 20 nm, which corresponds to a decrease in E of 0.25 eV as compared to the value for the untreated sample. Heating to 690 K for $\lambda_m = 280$ nm reduces E by 0.60 eV, and isothermal treatment in air at 470 K for 200 h reduces E by 0.20 eV.

The above studies permit the following conclusions to be drawn on the PTSEE in the $Fe_{64}Co_{21}B_{15}$ amorphous metal alloy observed to occur upon its transition to the crystalline state:

(1) The temperature dependences of the PTSEE response reflect a two-stage pattern in the structural changes taking place in the heated AMA sample under study. These stages are most clearly defined at low sample heating rates. By analyzing the PTSEE spectrum, one can determine the activation energy for each crystallization stage.

(2) The PTSEE spectrum is very sensitive to isothermal treatment temperatures and variations in the AMA heating regimes. At the same time, repeated heating of samples that have already crystallized, within the temperature range studied, and changing the heating regimes does not produce any peaks in the temperature dependences of the exoelectron emission intensity.

(3) Thermal treatment of the AMAs studied increases the exoelectron emission intensity, which is associated with the structural changes that the AMAs undergo in this treatment. The PTSEE intensity increase is the largest for the AMAs that went through the initial crystallization stage.

REFERENCES

1. L. Gryunberg, in *Exoelectron Emission: Collection of Articles*, Ed. by I. V. Krylov (Inostrannaya Literatura, Moscow, 1962), p. 118.
2. G. L. Sagalovich, V. P. Melekhin, and Yu. D. Dekhtyar, in *Exoelectron Spectroscopy of Defects in Solids* (NTO, Riga, 1981), p. 80.
3. Cz. Gorecki and T. Gorecki, Poverkhnost, No. 7, 63 (1993).
4. V. I. Boldyrev, A. S. Veksler, and N. I. Noskova, Fiz. Met. Metalloved. **87** (5), 83 (1999).
5. E. Ferrara, A. Infortuna, A. Magni, and M. Pasquale, IEEE Trans. Magn. **33**, 3781 (1997).
6. L. Kraus, V. Haslar, and P. Duhay, IEEE Trans. Magn. **30**, 530 (1994).
7. K. Suzuki, H. Fujimori, and K. Hashimoto, *Amorphous Metals* (Tokyo, 1982; Metallurgiya, Moscow, 1987), translated from Japanese.
8. N. M. Émanuél’ and D. G. Knorre, *Course of Chemical Kinetics* (Vysshaya Shkola, Moscow, 1979).
9. A. A. Zhukovskiĭ and L. A. Shvartsman, *Physical Chemistry* (Metallurgiya, Moscow, 1976).

Translated by G. Skrebtsov

Physics of the Solid State, Vol. 43, No. 12, 2001, pp. 2209–2212. Translated from Fizika Tverdogo Tela, Vol. 43, No. 12, 2001, pp. 2117–2120.
Original Russian Text Copyright © 2001 by Khirnyĭ, Kozlovskiĭ.

METALS AND SUPERCONDUCTORS

Magnetic Flux Trapping and Broken Abrikosov Vortices in Yttrium HTSC Ceramic Samples

V. F. Khirnyĭ and A. A. Kozlovskiĭ

Institute of Single Crystals, National Academy of Sciences of Ukraine, pr. Lenina 60, Kharkov, 61001 Ukraine

Received October 11, 2000; in final form, February 6, 2001

Abstract—Direct evidence of the existence of broken Abrikosov vortices is obtained from measurements of the distribution and values of residual magnetic fields in ceramic yttrium HTSC samples after the switching off of a transport current. In this case, the intergrain magnetic induction averaged over the sample volume has the same direction as the field that was in the sample before the current was switched off. © *2001 MAIK "Nauka/Interperiodica".*

1. INTRODUCTION

The critical current I_c in type II superconductors is determined by the pinning of quantized vortices; in ceramic HTSC samples, it also depends on the magnitude of the intergrain magnetic induction B_j [1]. It was reported in [2] that after switching off of a transport current, the magnetic field in weak bonds was in the opposite direction to the field produced by the current; that is, inversion of the sign takes place for the B_j distribution. As a result, when repeatedly measured, the critical current I_c had a higher value. In [3], the increase in I_c is explained by the fact that the process of penetration of the Josephson vortex rings into the samples is affected by the remanent circular magnetic fields H_{REM} that are created by the stray fields of the broken Abrikosov vortices. In order to document the existence of broken Abrikosov vortices, we investigated the field H_{REM} and its distribution outside ceramic yttrium HTSC samples.

2. EXPERIMENT AND DISCUSSION

We investigated HTSC ceramic samples of $\mathrm{YBa_2Cu_3O}_x$, whose superconducting properties were studied earlier [3].

To produce a circular transverse magnetic field H_t, an electric current I_t was passed through samples kept at room temperature. The samples were cooled to T = 77 K in this field, after which the current I_t was switched off and the distribution of the remanent magnetic field $H_{\mathrm{REM}}^{\mathrm{out}}$ was measured outside the samples (which were kept in liquid nitrogen) using a standard magnetometer [4]. The sensitivity of the measuring system was 0.01 Oe. It was established that the field H_t did not change during the transition from the normal to the superconducting state; that is, the field distribution outside the HTSC samples coincided with that predicted for a superconducting cylinder with a current flowing near the surface [5].

Figure 1 presents the distribution of the circular magnetic field $H_{\mathrm{REM}}^{\mathrm{out}}$ in the cross-sectional plane recorded outside a cylindrical yttrium HTSC sample 4.5 mm in diameter and 35 mm in length after switching off of the current I_t = 10 A; this current was passed perpendicular to the plane of the figure. The critical temperature of the sample was $T_c \cong 90$ K, and the critical current was I_c = 5.89 A at 77 K. The magnetic field of the Earth was not screened. The measurements were taken at discrete points in angular $\varphi = 30°$ intervals. A Hall cell (the crystal dimensions were 1.5×2 mm) was placed near the cylindrical sample surface. The sample

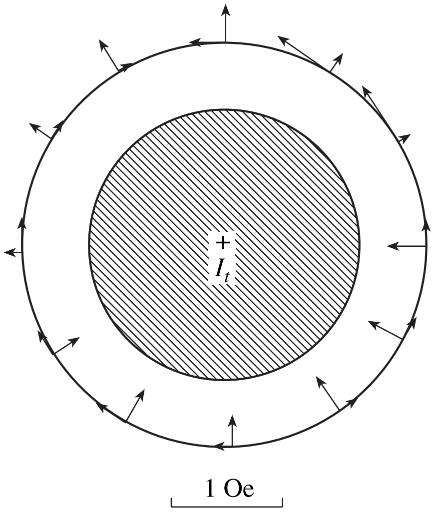

Fig. 1. Experimental distribution of the parallel and perpendicular components of the residual circular magnetic field outside a cylindrical sample (crosshatched) after switching off of the current I_t.

1063-7834/01/4312-2209$21.00 © 2001 MAIK "Nauka/Interperiodica"

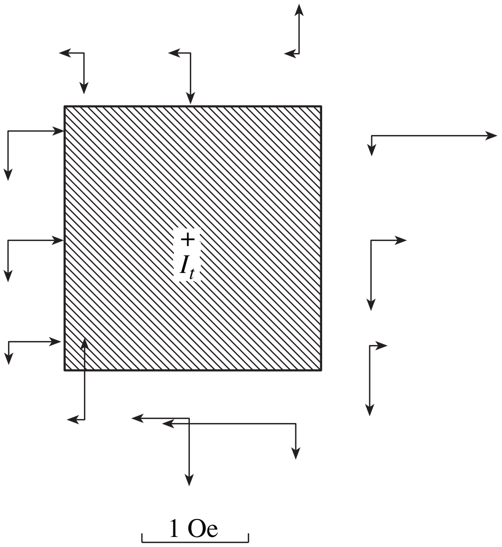

Fig. 2. Experimental distribution of the parallel and perpendicular components of the circular residual magnetic field outside a sample with a square cross section after switching off of the current I_t.

was in a vertical position. The field values and its distribution remained almost unchanged over the sample height. The measurements revealed no magnetic-field component parallel to the axis of the cylindrical sample. No residual magnetic field was detected at the cylinder end faces. Figure 2 shows the $H_{\mathrm{REM}}^{\mathrm{out}}$ field distribution in the cross section of a sample with cross-sectional dimensions 5 × 5 mm 35 mm in length. The measurements were taken under the same conditions as for the cylindrical sample.

As can be seen from Figs. 1 and 2, the $H_{\mathrm{REM}}^{\mathrm{out}}$ field distribution is similar to the field distribution for a magnet, with $\oint_L H_{\mathrm{REM}}^{\mathrm{out}} d\mathbf{l} = 0$, for any closed contour L passing outside the sample if $I = 0$. The results obtained are evidence in favor of the suggestion [3] that the increased values of the repeatedly measured critical current are due to the circular transverse magnetic field $H_{\mathrm{REM}}^{\mathrm{in}}$ [3] created by the intrinsic magnetic field H_t of the current and remains in the sample after the current I_t is switched off.

The capturing of a circular magnetic field by a ceramic HTSC sample can occur as follows. If a superconductor in the normal state carries a direct current, the circulation of the circular magnetic field H_i of the current I is equal to [6]

$$\oint_L \mathbf{H}_i d\mathbf{l} = (4\pi/c)I,$$

where $I = \oint \mathbf{J} d\mathbf{S}_0$ is the full current flowing through the cross section S_0 enclosed by loop L, c is the velocity of light in vacuum, and J is the current density. After the current I is switched off, the field $H_i = 0$. In ceramic HTSC samples, the field H_i behaves in a completely different way. When the sample passes over to the superconducting state, the configuration of this circular field has the form of rings that are formed from quantized magnetic Abrikosov vortices [3]. The unbroken vortex rings penetrate the grains, intergrain bonds, and nonhomogeneities. After the current I_t is switched off at 77 K, the vortex rings are pinned within the grains into which they had already penetrated at $T \cong T_c$, when the lower critical magnetic field for the grains was $H_{c1g} \cong 0$. Since the magnetic field H_v of an unbroken vortex toroid is completely inside the vortex [7], it cannot be detected outside the superconductor. The field will appear outside the superconductor if vortices are broken. In ordinary low-temperature superconductors, the vortices are attracted to nonhomogeneities with a force f_p equal to the energy gradient. For a nonhomogeneity with diameter d, we have [8] $f_p \sim H_c^2 \xi d$, where H_c is the thermodynamic critical magnetic field and ξ is the coherence length. This force is large: it is equal to the Lorentz force that acts on the vortex when the current passing through the sample is comparable with the critical current at which a Cooper pair is broken [8]. From the relation $E_1/E_0 = 3/\pi^2 \ln[\lambda_L(0)/\xi_0(0)]$ derived in [9], one can estimate the energy gain for a pure superconductor at $T = 0$, where the sum $E_1 + E_0$ is equal to the vortex energy E per unit length. Here, the term $E_0 = (\Phi_0/4\pi\lambda_L)^2 \ln(\lambda_L/\xi)$ allows for the change in the energy of electrons in a magnetic field and their kinetic energy (superconduction current) and $E_1 = (H_c^2 \xi^2/8\pi)$ is the energy necessary to transfer electrons from the superconducting to the normal state inside the vortex core; that is, it is equal to the condensation energy. In this case, $\Phi_0 = hc/2e$ is the magnetic flux quantum, h is Planck's constant, c is the velocity of light in vacuum, e is the electron charge, λ_L is the London penetration depth of a magnetic field, $\lambda_L(0)$ is the London depth of the magnetic field penetration at $T = 0$, and $\xi_0(0)$ is the coherence length for a pure superconductor at $T = 0$. If a vortex passes through a cavity of dimensions $d \geq \xi$, then the excess energy E_1 is absent. The total energy E_b of such a vortex is less than the energy E for a vortex that does not cross a cavity. For $YBa_2Cu_3O_x$, in which the Ginzburg–Landau parameter is $\kappa = \lambda_L/\xi \cong 50$, we have $E_1/E_0 \sim 8\%$. In the ceramic yttrium HTSCs under study, there are a lot of nonsuperconducting inclusions even with dimensions $d \gg \lambda_L$ [10]. In this case, putting $\lambda_L \cong 50\xi$, we find that the energy gain is even higher for vortices crossing such inclusions. Being attracted to pores and nonsuperconducting inclusions and crossing them, the vortex rings break. The magnetic fields H_v

inside the vortices dissipate in the regions of the ring breakage. The corresponding lines of magnetic induction remain continuous but are curved in a complicated way. These lines of the stray magnetic field, being trapped within the intergrain space outside the pinned vortex parts, penetrate to a depth λ_L into the grains and partially go out of the sample.

The conclusion that the vortex lines are broken by nonhomogeneities is supported by the following three arguments. First, the conditions under which this occurs, as well as the fact that in ceramic HTSCs there are broken vortex lines which consist of vortex segments separated from each other by nonhomogeneities, were established by analyzing the operation of dc superconducting thin-film transformers [11]. In these transformers, when the width of the insulating layer between the primary and secondary films is larger than λ_L, the magnetic coupling between the vortices present in these films is broken. The vortices created by the same field in the primary and secondary films move independently, sliding with respect to each other; that is, the vortex lines are broken. Second, the vortex lines are singular lines in the velocity distribution of Cooper pairs rotating around a certain axis. A vortex line is characterized by a quantized value of circulation of the velocity $\mathbf{v}_s$ of superconducting electrons $\oint_C \mathbf{v}_s d\mathbf{l} = \pi k\hbar/m$ ($k = 1$) [8] along the closed path C enclosing their rotation axis (m is the mass of superconducting electrons). This means [12] that the vortex line is either closed or terminates at the boundary between the superconducting region and a nonsuperconducting nonhomogeneity, being continuous in the pure superconducting region. Finally, third, as was noted in [8], the vortex section that is attracted to a nonhomogeneity disappears, because it and its virtual image annihilate each other; that is, the vortex breaks.

In a broken vortex ring, the axial lines of the magnetic induction H_V, as well as those near them, remain the same as in the unbroken one. The distinction from the unbroken ring is in that there is no rotation of Cooper pairs in the nonsuperconducting inclusions and the magnetic induction lines can deviate from one another. The broken vortex rings take a fine-saw-like form due to the chaotic distribution of nonhomogeneities in the ceramic HTSC samples.

The configuration of the magnetic field of the samples with a rectangular cross section (Fig. 2) suggests that broken vortex rings are also present in this case. The possible existence of vortex rings in samples of such geometry was discussed in [13].

In order to verify the mechanism of creation of residual magnetic fields considered above, we performed a model experiment in which cylindrical magnets 0.035 m in diameter and 0.01 m in height were used as broken vortex lines. The magnetic field strength at the end faces was 500 Oe. Twenty such magnets were vertically mounted on a horizontal nonmagnetic disk 0.22 m in diameter. The disk was attached to a rod joined to a reducing gear of an electric motor. Magnets of alternating polarity were arranged in a circle of radius 0.1 m at an equal distance from one another. A Hall cell with a magnetic sensitivity of 135 μV/T, placed at a certain distance from the disk edge, was used to determine the distribution of the circular magnetic field produced by the magnets in the disk plane. For this purpose, the electric motor was switched on and the disk was rotated slowly and uniformly. Figure 3 presents the Hall cell response (ordinate) as a function of the disk rotation angle. The Hall cell was placed at a distance of 0.235 m from the disk center. Figure 3 presents, in fact, the distribution of the circular magnetic field recorded by the Hall cell over a rotation period of the disk. The result obtained is analogous to that presented in Fig. 1, thereby verifying the suggestion that the residual circular magnetic fields are produced by broken quantized vortices in the ceramic yttrium HTSC samples. The circulation of the magnetic field in the model experiment was equal to zero irrespective of the distance of the Hall cell from the disk edge and regardless of the fact that the form of the distribution and the magnetic field magnitude were changed. When the Hall cell was placed near the disk edge, the signal value versus the disk rotation angle curve displayed maxima and minima and went through zero values. When the Hall cell was placed far from the disk edge, the number of maxima and minima decreased until the curve took the form shown in Fig. 3. Further increase in the distance between the Hall cell and the disk edge resulted in a decrease in the signal amplitude and in the conversion of the curve into a straight line.

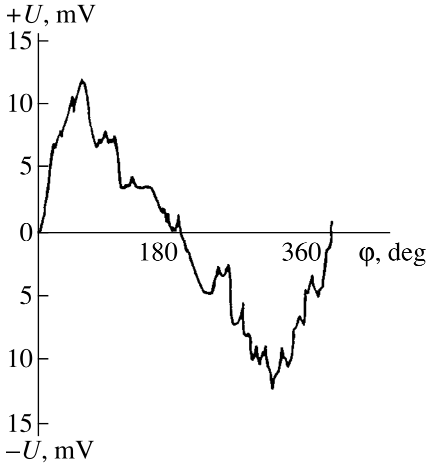

Fig. 3. Hall cell response U as a function of the disk rotation angle φ.

3. CONCLUSIONS

Thus, the field $H_{\mathrm{REM}}^{\mathrm{out}}$ detected outside the ceramic HTSC samples is shown to be produced by broken vortices. Inside the sample, the averaged magnetic flux remains in a net of weak bonds; its value $\Phi \le n\Phi_0$ has the same sign as the flux of the unbroken vortex rings. Here, n is the number of broken vortex rings in the sample. The field $H_{\mathrm{REM}}^{\mathrm{out}}$ is weak, which suggests that only an insignificant part of the magnetic field H_v inside the broken vortices dissipates and that most of this field remains in the sample.

Therefore, after the transport current is switched off in the sample, no inversion of the B_j sign occurs in the intergrain space. This follows from Stock's theorem and is supported by the character of the distribution of the residual magnetic field outside the sample, which is presented in Figs. 1 and 2.

REFERENCES

1. J. E. Evetts and B. A. Glowacki, Cryogenics **28** (10), 641 (1988).
2. A. A. Zhukov and V. V. Moshchalkov, Sverkhprovodimost: Fiz., Khim., Tekh. **4** (5), 850 (1991).
3. A. A. Kozlovskiĭ and V. F. Khirnyĭ, Fiz. Tverd. Tela (St. Petersburg) **42** (10), 1780 (2000) [Phys. Solid State **42**, 1825 (2000)].
4. V. I. Chechernikov, *Magnetic Measurings* (Mosk. Gos. Univ., Moscow, 1963).
5. J. Bardeen, in *Handbuch der Physik*, Bd. XIV–XV: Kältephysik, Ed. by S. Flügge (Springer, Berlin, 1956).
6. V. G. Levich, *Theoretical Physics; an Advanced Text* (Fizmatgiz, Moscow, 1962; North-Holland, Amsterdam, 1970), Vol. 1.
7. Yu. A. Genenko, Phys. Rev. B **49** (10), 6950 (1994).
8. A. A. Abrikosov, *Fundamentals of the Theory of Metals* (Nauka, Moscow, 1987; North-Holland, Amsterdam, 1988).
9. A. G. van Vijfeijken, *On the Theory of Vortices in Type-II Superconductors*, Thesis (University of Amsterdam, Amsterdam, 1967).
10. V. P. Seminozhenko, V. F. Khirnyi, N. I. Shevtsov, *et al.*, Funct. Mater. **1** (1), 19 (1994).
11. J. R. Clem, Phys. Rev. B **12** (6), 1742 (1975).
12. E. M. Lifshitz and L. P. Pitaevskiĭ, *Physical Kinetics* (Nauka, Moscow, 1979; Pergamon, Oxford, 1981).
13. A. M. Campbell and J. E. Evetts, Adv. Phys. **21** (2), 199 (1972).

Translated by N. Kovaleva

Physics of the Solid State, Vol. 43, No. 12, 2001, pp. 2213–2218. Translated from Fizika Tverdogo Tela, Vol. 43, No. 12, 2001, pp. 2121–2125.

The Band Structures of Superconducting MgB_2 and the Isostructural Compounds $CaGa_2$, AgB_2, AuB_2, $ZrBe_2$, and $HfBe_2$

I. R. Shein, N. I. Medvedeva, and A. L. Ivanovskiĭ

Institute of Solid-State Chemistry, Ural Division, Russian Academy of Sciences,
Pervomaĭskaya ul. 91, Yekaterinburg, 620219 Russia
e-mail: ivanovskii@ihim.uran.ru

Received April 27, 2001

Abstract—This paper reports on a self-consistent, full-potential LMTO calculation of the band structure of the medium-T_c superconductor MgB_2 and of the isostructural hexagonal phases of $CaGa_2$, $ZrBe_2$, $HfBe_2$, AgB_2, and AuB_2. The factors responsible for the superconducting properties of magnesium diboride are considered. The results obtained are compared with previous calculations and available experimental data. *© 2001 MAIK “Nauka/Interperiodica”.*

1. INTRODUCTION

The discovery of superconductivity in magnesium diboride [1] has focused considerable attention on its electronic structure. MgB_2 was the first compound found to occupy an intermediate place between low- and high-temperature superconductors in the magnitude of its T_c (~40 K). To stress this point, MgB_2 is referred to in the current literature as a medium-T_c superconductor (MTSC). An important feature of MgB_2 is its quasi-two-dimensional structure (AlB_2-type, space group D^1_{6h}–$P6/mmm$), which consists of hexagonal Mg layers and plane graphitelike boron networks stacked in the order…MgBMgB… [2–6].

As shown in studies on the isotope effect [7], tunneling [8], photoelectron [9], and vibrational spectroscopy [10], as well as on the band structure [11–17] and from phonon spectrum [18–20] calculations, the superconductivity in MgB_2 should be associated with strong electron–phonon coupling, the relatively high density of electronic states of the 2D-like $\sigma(p_{x,y})$ boron bands at the Fermi level [$N(E_F)$] and the existence of $p_{x,y}$ hole states at the Γ point in the Brillouin zone (BZ).

The above assumptions formed a basis for analyzing the superconducting characteristics of some solid solutions based on the MTSC phase (which were obtained by incorporating various electron or hole dopants into the magnesium or boron sublattices [14–17]), as well as of a number of related AlB_2-like stable and metastable diborides of Na, Li [13, 17], Be [14], Ca [16], and Al [15–17]. The band structure of 3d (Sc, Ti,…, Mn), 4d (Y, Zr,..., Ru), and 5d (La, Hf,…, Os) metal diborides was studied in [21, 22].

More than a hundred binary compounds with an AlB_2-type structure are presently known. In addition to the above diborides, this group contains various MX_2 phases, where Be, Si, Ga, Hg, Zn, Cd, Al, Cu, Ag, and Au can act as X elements forming graphitelike networks [2, 4]. The crystal structure parameters (the c/a ratio) of these phases vary within a wide range from 0.59 to 1.22. Because the main part in the electron–phonon interactions in the MgB_2 MTSC is played by the electronic and hole states and vibrational modes of boron atoms (in the networks) [18–20], it becomes obvious that possible nonboride analogs of MgB_2 should include light *sp* atoms as X elements.

We carried out a comparative analysis of the band structure of the MgB_2 MTSC (c/a = 1.142) and of the isostructural MX_2 phases where the graphitelike networks are formed of beryllium and gallium, namely, $ZrBe_2$, $HfBe_2$ (c/a = 0.85–0.84), and $CaGa_2$ (c/a = 1.00). Moreover, we considered the hypothetical diborides of Ag and Au. Although their existence (in equilibrium conditions) is questionable [2–6], these metals (as well as Cu), when added to MgB_2, may act as hole dopants. The radii of Ag and Au (1.13–1.37) are markedly larger than that of Mg^{2+} (0.74 Å); i.e., their incorporation into magnesium diboride is expected to increase the unit-cell volume and soften the phonon modes. Both above factors are considered [12–17] conducive to the possible improvement of the MTSC characteristics of MgB_2.

2. MODEL AND METHOD OF CALCULATION

Boron atoms in MgB_2 occupy the central position in Mg trigonal prisms, which share faces to form a three-dimensional arrangement [2–6]. The coordination numbers and coordination polyhedra of the Mg atoms are 20 and [$MgB_{12}Mg_8$], and those of the boron atoms

Table 1. Structural parameters of hexagonal MX_2 phases

Phase	a	c	c/a	X–X	M–X	V
MgB_2	3.084	3.522	1.142	1.781	2.504	29.010
$CaGa_2$	4.320	4.320	1.000	2.494	3.299	69.820
AgB_2	3.000	3.240	1.080	1.732	2.372	25.253
AuB_2	3.134	3.513	1.121	1.809	2.522	29.882
$ZrBe_2$	3.820	3.250	0.850	2.205	2.739	27.878
$HfBe_2$	3.788	3.168	0.836	2.187	2.700	27.177

Note: The lattice parameters a, c, c/a and the closest X–X and M–X atomic distances are given in Å, and the unit-cell volume V is given in Å^3 [2–6].

Table 2. Total density of states at the Fermi level $N(E_F)$ and the contributions of individual states (states/eV per unit cell) in hexagonal MX_2 phases

Phase	$N(E_F)$							
	total	Ms	Mp	Md	Mf	Xs	Xp	Xd
MgB_2	0.719	0.040	0.083	0.138	–	0.007	0.448	–
$CaGa_2$	1.486	0.028	0.177	0.696	–	0.012	0.546	0.027
AgB_2	2.000	0.032	0.066	0.570	–	0.057	1.333	–
AuB_2	2.153	0.144	0.068	0.655	–	0.069	1.258	–
$ZrBe_2$	1.680	0.002	0.112	1.091	–	0.002	0.473	–
$HfBe_2$	1.660	0.004	0.118	1.011	0.025	0.003	0.499	–

are 9 and [BMg_6B_3], respectively. The atom positions in the unit cell are as follows: the 1Mg(a) atom is at (0,0,0) and the 2B(d) atoms are at (1/3,2/3,1/2) and (2/3,1/3,1/2). The unit-cell parameters of MgB_2 and of the isostructural MX_2 phases ($CaGa_2$, $ZrBe_2$, $HfBe_2$, AgB_2, AuB_2) are given in Table 1. Their band structure was calculated using the self-consistent, full-potential, linear, muffin-tin orbital method (FLMTO) [23, 24] in terms of the density-functional theory with inclusion of relativistic effects in accordance with the scheme in [25] with the exchange correlation potential proposed in [26].

The atomic interactions in MX_2 were also analyzed using the tight-binding method in Hückel parametrization, which was used to estimate the crystal-orbital overlap population (a counterpart of the occupation (index) of pair atomic bonds that is well known in the quantum chemistry of molecules [27]).

3. DISCUSSION OF RESULTS

The results of the calculations made for MgB_2, $CaGa_2$, $ZrBe_2$, $HfBe_2$, AgB_2, and AuB_2 are presented in Figs. 1 and 2 and Table 2. We shall discuss them in comparison with the band structure of the MTSC MgB_2.

3.1. Magnesium Diboride

The energy bands and density-of-states functions of MgB_2 are displayed in Figs. 1 and 2. The valence-band energy spectrum of MgB_2 is seen to derive primarily from the B 2p states, which form two distinct groups of energy bands of the $\sigma(2p_{x,y})$ and $\pi(p_z)$ types with essentially different dispersion relations $E(k)$.

The dispersion $E(k)$ of the B $2p_{x,y}$ bands is the largest in the $k_{x,y}$ (Γ–K) direction. These bands reflect the boron-state distribution in the graphitelike network planes, are of the 2D type, and form plane sections in the k_z (Γ–A) direction. The B $2p_{x,y}$ bands contribute to the valence-band density of states (DOS) and form a resonant DOS peak (~2 eV below E_F, Fig. 2) associated with the van Hove singularity (VHS) at the M point of the BZ. These bands contribute noticeably to $N(E_F)$ and are responsible for the metal-like properties of the diboride. The B $2p_{x,y}$ bands within the Γ–A section lie above E_F and form cylindrical elements of the hole-type Fermi surface.

The B $2p_z$-like states are responsible for the weak interlayer coupling. These (3D-type) bands have maximum dispersion in the k_z (Γ–A) direction. The B s states are admixed to the B 2p-like bands near the valence band edge and in the conduction band (Fig. 2). A similar band structure was also obtained in other calculations [11–17] and can account for the MTSC properties of MgB_2 (for more details, see [11–13]).

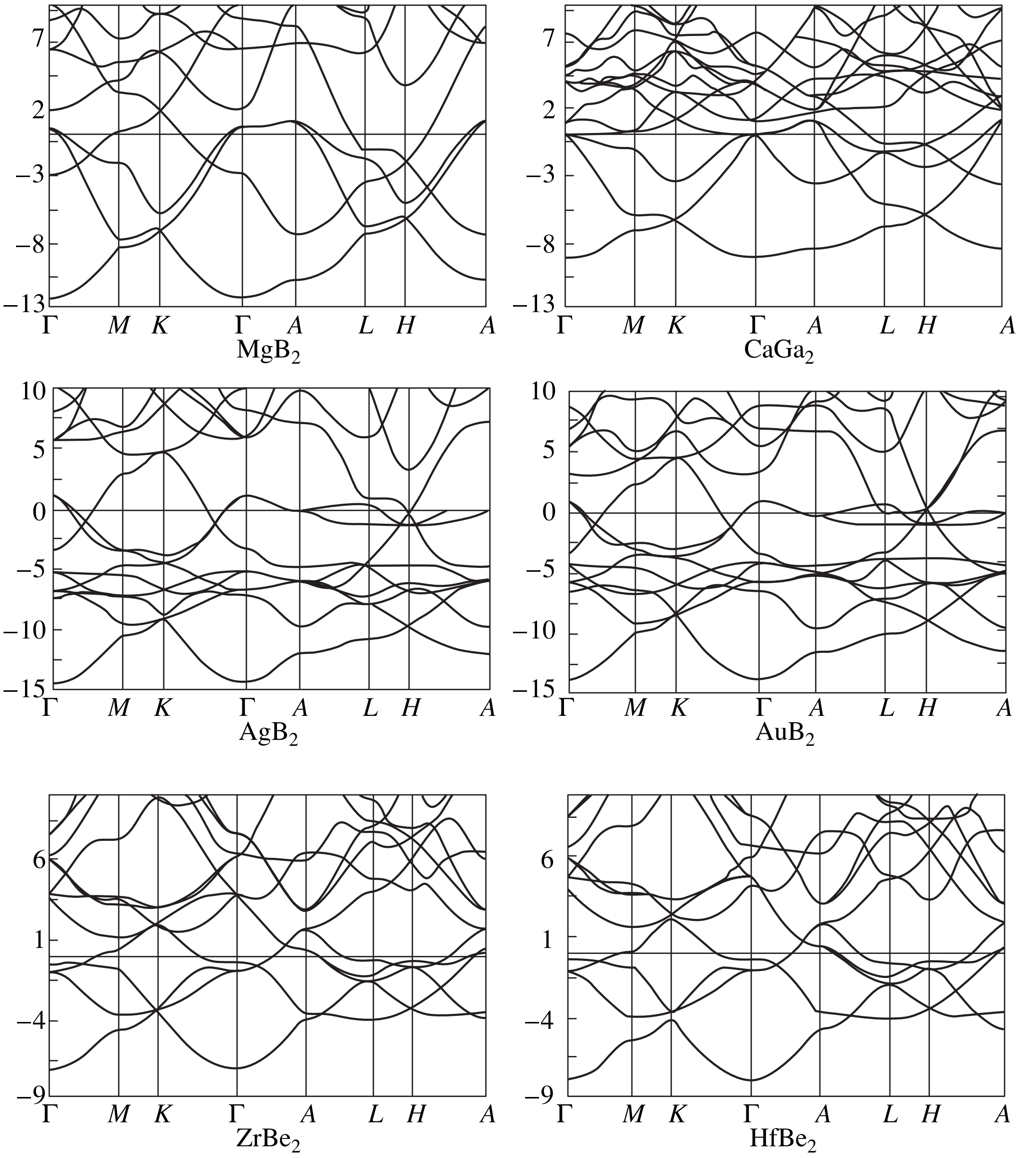

Fig. 1. Energy bands of MgB_2, $CaGa_2$, AgB_2, AuB_2, $ZrBe_2$, and $HfBe_2$.

Thus, the band spectrum of the MTSC MgB_2 has the following characteristic elements related to its superconducting properties and to the intra- and interlayer interactions: (1) the position of the degenerate 2*D*-like $\sigma(p_{x,y})$ bands relative to the BZ Γ point (the presence of hole states); (2) the energy splitting between the bonding and antibonding $\sigma(p_{x,y})$ bands (dependent on the intralayer B–B interactions); (3) the π-band dispersion in the Γ–*A* direction and the energy position of the crossing of the bonding and antibonding B 2*pz* bands (at the *K* point of the BZ; dependent on the interlayer Mg–B coupling); (4) the position of the VHSs of the quasi-two-dimensional σ bands relative to the Fermi level; and (5) the total density of states at the Fermi level and its partial composition. The above features of the band structure will be analyzed in the discussion of the other AlB_2-like phases.

3.2. $CaGa_2$

The energy bands of this phase (Fig. 1, see also [28]) differ strongly from those of the MTSC MgB_2. The $\sigma(p_{x,y})$ and $\pi(p_z)$ bands of the calcium gallide cross at the BZ Γ point and lie below E_F. The σ holes are present in low concentration near the *A* point. As a result, the topologies of the Fermi surface of MgB_2 and $CaGa_2$ are different: the cylinders (for MgB_2, in the Γ–*A* direction [11, 12]) degenerate into cones in $CaGa_2$. Note that a similar structure of the $\sigma(p_{x,y})$ bands was

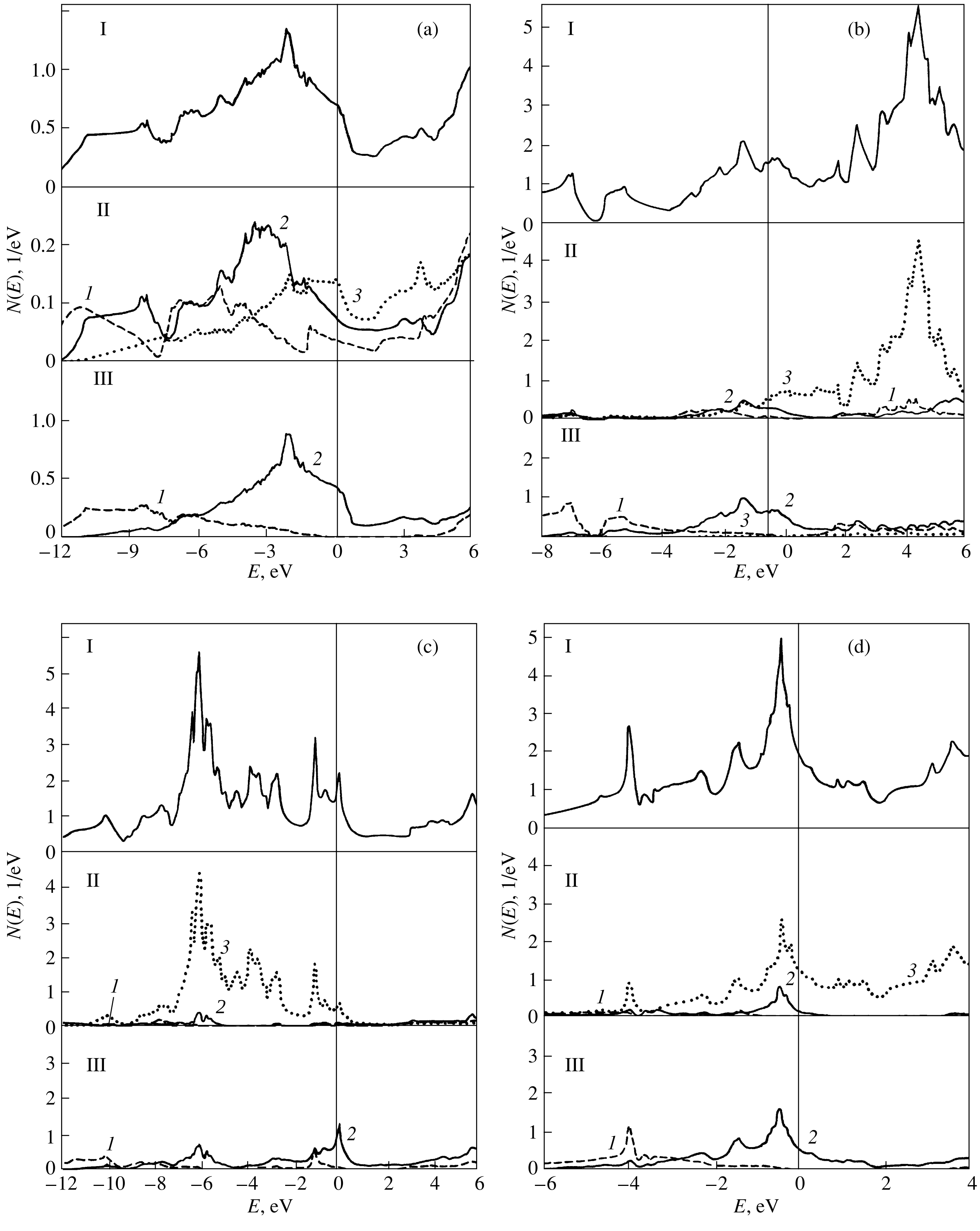

Fig. 2. Total (I) and local (II, III) densities of states of (a) MgB_2, (b) $CaGa_2$, (c) AgB_2, and (d) $ZrBe_2$. For each MX_2 phase, one can find the density-of-states contributions of (II) *M* atoms: (*1*) *s*, (*2*) *p*, (*3*) *d*; and (III) *X* atoms: (*1*) *s*, (*2*) *p*, (*3*) *d*.

obtained for isoelectronic and isostructural BeB_2 [15,16], which is not an MTSC [29].

The intra- (Ga–Ga) and interlayer (Ga–Ca) interactions in $CaGa_2$ are weaker than the respective interactions in MgB_2. This is seen from the decrease in both the splitting between the bonding and antibonding $\sigma(p_{x,y})$ bands and in the dispersion of the π band (in the Γ–A direction). The VHS of the σ band is shifted toward E_F, which may be due to the increasing unit-cell volume [$V(CaGa_2)/V(MgB_2) = 2.4$]. Similar shifts were shown to exist [14] for hypothetical CaB_2 and in model calculations of magnesium diboride with an extended lattice [17]. The main contribution to the density of states at the Fermi level (~61%) comes from the calcium states.

3.3. $ZrBe_2$ and $HfBe_2$

The structure of the valence band top of the beryllides is determined by the strong hybrid coupling between the (Zr, Hf) *d* and (Be) *sp* states (Figs. 1, 2). The Be σ bands exhibit noticeable dispersion in the Γ–A direction, and there are no hole states. The spectra of the Zr and Hf beryllides are similar (in the pattern of distribution of the energy bands, their composition, and filling) to those for the isostructural (and isoelectronic) diborides of Sc and Y [14, 16]. The latter are known to exhibit no superconductivity down to $T < 1.4$ K [4].

3.4. AgB_2 and AuB_2

The energy bands of these hypothetical diborides are the closest (among the phases considered here) to those of the MTSC MgB_2 (Fig. 1). The main differences in them are associated with the substantially smaller dispersion of the σ and π bands. The latter feature [as well as the lower energy position of the crossing point of the bonding and antibonding B $2p_z$ bands (at the K point of the BZ)] implies extremely weak interlayer coupling and is, apparently, one of the factors of instability (under normal conditions) of these diborides. On the other hand, the existence of a band of filled (Ag, Au) *d* states brings about an energy separation between the σ bands and the upper of them becomes localized near E_F (Figs. 1, 2). This entails a sharp increase (about threefold compared to MgB_2) in the density of B 2*p* states at the Fermi level (Table 2). This feature may be considered as conducive to the formation of superconducting properties in diborides.

In conclusion, consider the other bonding types (X–X, M–X, and M–M) using the crystal-orbital overlap population numbers (Table 3). For MgB_2, the in-plane B–B interactions in the graphitelike networks are dominant. This is in agreement with the calculated bond energies [30] (E_{bond} FLMTO calculation using the method from [21]), which indicates a dominant contribution from the B–B interactions [B–B (68%), B–Mg (23%), and Mg–Mg (9%)] to the total cohesion energy in MgB_2. A similar bonding type is also characteristic of $CaGa_2$ (Table 3).

Table 3. Crystal-orbital overlap populations of individual bonds in hexagonal MX_2 phases calculated using the tight-binding method (electron/bond)*

Phase	X–X	M–X	M–M
MgB_2	0.742	0.053	–0.009
$CaGa_2$	0.734	0.039	–0.002
AuB_2	0.292	0.030	0.022
$ZrBe_2$	0.241	0.102	0.039

* 12-atom M_4X_8 supercells were used in the calculations.

A radically different bonding system is realized in beryllides, where interactions of all types (e.g., for $ZrBe_2$, the Zr–Zr, Zr–Be, and Be–Be bonds) are comparable in strength (Table 2). Finally, similar calculations made for the hypothetical diborides of Ag and Au permit one to relate their instability both to the decrease in the M–B interlayer coupling (relative to MgB_2) and to the strong weakening of the B–B bonds in the networks. This undersaturation of the B–B bonds is accounted for by the substantially smaller electron density transfer from (Ag, Au) to B compared to the Mg ⟶ B transfer in magnesium diboride.

4. CONCLUSIONS

Thus, our calculations show that the band structure of the nonboride AlB_2-like phases, which involve *sp* elements making up graphitelike networks, differs strongly from that of MgB_2; therefore, a search for new MTSC phases among the former compounds (as well as among the *d* metal diborides, see [14, 16]) does not hold obvious promise. The main MTSC candidates among the AlB_2-like structures are probably the diborides of Group I and II elements, their solid solutions, or superstructures. As follows from calculations of the hypothetical Ag and Au diborides, the presence of these elements, e.g., as impurities (or in atomic layers) in solid solutions (or superstructures), can modify the MTSC properties of the magnesium diboride through an increase in the density of states at the Fermi level of the system.

REFERENCES

1. J. Nagamatsu, N. Nakagawa, T. Muranaka, *et al.*, Nature **410**, 63 (2001).
2. H. Goldschmidt, *Interstitial Alloys* (Butterworths, London, 1967).
3. G. V. Samsonov, T. I. Serebryakova, and V. A. Neronov, *Borides* (Atomizdat, Moscow, 1975).
4. G. V. Samsonov and I. M. Vinitskiĭ, *Refractory Compounds: Handbook* (Metallurgiya, Moscow, 1976).

5. Yu. B. Kuz'ma, *Crystal Chemistry of Borides* (Vishcha Shkola, Lvov, 1983).
6. T. I. Serebryakova, V. A. Neronov, and P. D. Peshev, *High-Temperature Borides* (Metallurgiya, Moscow, 1991).
7. S. L. Bud'ko, G. Lapertot, C. Petrovic, *et al.*, Phys. Rev. Lett. **86**, 1877 (2001).
8. A. Sharoni, I. Felner, and O. Millo, cond-mat/0102325 (2001).
9. T. Takahashi, T. Sato, S. Souma, *et al.*, cond-mat/0103079 (2001).
10. B. Gorshunov, C. A. Kutscher, P. Haas, *et al.*, cond-mat/0103164 (2001).
11. J. Kortus, I. I. Mazin, K. D. Belaschenko, *et al.*, cond-mat/0101446 (2001).
12. K. D. Belaschenko, M. van Schlifgaarde, and V. A. Antropov, cond-mat/0102290 (2001).
13. J. M. An and W. E. Pickett, cond-mat/0102391 (2001).
14. N. I. Medvedeva, A. L. Ivanovskii, J. E. Medvedeva, and A. J. Freeman, cond-mat/0103157 (2001).
15. G. Satta, G. Profeta, F. Bernardini, *et al.*, cond-mat/0102358 (2001).
16. N. I. Medvedeva, Yu. E. Medvedeva, A. L. Ivanovskiĭ, *et al.*, Pis'ma Zh. Éksp. Teor. Fiz. **73**, 378 (2001) [JETP Lett. **73**, 336 (2001)].
17. J. B. Neaton and A. Perali, cond-mat/0104098 (2001).
18. Y. Kong, O. V. Dolgov, O. Jepsen, and O. K. Andersen, cond-mat/0102499 (2001).
19. K. Bohnen, R. Heid, and B. Renker, cond-mat/0103319 (2001).
20. A. Liu, I. I. Mazin, and J. Kortus, cond-mat/0103570 (2001).
21. A. L. Ivanovskiĭ, N. I. Medvedeva, Yu. E. Medvedeva, *et al.*, Metallofiz. Noveĭshie Tekhnol. **20**, 41 (1998).
22. A. L. Ivanovskiĭ, N. I. Medvedeva, and Yu. E. Medvedeva, Metallofiz. Noveĭshie Tekhnol. **21**, 19 (1999).
23. M. Methfessel, C. Rodriquez, and O. K. Andersen, Phys. Rev. B **40**, 2009 (1989).
24. M. Methfessel and M. Scheffler, Physica B (Amsterdam) **172**, 175 (1991).
25. S. Y. Savrasov, Phys. Rev. B **54**, 16470 (1996).
26. S. H. Vosko, L. Wilk, and M. Nusair, Can. J. Phys. **58**, 1200 (1980).
27. A. L. Ivanovskiĭ and G. P. Shveĭkin, *Quantum Chemistry in Materials Science: Boron, Its Alloys and Compounds* (Izd. Ekaterinburg, Yekaterinburg, 1997).
28. S. Massidda and A. Baldereschi, Solid State Commun. **66**, 855 (1988).
29. I. Felner, cond-mat/0102508 (2001).
30. A. L. Ivanovskii and N. I. Medvedeva, Russ. J. Inorg. Chem. **45**, 1234 (2000).

Translated by G. Skrebtsov

Physics of the Solid State, Vol. 43, No. 12, 2001, pp. 2219–2228. Translated from Fizika Tverdogo Tela, Vol. 43, No. 12, 2001, pp. 2126–2134.
Original Russian Text Copyright © 2001 by Poklonski, Lopatin.

A Lattice Model of Thermopower in Hopping Conduction: Application to Neutron-Doped Crystalline Germanium

N. A. Poklonski and S. Yu. Lopatin
Belarussian State University, pr. F. Skoriny 4, Minsk, 220050 Belarus
e-mail: poklonski@bsu.by

Received April 13, 2001

Abstract—A model for describing hopping thermopower is proposed. Within the model, the majority and compensating impurities form a simple cubic lattice in a crystal matrix. The thermopower associated with hole (electron) hopping over hydrogen-like impurities is calculated with inclusion of their excited states. The results of calculations are compared with available experimental data on the low-temperature thermopower of Ge : Ga and the specific heat of Si : P in the dielectric region of the insulator–metal transition. *© 2001 MAIK “Nauka/Interperiodica”.*

1. INTRODUCTION

The differential thermopower α is equal to the ratio of the potential difference to the temperature difference across two points of a semiconductor sample when measured without loading. In the case when a higher electric potential corresponds to a lower temperature, the thermopower α is positive. In the short-circuit mode, the thermoelectric current inside a semiconductor flows from a hot point to a cold point; i.e., it is caused by the migration of positively charged particles [1–4].

The thermopower due to hopping transfer of electrons (holes) over hydrogen-like impurities in covalent crystalline semiconductors [5–9] has been less well understood compared to the thermopower associated with the hopping motion of small-radius polarons in the lattice of ionic crystals and glasses containing transition metal ions [10–14]. This can be explained in part by the fact that hopping conduction in crystalline semiconductors occurs over shallow-level impurities (Ge : Ga) at liquid-helium temperatures [8] and only over deep-level impurities (InP : Mn) at liquid-nitrogen temperatures [15].

In the case when a lattice site of an ionic crystal is occupied by one electron, the thermopower associated with hopping transfer of small-radius polarons is defined as [10, 11]

$$\alpha_{\text{pol}} = -\frac{k_{\text{B}}}{q}\left\{\ln\left(\beta\frac{1-C}{C}\right)+\frac{S_t^*}{k_{\text{B}}}\right\} = -\frac{1}{q}(S_c^*+S_t^*), \quad (1)$$

where k_{B} is the Boltzmann constant, q is the magnitude of the elementary charge, $C = n_p/N_s$ is the ratio of the number n_p of polarons to the number N_s of lattice sites per unit volume, S_t^* is the vibrational entropy corresponding to the ions surrounding a polaron (a crystal lattice site with a trapped electron), β is the degeneracy factor including the orbital and spin degeneracy of the polaron, $S_c^* = k_{\text{B}}\ln[\beta(1-C)/C]$ is the configurational entropy, and $S_t^* + S_c^*$ is the entropy carried by the polaron.

Note that, for the most part, relationship (1) adequately describes experimental data on the thermopower of polarons in glasses [13] at moderate temperatures. In the subsequent treatment, this relationship will be used only in order to establish an analogy between the thermopower of polarons and the thermopower caused by charge carrier hopping over impurities in covalent semiconductors when the thermal energy $k_{\text{B}}T$ exceeds the width W of the impurity energy band.

In many cases, it can be stated that the models describing incoherent hopping of small-radius polarons over lattice sites in ionic crystals are similar to those for hopping of electrons and holes over impurities (point lattice defects) in covalent crystals. In particular, Heikes [10] and Tuller and Nowick [11] assumed that incoherent migration of small-radius polarons over crystal lattice sites requires the formation of a barrier to hopping, i.e., the equalization of the energies of atomic configurations surrounding an electron between two lattice sites. In our recent work [16], the same assumption was used as the basis for calculating the hopping electrical conduction through hydrogen-like impurities forming a simple cubic lattice in a temperature-homogeneous (isothermal) crystal.

The aim of the present work was to generalize the model describing the hopping transfer of electrons (holes) over impurity lattice sites [16] to the case of covalent crystalline semiconductors with due regard for the temperature gradient, excited states, and finite degree of compensation of the impurity energy band.

2. HOPPING CURRENT IN THE PRESENCE OF A TEMPERATURE GRADIENT

For definiteness, we consider the hopping of holes over hydrogen-like acceptors that can occur only in the charge states 0 and –1. Compensating donors are completely ionized (i.e., they reside in a charge state +1) and do not participate in hopping conduction. The volume concentration of the majority dopant impurity is designated as N.

Let us assume that acceptors with the concentration $N = N_0 + N_{-1}$ and donors with the concentration KN form a simple cubic lattice with the translation period $R_h = [(1 + K)N]^{-1/3}$ in a crystal matrix. Here, K is the degree of compensation ($0 < K < 1$). In this case, acceptors and donors occupy lattice sites in a random manner. Hence, each of the impurity atoms has six nearest neighbors (the first coordination sphere of the impurity lattice). The crystal matrix is treated as a continuous medium with the permittivity $\varepsilon = \varepsilon_r\varepsilon_0$, where ε_0 is the permittivity of free space. The electroneutrality equation for the impurity lattice and matrix has the form $N_{-1} = KN$.

Now, we suppose that an external source produces a temperature gradient along the OX axis (the higher temperatures correspond to larger x) in a homogeneous crystal sample. In turn, this induces a thermoelectric field with the strength $E_i = -d\varphi/dx$, where $\varphi(x)$ is the electric potential along the OX axis.

The orientation of the coordinate system is chosen in such a way that the edge of a cubic unit cell in the impurity lattice is aligned parallel to the OX axis (i.e., it is parallel to the temperature gradient). Moreover, we assume that hole hopping occurs only between the nearest acceptors. This implies that the length of hole hopping from an acceptor in the charge state 0 to an acceptor in the charge state –1 is equal to R_h.

For the impurity lattice, the average probability that a neutral acceptor occupies an arbitrary site with the coordinate x is defined as $fN_0(x)/N$ and the average probability that an ionized acceptor is located at an arbitrary site with the coordinate $(x + R_h)$ is given by $fN_0(x + R_h)/N$. Here, $f = 1/(1 + K)$ is the correlation factor (the fraction of dopant atoms located at sites of the impurity lattice). Similarly, the probability that the nearest neighbor of a neutral acceptor (in the charge state 0) with the coordinate $x + R_h$ is an ionized acceptor (in the charge state –1) with the coordinate x is equal to $fN_{-1}(x)/N$. The surface concentrations of neutral acceptors in the impurity lattice planes, which are perpendicular to the OX axis and pass through sites with the coordinates x and $x + R_h$, are defined as $R_hN_0(x)$ and $R_hN_0(x + R_h)$, respectively.

The temperature gradient and the induced thermoelectric field bring about a change in the concentration of acceptors in the charge states 0 and –1 and a change in the frequency of hole hoppings along the OX axis. The difference between the mean number of holes hopping over acceptors along the OX axis and in the opposite direction determines the hopping current density $J_{0,-1} = J_h$, that is,

$$J_h = qR_hf\left[N_0(x)\frac{N_{-1}(x+R_h)}{N}\Gamma(x;\,x+R_h) - N_0(x+R_h)\frac{N_{-1}(x)}{N}\Gamma(x+R_h;\,x)\right], \tag{2}$$

where $\Gamma(x;\, x + R_h)$ and $\Gamma(x + R_h;\, x)$ are the average frequencies (dependent on the coordinate x and the distance R_h between sites of the impurity lattice) of hole hoppings along the OX axis and in the opposite direction, respectively, and $N_0(x) + N_{-1}(x) = N$.

In the absence of a temperature gradient, we have the equilibrium frequencies of hole hoppings in both directions, $\Gamma(x;\, x + R_h) = \Gamma(x + R_h;\, x) = \Gamma_h/2$, and the concentration of neutral acceptors $N_0(x) = N_0(x + R_h)$, so that the current density J_h is equal to zero.

For a weak thermoelectric field, we can write the following relationships:

$$N_0(x+R_h) \approx N_0(x) + R_h dN_0(x)/dx,$$
$$N_{-1}(x+R_h) \approx N_{-1}(x) + R_h dN_{-1}(x)/dx,$$
$$\Gamma(x+R_h;\,x) - \Gamma(x;\,x+R_h) \approx R_h d\Gamma/dx.$$

It follows from expression (2) that, in the linear approximation, the current density of holes hopping from acceptors in the charge state 0 to acceptors in the charge state –1 is represented by the formula

$$J_h = qN_h\left[-fR_h^2\frac{d\Gamma}{dx} - D_h\frac{d}{dx}\ln\left(\frac{N_0}{N_{-1}}\right)\right], \tag{3}$$

where $N_h(x) = N_0(x)N_{-1}(x)/N$ is the effective concentration of holes hopping between acceptors, $D_h = fR_h^2\Gamma_h/2$ is the diffusion coefficient of holes in the impurity lattice, and $dJ_h/dx = 0$.

Expression (3) can be transformed taking into account that the frequency of hole hoppings Γ and the concentration of neutral acceptors $N_0 = N - N_{-1}$ are functions of the electric potential $\varphi(x)$, the Fermi level $E_F(x)$, and the temperature $T(x)$ and that they depend on the coordinate x only through these quantities. We choose φ and T as independent variables for Γ, i.e., $\Gamma = \Gamma(\varphi, T)$, and E_F and T for N_0, i.e., $N_0(E_F, T)$. As a result, we obtain

$$\frac{d\Gamma}{dx} = \left(\frac{\partial\Gamma}{\partial\varphi}\right)\frac{d\varphi}{dx} + \left(\frac{\partial\Gamma}{\partial T}\right)\frac{dT}{dx},$$
$$\frac{dN_0}{dx} = -\frac{dN_{-1}}{dx} = \left(\frac{\partial N_0}{\partial E_F}\right)\frac{dE_F}{dx} + \left(\frac{\partial N_0}{\partial T}\right)\frac{dT}{dx}. \tag{4}$$

Here, the energy barriers to the migration of holes over acceptors are taken to be independent of the temperature gradient responsible for the phonon and hole fluxes in the crystal.

Upon substitution of relationships (4) into expression (3), we obtain the thermoelectric current density

$$J_h = qN_hM_h\left\{-\frac{d\varphi}{dx} - \frac{D_h}{M_h}\left(\frac{\partial}{\partial E_\mathrm{F}}\ln\frac{N_0}{N_{-1}}\right)\frac{dE_\mathrm{F}}{dx} - \frac{D_h}{M_h}\left(\frac{\partial}{\partial T}\ln\frac{N_0}{N_{-1}} + \frac{2}{\Gamma_h}\frac{\partial\Gamma}{\partial T}\right)\frac{dT}{dx}\right\}, \qquad (5)$$

where $M_h = fR_h^2\,\partial\Gamma/\partial\varphi > 0$ is the drift mobility of holes hopping over acceptors.

It should be noted that the parameters of the crystal, impurity atoms, and hopping holes in formula (5) are calculated under the assumption of a local thermodynamic equilibrium.

For an isothermal sample ($dT/dx = 0$) in an external electric field $E = -d\varphi/dx$, relationship (5) can be recast into the following expression for the dc density of holes hopping over acceptors [16]:

$$J_h = J_{0,-1}$$
$$= qN_h\left[M_hE - D_h\frac{d}{dx}\left(\ln\frac{N_0}{N_{-1}}\right)\right] = \sigma_hE - qD_h\frac{dN_0}{dx},$$

where $\sigma_h = qN_hM_h = qK(1-K)NM_h$ is the hopping electrical conductivity.

3. THERMOPOWER OF HOLES HOPPING OVER HYDROGEN-LIKE ACCEPTORS

Let us examine a lightly doped semiconductor with a classic impurity band in the case when the energy spread of impurity levels is considerably larger than the quantum resonant broadening of these levels [6]. As an example, we consider crystalline *p*-Ge with the concentration of gallium atoms $N = 3 \times 10^{16}$ cm^{-3} and the degree of their compensation $K = 0.35$ in the temperature range $T = 0$–10 K. At $K = 0.35$, the gallium concentration in germanium N_c, which corresponds to the insulator–metal transition, is equal to 1.85×10^{17} cm^{-3} [17].

It is assumed that the density of distribution of acceptor energy levels E_a in the band gap of the crystal can be described by the Gaussian [18]:

$$g = \frac{1}{W\sqrt{2\pi}}\exp\left(\frac{-(E_a - \overline{E_a})^2}{2W^2}\right), \qquad (6)$$

where $\overline{E_a} > 0$ is the average thermal ionization energy (reckoned from the valence band top of the undoped crystal) of a neutral acceptor and W is the root-mean-square fluctuation of the ionization energy of the neutral acceptor (the energy of affinity of a valence band hole with respect to a negatively charged acceptor).

According to the model proposed in [16], the effective width W of the acceptor band with inclusion of the Coulomb interaction of an ionized acceptor with ions involved in the first and second coordination spheres of the impurity lattice can be written as

$$W = \frac{q^2\sqrt{24}}{4\pi\varepsilon}\left(\frac{K}{1+K}\right)^{1/2}[(1+K)N]^{1/3}. \qquad (7)$$

Note that the inclusion of the interaction between each of the acceptors in the charge state –1 and ions involved only in the first coordination sphere of a simple cubic impurity lattice leads to an effective width W that is smaller than the width determined from formula (7) by a factor of $\sqrt{2}$.

We will first analyze the thermopower of holes hopping in the acceptor band at low temperatures when only the ground states of neutral acceptors are realized and then, at high temperatures, taking into account the excited states of these acceptors.

(A) For an isothermal crystal, the electroneutrality equation with allowance made for the distribution of ionization energies of neutral acceptor ground states [see relationship (6)] has the form

$$N_{-1} = N\int_{-\infty}^{+\infty} gf_{-1}dE_a = N\overline{f_{-1}} = N(1-\overline{f_0}) = KN, \qquad (8)$$

where $f_0 = 1 - f_{-1} = 1/\{1 + \beta_a^{-1}\exp[(E_\mathrm{F} - E_a)/k_\mathrm{B}T]\}$ is the probability that an acceptor with an ionization energy $E_a > 0$ occurs in a neutral charge state (i.e., it is filled with a hole), $E_\mathrm{F} > 0$ is the Fermi level reckoned from the valence band top (in the band gap of a *p*-type crystal), β_a is the degeneracy factor of an energy level ($\beta_a = 4$ for Ge : Ga), $\overline{f_{-1}} = N_{-1}/N = (1 - \overline{f_0}) = K$ is the average (over the impurity lattice) probability that a randomly chosen acceptor is ionized, and $k_\mathrm{B}T$ is the thermal energy.

The average ionization energy $\overline{E_a}$ of the neutral acceptor without regard for the shift and the distribution of energy states of the valence band top in the crystal is represented by the relationship [19]

$$\overline{E_a} = I_a - \frac{3q^2}{16\pi\varepsilon(\lambda + R_h)}. \qquad (9)$$

Here, I_a is the ionization energy of a single (isolated) acceptor, $R_h = [(1 + K)N]^{-1/3}$ is the minimum distance between ions in the impurity lattice, and λ is the screening length (radius) of an electrostatic field of an ion [20]:

$$\lambda^{-2} = \frac{q^2 N}{\varepsilon k_{\rm B} T}\int_{-\infty}^{+\infty} g f_0 f_{-1} dE_a \equiv \frac{q^2 K(1-K)N}{\varepsilon \xi_h k_{\rm B} T}. \tag{10}$$

According to [16, 20], the increase in the parameter

$$\xi_h = \frac{qD_h}{k_{\rm B} T M_h} = K(1-K)\left[\int_{-\infty}^{+\infty} g f_0 f_{-1} dE_a\right]^{-1} \geq 1 \tag{11}$$

with an increase in the amplitude of electrostatic potential fluctuations W reflects the fact that the hopping mobility M_h of holes decreases more rapidly compared to their diffusion coefficient D_h. This is explained by the fact that the actual trajectory of a hole diffusing over acceptors, on average, passes through lower barriers as compared to the barriers that are produced by an external electric field and are responsible for the drift mobility M_h of this hole (cf. the interpretation of the diffusion of atoms in disordered systems [21]).

Now, we assume that the energy location of the center of the acceptor band $\overline{E_a}$ with respect to the valence band top does not depend on the temperature and can be determined using formulas (9)–(11) in the case of a broad acceptor band ($W \gg k_{\rm B}T$). Then, the screening length squared can be written as $\lambda^2 = \varepsilon W\sqrt{2\pi}\exp(\eta^2)/(q^2N)$ [20], where η is determined from the electroneutrality equation (8) in the form $2K = 1 + \mathrm{erf}(\eta)$.

Since, in the linear transfer theory [1–4], the quantities outside the sign of differentiation with respect to x are treated as equilibrium parameters (independent of x), it follows from relationships (8) and (11) that

$$\frac{D_h}{M_h}\frac{\partial}{\partial E_{\rm F}}\left(\ln\frac{N_0}{N_{-1}}\right) = -\frac{1}{q}. \tag{12}$$

Hence, expression (5) with due regard for relationship (12) takes the form

$$J_h = \sigma_h\left\{\frac{d}{dx}\left(\frac{E_{\rm F}}{q} - \varphi\right) - \alpha_h\frac{dT}{dx}\right\}, \tag{13}$$

where α_h is the differential thermopower of holes hopping over acceptors.

From formulas (13) and (5) with allowance made for the expression $\partial N_{-1}/\partial T = -\partial N_0/\partial T$, we obtain the thermopower at $J_h = 0$:

$$\begin{aligned}\alpha_h &= \frac{d(E_{\rm F}/q - \varphi)/dx}{dT/dx}\\ &= \frac{\xi_h k_{\rm B} T}{q}\left\{\frac{\partial}{\partial T}\ln\frac{N_0}{N_{-1}} + \frac{2}{\Gamma_h}\frac{\partial \Gamma}{\partial T}\right\} = \alpha_{h1} + \alpha_{h2},\end{aligned} \tag{14}$$

where $\alpha_{h1} = \dfrac{\xi_h k_{\rm B} T}{qN_h}\dfrac{\partial N_0}{\partial T}$ and $\alpha_{h2} = \dfrac{\xi_h k_{\rm B} T}{q}\dfrac{2}{\Gamma_h}\dfrac{\partial \Gamma}{\partial T}$.

In order to elucidate the meaning of α_{h1} and α_{h2}, we express these quantities in terms of equilibrium parameters of the acceptor band and the crystal matrix.

The thermodynamic relationship for the differential of the electrochemical potential of holes ($E_{\rm F} - q\varphi$) in the acceptor band at a constant pressure and $J_h = 0$ has the form [12]

$$-dE_{\rm F} = -S_h dT - qd\varphi, \tag{15}$$

where S_h is the entropy of a hole in the acceptor band and $E_{\rm F}$ is the Fermi level ($E_{\rm F} > 0$).

From relationship (15), we obtain the differential thermopower

$$\alpha_h = \frac{1}{q}\frac{\partial(E_{\rm F} - q\varphi)}{\partial T} = \frac{S_c + S_t}{q}. \tag{16}$$

Here, by analogy with formula (1), the entropy S_h per hole is equal to the sum of the configurational S_c and thermal (vibrational) S_t entropies.

Next, we establish the correspondence between the kinetic and thermodynamic approaches to the calculation of the thermopower α_h of holes hopping over acceptors, i.e., the correspondence between formulas (14) and (16).

Using formulas (8) and (11) and the expression $\partial f_0/\partial T = (E_{\rm F} - E_a)f_0 f_{-1}/(k_{\rm B}T^2)$, we rewrite the first term in relationship (14) in the following form:

$$\begin{aligned}\alpha_{h1} &= \frac{1}{qT}\left[E_{\rm F} - \frac{\xi_h}{K(1-K)}\int_{-\infty}^{+\infty} gE_a f_0 f_{-1} dE_a\right]\\ &\equiv \frac{1}{qT}(E_{\rm F} - Q_a),\end{aligned} \tag{17}$$

where

$$Q_a = \frac{\int_{-\infty}^{+\infty} gE_a f_0 f_{-1} dE_a}{\int_{-\infty}^{+\infty} g f_0 f_{-1} dE_a}.$$

At high temperatures ($k_{\rm B}T \gg W$), when, according to formula (6), the density of distribution of acceptor energy levels $g \longrightarrow \delta(E - \overline{E_a})$ can be approximated by the Dirac delta function, we have $Q_a = \overline{E_a}$. In this case, from the electroneutrality equation (8) at $K = 0.35$ and $\beta_a = 4$, we obtain the Fermi level $E_{\rm F} = \overline{E_a} - k_{\rm B}T\ln[(1 - K)/(\beta_a K)]$. It is evident that the Fermi level shifts deep into the band gap with an increase in the temperature. Hence, it follows from expression (17) that $\alpha_{h1} = (E_{\rm F} -$

$\overline{E_a})/(qT) = (k_B/q)\ln[\beta_a K/(1-K)]$; i.e., α_{h1} for a narrow acceptor band takes a form similar to the first term on the left-hand side of formula (1) for the thermopower of small-radius polarons.

At low temperatures ($W \gg k_BT$), when $f_0 f_{-1} \longrightarrow k_BT\delta(E_a - E_F + k_BT\ln\beta_a)$, from relationship (17), we obtain the expression $Q_a = E_F - k_BT\ln\beta_a$ [19], so that $\alpha_{h1} = (k_B/q)\ln\beta_a$ at $T \longrightarrow 0$.

Therefore, by analogy with formula (1), the temperature behavior of α_{h1} defined by relationship (17) allows us to conclude that $q\alpha_{h1} = S_c$. Consequently, the term α_{h1} in expression (14) for the thermopower of holes is determined by the configurational entropy S_c of hole distribution over acceptors in the impurity lattice.

Let us demonstrate that the thermal entropy S_t [which, by comparing expressions (16) and (14), can be related to α_{h2}] is determined by the specific heat C_h per hole in the acceptor band at a constant pressure.

As follows from the temperature dependence of the average energy for a neutral acceptor,

$$E_h = \frac{1}{1-K}\int_{-\infty}^{+\infty} gE_a f_0 dE_a$$

and from Eq. (8), the specific heat (per hole in the acceptor band) can be represented in the form

$$C_h = -\frac{dE_h}{dT} = \frac{-1}{1-K}\left[\int_{-\infty}^{+\infty} gE_a\frac{\partial f_0}{\partial T}dE_a + \frac{dE_F}{dT}\int_{-\infty}^{+\infty} gE_a\frac{\partial f_0}{\partial E_F}dE_a\right] > 0. \tag{18}$$

By using the expression $d\overline{f_0}/dT = \partial\overline{f_0}/\partial T + (\partial\overline{f_0}/\partial E_F)(dE_F/dT) = 0$ and relationship (18), we obtain the specific heat of a hole in the acceptor band:

$$C_h = \frac{1}{(1-K)k_BT^2}\left[\int_{-\infty}^{+\infty} gE_a^2 f_0 f_{-1} dE_a - \frac{\xi_h}{K(1-K)}\left(\int_{-\infty}^{+\infty} gE_a f_0 f_{-1} dE_a\right)^2\right]. \tag{19}$$

From formula (19), we determine the thermal entropy S_t of the hole and the corresponding thermopower, that is,

$$\alpha_{h2} = \frac{S_t}{q} = \frac{1}{q}\int_0^T \frac{C_h}{T_*}dT_*. \tag{20}$$

At low temperatures ($W \gg k_BT$), from expression (19), we have $C_h = \gamma T$, where γ is a constant. Making allowance for the approximation $C_h = \gamma T$ in relationship (20), we obtain $\alpha_{h2} = C_h/q$.

(B) Now, we elucidate how the excited states of neutral acceptors affect the hopping thermopower.

The ionization energy of a neutral hydrogen-like acceptor in the lth excited state is defined as E_a/l^2. The degeneracy multiplicity of the energy level E_a/l^2 is expressed as $\beta_a l^2$, where $\beta_a = 4$ is the degeneracy multiplicity of the ground energy level E_a ($l = 1$) of the acceptor. According to [2, 4, 6], the probability of an acceptor occurring in the charge state 0 and the excited state $l \le l_t$ is determined by the formula

$$f_0(l) = \frac{\beta_a l^2\exp[(1-l^2)E_a/l^2k_BT]}{\beta_a(l_t) + \exp[(E_F - E_a)/k_BT]}, \tag{21}$$

where $\beta_a(l_t) = \beta_a\sum_{l=1}^{l_t} l^2\exp[(1-l^2)E_a/l^2k_BT]$ is the effective degeneracy factor of the acceptor level E_a.

It should be noted that the parameter l_t in formula (21) is chosen such that the Bohr radius $a_H(l_t) = l_t^2 q^2/(8\pi\varepsilon\overline{E_a})$ of the excited state of a hole on the acceptor does not exceed the mean distance between impurity dopant atoms [22]. In further calculations of the thermopower, we will restrict ourselves to the case of the ground state and three excited states ($l_t = 4$), because the Bohr radius becomes larger than the R_h parameter of the impurity lattice even at $l_t = 5$.

When l_t excited states are taken into account, according to relationship (21), the probability that the acceptor is not ionized is represented as

$$f_0(l_t) = \sum_{l=1}^{l_t} f_0(l) = \{1 + [\beta_a(l_t)]^{-1} \times\exp[(E_F - E_a)/k_BT]\}^{-1} = 1 - f_{-1}(l_t)$$

and the electroneutrality equation (8) takes the form

$$K = \int_{-\infty}^{+\infty} gf_{-1}(l_t)dE_a = \overline{f_{-1}(l_t)} = 1 - \overline{f_0(l_t)}, \tag{22}$$

where the Fermi level $E_F > 0$ depends on the number l_t of realized excited states of each neutral acceptor.

With due regard for expression (22), relationship (17) for the configurational thermopower of holes can be rearranged to give

$$\alpha_{h1}(l_t) = \frac{1}{qT}\left[E_F(l_t) - \frac{\xi_h(l_t)}{K(1-K)} \times\int_{-\infty}^{+\infty} gE_a f_0(l_t)f_{-1}(l_t)\frac{\gamma_a(l_t)}{\beta_a(l_t)}dE_a\right], \tag{23}$$

where

$$\xi_h(l_t) = K(1-K)\left(\int\limits_{-\infty}^{+\infty} g f_0(l_t) f_{-1}(l_t) dE_a\right)^{-1},$$

$$\gamma_a(l_t) = \beta_a \sum_{l=1}^{l_t} \exp\left[\frac{(1-l^2)E_a}{l^2 k_B T}\right].$$

The temperature dependence of the average energy of the neutral acceptor,

$$E_h(l_t) = \frac{1}{1-K}\int\limits_{-\infty}^{+\infty} g E_a \sum_{l=1}^{l_t} l^{-2} f_0(l) dE_a$$
$$= \frac{1}{1-K}\int\limits_{-\infty}^{+\infty} g E_a f_0(l_t)\frac{\gamma_a(l_t)}{\beta_a(l_t)} dE_a,$$

determines the specific heat per hole in the acceptor band:

$$C_h(l_t) = -\frac{dE_h(l_t)}{dT}$$
$$= \frac{-1}{1-K}\int\limits_{-\infty}^{+\infty} g E_a \frac{d}{dT}\left[f_0(l_t)\frac{\gamma_a(l_t)}{\beta_a(l_t)}\right] dE_a > 0, \quad (24)$$

where $dE_F(l_t)/dT = -\partial\overline{f_0(l_t)}/\partial T/(\partial\overline{f_0(l_t)}/\partial E_F)$.

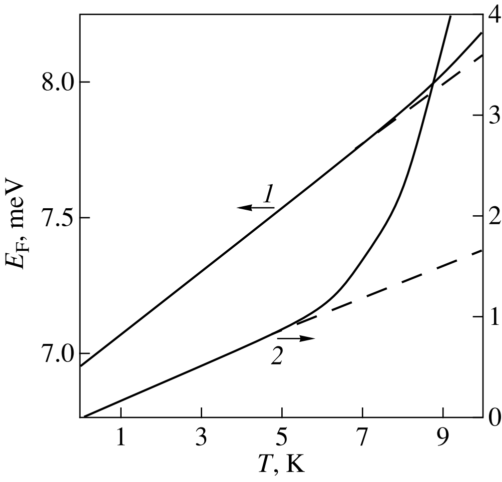

Fig. 1. Calculated temperature dependences of (*1*) the Fermi level [formulas (8) and (22)] and (*2*) the specific heat per hole in the acceptor band of Ge : Ga [formulas (19) and (24)] with inclusion of the ground state (dashed lines) and the ground and three excited states (solid lines) of neutral gallium atoms in germanium at $N = 3 \times 10^{16}$ cm^{-3} and $K = 0.35$.

Therefore, the thermopower that corresponds to the thermal entropy with inclusion of the excited states of neutral acceptors [see formula (21)] can be written as

$$\alpha_{h2}(l_t) = \frac{1}{q}\int\limits_0^T \frac{C_h(l_t)}{T_*} dT_*. \quad (25)$$

In the case when only the ground state of the neutral acceptor ($l_t = 1$) is taken into account, formulas (22)–(25) are transformed to relationships (8) and (17)–(20).

4. COMPARISON OF THEORETICAL AND EXPERIMENTAL DATA FOR Ge : Ga

Figure 1 shows the temperature dependences of the Fermi level E_F calculated using the electroneutrality equations (8) and (22) and the temperature dependences of the specific heat C_h determined from formulas (19) and (24) with and without inclusion of the excited states of neutral acceptors. As can be seen from Fig. 1, the effect of excited states on E_F and C_h for Ge : Ga ($N = 3 \times 10^{16}$ cm^{-3} and $K = 0.35$) manifests itself only at $T > 6$ K.

The temperature dependences of the hopping thermopower α_h calculated by formulas (17), (20), (23), and (25) for Ge : Ga ($\varepsilon_r = 15.4$ and $I_a = 11.32$ meV [23]) are displayed in Fig. 2. It is seen from Fig. 2 that the inclusion of the excited states of neutral acceptors (the fitting parameter is $l_t = 4$) enables us to explain the increase in the hopping thermopower with an increase in temperature. It is evident that the configurational component makes the main contribution to the hopping thermopower of Ge : Ga in the temperature range covered: $\alpha_{h1} \gg \alpha_{h2}$.

A drastic increase in the experimental values of the thermopower α at $T > 9$ K can be associated with the appearance of holes in the valence band and the hole–phonon drag [24].

5. DISCUSSION

5.1. We consider the thermopower associated with electron hopping among hydrogen-like donors in the charge states 0 and +1 with the concentration $N = N_0 + N_{+1}$ in the case when completely ionized acceptors with the concentration KN act as compensating impurities. The electroneutrality equation for a crystal without regard for excited states of neutral donors has the form

$$N_{+1} = N\int\limits_{-\infty}^{+\infty} g f_{+1} dE_d = N\overline{f_{+1}} = N(1-\overline{f_0}) = KN,$$

where $1 - f_{+1} = f_0 = \{1 + \beta_d \exp[-(E_F + E_d)/k_B T]\}^{-1}$ is the probability that a donor with an ionization energy $E_d > 0$ occurs in a neutral charge state (i.e., it is filled with an electron); $E_F < 0$ is the Fermi level reckoned from the conduction band bottom (in the band gap of an *n*-type crystal); β_d is the degeneracy factor of a donor energy level; and g is the density of distribution of energy levels in the donor band, which is defined by formulas (6) and (7).

According to relationships (3) and (13), the thermoelectric current density of electrons hopping over donors is represented by the expression

$$\begin{aligned} J_{0,+1} &= qN_h\left[fR_h^2\frac{d\Gamma}{dx} + D_h\frac{d}{dx}\ln\left(\frac{N_0}{N_{+1}}\right)\right] \\ &= \sigma_h\left[\frac{d}{dx}\left(\frac{E_F}{q} - \varphi\right) - \alpha_h\frac{dT}{dx}\right], \end{aligned} \tag{26}$$

where $N_h = K(1 - K)N$ is the effective concentration of electrons hopping among donors in the charge states 0 and +1. These electrons are characterized by the drift mobility $M_h = -fR_h^2\partial\Gamma/\partial\varphi > 0$ and the diffusion coefficients $D_h = fR_h^2\Gamma_h/2$.

After transformations similar to those represented by expressions (14)–(20), from relationship (26) at $J_{0,+1} = 0$, we obtain the differential thermopower of electrons in the donor band:

$$\alpha_h = \alpha_{h1} + \alpha_{h2} = -\frac{\xi_h k_B T}{q}\left\{\frac{\partial}{\partial T}\ln\frac{N_0}{N_{+1}} + \frac{2}{\Gamma_h}\frac{\partial\Gamma}{\partial T}\right\},$$

where

$$\alpha_{h1} = \frac{1}{qT}\left[E_F + \frac{\xi_h}{K(1-K)}\int_{-\infty}^{+\infty} gE_d f_0 f_{+1} dE_d\right],$$

$$\alpha_{h2} = \frac{1}{q}\int_0^T \frac{C_h}{T_*}dT_*,$$

$$\xi_h = K(1-K)\left(\int_{-\infty}^{+\infty} g f_0 f_{+1} dE_d\right)^{-1} \ge 1, \tag{27}$$

$$\begin{aligned} C_h &= \frac{1}{(1-K)k_B T^2}\left[\int_{-\infty}^{+\infty} gE_d^2 f_0 f_{+1} dE_d \right. \\ &\left. - \frac{\xi_h}{K(1-K)}\left(\int_{-\infty}^{+\infty} gE_d f_0 f_{+1} dE_d\right)^2\right] > 0. \end{aligned}$$

The calculations with the use of relationships (27) for Si : P ($\varepsilon_r = 11.5$, $I_d = 45.59$ meV [23], and $\beta_d = 1/2$) demonstrate that the dependence of C_h on T at low temperatures ($W \gg k_B T$) exhibits a nearly linear behavior. For example, at $N = 3.5 \times 10^{17}$ cm^{-3} and $K = 0.01$, from relationships (27), we have $C_h/T \approx 1.4$ μJ K^{-2} mol^{-1}. This agrees with the experimental data on the electronic specific heat of Si : P samples in the dielectric region with respect to the insulator–metal transition [25, 26] ($N < N_c = 3.5 \times 10^{18}$ cm^{-3} according to the data on N_c taken from [27]).

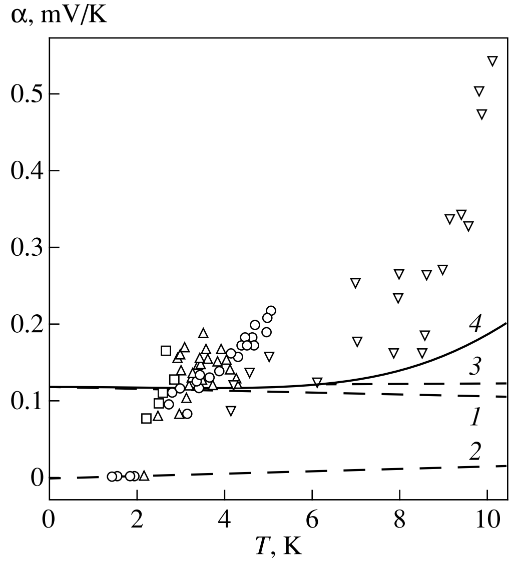

Fig. 2. Temperature dependences of the hopping thermopower α_h calculated according to formulas (17), (23) and (20), (25) for Ge : Ga ($N = 3 \times 10^{16}$ cm^{-3}, $K = 0.35$): (*1*) α_{h1}, (*2*) α_{h2}, (*3*) $\alpha_h = \alpha_{h1} + \alpha_{h2}$ (without regard for excited states), and (*4*) α_h with inclusion of three excited states of neutral Ga atoms. Points are the experimental thermopowers α taken from [7, 8]. The sample volume is 13 × 2.5 × 0.5 mm^3.

The specific heats C_h calculated from relationships (27) are also in agreement with the results obtained by the Monte Carlo simulation of thermal excitations of electrons within the donor band in a semiconductor at the degree of compensation $K = 0.5$ [28]. In particular, at $N = 3.5 \times 10^{17}$ cm^{-3} and $T \approx 2.6$ K, the specific heat C_h per neutral donor in Si is approximately equal to 4 μeV/K [28] (cf. Fig. 1).

5.2. It is known that, in a doped crystalline semiconductor, acceptors of the same sort at low temperatures can reside in three charge states: +1, 0, and –1 [29, 30]. The total concentration of acceptors is taken as $N = N_{+1} + N_0 + N_{-1}$. The electroneutrality equation has the form $N_{-1} = N_{+1} + KN$, where KN is the concentration of donors that compensate for acceptors and reside in the charge state +1. Hence, the acceptor energy levels form two energy bands A^0 and A^+ in the band gap [29].[1] These are the so-called bottom (*b*) and top (*t*) Hubbard bands. In this case, apart from the hopping of holes from acceptors in the charge state 0 to acceptors in the charge state –1, hole hopping from acceptors in the charge state +1 to acceptors in the charge state 0

---

[1] Note that both the A^+ band and excited states of hydrogen-like acceptors can simultaneously manifest themselves in the case of hopping conduction in lightly compensated doped semiconductors [30].

becomes possible. For an isothermal sample in an external electric field E, the current density $J_{+1,0}$ of holes in the A^+ band is represented in the form [31]

$$J_{+1,0} = qN_{+1,0}\left[M_{+1,0}E - D_{+1,0}\frac{d}{dx}\ln\left(\frac{N_{+1}}{N_0}\right)\right], \qquad (28)$$

where $N_{+1,0} = N_{+1}N_0/N$ is the concentration of holes hopping among acceptors in the charge states +1 and 0, $M_{+1,0} = fR_h^2\partial\Gamma_{+1,0}/\partial\varphi > 0$ is the drift mobility of holes in the A^+ band, $D_{+1,0} = fR_h^2\Gamma_{ht}/2$ is the diffusion coefficient of holes in the A^+ band, $\Gamma_{ht}/2$ is the equilibrium frequency of hole hoppings in the A^+ band in the same direction along the OX axis, $f = 1/(1+K)$, and $R_h = [(1+K)N]^{-1/3}$.

Without regard for the excited states of holes, the probability of an acceptor with an energy E_k occurring in one of the three charge states $k = -1$, 0, and +1 is determined by the relationship [2, 32]

$$f_k = \left\{\sum_{s=-1}^{+1}\frac{\beta_s}{\beta_k}\exp\left[\frac{(k-s)E_F + E_k - E_s}{k_BT}\right]\right\}^{-1}, \qquad (29)$$

where $E_{-1} - E_0 = E_b > 0$ and $E_0 - E_{+1} = E_t > 0$ are the acceptor energy levels forming the A^0 and A^+ bands, respectively; $E_F > 0$ is the Fermi level in the band gap of a p-type crystal; and $\beta_0/\beta_{-1} = \beta_{+1}/\beta_0 = 4$ are the degeneracy factors of the E_b and E_t levels for Ge : Ga, respectively.

The densities of distributions g_b and g_t of the energy levels E_b and E_t with respect to $\overline{E}_b$ and $\overline{E}_t$, which correspond to the centers of the A^0 and A^+ bands, can be written, by analogy with formula (6), in the following form:

$$g_{b(t)} = \frac{1}{\sqrt{2\pi}W_{b(t)}}\exp\left[\frac{-(E_{b(t)} - \overline{E}_{b(t)})^2}{2W_{b(t)}^2}\right], \qquad (30)$$

where the subscript b refers to the A^0 band, the subscript t denotes the A^+ band located at a shorter distance from the valence band, and $W_b = W_t \geq W$.

The average (over the crystal) concentration of acceptors in the charge state k ($k = -1$, 0, and +1) with allowance made for expressions (29) and (30) can be expressed by the formula

$$N_k = N\int_{-\infty}^{+\infty}\int_{-\infty}^{+\infty} g_bg_tf_k\,dE_b\,dE_t. \qquad (31)$$

By analogy with the derivation of formula (14), from relationships (28)–(31), we obtain the thermopower related to the configurational entropy S_c of holes hopping in the A^0 and A^+ bands, that is,

$$\alpha_{b1} = \frac{\xi_bk_BT}{q}\frac{\partial}{\partial T}\ln\frac{N_0}{N_{-1}}, \qquad \alpha_{t1} = \frac{\xi_tk_BT}{q}\frac{\partial}{\partial T}\ln\frac{N_{+1}}{N_0}, \qquad (32)$$

where

$$\xi_{b(t)} = \int_{-\infty}^{+\infty}\int_{-\infty}^{+\infty} g_bg_tf_{-1(+1)}\,dE_b\,dE_t\int_{-\infty}^{+\infty}\int_{-\infty}^{+\infty} g_bg_tf_0\,dE_b\,dE_t \times\left(\int_{-\infty}^{+\infty}\int_{-\infty}^{+\infty} g_bg_tf_{-1(+1)}f_0\,dE_b\,dE_t\right)^{-1} \geq 1.$$

According to [7, 8], the energy gap $\varepsilon_2 = \overline{E}_b - \overline{E}_t$ between the A^0 and A^+ bands in Ge : Ga ($N = 3\times10^{16}$ cm^{-3} and $K = 0.35$) is taken equal to 2 meV. Then, the calculation with the use of relationships (32) at $W_b = W_t = W$ and $T \leq 10$ K yields the configurational component of the thermopower of holes in the A^0 band $\alpha_{b1} \approx 0.1$ mV/K, which is larger in magnitude than the configurational component α_{t1} for the A^+ band by a factor of approximately 1.5. The thermopower component $\alpha_{b(t)2}$, which corresponds to the thermal entropy in each of the bands, is considerably less than the configurational component $\alpha_{b(t)1}$.[2] Hence, the thermopowers of holes in the A^0 and A^+ bands can be represented as $\alpha_b = \alpha_{b1} + \alpha_{b2} \approx \alpha_{b1}$ and $\alpha_t = \alpha_{t1} + \alpha_{t2} \approx \alpha_{t1}$.

The total thermopower with the inclusion of hole hopping in the A^0 and A^+ bands is determined from the relationship [1–4]

$$\alpha_h = \frac{\sigma_b\alpha_b + \sigma_t\alpha_t}{\sigma_b + \sigma_t}, \qquad (33)$$

where σ_b and σ_t are the electrical conductivities in the A^0 and A^+ acceptor bands, respectively.

It follows from relationship (33) that the total thermopower α_h cannot exceed the largest thermopower component (α_b or α_t) at an arbitrary ratio between the σ_b and σ_t hopping electrical conductivities.

Thus, the inclusion of the A^+ acceptor band (in addition to the A^0 band) does not lead to better agreement between the calculated and experimental thermopowers [7, 8].

5.3. To this point, the question as to the observed decrease in the thermopower α of Ge : Ga at $T \leq 2$ K to vanishingly small and experimentally unobservable values [7, 8] remains open. In the local thermodynamic

---

[2] The validity of the inequality $\alpha_{h1} \gg \alpha_{h2}$ in the case of a single A^0 band without regard for the excited states of neutral acceptors is evident from Fig. 2.

equilibrium approximation for samples of an infinite size, relationship (17) gives a finite thermopower $\alpha_{h1} = (k_B/q)\ln\beta_a \approx 0.12$ mV/K at $T \longrightarrow 0$. Since the mechanisms of scattering of a nonequilibrium phonon flux at $T < 2$ in samples of a finite size have not been clearly understood, we restrict ourselves to qualitative considerations.

As is known [33, 34], holes are dragged only by phonons whose energy corresponds to the difference between the levels of two acceptors (the potential well of elastic strain can trap a hole from a neutral acceptor and carry it to an ionized acceptor). A decrease in the temperature leads to a decrease in the number of these phonons, and, as a consequence, the thermopower decreases to zero. In this case, the hopping electrical conductivity exhibits a finite value, because the change in the frequency of hole hoppings over acceptors along the sample is caused by an external electric field.

Zvyagin [9] assumed that the electron–phonon interaction ceases at temperatures at which the mean free path of phonons exceeds the sample size.

It should also be noted that the thermal conductivity of liquid helium at $T < 1$ K is so high that vapor bubbles have no time to be formed in the bulk of the liquid, whereas the heat is rapidly removed toward the liquid surface [35]. The use of partially superfluid helium as a thermostat (when phonons leave the sample after their first collision with the sample surface) leads to a radical change in the boundary conditions on the surface [36]. Hence, the inequality $\alpha(T = 1.5\ K) \lll \alpha(T = 2.5\text{ K})$ [7, 8] can be dictated by the conditions of heat removal into the cryogenic medium rather than by the properties of the p-Ge sample itself. It is quite possible that the observed decrease in the thermopower α at $T \le 2$ K to experimentally unobservable values is caused by both diffusion processes and a rapid escape of nonequilibrium phonons from the sample ($13 \times 2.5 \times 0.5$ mm^3) owing to the unique properties of liquid helium at temperatures below the λ point ($T < 2.17$ K).

6. CONCLUSION

Thus, we obtained the relationship for the thermopower associated with phonon-assisted motion of holes over hydrogen-like acceptors. This relationship was derived within the lattice approximation on the basis of the hopping current density equation. It was demonstrated that the expression derived for the thermopower of hopping holes provides a satisfactory explanation of the plateau (in the range 2–8 K) occurring in the experimental temperature dependence of the thermopower for Ge : Ga at an intermediate degree of compensation [7, 8]. The increase in thermopower with an increase in temperature was interpreted in terms of the contribution from excited states of hopping holes to the thermopower. It was shown that the lattice approach can be applied to the description of the specific heat of electrons hopping over hydrogen-like donors in Si : P.

ACKNOWLEDGMENTS

We are grateful to A.G. Zabrodskiĭ, S.V. Egorov, and S.A. Vyrko for their participation in discussions of the results.

REFERENCES

1. F. J. Blatt, P. A. Schroeder, C. L. Foiles, and D. Greig, *Thermoelectric Power of Metals* (Plenum, New York, 1976; Metallurgiya, Moscow, 1980).
2. V. L. Bonch-Bruevich and S. G. Kalashnikov, *Physics of Semiconductors* (Nauka, Moscow, 1990).
3. Yu. G. Gurevich and G. N. Logvinov, Fiz. Tekh. Poluprovodn. (St. Petersburg) **26** (11), 1945 (1992) [Sov. Phys. Semicond. **26**, 1091 (1992)].
4. K. Seeger, *Semiconductor Physics* (Springer-Verlag, Berlin, 1999).
5. V. V. Kosarev, Fiz. Tekh. Poluprovodn. (Leningrad) **8** (7), 1378 (1974) [Sov. Phys. Semicond. **8**, 897 (1974)].
6. I. P. Zvyagin, in *Kinetic Phenomena in Disordered Semiconductors* (Moscow Gos. Univ., Moscow, 1984), p. 192.
7. A. G. Andreev, A. G. Zabrodskiĭ, I. P. Zvyagin, and S. V. Egorov, Fiz. Tekh. Poluprovodn. (St. Petersburg) **31** (10), 1174 (1997) [Semiconductors **31**, 1008 (1997)].
8. A. G. Andreev, A. G. Zabrodskii, S. V. Egorov, and I. P. Zvyagin, Phys. Status Solidi B **205** (1), 381 (1998).
9. I. P. Zvyagin, Phys. Status Solidi B **205** (1), 391 (1998).
10. R. R. Heikes, in *Thermoelectricity: Science and Engineering* (Interscience, New York, 1961), Chap. 4, p. 75.
11. H. L. Tuller and A. S. Nowick, J. Phys. Chem. Solids **38** (8), 859 (1977).
12. J. M. Honig, in *Problems in Thermodynamics and Statistical Physics*, Ed. by P. T. Landsberg (PION, London, 1971; Mir, Moscow, 1974), Chap. 19.
13. T. N. Kennedy and J. D. Mackenzie, Phys. Chem. Glasses **8** (5), 169 (1967).
14. D. Emin, Phys. Status Solidi B **205** (1), 385 (1998).
15. V. P. Kuznetsov, M. A. Messerer, and É. M. Omel'yanovskiĭ, Fiz. Tekh. Poluprovodn. (Leningrad) **18** (3), 446 (1984) [Sov. Phys. Semicond. **18**, 278 (1984)].
16. N. A. Poklonskiĭ, S. Yu. Lopatin, and A. G. Zabrodskiĭ, Fiz. Tverd. Tela (St. Petersburg) **42** (3), 432 (2000) [Phys. Solid State **42**, 441 (2000)].
17. A. G. Zabrodskii, A. G. Andreev, and S. V. Egorov, Phys. Status Solidi B **205** (1), 61 (1998).
18. J. M. Ziman, *Models of Disorder: The Theoretical Physics of Homogeneously Disordered Systems* (Cambridge Univ. Press, Cambridge, 1979; Mir, Moscow, 1982).
19. N. A. Poklonskiĭ, A. I. Syaglo, and G. Biskupski, Fiz. Tekh. Poluprovodn. (St. Petersburg) **33** (4), 415 (1999) [Semiconductors **33**, 402 (1999)].
20. N. A. Poklonski and V. E. Stelmakh, Phys. Status Solidi B **117** (1), 93 (1983).
21. D. K. Belashchenko, Usp. Fiz. Nauk **169** (4), 361 (1999).
22. W. Ebeling, W. D. Kraeft, and D. Kremp, *Theory of Bound States and Ionization Equilibrium in Plasmas and Solids* (Akademie-Verlag, Berlin, 1976; Mir, Moscow, 1979).

23. T. M. Lifshits, Prib. Tekh. Éksp., No. 1, 10 (1993).
24. E. Kaden and H.-L. Günter, Phys. Status Solidi B **126** (2), 733 (1984).
25. N. Kobayashi, S. Ikehata, S. Kobayashi, and W. Sasaki, Solid State Commun. **24** (1), 67 (1977).
26. J. R. Marko, J. P. Harrison, and J. D. Quirt, Phys. Rev. B **10** (6), 2448 (1974).
27. N. A. Poklonskiĭ and A. I. Syaglo, Fiz. Tverd. Tela (St. Petersburg) **40** (1), 147 (1998) [Phys. Solid State **40**, 132 (1998)].
28. S. D. Baranovskiĭ, A. A. Uzakov, and A. L. Éfros, Zh. Éksp. Teor. Fiz. **83** (2), 756 (1982) [Sov. Phys. JETP **56**, 422 (1982)].
29. A. P. Mel'nikov, Yu. A. Gurvich, L. N. Shestakov, and E. M. Gershenzon, Pis'ma Zh. Éksp. Teor. Fiz. **66** (4), 232 (1997) [JETP Lett. **66**, 249 (1997)].
30. Ya. E. Pokrovskiĭ, O. I. Smirnova, and N. A. Khval'kovskiĭ, Zh. Éksp. Teor. Fiz. **112** (1), 221 (1997) [JETP **85**, 121 (1997)].
31. N. A. Poklonskiĭ and S. Yu. Lopatin, Fiz. Tverd. Tela (St. Petersburg) **40** (10), 1805 (1998) [Phys. Solid State **40**, 1636 (1998)].
32. N. A. Poklonskiĭ and A. I. Syaglo, Fiz. Tekh. Poluprovodn. (St. Petersburg) **33** (4), 402 (1999) [Semiconductors **33**, 391 (1999)].
33. A. G. Kozorezov, Zh. Éksp. Teor. Fiz. **100** (5), 1577 (1991) [Sov. Phys. JETP **73**, 872 (1991)].
34. B. A. Danil'chenko and S. Kh. Rozhko, Fiz. Tverd. Tela (Leningrad) **32** (4), 984 (1990) [Sov. Phys. Solid State **32**, 579 (1990)].
35. R. F. Barron, *Cryogenic Systems* (Oxford Univ. Press, Oxford, 1985; Énergoatomizdat, Moscow, 1989).
36. V. I. Kozub and A. M. Rudin, Fiz. Tverd. Tela (St. Petersburg) **38** (2), 337 (1996) [Phys. Solid State **38**, 189 (1996)].

Translated by O. Borovik-Romanova

Physics of the Solid State, Vol. 43, No. 12, 2001, pp. 2229–2233. Translated from Fizika Tverdogo Tela, Vol. 43, No. 12, 2001, pp. 2135–2139.
Original Russian Text Copyright © 2001 by Kukushkin, Bessolov, Osipov, Luk'yanov.

SEMICONDUCTORS AND DIELECTRICS

Nucleation of III Nitride Semiconductors in Heteroepitaxy

S. A. Kukushkin*, V. N. Bessolov, A. V. Osipov*, and A. V. Luk'yanov*****
** Institute for Problems of Mechanical Engineering, Russian Academy of Sciences,*
Bol'shoĭ pr. 61, Vasil'evskiĭ ostrov, St. Petersburg, 199178 Russia
*** Ioffe Physicotechnical Institute, Russian Academy of Sciences, Politekhnicheskaya ul. 26, St. Petersburg, 194021 Russia*
**** Foundation for Support of Science and Education, St. Petersburg, 192007 Russia*
e-mail: ksa@math.ipme.ru

Received April 18, 2001; in final form, May 7, 2001

Abstract—The nucleation of III nitride semiconductors in heteroepitaxy is theoretically investigated using GaN nucleation on the AlN surface as an example. It is inferred that the mechanism of this process is determined by the temperature at the initial stage of the layer formation (T). At low temperatures ($T < 500$°C), liquid gallium droplets appear and the chemical reaction between the Ga and N atoms results in the formation of GaN nuclei. At substrate temperatures $T > 650$°C, there arise only GaN nuclei. It is revealed that the GaN nucleation is governed by the generalized diffusion coefficient of GaN, which is a combination of the diffusion coefficients for gallium and nitrogen atoms. It is shown that the generalized diffusion coefficient of GaN on the crystal surface increases by seven orders of magnitude as the growth temperature increases from 600 to 800°C. This is accompanied by a change in the growth mechanism of the III nitride semiconductor epitaxial layers. © *2001 MAIK "Nauka/Interperiodica".*

1. INTRODUCTION

In recent years, gallium nitride epitaxial films have found wide application in microwave electronics. However, the development of high-efficient gallium nitride elements has been hampered by two factors: (1) the absence of a perfect substrate material and (2) problems associated with the incorporation of nitrogen atoms into a growing layer. Single crystals (GaAs, ZnO, MgO, $MgAl_2O_3$ and, especially, SiC, Al_2O_3, and Si) are extensively used as substrates for the heteroepitaxial growth of GaN. A substantial mismatch between the parameters of a GaN epitaxial wurtzite layer and ^6H-SiC (~4%), Al_2O_3 (~15%) [1], and Si (22.3%) [2] substrates and a large difference between the adsorption energies of Ga and N atoms (the adsorption energy for nitrogen atoms is 1.5 times higher than that of III–V semiconductors [3]) considerably impede the epitaxial growth of III nitride semiconductor films. As is known, the early stages of formation of these films (nucleation and the subsequent evolution of islands) are of crucial importance in preparing qualitative epitaxial layers of III nitride semiconductors. Recent attempts have been made to optimize the conditions of the formation of a GaN buffer layer on a sapphire substrate due to chemical gas-transport reactions [or metal–organic chemical vapor deposition (MOCVD)] through changing the conditions of GaN nucleation [4] and to improve the kinetic transport of reactants to substrates [5]. Chen *et al.* [6] revealed that the nucleation during GaN epitaxy on different GaN and AlN buffer layers grown on GaAs substrates proceeds by different mechanisms. Moreover, King *et al.* [7] proved that the growth of epitaxial layers of GaN on AlN (and AlN on GaN) in molecular beam epitaxy (MBE) with an NH_3 gas source occurs through the Stranski–Krastanov mechanism at low substrate temperatures ($T_{sub} < 800$°C) and the Frank–van der Merve mechanism at high substrate temperatures ($T_{sub} > 800$°C).

However, the mechanisms of III nitride semiconductor nucleation and the specific features of film growth are still not clearly understood. In the present paper, we propose a model that describes the initial stages of growth of a gallium nitride film in heteroepitaxy. This approach is based on the theory of nucleation and growth of thin films, which was described in detail in [8, 9]. According to this theory, the growth of crystal films occurs in several stages: nucleation, evolution of new-phase islands, interaction of islands with one another, and interaction of islands with the flux of atoms arriving at the surface (the Ostwald ripening stage). Different islands can also move as a unit over the substrate surface, coalesce, and participate in other interactions [8, 9].

2. THEORETICAL ANALYSIS

The growth of gallium nitride films will be treated within the modern theory of first-order phase transitions. We consider the nucleation stage by using the example of MBE and MOCVD growth of GaN films on a sapphire substrate covered with an AlN buffer layer. In the former case (molecular-beam epitaxial growth), GaN is prepared through the evaporation of gallium and nitrogen. Nitrogen is formed by the decomposition of ammonia, and then the following reaction proceeds:

$$\mathrm{Ga}_{(g)} + \mathrm{N}_{(g)} \longrightarrow \mathrm{GaN}_s, \tag{1}$$

where the subscripts g and s refer to the gaseous and solid reaction products, respectively.

In the latter case, the growth of GaN occurs through the reaction

$$2\mathrm{Ga}_{(g)} + 2\mathrm{NH}_{3_{(g)}} \longrightarrow 2\mathrm{GaN}_{(s)} + 3\mathrm{H}_{2_{(g)}}\uparrow. \tag{2}$$

In our consideration, we disregard the effect of elastic stresses on all stages of GaN layer growth.

Gallium nitride is a stoichiometric compound. According to the theory developed earlier in [10], the formation of GaN islands can occur in accordance with the following scenarios.

(1) The rate of the chemical reaction considerably exceeds the rate of formation of new-phase islands. In this case, the formation of molecules of the chemical compound precedes the nucleation of islands from these molecules.

(2) If the rate of island nucleation is substantially higher than the rate of formation of the chemical compound on a substrate, heterophase fluctuations bring about the formation of islands consisting of a mixture of the compounds involved and then the chemical reaction proceeds inside these islands with the formation of a stoichiometric compound.

(3) The rate of the chemical reaction is comparable to the rate of island formation, the rate of the chemical reaction exhibits a nonlinear behavior, and the reaction product acts as a catalyst of the chemical reaction. In this case, self-sustained oscillations of the number of nuclei and their self-organization become possible.

The formation of GaN nuclei according to scheme (1) is a result of the first-order phase transition between the gaseous and solid phases. The GaN nucleation according to scheme (2) should occur in several stages [11]. The steady fluxes of multicomponent islands (of stoichiometric composition) arising on the substrate surface can be described by the following relationships [8–10]:

$$I'_s(\xi) = \alpha'_s(\xi+1)\ln^{1/2}(\xi+1)\exp[-a/\ln(\xi+1)] \tag{3}$$

for nuclei in the form of a flat disk of height h and

$$I''_s(\xi) = \alpha''_s(\xi+1)\ln(\xi+1)\exp[-b/\ln^2(\xi+1)]. \tag{4}$$

for nuclei in the form of a spherical segment.

Here,

$$\alpha'_s = A_{1s}N_0^2D_s^0, \quad \alpha''_s = A_{2s}N_0^2D_s^0,$$

$$A_{1s} = (v_s/h)^{1/2}, \quad v_s = \sum_{i=1}^{n^s}\nu_i w_i,$$

where v_s is the molecular volume of the chemical compound, w_i is the atomic volume of the ith component, ν_i is the stoichiometric coefficient of the ith component, $N_0 \sim 1/B^2$ is the number of adsorption sites on the substrate surface (B is the lattice parameter of the substrate), $a = (\sigma_{\mathrm{st}}/k_{\mathrm{B}}T)^2 v_s\pi/h$, $b = 4\pi(\sigma/k_{\mathrm{B}}T)^3 v_s^2(2 + \cos\theta)(1 - \cos\theta)^2/3$, σ is the nucleus–natural vapor interfacial tension, $\sigma_{\mathrm{st}} = \sigma h$ is the surface tension per unit length of a disk, h is equal to one monolayer,

$$D_s^0 = \left[\sum_{i=1}^{n^s}\frac{p_i^2 l_i}{D_{ai}C_{i0}}\right]^{-1} \tag{5}$$

is the generalized diffusion coefficient (which characterizes the motion of the boundary of a growing island during crystallization of the multicomponent compound), C_{i0} stands for the equilibrium concentrations of adatoms on the substrate,

$$p_i = \frac{\nu_i}{\sum_{i=1}^{n^s}\nu_i}$$

is the reduced stoichiometric coefficient of the ith component, and D_{ai} is the diffusion coefficient of the ith component. In order to estimate the diffusion coefficient D_{ai}, we assume that the substrate has a simple square lattice. As a result, we obtain

$$D_{ai} = \frac{l_{0i}^2\gamma_{it}}{4}\exp(-E_{di}/k_{\mathrm{B}}T), \tag{6}$$

where k_{B} is the Boltzmann constant, γ_{it} is the frequency of tangential vibrations of the ith atom on the substrate surface (for convenience, this frequency is taken equal to the frequency of normal vibrations), and l_{0i} is the length of diffusion hopping of atoms.

The supersaturation ξ for a multicomponent system can be written as

$$\xi = \frac{\prod_{i=1}^{n^s}\bar{C}_i^{\nu_i} - K_\infty^s}{K_\infty^s}, \tag{7}$$

where $K_\infty^s = \prod_{i=1}^{n^s}\bar{C}_{i0}^{\nu_i}$ is the equilibrium constant for the chemical reaction of formation of a nucleus of the compound with composition s and $\bar{C}_i$ is the concentration of the ith component on the substrate.

In the course of GaN nucleation, the formation of both GaN nuclei and liquid Ga droplets can occur on the substrate surface. The probability of a particular phase forming is determined by the nucleation rates or, more specifically, by the steady fluxes (3) and (4). Let

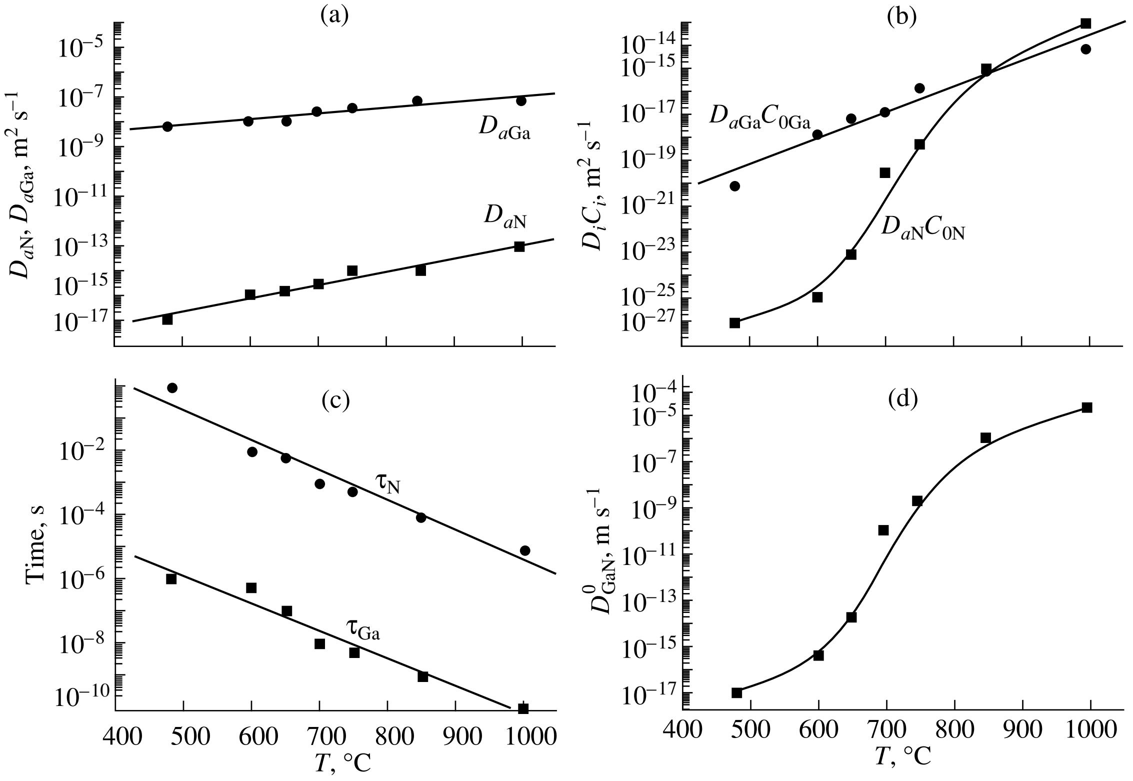

Fig. 1. Temperature dependences of (a) the surface diffusion coefficients $D_{a\mathrm{Ga}}$ for Ga atoms and $D_{a\mathrm{N}}$ for N atoms, (b) the products of the equilibrium concentrations $C_{0\mathrm{Ga}}$ and $C_{0\mathrm{N}}$ of Ga and N atoms into their surface diffusion coefficients $D_{a\mathrm{Ga}}$ and $D_{a\mathrm{N}}$, (c) the lifetimes τ_{Ga} and τ_{N} of Ga and N atoms, and (d) the generalized diffusion coefficient D^0_{GaN} of GaN.

us evaluate the fluxes of formation of disk-shaped GaN nuclei and cupola-shaped liquid Ga droplets.

The generalized diffusion coefficient D^0_{GaN} [formula (5)] for GaN can be represented in the form

$$D^0_{\mathrm{GaN}} = \frac{D_{a\mathrm{Ga}}D_{a\mathrm{N}}C_{0\mathrm{Ga}}C_{0\mathrm{N}}}{4(D_{a\mathrm{Ga}}C_{0\mathrm{Ga}}l_{\mathrm{N}} + D_{a\mathrm{N}}C_{0\mathrm{N}}l_{\mathrm{Ga}})}. \qquad (8)$$

This expression can be rewritten as

$$D^0_{\mathrm{GaN}} = \frac{D_{0\mathrm{N}}C_{0\mathrm{N}}}{4l_{\mathrm{N}}\left(1 + \dfrac{D_{a\mathrm{N}}C_{0\mathrm{N}}l_{\mathrm{Ga}}}{D_{a\mathrm{Ga}}C_{0\mathrm{Ga}}l_{\mathrm{N}}}\right)}. \qquad (9)$$

The diffusion coefficients of Ga and N atoms on the GaN surface can be estimated from the data obtained by Neugebauer *et al.* [12]. According to [12], the activation energy $E_{d\mathrm{Ga}}$ of Ga atoms is equal to 0.2 eV and the activation energy $E_{d\mathrm{N}}$ of N atoms is 1.5 eV. For the simplest estimates, we assumed that the diffusion hopping lengths of Ga and N atoms are approximately equal to the lattice parameter of the substrate; i.e., $l_{\mathrm{N}} \sim l_{\mathrm{Ga}} \sim B$. As can be seen from Fig. 1a, the diffusion coefficients of Ga and N atoms increase with an increase in the substrate temperature. In order to determine the generalized diffusion coefficient of GaN, it is necessary to calculate the equilibrium concentrations of Ga ($C_{0\mathrm{Ga}}$) and N ($C_{0\mathrm{N}}$) atoms. These concentrations can be estimated as follows. The concentration of the ith component on the substrate surface can be calculated by the formula

$$C_i = J_i\tau_i/N_0, \qquad (10)$$

where J_i is the flux of atoms incident on the substrate and τ_i is the lifetime of the ith component on the substrate:

$$\tau_i = \gamma_i^{-1}\exp(E_{ai}/k_{\mathrm{B}}T). \qquad (11)$$

Here, γ_i is the frequency of normal vibrations of atoms on the substrate surface and E_{ai} is the activation energy of adsorption. It should be noted that the vibrational frequency is generally taken to be approximately equal to ~10^{13} s^{-1} [8–10]. To calculate the equilibrium concentrations C_{0i} of adatoms on the substrate, we need to determine the equilibrium evaporation and condensation fluxes J_{0i}. Then, the concentrations C_{0i} can be obtained from relationship (10). In the general case, the equilibrium fluxes J_{0i} can be evaluated by the formula [8–10]

$$J_{0i} = n_{si}\gamma_{\mathrm{GaN(Ga)}}\exp(-E_{av_i}/k_{\mathrm{B}}T), \qquad (12)$$

where E_{av} is the evaporation energy, $\gamma_{\mathrm{GaN(Ga)}}$ is the frequency of vibrations of Ga and N atoms on the GaN surface (or the frequency of vibrations of Ga atoms on the liquid gallium surface), and $n_{si} \sim 1/B^2$ is the number density of the *i*th atom on the GaN surface (or on the liquid gallium surface). For estimates, we assume that $\gamma_{\mathrm{GaN(Ga)}} \sim 10^{13}$ s^{-1}. Formula (12) can only be used for approximate estimates. In a more general case, it is necessary to determine the desorption fluxes. The values of J_{0i} and C_{0i} can be estimated from the data obtained by Koleske *et al.* [13]. Finally, from relationships (8)–(12), we calculate the temperature dependence of the generalized diffusion coefficient D^0_{GaN} (Fig. 1d). The results of our calculations demonstrate that, as the temperature increases from 600 to 800°C, the equilibrium concentration of Ga atoms increases by three orders of magnitude, whereas the equilibrium concentration of N atoms increases by eight orders of magnitude. As a consequence of this behavior of the equilibrium concentrations with an increase in the temperature, the products of the diffusion coefficients for Ga and N atoms into their equilibrium concentrations become comparable in magnitude at $T > 800$°C (Fig. 1b). This results in a drastic increase in the diffusion coefficient D^0_{GaN} in this temperature range, which should affect the growth mechanism of III nitride semiconductors. King *et al.* [7] experimentally observed a change-over from the Stranski–Krastanov mechanism of growth of the GaN and AlN epitaxial layers to the Frank–van der Merve mechanism with an increase in the growth temperature above 800°C.

In order to determine the lifetimes of Ga and N atoms on the AlN surface, we evaluate the activation energies of adsorption E_{ai} for Ga and N atoms. According to [10], the activation energy E_{ai} can be represented as

$$E_{ai} = E_{av} - E_{0i},$$

where E_{0i} and E_{av} are the activation energies of formation and evaporation of an adatom, respectively.

As is known [9], the evaporation energy is defined as $E_{av} = ZE_i/2$, where Z is the configuration number (for GaN, $Z = 6$). The energy of formation is given by $E_{0i} = 2E_i$ (in simple models for the (100) surfaces) [10]. By using the data obtained in [13] for the energies of evaporation of Ga and N atoms from the GaN surface, we obtained $E_{a\mathrm{Ga}} \sim 0.84$ eV and $E_{a\mathrm{N}} \sim 2$ eV. The lifetimes of adatoms on the GaN surface decrease with an increase in the epitaxy temperature. Note that the lifetime of N atoms is five orders of magnitude longer than that of Ga atoms (Fig. 1c). Thus, the estimates demonstrate that, at substrate temperatures $T < 700$°C, the GaN nucleation is limited by the diffusion of N atoms, whereas at $T > 850$°C, the nucleation process is controlled by the diffusion of Ga atoms.

Now, we calculate the fluxes of GaN and liquid gallium nuclei. The surface tension δ is estimated at ~2 J m^{-2} for GaN [12] and at ~0.7 J m^{-2} for liquid gallium. The wetting angle for liquid gallium is taken as $\theta \sim \pi/6$. When estimating the supersaturation in the MOCVD growth, it is assumed that all molecules of the organometallic compound are transformed into Ga atoms, whereas the fraction of N atoms produced by ammonia decomposition is approximately 4%. In this case, the mean fluxes of Ga and N atoms are as follows: $J_{\mathrm{Ga}} \sim 10^{18}$ m^{-2} s^{-1} and $J_{\mathrm{N}} \sim 10^{19}$ m^{-2} s^{-1} [1]. The concentrations of adatoms on the GaN surface can be determined from formula (10). Substitution of these concentrations into relationship (7) gives a supersaturation large enough to persist for a very short time, because, in this case, islands rapidly absorb the material and, hence, the supersaturation should decrease.

Let us consider the conditions of the formation of GaN and Ga nuclei at low temperatures ($T = 480$°C is the temperature of formation of a buffer layer on the AlN/sapphire substrate). For liquid gallium, we have $b = 3$, $\alpha'' \sim 4 \times 10^{18}$ m^{-2} s^{-1}, $\xi \sim 0.8$, and $I_{\mathrm{Ga}} \sim 10^{14}$ m^{-2} s^{-1}. For this flux of Ga nuclei and the number density of Ga atoms on the surface $n_{\mathrm{Ga}} = J_{\mathrm{Ga}}\tau_{\mathrm{Ga}} = 10^{10}$ m^{-2}, the time it takes for Ga atoms to be involved in the phase transition is $t_f \sim n_{\mathrm{Ga}}/I_{\mathrm{Ga}} \sim 10^{-4}$ s. Consequently, excessive supersaturation disappears for a time t_f and the supersaturation ξ reaches its normal value of ~0.1–0.2. For GaN nuclei, we have $\alpha' \sim 3 \times 10^{12}$ m^{-2} s^{-1} and $a \sim 40$. Hence, it follows that the flux I_{GaN} of GaN nuclei at the same supersaturation ξ is virtually equal to zero. Therefore, at low temperatures, liquid gallium alone nucleates, after which the chemical reaction between Ga nuclei and N proceeds to form GaN. It is evident that, at these temperatures, the GaN layer is disordered and contains a large amount of gallium inclusions and dislocations.

At higher temperatures ($T > 650$°C), the generalized diffusion coefficient D^0_{GaN} increases drastically and the coefficient a in the relationship for the work of nucleation decreases to ~15 at $T \sim 650$°C. As a result, the flux I_{GaN} of GaN nuclei becomes nonzero and equal to ~10^{14} m^{-2} s^{-1} whereas the flux of liquid gallium droplets vanishes. This can be explained by the fact that, at this temperature, the supersaturation with respect to gallium becomes zero due to equalization of the concentration of Ga atoms produced by external sources and the equilibrium gallium concentration.

At $T > 800$°C, no formation of GaN islands occurs, because the supersaturation becomes zero at the fluxes $J_{\mathrm{Ga}} \sim 10^{18}$ m^{-2} s^{-1} and $J_{\mathrm{N}} \sim 10^{19}$ m^{-2} s^{-1} and the Ga and N flux densities taken from [13].

3. CONCLUSION

Thus, the anomalously high adsorption energy for nitrogen atoms leads to (1) considerable differences (by six or eight orders of magnitude) between the diffusion coefficients of nitrogen and gallium atoms on the crystal surface over the entire range of growth temperatures; (2) an anomalously large difference between the equilibrium concentrations of nitrogen and gallium (indium) atoms; and (3) an increase in the generalized diffusion coefficient $D^0_{\text{III-N}}$ with an increase in the temperature, which affects both the nucleation conditions of III nitride semiconductors and the mechanism of their growth.

The nucleation of liquid gallium droplets at low temperatures ($T < 600°\text{C}$) can be explained by the considerable work of formation of GaN nuclei.

ACKNOWLEDGMENTS

This study was supported by the St. Petersburg Research Center of the Russian Academy of Sciences and the Foundation for Support of Science and Education (St. Petersburg).

REFERENCES

1. S. G. Jain, M. Willander, J. Narayan, and R. V. Overstraeten, J. Appl. Phys. **87** (3), 965 (2000).
2. R. D. Vispute, J. Narayan, H. Wu, and K. Jagannadham, J. Appl. Phys. **77** (9), 4724 (1995).
3. *Handbook of Chemistry and Physics*, Ed. by D. R. Lide (CRC Press, Boca Raton, 1996), p. 76.
4. X. Zhang, R. R. Li, P. D. Dapkus, and D. H. Rich, Appl. Phys. Lett. **77** (14), 2213 (2000).
5. R. S. Q. Fareed, J. W. Yang, J. Zhang, *et al.*, Appl. Phys. Lett. **77** (15), 2343 (2000).
6. Z. Li, H. Chen, H. Liu, *et al.*, Jpn. J. Appl. Phys., Part 1 **39** (8), 4704 (2000).
7. S. W. King, E. P. Carlson, R. J. Therrien, *et al.*, J. Appl. Phys. **86** (10), 5584 (1999).
8. S. A. Kukushkin and A. V. Osipov, Usp. Fiz. Nauk **168**, 1083 (1998) [Phys. Usp. **41**, 983 (1998)].
9. S. A. Kukushkin and V. V. Slezov, *Disperse Systems on Solid Surfaces* (Nauka, St. Petersburg, 1996).
10. S. A. Kukushkin and A. V. Osipov, Fiz. Tverd. Tela (St. Petersburg) **36** (5), 1258 (1994) [Phys. Solid State **36**, 687 (1994)].
11. T. K. Harafuji, Y. Hasegawa, A. Ishibashi, *et al.*, Jpn. J. Appl. Phys., Part 1 **39** (11), 6180 (2000).
12. J. Neugebauer, T. Zywietz, M. Scheffer, and J. Northrup, Appl. Surf. Sci. **159–160**, 355 (2000).
13. P. P. Koleske, A. E. Wickenden, *et al.*, J. Appl. Phys. **84** (4), 1998 (1998).

Translated by O. Borovik-Romanova

Physics of the Solid State, Vol. 43, No. 12, 2001, pp. 2234–2236. Translated from Fizika Tverdogo Tela, Vol. 43, No. 12, 2001, pp. 2140–2141.
Original Russian Text Copyright © 2001 by Atabaev, Matchanov, Bakhranov.

SEMICONDUCTORS AND DIELECTRICS

Low-Temperature Diffusion of Lithium in Silicon–Germanium Solid Solutions

I. G. Atabaev, N. A. Matchanov, and É. N. Bakhranov
Physicotechnical Institute of the Physics–Sun Research and Production Association, Academy of Sciences of Uzbekistan, Tashkent, 700084 Uzbekistan
e-mail: atvi@physic.uzsci.net

Received March 5, 2001

Abstract—The influence of germanium content on lithium diffusion in $Si_{1-x}Ge_x$ solid solutions is investigated at temperatures from 300 to 500°C. It is found that the diffusion coefficient and the solubility of lithium abruptly decrease with a decrease in the temperature and an increase in the germanium content. As the diffusion temperature increases, the decrease in the lithium diffusion coefficient slows down with a change in the solid solution composition due to the effect of lattice elastic strains induced by germanium isovalent impurities. *© 2001 MAIK “Nauka/Interperiodica”.*

1. INTRODUCTION

It is known that lithium is the only shallow-level impurity used for producing highly compensated *i*-regions of silicon ionizing-radiation detectors [1]. The compensation is accomplished through electric drift of lithium ions from a thin surface layer. This layer is preliminary saturated with lithium at temperatures from 500 to 600°C for ~5 min with subsequent rapid cooling. The electric drift is carried out at temperatures from 65 to 100°C.

The available data on the lithium diffusion coefficient D_{Li} for silicon and other semiconductors are characterized by a very large spread about the mean D_{Li} value (several orders of magnitude) [2]. This circumstance is primarily due to the fact that lithium diffusing over interstices efficiently interacts with grown-in background impurities and defects, as well as with those introduced during thermal and other treatments of the material.

Saidov *et al.* [3] demonstrated that the counting rate of nuclear radiation detectors based on single crystals of the $Si_{1-x}Ge_x$ alloy is three times higher than that of silicon detectors. However, a number of problems associated with the low-temperature diffusion of lithium in the $Si_{1-x}Ge_x$ alloy remain unresolved. It is known that the incorporation of germanium isovalent impurities into the silicon lattice leads to distortions of the crystal structure, which, in turn, can substantially affect the diffusion and solubility of impurities. For example, the diffusion coefficient of phosphorus in the $Si_{1-x}Ge_x$ alloys increases with an increase in germanium content [4].

In the case of lithium, whose diffusion occurs through the interstitial mechanism, local strains induced in the lattice of $Si_{1-x}Ge_x$ single crystals can also substantially affect this process. However, data on the low-temperature diffusion of lithium in this material are unavailable.

In the present work, we investigated the influence of germanium content on lithium diffusion in single crystals of $Si_{1-x}Ge_x$ solid solutions at temperatures from 300 to 500°C.

2. EXPERIMENTAL TECHNIQUE

The diffusion of lithium was performed in an SUOL-44 furnace by immersing the samples in a lithium-saturated gallium melt for 1 h. Owing to the low temperature of the melt, gallium did not occur in the bulk of the crystal, whereas fast-diffusing lithium impurities penetrated into the crystal bulk to several micrometers during this time.

As is known, lithium diffusion strongly depends on the crystal prehistory. For this reason, in order to provide a more reliable interpretation of the results, all the samples to be studied were prepared in the form of wafers cut out from the same variband single crystal, $Si_{1-x}Ge_x$, with a variable composition from $x = 0$ to 35 at. % and a concentration gradient of approximately 0.7 at. % per millimeter. The wafers were approximately 300 μm thick. We assumed that the germanium content in each of the wafers was equal to the mean value. It should be noted that, due to the variband properties, the change in the germanium content in the wafers was approximately equal to 0.21 at. %. Since all the wafers were taken from the same crystal, which was apparently grown in the same technological process, the growing conditions of all the samples were identical. Therefore, the parameters of the samples, except for the germanium content, were also identical.

Single crystals of the $Si_{1-x}Ge_x$ solid solutions were grown by electron-beam crucibleless melting [5]. The single-crystal samples of the $Si_{1-x}Ge_x$ solid solutions with a germanium content in the range $0 < x < 35$ exhibited a *p*-type conductivity.

The electrical conductivity of semiconductors is determined by the relationship $\sigma = en\mu$, where n is the electron concentration and μ is the electron mobility. For the electron concentration at room temperature, we can write the equality $n = N_{Li}$. Consequently, we obtain $\sigma = eN_{Li}\mu$. Therefore, the distribution $\sigma(l)$ over the sample depth l can be used for determining the lithium concentration profile $N_{Li}(l)$.

The distribution $\sigma(l)$ for the samples was determined using a single-point probe technique [6]. When calculating the concentration profile $N_{Li}(l)$, the dependence of the carrier mobility on the composition of the silicon–germanium alloy was taken into account [7, 8].

3. RESULTS AND DISCUSSION

It is known that, at comparable temperatures of diffusion, the diffusion coefficient and the solubility of lithium in germanium are higher than those in silicon. However, Figs. 1 and 2 demonstrate an anomalous behavior of these parameters at diffusion temperatures of 325 and 400°C. The diffusion coefficient (Fig. 1) and the limiting solubility (Fig. 2) of lithium drastically decrease with an increase in germanium content. The decrease in the lithium diffusion coefficient with a change in the composition of the solid solution is more pronounced at low diffusion temperatures. As was mentioned above, the diffusion through the vacancy mechanism is accompanied by an increase in the phosphorus diffusion coefficient with an increase in the content x. We assume that this behavior is associated with the generation of vacancies in the field of lattice elastic strains.

In the case of interstitial diffusion, the incorporation of germanium atoms into the lattice induces elastic strains, which, apparently, disturb the periodicity of the interstitial potential of the lattice and prevent hopping of lithium atoms over interstices at diffusion temperatures up to 500°C. The increase in the diffusion coefficient, which is observed at $x > 0.20$ is caused by an increase in the elasticity of the alloy lattice with an increase in germanium content.

As is known, the solubility of impurities (x_{Li}) in semiconductors is determined by the quantity ΔH_{Li}^{α} (the enthalpy of transition of impurity atoms in the solid solution), the change in the vibrational entropy ΔS_{vib} [2], and the contribution from the Coulomb interaction with charge carriers [9, 10], that is,

$$\ln(x_{Li}) = -\Delta H_{Li}^{\alpha}/T + \Delta S_{vib} + Q(T). \tag{1}$$

Here, $Q(T)$ is the Coulomb component in expression (1) taken from [9, 10].

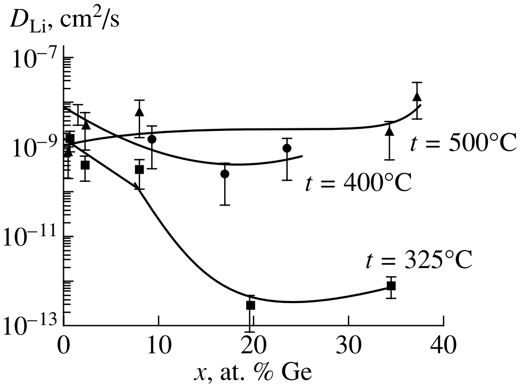

Fig. 1. Dependences of the lithium diffusion coefficient on the germanium content in silicon–germanium solid solutions.

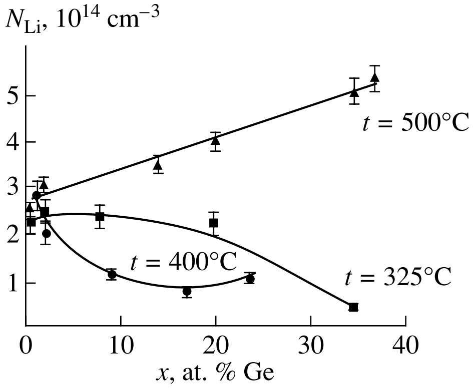

Fig. 2. Dependences of the limiting solubility of lithium on the germanium content in silicon–germanium solid solutions.

Analysis of the concentration dependence of the lithium solubility with the use of expression (1) revealed that an increase in the lithium solubility is determined by the change in the ΔH_{Li}^{α} quantity. However, at a diffusion temperature of 500°C and above, the thermal energy of lithium atoms in the alloy lattice becomes comparable to the potential barriers formed through lattice elastic strains due to the presence of germanium isovalent impurities. As a result, the behavior of lithium atoms in the alloy lattice ceases to be anomalous. Since the kT value at a temperature of 500°C is approximately equal to 0.044 eV, the potential barriers created by germanium atoms should be of the order of several hundredths of electron-volts.

4. CONCLUSION

Thus, the anomalous behavior of the diffusion coefficient and the solubility of lithium in the $Si_{1-x}Ge_x$ alloys was revealed at low temperatures. The assumption was made that this behavior is associated with the disturbance of the periodicity of the interstitial potential in the lattice due to local elastic strains generated by germanium isovalent impurity atoms.

REFERENCES

1. S. A. Azimov, R. A. Muminov, S. Kh. Shamirzaev, and A. Ya. Yafasov, *Silicon–Lithium Nuclear Radiation Detectors* (FAN, Tashkent, 1981).
2. V. M. Glazov and V. S. Zemskov, *Physicochemical Principles of Semiconductor Doping* (Nauka, Moscow, 1967; Israel Program for Scientific Translations, Jerusalem, 1968).
3. M. S. Saidov, R. A. Muminov, U. B. Dzhuraev, and N. A. Matchanov, At. Énerg. **81** (4), 56 (1994).
4. M. S. Saidov, I. G. Atabaev, and N. A. Matchanov, Uzb. Fiz. Zh., No. 4, 75 (1994).
5. M. S. Saidov, A. Yusupov, and R. S. Umerov, J. Cryst. Growth **52**, 514 (1981).
6. V. V. Botavin, in *Parameter Control of Semiconducting Materials and Epitaxial Layers* (Sov. Radio, Moscow, 1976).
7. M. S. Saidov, A. Yusupov, V. V. Nikitin, *et al.*, Fiz. Tekh. Poluprovodn. (Leningrad) **15** (6), 1221 (1981) [Sov. Phys. Semicond. **15**, 704 (1981)].
8. M. S. Saidov, A. Yusupov, and U. Sirozhov, in *Proceedings of the 6th Coordinating Conference on Investigations of Silicon–Germanium Alloys, Tbilisi, 1986*, p. 21.
9. I. G. Atabaev, Fiz. Tverd. Tela (St. Petersburg) **38** (8), 2338 (1996) [Phys. Solid State **38**, 1286 (1996)].
10. M. S. Saidov, I. G. Atabaev, and É. N. Bakhranov, Uzb. Fiz. Zh., No. 6, 25 (1998).

Translated by N. Korovin

Physics of the Solid State, Vol. 43, No. 12, 2001, pp. 2237–2241. Translated from Fizika Tverdogo Tela, Vol. 43, No. 12, 2001, pp. 2142–2146.
Original Russian Text Copyright © 2001 by Bondarev, Pikhitsa.

SEMICONDUCTORS AND DIELECTRICS

Kinetics of Luminescence in Porous Silicon: A Fluctuation Approach

V. N. Bondarev and P. V. Pikhitsa
Research Institute of Physics, Odessa National University, ul. Pastera 27, Odessa, 65026 Ukraine
e-mail: akhmerov@niif.odessa.ua
e-mail: pvp@dtp.odessa.ua

Received April 5, 2001

Abstract—The kinetics of photoluminescence due to tunneling radiative recombination of photoexcited electrons and holes localized at a crystallite–matrix interface is theoretically treated within the framework of a model concept according to which the structure of porous silicon is treated as a random set of nanometer-sized silicon crystallites embedded into the SiO_2 matrix. The developed theory predicts a relatively slow (stretched exponential) decay of photoluminescence intensity that results from averaging of the intensity in each of the photoluminescence events over the mutual arrangement of electrons and holes (localized on the surface of a particular crystallite) and over the crystallite sizes. The proposed approach provides an adequate quantitative description of low-temperature experimental data on the photoluminescence kinetics at a fixed radiant energy and the time evolution of the photoluminescence spectra of porous silicon. *© 2001 MAIK “Nauka/Interperiodica”.*

1. INTRODUCTION

Recent progress in nanoelectronics has been achieved in many respects owing to the advent, development, and application of different-type devices based on elements fabricated from disordered silicon materials [1], including porous silicon and amorphous silicon [2]. However, the use of materials based on disordered silicon is hindered by the lack of a clear understanding of the mechanisms responsible for photoluminescence, photoconduction, and other phenomena that render disordered silicon attractive from the practical standpoint. These phenomena are associated with fast (on a millisecond scale and even faster) processes of radiative recombination (see, for example, the review by Bisi *et al.* [1] and references therein) and slow processes caused by fatigue effects in materials [3, 4].

Systems based on disordered silicon exhibit features inherent in disordered media, for example, the non-Debye behavior of photoluminescence decay [1, 2]. As is known (see, for example, [5]), the non-Debye response can be adequately described by the most general models of disordered media. Dunstan and Boulitrop [6] demonstrated that, within the model of tunneling recombination of electrons and holes localized in states of the conduction band and valence band tails, the kinetics of photoluminescence in amorphous hydrogenated silicon is described by a very slowly decreasing function.

Kuskovsky *et al.* [7] experimentally revealed a similar slow decay of donor–acceptor photoluminescence in highly doped compensated semiconductors of the ZnSe : N type. These authors developed the fluctuation theory for this phenomenon and proved that the time decay of photoluminescence at a fixed energy obeys even a slower law than the Kohlrausch stretched exponential. Since the physical types of disorders in amorphous silicon and the aforementioned highly doped semiconductors are similar to each other, the results of the fluctuation theory proposed in [7] can be applied to quantitative interpretation of experimental data on the photoluminescence kinetics in amorphous silicon.

On the other hand, unlike the case of amorphous silicon, the experimental dependences of the photoluminescence on the time t in the case of porous silicon (see, for example, [1]) can be described by the Kohlrausch empirical function $\exp[-(t/\tau_K)^\beta]$, where τ_K is the characteristic time and β is the Kohlrausch exponent ($0 < \beta \le 1$). The distinction between these two cases is a natural consequence of differences in the structural disorder of amorphous hydrogenated silicon and porous silicon. According to modern concepts [1], the structure of porous silicon involves well-defined structured units that consist of crystalline silicon and have characteristic sizes on the nanometer scale. The structural units of porous silicon are usually simulated by either quantum wires [4, 8] or spherical crystallites (the so-called quantum dots) surrounded by silicon oxide layers. However, at present, preference is given to the latter model [1].

The quantum confinement effect can manifest itself in a shift of the photoluminescence spectrum of porous silicon toward the short-wavelength range with a decrease in the mean size of silicon crystallites [1]. Hence, it is believed [9–11] that the photogeneration of an electron–hole pair occurs inside a particular silicon crystallite, after which the electron and the hole are localized in traps arranged within the interface between this crystallite and the surrounding silicon oxide, and then they undergo recombination through tunneling and (or) activation mechanisms with emission of a light photon. From this inference, it follows that the quasi-two-dimensional trap arrangement (confined to crystallite surfaces) should lead to a more rapid decay of photoluminescence in porous silicon as compared to the photoluminescence kinetics in amorphous hydrogenated silicon in which the long-term time asymptotics of the photoluminescence is determined by the presence of electrons and holes that can be infinitely distant from each other.

As far as we know, a unified theoretical approach to the description of all available experimental data on photoluminescence kinetics and stationary photoluminescence has never been developed. However, with knowledge of the basic principles of the radiative recombination mechanism in porous silicon, it is possible to obtain important information on the characteristic parameters of a material through analysis of the spectra and time relaxation of photoluminescence.

Investigation into the time evolution of the photoluminescence spectra of porous silicon seems more informative. Unfortunately, there exist few research works dealing with the modeling of these phenomena in porous silicon. Special mention should be made of the work by Pavesi [12], who explained the stretched exponential time decay of photoluminescence in porous silicon within the model of hopping diffusion of photoexcited excitons between different crystallites. However, it is hard to agree with the inference drawn in [12] that a strictly exponential decay of photoluminescence should occur in the absence of hopping diffusion (which, in essence, follows from the highly improbable assumption that the recombination time is independent of the crystallite size in the structure wherein this size is a random quantity). At the same time, the electric fields induced by the possible disturbance of local electroneutrality at the crystallite–silicon oxide interface can easily destroy an exciton in the case of its diffusion between crystallites; hence, the assumption of hopping diffusion in porous silicon is incorrect. Moreover, the conclusion made by Pavesi [12] that the Monte Carlo calculation of the time decay of photoluminescence in terms of this model results in the Kohlrausch function is declarative in character, because the key features of the computational procedure are omitted in his paper.

Unfortunately, reliable theoretical data on radiative recombination in porous silicon are unavailable. In the present work, we made an attempt to fill this gap. The purpose of this work was to elaborate a consistent theory that would provide an adequate quantitative description of experimental data on the photoluminescence kinetics in porous silicon. We restricted our consideration to the limit of absolute zero temperature (the generalization of the theory to the case of finite temperatures and a theoretical analysis of the stationary photoluminescence will be given in a separate work). In this paper, we demonstrated that the experimentally observed kinetics of photoluminescence in porous silicon is similar to the Kohlrausch kinetics and agrees with the aforementioned concepts regarding the mechanism of radiative recombination of photoexcited electrons and holes localized in random positions at a crystallite–silicon oxide interface. Moreover, we proved the self-consistency of the developed theory by way of quantitative interpretation of the time evolution in the experimental photoluminescence spectra of porous silicon.

2. THEORETICAL ANALYSIS OF THE RADIATIVE RECOMBINATION KINETICS IN POROUS SILICON

As in [1, 9], we assume that the structure of porous silicon can be treated as an infinite set of randomly arranged crystalline silicon spheres surrounded by silicon oxide layers. In this case, the silicon–silicon dioxide interfaces, which are deficient in oxygen (SiO_x, $x < 2$ [1]), can contain traps for electrons and holes [9]. For definiteness, these traps are assumed to be impurities of the donor and acceptor types that can be filled through photogeneration of electron–hole pairs in a crystallite upon its photoexcitation. An electron trapped on a donor and a hole trapped on an acceptor form the so-called distant pair (according to the terminology used by Sakurai *et al.* [11]) and can subsequently recombine by tunneling through the crystallite material with the emission of a light photon. (Apart from this sufficiently slow process, ultrafast luminescence was also observed in porous silicon [13, 14], which could be brought about by the annihilation of photoexcited excitons inside a particular crystallite without trapping of electrons and holes.)

By analogy with the case of amorphous hydrogenated silicon [2] (and highly doped semiconductors [7, 15]), the time of tunneling recombination for an electron–hole pair is determined by the relationship

$$W^{-1}(r) = W_{\max}^{-1}\exp(2r/R_0), \qquad (1)$$

where r is the "arm" of the electron–hole pair (the distance between the electron and the hole localized on the crystallite surface), R_0 is the maximum (among the particles in the electron–hole pair) localization length, and $W_{\max}$ is a constant. The contribution from the relevant electron–hole pair to the photoluminescence kinetics is described by the function [15]

$$I_r(t) = -dQ_r(t)/dt = W(r)\exp[-W(r)t], \qquad (2)$$

where $Q_r(t) = \exp[-W(r)t]$ is the instantaneous probability that the recombination event has not yet occurred.

It is clear that the energy of a photon emitted upon recombination should depend on r. Indeed, on the one hand, as was shown earlier by Thomas *et al.* [15], the inclusion of the Coulomb interaction between a charged donor and a charged acceptor (which serve as traps of a photoexcited electron and a photoexcited hole and are separated by a finite distance r) leads to an increase in the energy of the emitted photon by $E_{DA}(r) =$

$e^2/(\varepsilon r)$, where e is the elementary charge and ε is the effective permittivity of the medium. On the other hand, the energy of the emitted photon should carry information on the band gap in the crystal (and on the energies of the donor and acceptor levels from which, according to [15], the electron and the hole recombine). By virtue of the quantum confinement effect, the band gap E_g for the crystallite under investigation should be dependent on the crystallite diameter L. From general considerations, it can be expected that $E_g(L) \sim L^{-2}$ (see, for example, [8] and references therein). However, reasoning from an analysis of the experimental data on photoluminescence in porous silicon, the dependence $E_g(L)$ is generally represented in the form [1]

$$E_g(L) = E_g + \frac{c_1}{L} + \frac{c_2}{L^2}, \tag{3}$$

where E_g is the band gap in a macroscopic crystal and c_1 and c_2 are constants. Rama-Krishna and Friesner [16] performed numerical pseudopotential calculations of the electron energies in semiconductor nanoclusters and obtained the dependence $E_g(L)$ in a form similar to expression (3). It should be noted that the contribution $E_{DA}(r)$ to the energy of the light photon is similar in form to the contribution $\sim L^{-1}$ in expression (3).

The resultant instantaneous photoluminescence intensity for a system of spherical nanoclusters can be obtained by the averaging of function (2) [taking into account expressions (1) and (3)] over (a) the sizes of nanospheres with an appropriate distribution function and (b) the geometrical arrangement of donors and acceptors that serve as traps of photoexcited electrons and holes on the surface of a particular nanosphere. Let us now make the simple assumption that the nanosphere surface contains no more than one donor–acceptor pair. For example, setting $L = 5$ nm (the characteristic diameter of crystallites in porous silicon samples used in the photoluminescence experiments [1]) and the concentration $\sim 10^{18}$ cm^{-3} for charged oxygen centers in the SiO$_x$ structure [17], we find that the number of donor–acceptor pairs at the crystallite–SiO$_x$ interface is close to unity. Finally, under the assumption that the size distribution of nanospheres has a Gaussian shape (see, for example, [18]), we have

$$\begin{aligned} I_E(t) = {} & \frac{1}{2\sqrt{\pi}\Delta}\int_0^\infty dL \exp\left[-\frac{(L-L_0)^2}{\Delta^2}\right]\int_0^\pi d\theta \sin\theta \\ & \times W\left[L\cos\left(\frac{\theta}{2}\right)\right]\exp\left\{-W\left[L\cos\left(\frac{\theta}{2}\right)\right]t\right\} \\ & \times \delta\left\{E - E_g(L) - E_{DA}\left[L\cos\left(\frac{\theta}{2}\right)\right]\right\}, \end{aligned} \tag{4}$$

where L_0 is the mean diameter of crystallites in a porous silicon sample, Δ is the variance of the Gaussian distribution, and $r = L\cos(\theta/2)$ is the distance between the localized electron and the localized hole in terms of the azimuthal angle θ and the crystallite diameter L. When deriving relationship (4), the normalization constant was taken equal to a value that could be obtained from the Gaussian distribution by integrating it between infinite limits. This is justified in the case of a sufficiently narrow distribution, which, in actual fact, reflects the experimental pattern in porous silicon (see below).

After introduction of the dimensionless quantities $\xi_0 = L_0R_0$ and $\Delta_0 = \Delta/R_0$ and integration over θ, relationship (4) with allowance made for expression (3) takes the form

$$\begin{aligned} I_E(t) = {} & \frac{2W_{\max}}{\sqrt{\pi}\Delta_0 E_0}\int_{\xi_{\min}}^{\infty} \exp\left\{-\frac{(\xi-\xi_0)^2}{\Delta_0^2} - 2\xi x(\xi)\right. \\ & \left. - W_{\max} t \exp[-2\xi x(\xi)]\right\} x^3(\xi)\xi d\xi, \end{aligned} \tag{5}$$

where

$$\begin{aligned} x(\xi) &= E_0\xi/(\tilde{E}\xi^2 - E_1\xi - E_2), \\ \xi_{\min} &= \left(E_1 + E_0 + \sqrt{(E_1+E_0)^2 + 4\tilde{E}E_2}\right)/(2\tilde{E}), \\ \tilde{E} &= E - E_g, \quad E_1 = c_1/R_0, \\ E_2 &= c_2/R_0^2, \quad E_0 = e^2/(\varepsilon R_0). \end{aligned}$$

Formula (5) is the principal result obtained in our work. Before proceeding to the description of experimental data on the photoluminescence decay in porous silicon and the time evolution of the photoluminescence spectra with the use of the derived formula, we dwell briefly on the qualitative analysis of its features. The distinctive feature of this formula is that the Gaussian size distribution function in the integrand accounts for the time spectrum of radiative recombination in the given system. Relationship (5) closely resembles the electric relaxation function obtained for disordered conductors in our earlier work [19]. As was shown in [19], the electric relaxation function reproduces the behavior of the Kohlrausch function with a high accuracy. Therefore, the behavior predicted by expression (5) for the time decay of photoluminescence in porous silicon should also be reproduced by a dependence similar to the Kohlrausch function (in this case, the wider the Gaussian distribution, the broader the range in which this dependence holds [19]). Recent experiments [1, 9] also demonstrated that the time decay of photoluminescence in porous silicon obeys the Kohlrausch empirical law.

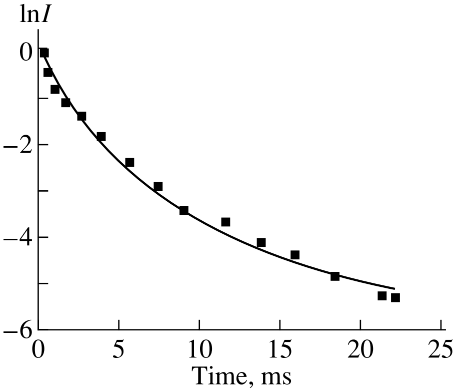

Fig. 1. Experimental (points) and theoretical (solid line) time decays of the photoluminescence intensity *I* in porous silicon. The experimental data at T = 11 K are taken from [12]. The theoretical curve is plotted using formula (5) with the parameters given in the text.

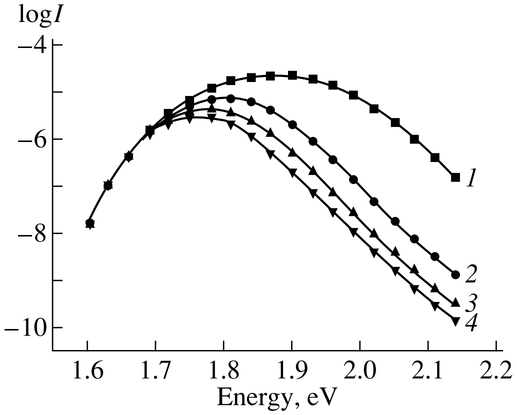

Fig. 2. Time evolution of the photoluminescence spectra according to the calculations from formula (5) with the same parameters as for the theoretical curve shown in Fig. 1 (*I* is the photoluminescence intensity). Time *t*, ms: (*1*) 1, (*2*) 5, (*3*) 10, and (*4*) 15.

3. ANALYSIS OF EXPERIMENTAL DATA

In order to describe quantitatively the experimental data on the photoluminescence kinetics in porous silicon (Figs. 1, 3), it is necessary to specify the numerical parameters in relationship (5). Certain of these parameters are known from independent measurements. In particular, data processing of optical absorption measurements in porous silicon samples gives the following parameters: E_g = 1.17 eV, c_1 = 18.4 eV Å, and c_2 = 202 eV Å^2 [1]. The mean size of crystallites L_0 and the variance of the size distribution can be considered to be known (for example, according to electron microscopic observations [1, 9], the characteristic values of L_0 for luminescent porous silicon samples fall in the range 5–7 nm). As regards the $W_{\max}$ constant, its value can easily be estimated from the rate of photoluminescence decay (see Fig. 1): $W_{\max} \sim 10^6$ s^{-1} (note that the $W_{\max}$ constant of the same order of magnitude determines the photoluminescence decay in doped semiconductors GaP [15]). The effective permittivity ε can be obtained from the experimental effective refractive index of porous silicon [1]: ε ~ 2–6. Since the possible values of localization length R_0 are unknown, this parameter is determined by fitting the theoretical results to the experimental data on the photoluminescence in porous silicon.

The applicability of formula (5) to the quantitative description of experimental data on the photoluminescence kinetics in porous silicon is illustrated in Fig. 1. For this purpose, the theoretical curve plotted using this formula is compared with the experimental data obtained in [12] for the radiant energy E = 1.86 eV at a temperature of 11 K (Fig. 1). The calculations were performed with the following parameters: L_0 = 75 Å, Δ = 12 Å, ε = 3.1, R_0 = 2.6 Å, and $W_{\max} = 10^6$ s^{-1} (the other parameters are given above).

Relationship (5) makes it possible to trace the time evolution of the photoluminescence spectra of porous silicon. The theoretical spectra calculated from formula (5) with the same parameters but at different times of photoluminescence decay are displayed in Fig. 2. Since experimental data on the photoluminescence spectra at temperatures close to absolute zero are unavailable, the time evolution of the peak energy in the photoluminescence spectra depicted in Fig. 2 and the experimental data taken from [12] are shown in Fig. 3. Note that the time dependence of the width of the theoretical spectra depicted in Fig. 2 is in qualitative agreement with that obtained experimentally in [12]; however, the theoretical width at the given parameters turns out to be less than the experimental width.

Thus, the proposed approach provides an adequate quantitative description of the photoluminescence

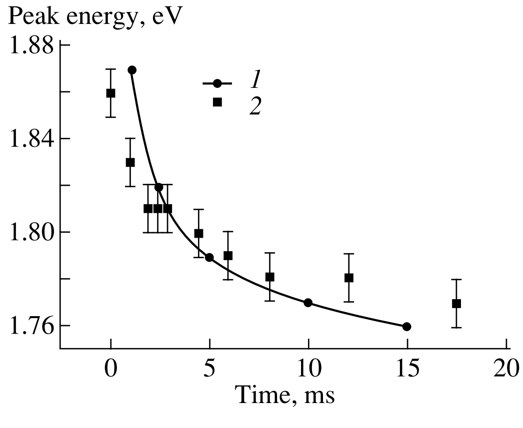

Fig. 3. (*1*) Time evolution of the peak energy in the photoluminescence spectra shown in Fig. 2 and (*2*) the experimental data at T = 11 K [12].

kinetics and the time evolution of the photoluminescence spectra of porous silicon with actual parameters.

4. CONCLUSION

The fluctuation approach proposed in the present work enabled us, within a unified context, to describe quantitatively the main features of nonstationary photoluminescence in disordered structures (such as porous silicon) at low temperatures. The origin of these features (nonexponential photoluminescence decay similar to the Kohlrausch empirical law, the shape of the photoluminescence spectra of porous silicon, and the red shift of the peak energy in the photoluminescence spectra with time) was interpreted within the concept of tunneling radiative recombination of a photoexcited electron and a photoexcited hole trapped on the surface of each crystallite whose size distribution has a Gaussian shape. The theoretical parameters accounting for the characteristics of porous silicon have a clear physical meaning, and their numerical values can be obtained from experimental data on the photoluminescence kinetics.

The developed theory can be extended to a larger number of donor–acceptor recombination channels. In this case, the theoretical spectra should be slightly broadened, which is essential to achieve quantitative agreement with the experimental spectral characteristics of the photoluminescence in porous silicon.

The results obtained suggest that the proposed approach can provide a basis for the development of a consistent theory of optical phenomena in disordered materials of the porous silicon type.

REFERENCES

1. O. Bisi, S. Ossicini, and L. Pavesi, Surf. Sci. Rep. **38**, 1 (2000).
2. W. Wang and H. Fritzsche, in *Advances in Disordered Semiconductors*, Vol. 1: *Amorphous Silicon and Related Materials*, Ed. by H. Fritzsche (World Scientific, Singapore, 1989; Mir, Moscow, 1991).
3. I. M. Chang, S. C. Pan, and Y. F. Chen, Phys. Rev. B **48**, 8747 (1993).
4. M. E. Kompan and I. Yu. Shabanov, Fiz. Tverd. Tela (St. Petersburg) **39** (7), 1165 (1997) [Phys. Solid State **39**, 1030 (1997)].
5. R. G. Palmer, D. L. Stein, E. Abrahams, and P. W. Anderson, Phys. Rev. Lett. **53**, 958 (1984).
6. D. J. Dunstan and F. Boulitrop, Phys. Rev. B **30**, 5945 (1984).
7. I. Kuskovsky, G. F. Neumark, V. N. Bondarev, and P. V. Pikhitsa, Phys. Rev. Lett. **80**, 2413 (1998).
8. M. S. Bressler and I. N. Yassievich, Fiz. Tekh. Poluprovodn. (St. Petersburg) **27**, 873 (1993) [Semiconductors **27**, 475 (1993)].
9. Y. Kanemitsu, T. Ogawa, K. Shiraishi, and K. Takeda, Phys. Rev. B **48**, 4883 (1993).
10. L. N. Dinh, L. L. Chase, M. Balooch, *et al.*, Phys. Rev. B **54**, 5029 (1996).
11. Y. Sakurai, K. Nagasawa, H. Nishikawa, and Y. Ohki, J. Appl. Phys. **86**, 370 (1999).
12. L. Pavesi, J. Appl. Phys. **80**, 216 (1996).
13. T. Matsumoto, T. Futagi, H. Mimura, and Y. Kanemitsu, Phys. Rev. B **47**, 13876 (1993).
14. K. Shiba, S. Miyazaki, and M. Hirose, Jpn. J. Appl. Phys. **37**, 1684 (1998).
15. D. G. Thomas, J. J. Hopfield, and W. M. Augustyniak, Phys. Rev. **140**, A202 (1965).
16. M. V. Rama-Krishna and R. A. Friesner, Phys. Rev. Lett. **67**, 629 (1991).
17. D. L. Griscom, J. Non-Cryst. Solids **73**, 51 (1985).
18. X. Chen, J. Zhao, G. Wang, and X. Shen, Phys. Lett. A **212**, 285 (1996).
19. V. N. Bondarev and P. V. Pikhitsa, Phys. Rev. B **54**, 3932 (1996).

Translated by O. Borovik-Romanova

Physics of the Solid State, Vol. 43, No. 12, 2001, pp. 2242–2246. Translated from Fizika Tverdogo Tela, Vol. 43, No. 12, 2001, pp. 2147–2150.
Original Russian Text Copyright © 2001 by Krygin, Prokhorov, Neĭlo, Prokhorov.

SEMICONDUCTORS AND DIELECTRICS

Inversion of Spin Levels in Ni^{2+} : $Zn(BF_4)_2 \cdot 6H_2O$ under Uniform Compression and the Effect of Transition Coincidence

I. M. Krygin, A. A. Prokhorov, G. N. Neĭlo, and A. D. Prokhorov
Donetsk Physicotechnical Institute, National Academy of Sciences of Ukraine, Donetsk, 83114 Ukraine
e-mail: prohorov@pr.fti.ac.donetsk.ua

Received April 5, 2001

Abstract—The electron paramagnetic resonance (EPR) spectra of Ni^{2+} ions substituting for Zn^{2+} ions in $Zn(BF_4)_2 \cdot 6H_2O$ crystals are studied over a wide range of temperatures under uniform compression. Measurements are performed in the *X*- and *Q*-bands. The parameter *D*, which characterizes the initial splitting, undergoes considerable variations with changes in temperature and pressure, whereas the *g* factor remains virtually unchanged. An increase in the temperature is accompanied by a nonlinear increase in *D*. Under uniform compression, the initial splitting varies linearly and the parameter *D* changes its sign at 3.5 kbar, which indicates inversion of the spin levels. The coincidence of the EPR lines associated with different transitions leads to the appearance of line-profile dips in the spectra due to cross-relaxation inside the spin system. *© 2001 MAIK "Nauka/Interperiodica".*

1. INTRODUCTION

Crystals of $Zn(BF_4)_2 \cdot 6H_2O$ belong to the family of isomorphic crystals in which the metal ion can be replaced by Co, Ni, Fe, Mn, and Mg ions and Cl can substitute for B. Investigation of crystals with a perchlorate-type structure, for example, $Zn(BF_4)_2 \cdot 6H_2O$ and $Zn(ClO_4)_2 \cdot 6H_2O$ crystals, which contain paramagnetic bivalent impurity ions of the iron group, is of considerable interest for several reasons. First, these crystals undergo a series of phase transitions induced by weak orientation interaction forces [1]. Second, their structure contains bivalent impurity ions arranged in the form of chains weakly linked to each other [2]; this could be responsible for the unusual properties of these compounds. Third, these crystals are readily compressible and can serve as model objects in investigations at high pressures [3].

Analysis of the phase diagrams constructed for these materials and investigations into the microscopic properties of different phases, including electron paramagnetic resonance (EPR) study of temperature variations in the ground state of paramagnetic ions under an external pressure, can provide new information necessary for better understanding the nature and mechanisms of phase transitions in these crystals.

The EPR spectra of Mn^{2+} and Ni^{2+} ions in fluoroborate compounds were studied earlier in [4–8]. In these works, the phase transition was found to be in the temperature range 180–190 K. This transition manifested itself in temperature dependences for both ions. Some specific features of the EPR spectra for the Mn^{2+} ion at a high pressure were investigated in our recent work [3].

In the present paper, we report the results of an EPR study of the Ni^{2+} ($3d^8$) ion in the $Zn(BF_4)_2 \cdot 6H_2O$ crystal at 4.2 K and in the temperature range 77–320 K and the data obtained at a high pressure with the purpose of elucidating the specific features of the temperature and pressure dependences of the EPR spectrum.

2. EXPERIMENTAL TECHNIQUE, SAMPLES, AND CRYSTAL STRUCTURE

The EPR spectra were measured on superheterodyne EPR spectrometers operating in 3-cm and 8-mm bands with special leucosapphire cavities, which made it possible to carry out investigations under high hydrostatic pressures over a wide range of temperatures. Hydrostatic pressure was produced in a high-pressure piston–cylinder-type chamber fabricated from a nonmagnetic material (beryllium bronze). The sample to be studied was placed in a leucosapphire cavity, which, in turn, was enclosed in the high-pressure chamber. A mixture of dehydrated transformer oil and kerosene taken in equal amounts served as the pressure-transferring medium. Special care was taken to provide a hydrostatic pressure. For this purpose, the sapphire cavity was covered with a thin Teflon cap filled with dehydrated gasoline, which could remain liquid up to 20 kbar. The cavity was connected to a heterodyne channel of the spectrometer through a thin coaxial. The pressure over the entire temperature range was measured with a manganin transducer simultaneously with the temperature measurement using a calibrated copper resistance thermometer. In order to maintain the required temperature, a nichrome heater was placed on the surface of the high-pressure chamber and the construction, as a whole, was insulated by a thin vacuum spacing. The electronic system ensured stabilization of the temperature with an accuracy of 0.1 K and its gradual variation.

The $Zn(BF_4)_2 \cdot 6H_2O$ single crystals with a 1% Ni^{2+} impurity were grown from a water solution by using two techniques: (1) a slow decrease in temperature in a thermostat and (2) evaporation of the solution at room temperature. In both cases, crystals grew in the form of hexahedral prisms with a clearly pronounced faceting, which permitted their easy orientation. The crystals were not hygroscopic under standard atmospheric conditions.

Zinc fluoroborate, like perchlorate, has a pseudohexagonal structure ($P6_3mc$) that exhibits three-component orthorhombic twinning ($Pmn2_1$) [2]. A schematic drawing of the structure (a = 7.62, b = 13.2, c = 5.30, and Z = 2) is presented in [2, 4].

The bivalent metal impurity ion is surrounded by six H_2O molecules forming an octahedron slightly distorted along the c axis. The water octahedron, in turn, is surrounded by six BF_4 tetrahedra, which also form an octahedral structure. Two water octahedra in a unit cell are rotated relative to each other through 60° around the c axis.

3. TEMPERATURE DEPENDENCE OF THE EPR SPECTRUM OF THE Ni^{2+} ION

The EPR spectrum of the Ni^{2+} ion at a normal pressure can be described by the axial spin Hamiltonian over the entire temperature range with sufficient accuracy:

$$\hat{H} = \beta \mathbf{H} g \hat{\mathbf{S}} + D[\hat{S}_z^2 - S(S+1)/3]. \qquad (1)$$

Here, g is the tensor of the spectroscopic splitting, β is the Bohr magneton, $\mathbf{H}$ is the magnetic induction vector, $\hat{\mathbf{S}}$ is the spin operator, and D is the parameter characterizing the splitting of energy levels in an axially symmetric crystal field. For all the temperatures used in the experiment and an arbitrary direction of the external magnetic field, the EPR spectrum of Ni^{2+} consists of three absorption lines (electron spin S = 1). Two of these lines correspond to the allowed transitions between the states $\langle +1| \longleftrightarrow \langle 0|$ and $\langle -1| \longleftrightarrow \langle 0|$, and the third line is attributed to the forbidden transition $\langle +1| \longleftrightarrow \langle -1|$. The spin Hamiltonian parameters for three temperatures are listed in the table. The sign of the parameter D was determined from the intensity ratio of the low-field and high-field lines at liquid-helium temperature. At $D < 0$, the low-field line is more intense. In the entire temperature range covered, except for the low-temperature range in which the weak anisotropy is observed, the g factor is isotropic and varies only slightly. The parameter of the initial splitting D changes substantially. The temperature dependence of the spin Hamiltonian parameter D (Fig. 1) has two linear portions, which intersect each other at 196 K. In the low-temperature range 77–196 K, the slope of the linear portion $\Delta D/\Delta T$ is equal to -2.44×10^{-3} cm^{-1}/K. The slope of the high-temperature portion in the range 196–320 K is $\Delta D/\Delta T = -1.34 \times 10^{-3}$ cm^{-1}/K. A similar dependence is observed for the EPR spectra of the Mn^{2+} and Ni^{2+} ions in $Zn(BF_4)_2 \cdot 6H_2O$ and $ZnSiF_6 \cdot 6H_2O$ crystals [3, 6, 9]. These variations can be explained by the second-order phase transition, which is accompanied by a change in the thermal expansion coefficient. It is quite possible that the nature of this transition is identical for the $ZnSiF_6 \cdot 6H_2O$ and $Zn(BF_4)_2 \cdot 6H_2O$ crystals.

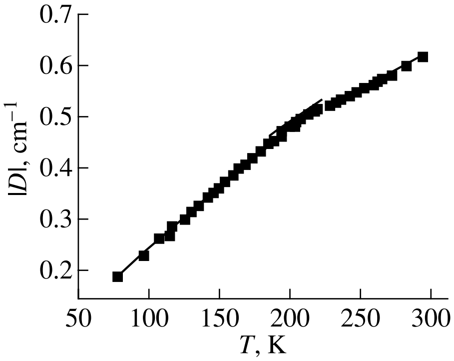

Fig. 1. Temperature dependence of the spin Hamiltonian parameter D.

4. PRESSURE DEPENDENCE OF THE EPR SPECTRUM OF THE Ni^{2+} ION

The EPR spectrum of the $Ni^{2+} : Zn(BF_4)_2 \cdot 6H_2O$ ion was studied at a high hydrostatic pressure and T = 77 K. This spectrum can be described by the spin Hamiltonian (1). The g factor is independent of pressure within the limits of experimental error. The parameter D, which characterizes the deviation of the crystal field from the cubic symmetry, turned out to be very sensitive to uniform compression. Figure 2 shows the experimental pressure dependences of the spin Hamiltonian parameter D at liquid-nitrogen temperatures, which can be described by the expression

$$D = (-0.196 + 0.06P)\ \text{cm}^{-1},$$

Temperature dependence of the spin Hamiltonian parameters

T, K	$g_{\parallel}$	$g_{\perp}$	D, 10^{-4} cm^{-1}
4.2	2.23 ± 0.002	2.19 ± 0.002	−1350 ± 4
77	2.23 ± 0.005	2.23 ± 0.005	−1908 ± 4
295	2.22 ± 0.005	2.22 ± 0.005	−6314 ± 30

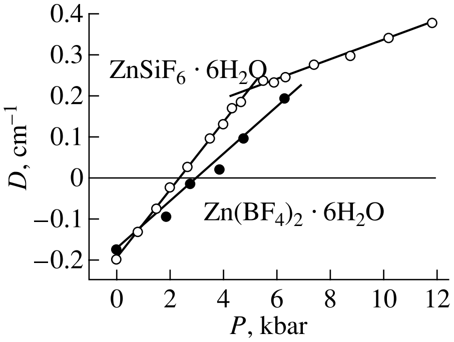

Fig. 2. Pressure dependences of the spin Hamiltonian parameter *D*. Open and closed circles correspond to $ZnSiF_6 \cdot 6H_2O$ and $Zn(BF_4)_2 \cdot 6H_2O$, respectively.

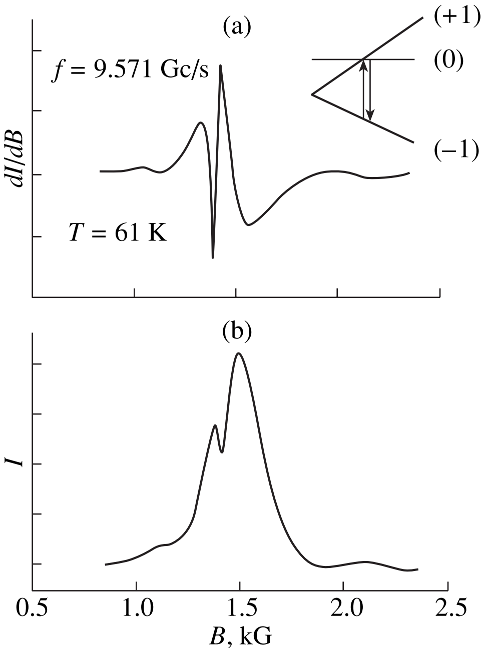

Fig. 3. (a) Coincidence of the allowed and forbidden transitions in the 3-cm band and (b) the integral curve.

where *P* is measured in kbar.

An interesting feature of this dependence is that the parameter *D* becomes zero at $P = 3.5$ kbar. This means that the local electric field reaches cubic symmetry in a site occupied by a bivalent nickel impurity ion. As the pressure increases above $P = 3.5$ kbar, the parameter *D* changes its sign and the singlet ground state is observed.

A more noticeable effect should be observed upon excitation of the triplet Γ_5, which is related to the ground orbital singlet Γ_2 through the spin–orbit interaction. It follows from the theoretical treatment [10] that

$$D = 4\lambda^2\delta/\Delta_0\Delta_1,$$

where $\delta = \Delta_0 - \Delta_1$ and Δ_0 and Δ_1 are the energies of the excited orbital triplet Γ_5 with $l_z = 0$ and $l_z = \pm 1$, respectively.

The value of $\Delta_0 \approx \Delta_1$ for the $[Ni(H_2O)_6]$ complex in solution, which was determined from the optical absorption spectrum, is approximately equal to 8400 cm^{-1}, and the parameter λ is –270 cm^{-1} [10]. Hence, it follows that $\delta = 242D$ cm^{-1}. From the aforementioned experimental data, we obtain $\partial\delta/\delta P$ = 14 cm^{-1}/kbar; i.e., at 10 kbar, the splitting of excited levels is 140 cm^{-1}. This should affect the optical absorption spectra and can lead to a change in the color of crystals containing the Ni^{2+} impurity.

Vasyukov *et al.* [11, 12] demonstrated that, in the case of slight variation in the cubic potential when the crystal lattice is distorted along the threefold axis, the parameter *D* can be expanded in powers of $(\beta - \beta_0)$. The quantity $(\beta - \beta_0)$ is a measure of distortion of the molecular complex of water. Here, β_0 is the angle between the direction toward the nearest ligand and the C_3 axis of a regular octahedron and β is the same angle for the distorted octahedron. The expansion reduced to the first term has the following form:

$$D = (\beta - \beta_0)\partial D/\partial\beta.$$

For all the studied crystals with a trigonal distortion, $\partial D/\partial\beta$ has a negative value [11, 12]. Therefore, the sign of the parameter *D* depends on the sign of $(\beta - \beta_0)$. In our case, at normal pressure, we have the parameter $D < 0$ and, consequently, $(\beta - \beta_0) > 0$. This means that the octahedron is oblate along the C_3 axis. At pressure $P > 3.5$ kbar, the parameter *D* changes its sign and the octahedron is elongated along the C_3 axis. Despite the fact that the crystals we considered have a lower symmetry, the deviations from trigonal symmetry are insignificant [2]. Hence, we can use the above inferences in our consideration.

A comparison shows that our data closely coincide with the pressure dependences of the parameter *D* for $ZnSiF_6 \cdot 6H_2O$ and $MgSiF_6 \cdot 6H_2O$ crystals [13, 14] (Fig. 2). This coincidence can be explained by the fact that the water complexes of these crystals exhibit virtually the same compressibility, even though the SiF_6 and BF_4 anions forming the second coordination shell differ from each other and the crystals are described by different space groups: $\bar{R}$ for $ZnSiF_6 \cdot 6H_2O$ and $Pmn2_1$ for $Zn(BF_4)_2 \cdot 6H_2O$. The elastic properties of these complexes are formed by the nearest environment of the bivalent metal impurity (in our case, six H_2O molecules) and through the hydrogen bonding between the metal atoms and the anion environment. According to our results and the data obtained in [3] for the pressure dependences of the Mn^{2+} ion, the hydrogen bonding is similar in all the aforementioned crystals.

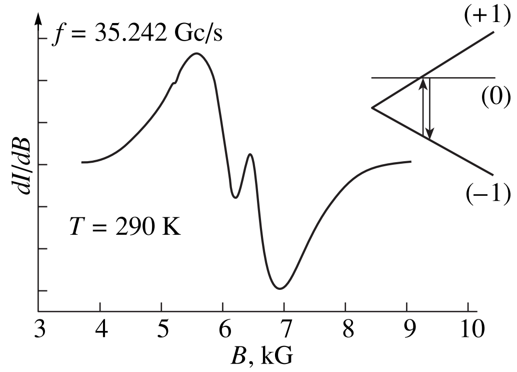

Fig. 4. Coincidence of the allowed and forbidden transitions in the 8-mm band.

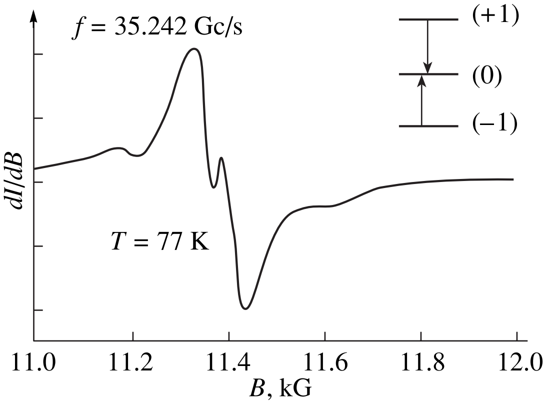

Fig. 5. Coincidence of two allowed transitions (θ = 54.4°).

5. EFFECT OF THE COINCIDENCE OF TRANSITIONS

The strong dependence of the parameter D on the temperature and pressure suggests an arrangement of spin levels that is actually impossible under standard conditions. Let us now consider two variants of the arrangement of spin levels that lead to interesting effects.

5.1. Coincidence of the allowed and forbidden transitions. The situation when both transitions coincide with each other is illustrated in Figs. 3–5. At a frequency of 9 GHz, the narrow line attributed to the forbidden transition with an opposite phase is observed against the background of the broad absorption line of the allowed transition, which corresponds to the emission curve. In the antiderivative of the EPR signal (Fig. 3), the narrow line has the shape of a dip. A similar pattern is observed at a frequency of 35 GHz (Fig. 4). In the latter case, the coincidence of the allowed and forbidden transitions occurs at room temperature; however, the effect is substantially smaller in magnitude.

5.2. Coincidence of two allowed transitions. A similar pattern is also observed for the coincidence of two allowed transitions. Figure 5 depicts the absorption line in the case of exact coincidence between two lines of the fine structure when the direction of an external magnetic field corresponds to the magic angle $\theta = 54.4°$. A similar situation can arise under uniform compression. At $P = 3.5$ kbar (Fig. 2), the parameter D is zero, the lines associated with the allowed transitions coincide with each other, and a dip is observed in the region of overlapping of the EPR lines.

This phenomenon can be explained in terms of cross-relaxation in a three-level system. Specifically, if there are two pairs of nearly equidistant levels, the spin–spin interaction results in the following processes [15]: the first ion absorbs the energy $h\nu_1$ and the second ion emits the energy $h\nu_2$. For the exact coincidence of the frequencies, the reemission processes have the highest probability, which leads to a decrease in the intensity of the absorption line. Since the lines of the allowed spectrum of the Ni^{2+} ion are nonuniformly broadened, the transition energies coincide only in a narrow frequency range, as is the case in the two-photon transition observed at a high power supplied to the sample [16].

Rather strong spin–spin interactions between the Ni^{2+} ions can be judged from the clearly distinguishable additional lines in the spectrum, which are attributed to the ion pairs located along the c axis. The distinction of the observed phenomenon from the conventional cross-relaxation lies in the fact that these transitions occur between the levels attributed to a single spin system. Theoretical treatment of this phenomenon, as applied to a MgO cubic crystal, was performed in [17].

ACKNOWLEDGMENTS

We would like to thank L.F. Chernysh and G.Ya. Samsonova for growing the high-quality crystals used in these experiments.

REFERENCES

1. M. A. White and M. Falk, J. Chem. Phys. **84**, 3484 (1986).
2. S. Ghosh, M. Mukherjee, A. Seal, and S. Ray, Acta Crystallogr. B **53**, 639 (1997).
3. G. N. Neĭlo, A. A. Prokhorov, and A. D. Prokhorov, Fiz. Tverd. Tela (St. Petersburg) **42**, 1100 (2000) [Phys. Solid State **42**, 1134 (2000)].
4. A. K. Jain and M. Geoffroy, J. Phys. Chem. Solids **44**, 535 (1983).
5. E. D. Mauro and W. Sano, J. Phys. Chem. Solids **48**, 29 (1987).
6. W. Sano, S. Isotani, J. A. Ochi, and J. C. Sartorelli, J. Phys. Soc. Jpn. **46**, 26 (1979).
7. J. B. Domiciano, W. Sano, K. R. Juraitis, and S. Isotani, J. Phys. Soc. Jpn. **48**, 1449 (1980).

8. W. Sano, J. B. Domiciano, and J. A. Ochi, Phys. Rev. B **50**, 2958 (1994).
9. A. D. Prokhorov, Fiz. Tverd. Tela (St. Petersburg) **37**, 1362 (1995) [Phys. Solid State **37**, 740 (1995)].
10. A. Abragam and B. Bleaney, *Electron Paramagnetic Resonance of Transition Ions* (Clarendon Press, Oxford, 1970; Mir, Moscow, 1972), Vol. 1.
11. V. N. Vasyukov, S. N. Lukin, and G. A. Tsintsadze, Fiz. Tverd. Tela (Leningrad) **20**, 2260 (1978) [Sov. Phys. Solid State **20**, 1304 (1978)].
12. V. G. Vasyukov and B. Ya. Sukharevskiĭ, Fiz. Nizk. Temp. **21**, 247 (1995) [Low Temp. Phys. **21**, 187 (1995)].
13. A. Yu. Kozhukhar', S. N. Lukin, and G. A. Tsintsadze, Fiz. Tverd. Tela (Leningrad) **17**, 1870 (1975) [Sov. Phys. Solid State **17**, 1231 (1975)].
14. S. N. Lukin and A. D. Prokhorov, Fiz. Tverd. Tela (St. Petersburg) **35**, 2278 (1993) [Phys. Solid State **35**, 1133 (1993)].
15. N. Bloembergen, S. Shapiro, P. S. Pershan, and J. O. Artman, Phys. Rev. **114**, 445 (1959).
16. S. A. Al'tshuler and B. M. Kozyrev, *Electron Paramagnetic Resonance in Compounds of Transition Elements* (Nauka, Moscow, 1977).
17. S. R. P. Smith, F. Dravnieks, and J. Werts, Phys. Rev. **178**, 471 (1969).

Translated by N. Korovin

Physics of the Solid State, Vol. 43, No. 12, 2001, pp. 2247–2249. Translated from Fizika Tverdogo Tela, Vol. 43, No. 12, 2001, pp. 2151–2153.
Original Russian Text Copyright © 2001 by Pshenichnyuk.

DEFECTS, DISLOCATIONS, AND PHYSICS OF STRENGTH

On the Capacity of Grain Boundary Dislocation Pileups

A. I. Pshenichnyuk
Institute of Problems of Metal Superplasticity, Russian Academy of Sciences,
ul. Khalturina 39, Ufa, 450001 Bashkortostan, Russia
e-mail: aipsh@anrb.ru

Received January 16, 2001

Abstract—It is demonstrated on model examples that inclusion of the interaction between pileups of grain boundary dislocations formed in the vicinity of triple grain-boundary junctions leads to a multifold increase in the capacity of these pileups. *© 2001 MAIK “Nauka/Interperiodica”.*

1. The pileups of grain boundary dislocations formed in the vicinity of triple grain-boundary junctions at the initial stage of plastic deformation of fine-grained materials are responsible for important physical processes, such as the development of cavitation under creep conditions, formation of cracks at high loading rates [1], restructuring of a triple junction under stresses typical of superplasticity [2], and inelastic relaxation of a material after unloading [3]. The density of edge dislocations $\rho_0(x)$ in an isolated one-sided pileup, which is distributed over the interval $x_0 \le x \le x_x$ under the shear stress τ acting in the dislocation glide plane, is determined by the standard equation [4]

$$\int_{x_0}^{x_s} \frac{\rho_0(x')dx'}{x'-x} = -\frac{\tau}{\mu_0 b}, \quad \mu_0 = \frac{\mu}{2\pi(1-\nu)}, \tag{1}$$

where μ is the shear modulus, ν is the Poisson ratio, and b is the strength of grain boundary dislocations; the principal value of the integral is considered. If the dislocations are emitted by a source located at a point with the coordinate $x = L/2$ and the threshold stress $\tau_c \sim \mu b/l$, the length of the pileup is determined by the condition of blocking of the source by the reverse field of the emitted dislocations:

$$\tau + \mu_0 b \int_{x_0}^{x_s} \frac{\rho_0(x')dx'}{x'-L/2} = \tau_c. \tag{2}$$

From relationships (1) and (2), it follows [4] that

$$\rho_0(x) = \frac{\tau}{\pi\mu_0 b}\sqrt{\frac{x_s-x}{x-x_0}}, \tag{3}$$

$$x_s - x_0 = \left(\frac{L}{2} - x_0\right)\left(1 - \frac{\tau_c^2}{\tau^2}\right). \tag{4}$$

In this case, the number of dislocations in the pileup is given by

$$N_0 = \int_{x_0}^{x_s} \rho_0(x)dx = \frac{\tau(x_s - x_0)}{2b\mu_0}. \tag{5}$$

Relationship (3) for the dislocation density is used for analyzing the formation of a crack in a triple junction [1], whereas expression (5) is applied to the description of the inelastic relaxation of a superplastic material [3]. However, for a triple junction in the general case (shear stresses act at each boundary of the triple junction), the grain boundary dislocations can be formed at all three boundaries and their interaction substantially modifies expressions (3)–(5). For an arbitrary triple junction, the problem reduces to a complex system of three integral equations. In order to obtain a preliminary estimate of the effect of the interaction between pileups of grain boundary dislocations, we consider two model examples admitting exact analytical solution.

2. Let us assume that, in addition to the already introduced pileup, there exists a second pileup of dislocations of opposite sign in the vicinity of the triple junction $x = 0$ in the interval $-x_s \le x \le -x_0$. This pileup is formed by a source located at the point $x = -L/2$. The region $|x| \le x_0$ is an obstacle to the motion of dislocations and can be considered a kernel of a triple junction that has a crystal structure different from the structure of the boundaries. Since the densities of dislocations are identical in the two pileups according to the symmetry considerations, we obtain the equation for the dislocation density,

$$\int_{x_0}^{x_s} \frac{\rho_1(x')dx'}{x'-x} + \int_{x_0}^{x_s} \frac{\rho_1(x')dx'}{x'+x} = -\frac{\tau}{\mu_0 b} \tag{6}$$

and the condition of the source blocking:

$$\tau + \mu_0 b\int_{x_0}^{x_s}\frac{\rho_1(x')dx'}{x'-L/2} + \int_{x_0}^{x_s}\frac{\rho_1(x')dx'}{x'+L/2} = \tau_c. \qquad (7)$$

After replacing the independent variable $x^2 = y$ [5], expression (6) reduces to an equation of type (1) and has the solution

$$\rho_1(x) = \frac{\tau}{\pi\mu_0 b}\sqrt{\frac{x_s^2-x^2}{x^2-x_0^2}}. \qquad (8)$$

From condition (7), we obtain the relationship

$$x_s^2 - x_0^2 = \left(\frac{L^2}{4}-x_0^2\right)\left(1-\frac{\tau_c^2}{\tau^2}\right). \qquad (9)$$

Consequently, the number of dislocations in the pileup is represented as

$$N_1 = \frac{\tau x_s}{\pi\mu_0 b}[K(q)-E(q)], \qquad (10)$$

where x_s is determined from relationship (9), $q = \sqrt{x_s^2-x_0^2}/x_s$, and K and E are the complete elliptic integrals of the first and second kinds, respectively [6].

3. Under the assumption that L is the length of the grain boundary, a triple junction, which is an obstacle to the propagation of dislocations, should be located at points $x = L$ and $x = 0$. In this case, the source at the point $x = L/2$ forms both the pileup in the interval $x_0 \le x \le x_s$ and the pileup of dislocations of the opposite sign in the interval $L - x_s \le x \le L - x_0$. The interaction of these pileups can either decrease or increase the effect of the mutual attraction of the pileups considered in the first example (see Section 2) and, consequently, can affect the concentration of stresses in the region of the triple junction $|x| \le x_0$. In order to estimate this effect, we consider the second model example.

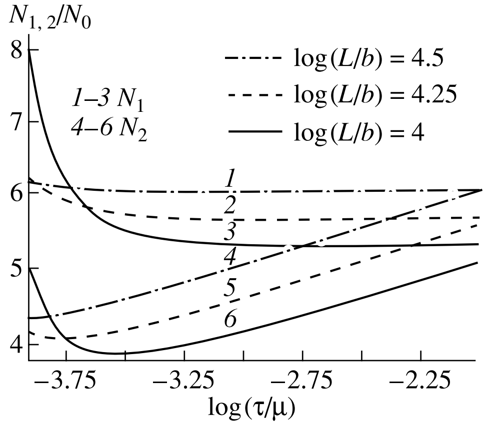

Capacities of the interacting pileups of grain boundary dislocations in terms of the capacity of an isolated pileup.

It is assumed that the obstacles to the motion of dislocations lie along a straight line at points $x_i = \pm nL$ (n = 0, 1, 2, …) and that sources with identical threshold stresses are located at points $x_m = \pm mL/2$ (m = 1, 3, 5, …). Hence, the density of dislocations in any pileup satisfies the equation

$$\sum_{n=-\infty}^{\infty}\int_{x_0}^{x_s}\frac{\rho_2(x')dx'}{x'+x-nL} + \sum_{n=-\infty}^{\infty}\int_{x_0}^{x_s}\frac{\rho_2(x')dx'}{x'-x-nL} = -\frac{\tau}{\mu_0 b},$$

which, in view of the relationship $\sum_{n=-\infty}^{\infty}\frac{1}{\xi - n\alpha} = \frac{\pi}{\alpha}\cot\frac{\pi\xi}{\alpha}$, takes the form

$$\frac{2\pi}{L}\int_{x_0}^{x_s}\frac{\rho_2(x')\sin\frac{2\pi x'}{L}}{\cos\frac{2\pi x}{L}-\cos\frac{2\pi x'}{L}}dx' = -\frac{\tau}{\mu_0 b}. \qquad (11)$$

The condition of the source blocking is determined by the following equation:

$$\tau - \frac{2\pi\mu_0 b}{L}\int_{x_0}^{x_s}\frac{\rho_2(x')\sin\frac{2\pi x'}{L}}{1+\cos\frac{2\pi x'}{L}}dx' = \tau_c. \qquad (12)$$

After replacing the independent variable $\cos(2\pi x/L) = y$, expression (11), as in the first example, reduces to an equation of type (1) with the solution

$$\rho_2(x) = \frac{\tau}{\pi\mu_0 b}\sqrt{\frac{\cos(2\pi x/L)-\cos(2\pi x_s/L)}{\cos(2\pi x_0/L)-\cos(2\pi x/L)}}. \qquad (13)$$

It follows from Eq. (12) that

$$\cos\frac{\pi x_s}{L} = \frac{\tau_c}{\tau}\cos\frac{\pi x_0}{L}. \qquad (14)$$

Finally, the number of dislocations in the pileup is determined by the expression

$$N_2 = \frac{\tau L}{\pi^2\mu_0 b}\sqrt{\frac{1-\nu_s}{1+\nu_0}}\left[K(t)-\frac{1-\nu_0}{1-\nu_s}\Pi(\pi/2, n, t)\right], \qquad (15)$$

where $\nu_0 = \cos(2\pi x_0/L)$, $\nu_s = \cos(2\pi x_s/L)$, $n = \frac{\nu_0-\nu_s}{1-\nu_s}$, $t = \sqrt{\frac{2(\nu_0-\nu_s)}{(1-\nu_s)(1+\nu_0)}}$, and Π is the elliptic integral of the third kind.

4. Under the condition $L \gg x_0$ ($x_0 \sim 5b$), the dependence of the capacity of an isolated one-sided grain boundary dislocation pileup on the boundary length L exhibits a nearly linear behavior. The linearity of the dependence of N_0 on τ breaks down only near the threshold stress τ_c. The figure shows the dependences N_1/N_0 and N_2/N_0. For weak stresses, the effect of the interaction between two pileups is especially significant at small L. When both parameters L and τ increase, the role of the interaction between these pileups is less pronounced. However, in this case, too, the number of dislocations involved in interacting pileups is five or six times larger than that in an isolated pileup. The screening effect of a chain of dislocation pileups is also more evident compared to that of a two-sided pileup under weak stresses (the screening effect causes an approximate twofold decrease in the capacity of interacting pileups; however, this capacity is still four times higher than the capacity of an isolated pileup). As the stress increases, the effect of the screening is leveled and the capacity of a chain of pileups and that of the two-sided pileup become close to each other.

The dislocation densities represented by expressions (8) and (13) bring about a substantial increase in the concentration of stresses at the triple junction point as compared to a one-sided pileup described by relationship (3). Note that especially favorable conditions for the formation of a crack are observed at high strain rates.

The simple and sufficiently accurate estimates of expressions (10) and (15) lead to the principal terms of the expansions with respect to the small parameter $x_0/L \ll 1$:

$$N_1 \cong \frac{\tau L}{2\pi\mu_0 b}\sqrt{1-\frac{\tau_c^2}{\tau^2}}\ln\left(\frac{2L}{x_0}\sqrt{1-\frac{\tau_c^2}{\tau^2}}\right),$$

$$N_2 \cong \frac{\tau L}{\pi^2\mu_0 b}\sqrt{1-\frac{\tau_c^2}{\tau^2}}\ln\left(\frac{4L}{\pi x_0}\sqrt{\frac{\tau^2}{\tau_c^2}-1}\right).$$

Thus, the consideration of the processes occurring in triple grain-boundary junctions during plastic deformation should be based on a more thorough description of the interacting pileups of grain boundary dislocations than is usually used for noninteracting pileups.

REFERENCES

1. M. S. Wu and J. Niu, Philos. Mag. A **71** (4), 831 (1995).
2. V. V. Astanin, A. V. Sisanbaev, A. I. Pshenichnyuk, and O. A. Kaibyshev, Scr. Metall. Mater. **36** (1), 117 (1997).
3. J. H. Schneibel and P. M. Hazzledine, Acta Metall. **30**, 1223 (1982).
4. L. D. Landau and E. M. Lifshitz, *Course of Theoretical Physics*, Vol. 7: *Theory of Elasticity* (Pergamon, New York, 1986; Nauka, Moscow, 1987).
5. Sh. Kh. Khannanov, *Dislocation Arrangement* (Bashkir. Nauchn. Tsentr Ural. Otd. Ross. Akad. Nauk, Ufa, 1992).
6. I. S. Gradshteyn and I. M. Ryzhik, *Table of Integrals, Series, and Products* (Nauka, Moscow, 1971; Academic, New York, 1980).

Translated by O. Moskalev

Physics of the Solid State, Vol. 43, No. 12, 2001, pp. 2250–2252. Translated from Fizika Tverdogo Tela, Vol. 43, No. 12, 2001, pp. 2154–2156.
Original Russian Text Copyright © 2001 by Smirnov, Peschanskaya, Nikolaev.

DEFECTS, DISLOCATIONS, AND PHYSICS OF STRENGTH

Magnetoplastic Effect in $NaNO_2$ Ferroelectric Crystals

B. I. Smirnov, N. N. Peschanskaya, and V. I. Nikolaev
Ioffe Physicotechnical Institute, Russian Academy of Sciences, Politekhnicheskaya ul. 26, St. Petersburg, 194021 Russia
e-mail: smir.bi@pop.ioffe.rssi.ru

Received May 22, 2001

Abstract—This paper reports on a laser interferometric study of the effect of a dc magnetic field (MF) on the rate of plastic deformation (creep) $\dot{\varepsilon}$ of $NaNO_2$ ferroelectric crystals under compression. It is established that the application of a dc MF to a loaded specimen results in an increase in the creep rate and that removal of the MF brings about a decrease in $\dot{\varepsilon}$. Subjecting an unloaded specimen to a dc MF beforehand also affects its strain rate under the subsequent loading. The observed magnetoplastic effect is most clearly pronounced within a certain $\dot{\varepsilon}$ interval, and the magnitude of this effect for the $NaNO_2$ ferroelectric is several times larger than that for LiF crystals. © *2001 MAIK "Nauka/Interperiodica".*

1. INTRODUCTION

The magnetoplastic effect (MPE) was originally observed in nonmagnetic crystals (NaCl) on a microscopic scale in the form of dislocation motion in unloaded specimens placed in a pulsed [1] or dc [2] magnetic field. However, in [1], the observed effect was assigned not to the magnetic field itself but rather to the induced vortex electric field acting on the dislocations.

It was subsequently established that the MPE not only consists of an increased mobility of single dislocations [3, 4] but also becomes manifest on the macroscopic level by lowering the yield point [5, 6], reducing the microhardness [7], and changing the acoustic parameters (internal friction) [8]. The magnetic field has been observed to affect the plasticity of a number of nonmagnetic materials, more specifically, of ionic crystals [1–8], polymers [9–11], semiconductors [12, 13], molecular crystals [14, 15], and diamagnetic metals [16–18]. (For a more extensive list of references to the MPE, see review [19].) According to [6], the nature of the MPE is usually associated with spin conversion in impurity centers, which gives rise to a rearrangement of their electronic structure and the corresponding weakening of their interaction with dislocations.

The experiments carried out thus far suggest that practically any nonmagnetic material can exhibit the MPE under certain conditions. We have chosen, as a subject for the study, $NaNO_2$ ferroelectric crystals, which contain polarized regions (domains) and, as shown previously in [20], exhibit a specific polarization-induced electroplastic effect. These crystals were used to study the influence of a magnetic field on the plastic-strain rate under a constant compressive stress, and it was established that the magnetic field stimulates, under certain conditions, a substantial increase in this rate.

2. EXPERIMENTAL

The $NaNO_2$ single crystals used in the work were grown by the Kyropoulos method from melt and annealed at 500 K for 48 h. The specimens were $2 \times 3 \times 6$-mm rectangular parallelepipeds cut with a thread saw. The crystallographic orientation of the specimens was chosen such that they could be plastically deformed along the well-known slip systems $\{110\}\langle 111\rangle$ and $(001)[100]$ [21].

The specimens were deformed by a constant compressive stress σ at room temperature. The course of the deformation with time was monitored using laser interferometry [22], a method that permits one to measure the relative strain rate $\dot{\varepsilon}$ under small variations of the specimen length l_0. One beat in an interferogram corresponds to a strain increment of 0.3 μm, and $\dot{\varepsilon} = \lambda\nu/2l_0$, where $\lambda = 0.6$ μm is the laser wavelength and ν is the beat frequency. As a result, the inelastic strain rate can be measured over a base length of $\Delta l = 0.3$ μm to within ~1%, thus permitting one to detect weak effects, which would otherwise be washed out in the traditional strain–time creep curves.

The deformation experiments, both in the presence of a dc magnetic field and without it, were performed on a setup whose components, located within the region of the magnetic field, were made of nonmagnetic materials. To study the influence of a magnetic field with induction $B = 0.2$ T (generated by a permanent magnet) on specimen deformation, a strained specimen was placed between the magnet poles. The magnetic field was oriented perpendicular to the specimen axis. Particular attention was focused on the possible change in strain rate upon both application and removal of the dc magnetic field (MF). The magnitude of $\dot{\varepsilon}$ was measured at the same increments of the strain before and after the field was varied.

1063-7834/01/4312-2250$21.00 © 2001 MAIK "Nauka/Interperiodica"

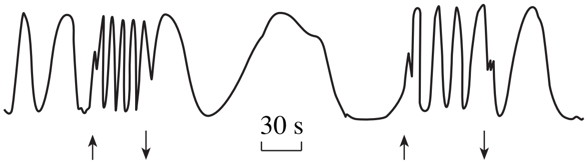

Fig. 1. An interferogram displaying the variation of the creep rate along the (001)[100] slip plane of a loaded $NaNO_2$ specimen under application (↑) and removal (↓) of a magnetic field; $B = 0.2$ T and $\sigma = 8.6$ MPa.

Experimental study on the creep rate of a specimen was also performed after its exposure to a magnetic field in the unloaded state. The exposure time was 10 min, and the creep rate was measured 5 s after the loading, immediately following the removal of the dc MF.

For comparison, similar experiments were also carried out on $5 \times 5 \times 10$-mm LiF single crystals subjected to slip over the $\{110\}\langle 110\rangle$ systems.

3. RESULTS OF THE STUDY AND DISCUSSION

Figure 1 presents interferograms in which the oscillation frequency reflects the variation of the creep rate of a loaded $NaNO_2$ specimen at the instant of application (arrow up) and removal (arrow down) of a magnetic field. This interferogram clearly demonstrates the manifestation of a repeating MPE in the $NaNO_2$ crystals; this effect consists in a sharp increase in the creep rate under a magnetic field and in a decrease in $\dot{\varepsilon}$ when the field is removed.

Figure 2 illustrates the dependence of $\dot{\varepsilon}$ on time t for $NaNO_2$ and LiF crystals, including the instants of application and removal of a dc MF. One clearly sees the manifestation of the above-mentioned MPE, with the $NaNO_2$ crystal response to the magnetic field being noticeably stronger than the LiF response. A similar enhancement of the creep rate was also observed to occur after the exposure of unloaded specimens to a magnetic field.

In the case of creep, the MPE can be quantitatively characterized by the ratio of the creep rates obtained with and without the field, i.e., by the quantity $\dot{\varepsilon}_f/\dot{\varepsilon}_0$. Because the creep rate for σ = const decreases with time, the $\dot{\varepsilon}_f/\dot{\varepsilon}_0$ ratio was measured for various values of $\dot{\varepsilon}_0$. Figure 3 displays the dependences of $\dot{\varepsilon}_f/\dot{\varepsilon}_0$ on the creep rate at which the MPE was measured on a loaded specimen or on a specimen after its exposure to a dc MF in an unloaded state. One does not see any noticeable effect of the magnetic field on the $NaNO_2$ crystals at small strain rates ($\dot{\varepsilon}_0 < 5 \times 10^{-7}$ s^{-1}). At the same time, even a small further increase in $\dot{\varepsilon}_0$ results in the onset and sharp growth of the MPE up to values

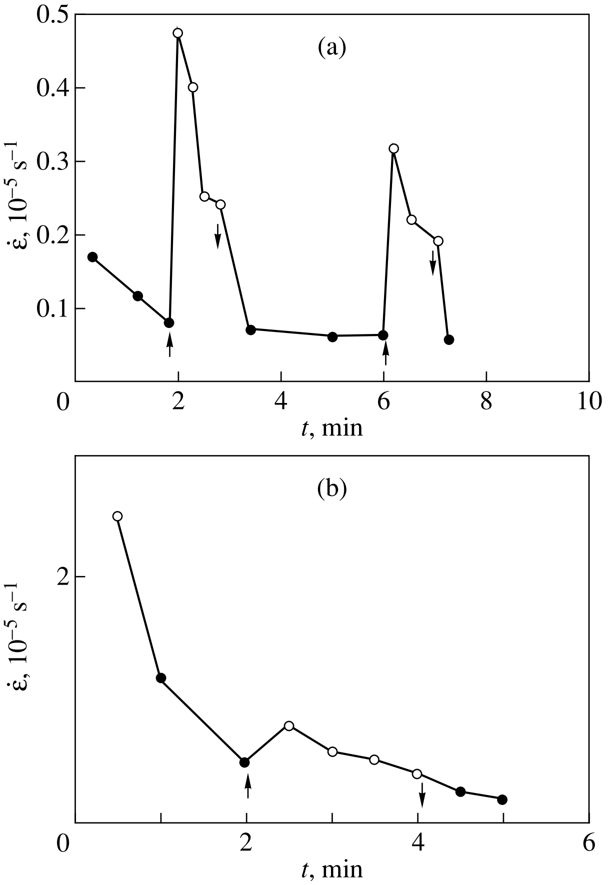

Fig. 2. Creep rate vs. time plots including the instants of application (↑) and removal (↓) of a magnetic field: (a) $NaNO_2$ (slip plane system $\{110\}\langle 111\rangle$), $\sigma = 8.5$ MPa; and (b) LiF, $\sigma = 7$ MPa.

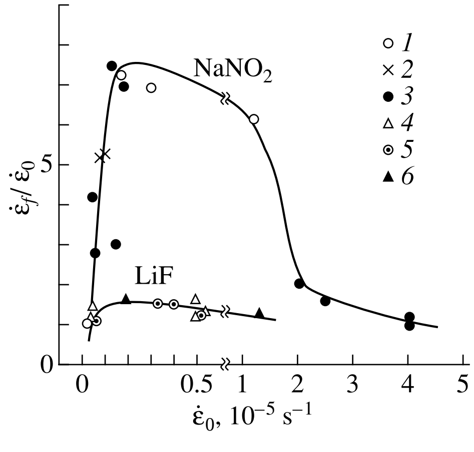

Fig. 3. Dependence of the $\dot{\varepsilon}_f/\dot{\varepsilon}_0$ ratio on the creep rate at which the MPE was measured in (*1–3*) $NaNO_2$ and (*4–6*) LiF crystals. The data were obtained under (*1*, *2*, *4*) application or (*5*) removal of a dc magnetic field ($B = 0.2$ T), as well as (*3*, *6*) after 10-min exposure to a field. The slip planes in the $NaNO_2$ crystals: (*1*, *3*) $\{110\}\langle 111\rangle$ and (*2*) (001)[100].

$\dot{\varepsilon}_f/\dot{\varepsilon}_0 \approx 7$. This MPE level remains nearly unchanged up to $\dot{\varepsilon}_0 \approx 1 \times 10^{-5}$ s^{-1}, after which it falls off rapidly and practically disappears at $\varepsilon_0 \approx 4 \times 10^{-5}$ s^{-1}. The $\dot{\varepsilon}_f/\dot{\varepsilon}_0$ relation for the LiF crystals behaves in the same way; however, the maximum value of this ratio does not exceed 1.6.

Interestingly, in the earlier experiments carried out on NaCl and LiF crystals under constant rates of strain [6] or loading [19], the maximum values of $\dot{\varepsilon}_f/\dot{\varepsilon}_0$ in weak magnetic fields likewise did not exceed 2 even for specimens containing a large amount of divalent impurities, which enhances the MPE [19]. In this case, the MPE in LiF crystals was observed for $B = 0.2$ T only for $\dot{\varepsilon}_0 < 2 \times 10^{-5}$ s^{-1} [6].

4. CONCLUSIONS

Thus, the experimental data obtained in this work indicate a manifestation of the MPE in ferroelectric crystals. In this case, the MPE reveals itself in an $NaNO_2$ crystals as a substantial increase in the plastic strain rate of a loaded specimen upon the application of a magnetic field or after subjection of the specimen to it. In these conditions, the MPE is observed only within the strain rate interval $\dot{\varepsilon} \approx (0.1–3) \times 10^{-5}$ s^{-1}. The results obtained can be interpreted qualitatively within a model that takes into account thermally activated and magnetically stimulated depinning of dislocations from various pinning centers, primarily the impurity centers present in the crystals [6, 19]. One should, naturally, also take into account the specific features of the structure of the dislocations themselves and of the pinning centers for each crystal considered. In particular, the formation of a polarization electric charge on dislocations may play a considerable role in ferroelectrics [23], but clarification of the part played by this charge in the MPE would require additional studies.

REFERENCES

1. N. V. Zagoruĭko, Kristallografiya **10**, 81 (1965) [Sov. Phys. Crystallogr. **10**, 63 (1965)].
2. V. I. Al’shits, E. V. Darinskaya, T. M. Perekalina, and A. A. Urusovskaya, Fiz. Tverd. Tela (Leningrad) **29**, 467 (1987) [Sov. Phys. Solid State **29**, 265 (1987)].
3. V. I. Alshits, E. V. Darinskaya, O. L. Kazakova, *et al.*, Mater. Sci. Eng. A **234–236**, 617 (1997).
4. Yu. I. Golovin and R. B. Morgunov, Zh. Éksp. Teor. Fiz. **115**, 605 (1999) [JETP **88**, 332 (1999)].
5. A. A. Urusovskaya, V. I. Al’shits, N. N. Bekkauer, and A. E. Smirnov, Fiz. Tverd. Tela (St. Petersburg) **42**, 267 (2000) [Phys. Solid State **42**, 274 (2000)].
6. V. I. Al’shits, A. A. Urusovskaya, A. E. Smirnov, and N. N. Bekkauer, Fiz. Tverd. Tela (St. Petersburg) **42**, 270 (2000) [Phys. Solid State **42**, 277 (2000)].
7. Yu. I. Golovin, R. B. Morgunov, D. V. Lopatin, and A. A. Baskakov, Phys. Status Solidi A **160**, R3 (1997).
8. N. A. Tyapunina, V. L. Krasnikov, and E. P. Belozerova, Fiz. Tverd. Tela (St. Petersburg) **41**, 1035 (1999) [Phys. Solid State **41**, 942 (1999)].
9. N. N. Peschanskaya, V. Yu. Surovova, and P. N. Yakushev, Fiz. Tverd. Tela (St. Petersburg) **34**, 2111 (1992) [Sov. Phys. Solid State **34**, 1127 (1992)].
10. N. N. Peschanskaya and P. N. Yakushev, Fiz. Tverd. Tela (St. Petersburg) **39**, 1690 (1997) [Phys. Solid State **39**, 1509 (1997)].
11. Yu. I. Golovin, R. B. Morgunov, and S. Yu. Liksutin, Vysokomol. Soedin., Ser. B **40**, 373 (1998).
12. Yu. I. Golovin, R. B. Morgunov, A. A. Baskakov, *et al.*, Pis’ma Zh. Éksp. Teor. Fiz. **69**, 114 (1999) [JETP Lett. **69**, 127 (1999)].
13. E. V. Darinskaya, E. A. Petrzhik, S. A. Erofeeva, and V. P. Kisel’, Pis’ma Zh. Éksp. Teor. Fiz. **70**, 298 (1999) [JETP Lett. **70**, 309 (1999)].
14. Yu. A. Osip’yan, Yu. I. Golovin, D. V. Lopatin, *et al.*, Pis’ma Zh. Éksp. Teor. Fiz. **69**, 110 (1999) [JETP Lett. **69**, 123 (1999)].
15. Yu. A. Osip’yan, Yu. I. Golovin, R. B. Morgunov, *et al.*, Fiz. Tverd. Tela (St. Petersburg) **43**, 1333 (2001) [Phys. Solid State **43**, 1389 (2001)].
16. V. I. Al’shits, E. V. Darinskaya, I. V. Gektina, and F. F. Lavrent’ev, Kristallografiya **35**, 1014 (1990) [Sov. Phys. Crystallogr. **35**, 597 (1990)].
17. V. I. Al’shits, R. Voska, E. V. Darinskaya, and E. A. Petrzhik, Fiz. Tverd. Tela (St. Petersburg) **35**, 70 (1993) [Phys. Solid State **35**, 37 (1993)].
18. O. I. Datsko, V. I. Alekseenko, and A. D. Shakhova, Fiz. Tverd. Tela (St. Petersburg) **39**, 1234 (1997) [Phys. Solid State **39**, 1094 (1997)].
19. Yu. I. Golovin and R. B. Morgunov, Materialovedenie, Nos. 3–6, 2 (2000).
20. V. I. Nikolaev and B. I. Smirnov, Fiz. Tverd. Tela (Leningrad) **27**, 3369 (1985) [Sov. Phys. Solid State **27**, 2028 (1985)].
21. V. I. Nikolaev, B. I. Smirnov, and V. A. Ivantsov, Fiz. Tverd. Tela (Leningrad) **27**, 2519 (1985) [Sov. Phys. Solid State **27**, 1510 (1985)].
22. N. N. Peschanskaya, G. S. Pugachev, and P. N. Yakushev, Mekh. Polim., No. 2, 490 (1977).
23. V. I. Nikolaev, N. A. Pertsev, and B. I. Smirnov, Fiz. Tverd. Tela (Leningrad) **33**, 93 (1991) [Sov. Phys. Solid State **33**, 51 (1991)].

Translated by G. Skrebtsov

Physics of the Solid State, Vol. 43, No. 12, 2001, pp. 2253–2256. Translated from Fizika Tverdogo Tela, Vol. 43, No. 12, 2001, pp. 2157–2160.
Original Russian Text Copyright © 2001 by Kamzin, Lutsev, Petrov.

MAGNETISM AND FERROELECTRICITY

Epitaxial Films of Ba–*M* Type Hexagonal Ferrites

A. S. Kamzin, L. V. Lutsev, and V. A. Petrov
Ioffe Physicotechnical Institute, Russian Academy of Sciences, Politekhnicheskaya ul. 26, St. Petersburg, 194021 Russia
e-mail: kamzin@kas.ioffe.rssi.ru

Received February 26, 2001; in final form, April 5, 2001

Abstract—Single-crystal films of the $Ba_{0.87}Bi_{0.13}Al_{3.96}Fe_{8.04}O_{19}$ hexagonal ferrite were prepared by liquid-phase epitaxy on single-crystal plates of the nonmagnetic material $SrGa_{12}O_{19}$, whose crystal structure is similar to that of the film grown on it. A Mössbauer study of the films revealed that the magnetic moments of the iron ions in the bulk of a film are perpendicular to the film growth plane, whereas the moments of the ions residing in a surface layer ~300-nm thick are canted away from the normal of the film by 30° ± 5°. *© 2001 MAIK "Nauka/Interperiodica".*

Widespread application of magnetic materials in the form of epitaxial films of hexagonal ferrites in various areas of microelectronics requires not only investigation of the characteristics of the films themselves but also our understanding of the properties of the surface and of their relationships with the bulk characteristics. The fact is that the method used to prepare the films, namely, liquid-phase epitaxy (LPE) on substrates from a supercooled solution in a melt, brings about the formation of transition layers on the film–substrate and film–air interfaces. Indeed, it has been experimentally shown [1] that the magnetic structure of the surface layer adjoining the film–air interface differs from that of the bulk of the film. It has been established [2] that the differences in magnetic structure increase as one approaches the film surface. On the garnet-ferrite-film–substrate and the film–air interfaces, transition layers were detected [3–5] that differed in chemical composition from the bulk of the film, with these differences increasing as one moves closer to the film interfaces. However, the nature of the differences between the magnetic structures of the surface and of the bulk was not discussed in [1, 2]. It should be pointed out that the fact that a surface transition layer differing in magnetic structure from the bulk exists on the surface of macroscopic crystals was first demonstrated experimentally in [6, 7] using antiferromagnets with a weak ferromagnetic moment as an example. Such a transition layer was later shown to be present in hexagonal ferrites as well [8–10].

Thus, the crystallization process and the formation of surface properties in thin films of such complex oxide compounds as ferrites require further investigation. This work was aimed at studying the magnetic properties of the bulk and of the surface layer in films of Ba–*M*-type hexagonal ferrites.

Single-crystal films of the hexagonal ferrite were LPE-grown from a $Ba_{0.87}Bi_{0.13}Al_{3.96}Fe_{8.04}O_{19}$ batch. The films were prepared on (0001) single-crystal substrates of nonmagnetic $SrGa_{12}O_{19}$. This orientation of the substrate was chosen to obtain a film with its magnetization perpendicular to its growth plane. The films were grown without substrate rotation at a melt temperature ~1040°C for 10 min. The ^{57}Fe isotopic content in the films was equal to its natural abundance ratio. The film thickness was ~3 μm.

We studied the crystalline and magnetic structures of the films using x-ray diffraction and simultaneous gamma, x-ray, and electron Mössbauer spectroscopy (SGXEMS) [11]. Mössbauer spectroscopy provides direct information both on the phase state of the substance under study and on the orientation of the magnetic moment in a sample. The SGXEMS method permits one to simultaneously obtain Mössbauer spectra in γ rays, x-ray characteristic radiation, and conversion and Auger electrons (CAE). The spectra thus obtained can be used to derive information on the properties of the bulk, of layers a few micrometers thick, and of surface layers ~300 nm thick of the sample under study.

The Mössbauer spectra of the $Ba_{0.87}Bi_{0.13}Al_{3.96}Fe_{8.04}O_{19}$ films were measured on a SGXEMS-based computer-controlled system [12]. The wave vector of the γ radiation was oriented perpendicular to the surface of the films studied. The $SrGa_{12}O_{19}$ substrates were ~500-μm thick and, therefore, opaque to the 14.4 keV Mössbauer radiation. To measure Mössbauer spectra with detection of γ rays in the film transmission mode, the substrates were ground off to a thickness ~100 μm.

Figure 1 shows room-temperature Mössbauer spectra of our films. They are seen to consist of several Zeeman sextuplets, which are due to iron ions occupying inequivalent sites. A least squares computer analysis of the spectral data showed them to be spectra of the hexagonal ferrite. The experimental spectra were used to derive the hyperfine-interaction parameters. The values of the effective fields H_{eff} at the iron-nucleus sites in the

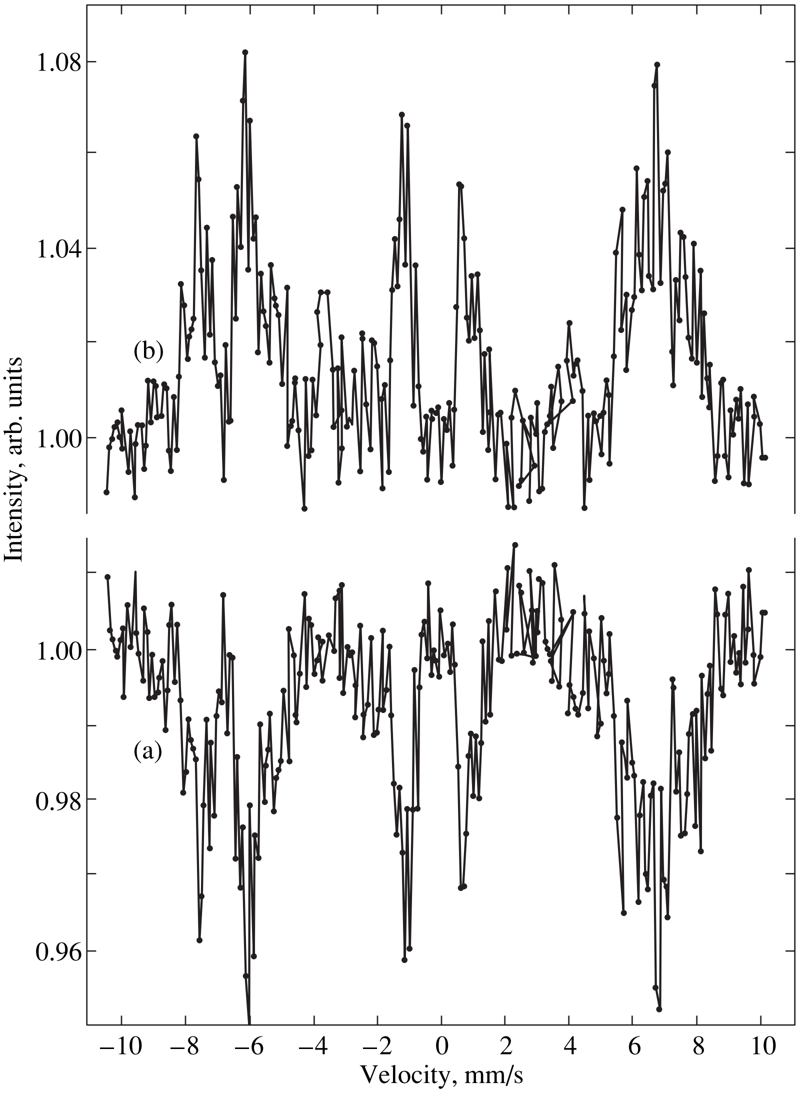

Fig. 1. Mössbauer spectra of an epitaxial film of the $Ba_{0.87}Bi_{0.13}Al_{3.96}Fe_{8.04}O_{19}$ hexagonal ferrite obtained at 300 K by detecting (a) γ-rays passing through the sample and (b) conversion and Auger electrons escaping out of a surface layer ~300-nm thick.

300-nm thick surface layer and in the bulk of the film were found to coincide to within experimental error. The effective fields are listed in the table together with the corresponding figures for bulk crystals of the hexagonal ferrites. As seen from the table, the effective fields in the films under study, in which the number of diamagnetic Al ions per formula unit is $x = 3.96$, are substantially lower than those in the unsubstituted Ba–*M* ferrites, even though doping the Sr–*M* ferrites with Al ions to a value of $x = 1.8$ does not produce a noticeable decrease in H_{eff} [10].

The spectra obtained with γ rays (Fig. 1a) do not have the second and fifth sextuplet lines corresponding to $\Delta m = 0$ transitions, which indicates that the magnetic moments of the iron ions in the bulk of the film are parallel to the wave vector of the γ-ray beam. The CAE spectrum contains weak lines corresponding to the second and fifth lines of the Zeeman sextuplets. This implies that the magnetic moments of the iron ions residing in the ~300-nm-thick surface layer are canted away from the film surface normal.

The experimental spectral-line intensity ratio can be used to calculate the angle θ defining the orientation of the magnetic moment in the crystal relative to the γ-radiation wave vector. This can be done using the relation (see, e.g., [13])

$$\theta = \arccos\left(\frac{4A_{1,6} - 3A_{2,5}}{4A_{1,6} + 3A_{2,5}}\right)^{1/2} = \arcsin\left(\frac{(3/2)A_{2,5}/A_{1,6}}{1 + (3/4)A_{2,5}/A_{1,6}}\right)^{1/2}, \quad (1)$$

Effective magnetic fields H_{eff} for iron ions in the bulk of an *M*-type hexaferrite ($MAl_xFe_{12-x}O_{19}$) at room temperature

Sublattice	$SrFe_{12}O_{19}$ [10]	$SrAl_{1.8}Fe_{10.2}O_{19}$ [10]	$BaFe_{12}O_{19}$ [9]	This work, $Ba_{0.87}Bi_{0.13}Al_{3.96}Fe_{8.04}O_{19}$ film
$12k$	413 ± 1	415 ± 1	416 ± 1	325 ± 5
$4f_1$	498 ± 1	482 ± 2	493 ± 1	390 ± 7
$4f_2$	519 ± 2	518 ± 2	520 ± 3	471 ± 7
$2a$	510 ± 2	510 ± 2	508 ± 3	457 ± 7
$2b$	405 ± 4	405 ± 4	403 ± 5	312 ± 8

where $A_{1,6}$ are the intensities of the first and sixth lines and $A_{2,5}$ are the intensities of the second and fifth lines. The line intensity calculations made using Eq. (1) for a spectrum obtained with the detection of γ rays and CAE yielded 0 and ~30° ± 5° for the angle θ, respectively. This implies that the magnetic moments of the iron ions in the bulk of the film are oriented perpendicular to the film plane and parallel to the crystallographic axis *C*.

It is known that the diamagnetic cations Al, Ga, Cr, or Mn substituting for Fe^{3+} ions are distributed uniformly over all the sublattices of an *M*-type hexaferrite [14]. The exception is the 2*b* sublattice, where the iron ions remain unsubstituted up to $x = 4–6$. Therefore, *M*-type hexaferrites doped with such substituting ions do not exhibit a sharp change in their magnetic properties with increasing concentration of diamagnetic substituting ions, as is the case with iron ions replaced by ions of Sc, In, and Zn [9, 14]. The collinearity of the magnetic structure in hexaferrites with Al, Ga, Cr, and Mn substituting ions breaks down at room temperature for $x \geq 3$ (see [10] and references therein). Magnetic ordering in such ferrites fails at $x \geq 6–8$.

We did not observe any violation of collinearity in the orientation of the magnetic moment with the *C* axis in the bulk of the films studied. It may be conjectured that the concentrations of diamagnetic cations substituting for iron ions are not high enough for a noncollinear structure to form in the bulk of a film.

The ~300-nm thick surface layer of the films under study exhibits a different scenario; namely, the magnetic moments in this layer are canted away from the *C* crystallographic axis. The onset of this misorientation of moments can be interpreted in the following way. As shown experimentally, a transition surface layer in which the orientation of the magnetic moment differs from that in the bulk of the sample exists in weakly ferromagnetic crystals [6, 7] and hexagonal ferrites [8–10]. This transition layer is formed due to the exchange interactions being reduced near the surface. Another factor capable of influencing the orientation of the magnetic moment in the surface layer is the slight change in the composition as one approaches the surface of films prepared through liquid-phase epitaxy. The fact is that, when the substrate with the film is taken out of the melt solution, a change in the temperature conditions in which the film surface layer forms may affect its properties. This work was not aimed at investigating the surface layer composition. However, studies of YIG films [3–5] have provided experimental evidence of changes in the surface layer composition.

Thus, we have used the method of simultaneous gamma, x-ray, and electron Mössbauer spectroscopy to study the magnetic properties of the bulk and a ~300-nm-thick surface layer of films of $Ba_{0.87}Bi_{0.13}Al_{3.96}Fe_{8.04}O_{19}$ hexagonal ferrites prepared through liquid-phase epitaxy. It has been established that the magnetic moments of the iron ions located in the bulk are oriented perpendicular to the film surface and parallel to the *C* crystallographic axis, whereas those of the iron ions in the surface layer are canted away from the moments in the bulk of the films at an angle of 30° ± 5°. This difference is probably due both to the presence of the surface and to a change in the cation distribution in the surface layer observed as one goes over from the bulk to the surface of the film.

ACKNOWLEDGMENTS

This study was supported by the Russian Foundation for Basic Research, project no. 01-02-17889.

REFERENCES

1. A. S. Kamzin, V. A. Bokov, E. S. Sher, *et al.*, Fiz. Tverd. Tela (Leningrad) **24** (7), 2016 (1982) [Sov. Phys. Solid State **24**, 1151 (1982)].
2. K. Saneyoshi, T. Toriyama, J. Itoh, *et al.*, J. Magn. Magn. Mater. **31–34**, 705 (1983).
3. V. V. Randoshkin, A. N. Shaposhnikov, G. N. Shaposhnikova, and A. V. Shirokov, Pis'ma Zh. Tekh. Fiz. **10** (4), 224 (1984) [Sov. Tech. Phys. Lett. **10**, 93 (1984)].
4. N. A. Groshenko, A. M. Prokhorov, V. V. Randoshkin, *et al.*, Fiz. Tverd. Tela (Leningrad) **27** (6), 1712 (1985) [Sov. Phys. Solid State **27**, 1029 (1985)].
5. A. S. Kamzin and Yu. N. Mal'tsev, Fiz. Tverd. Tela (St. Petersburg) **39** (7), 1248 (1997) [Phys. Solid State **39**, 1108 (1997)].
6. G. S. Krinchik and V. E. Zubov, Zh. Éksp. Teor. Fiz. **69** (2), 707 (1975) [Sov. Phys. JETP **42**, 359 (1975)].

7. A. S. Kamzin and L. A. Grigor'ev, Zh. Éksp. Teor. Fiz. **104**, 3489 (1993) [JETP **77**, 658 (1993)].
8. A. S. Kamzin, L. P. Ol'khovik, and V. L. Rozenbaum, Pis'ma Zh. Éksp. Teor. Fiz. **67** (4), 798 (1998) [JETP Lett. **67**, 843 (1998)].
9. A. S. Kamzin, Zh. Éksp. Teor. Fiz. **116** (5), 1648 (1999) [JETP **89**, 890 (1999)].
10. A. S. Kamzin and L. P. Ol'khovik, Fiz. Tverd. Tela (St. Petersburg) **41** (10), 1806 (1999) [Phys. Solid State **41**, 1658 (1999)].
11. A. S. Kamzin and L. A. Grigor'ev, Pis'ma Zh. Tekh. Fiz. **16** (16), 38 (1990) [Sov. Tech. Phys. Lett. **16**, 616 (1990)].
12. A. S. Kamzin and L. A. Grigor'ev, Pis'ma Zh. Tekh. Fiz. **19** (8), 50 (1993) [Tech. Phys. Lett. **19**, 245 (1993)].
13. *Chemical Applications of Mössbauer Spectroscopy*, Ed. by V. I. Gol'danskii and R. H. Herber (Academic, New York, 1968; Mir, Moscow, 1970).
14. Sh. Sh. Bashkirov, A. B. Liberman, and V. I. Sinyavskiĭ, *Magnetic Microstructure of Ferrites* (Kazan. Univ., Kazan, 1978).

Translated by G. Skrebtsov

Physics of the Solid State, Vol. 43, No. 12, 2001, pp. 2257–2261. Translated from Fizika Tverdogo Tela, Vol. 43, No. 12, 2001, pp. 2166–2170.
Original Russian Text Copyright © 2001 by Dunaevskiĭ.

MAGNETISM AND FERROELECTRICITY

Influence of the Degenerate *d* Level and of the Jahn–Teller Effect on the Manganite Electronic Structure Calculated in the Tight-Binding Approximation

S. M. Dunaevskiĭ
St. Petersburg Institute of Nuclear Physics, Russian Academy of Sciences,
Gatchina, St. Petersburg, 188350 Russia
e-mail: dunaevsk@mail.pnpi.spb.ru

Received April 18, 2001

Abstract—$E(\mathbf{k})$ dispersion curves for the charge carriers in the $LaMnO_3$-like perovskites were calculated for the basic types of canted antiferromagnetic ordering of the Mn sublattice in the framework of the tight-binding approximation. The $E(\mathbf{k})$ spectrum of the antiferromagnetic structures was calculated for the first time taking into account the degeneracy of the Mn e_g level and the Jahn–Teller distortion of the cubic perovskite structure. This calculation involved diagonalization of the 8×8 Hamiltonian matrix. Analytical expressions for the $E(\mathbf{k})$ function at separate points and symmetry lines of the Brillouin zone were derived. The calculations showed that the properties of the $La_{1-x}Ca_xMnO_3$ system do not have electron–hole symmetry. *© 2001 MAIK “Nauka/Interperiodica”.*

1. INTRODUCTION

At the present time, doped $R_{1-x}L_xMnO_3$ manganites (R = La, Pr, Nd, Sm; L = Ca, Ba, Sr) are objects of intense experimental and theoretical investigations, in which particular attention is given to their unique physical properties (colossal magnetoresistance, metal–insulator phase transitions, charge ordering, etc.) [1]. Now, it is evident that, in order to correctly describe the phase diagrams and the transport properties of manganites, the degree of freedom associated with the double orbital degeneracy of the Mn e_g level should be taken into account in addition to the spin and the charge degrees of freedom [2, 3].

The anomalous electric conductivity of manganites in the vicinity of the Curie point is explained in terms of the Zener–Anderson–Hasegawa double-exchange (DE) model [4–6]. This model allows one to calculate the energy band spectrum $E(\mathbf{k})$ and the kinetic energy of the charge carriers for different magnetic phases of the perovskite crystalline structure. In the DE model, the hopping integral t_{ij} between the manganese ions depends on the angle θ between the magnetic moments of the nearest neighbor Mn^{4+} ions, $t_{ij} = t\cos(\theta_{ij}/2)$. In order to calculate the $E(\mathbf{k})$ spectrum of a certain magnetic structure (only the manganese sublattice is usually considered in manganites), it is necessary to specify the angles θ_{ij} and solve the corresponding secular equation. The order of this equation is equal to the product of the number of atomic orbitals and the number of magnetically nonequivalent manganese ions.

The electronic band structure of the basic magnetic structures of manganites (without regard for the orbital degeneracy [7] of the e_g level) is well known. With allowance for the double degeneracy of this level, the electronic band structure has been calculated only for the ferromagnetic (FM) state of the manganese sublattice [8]. Unfortunately, the results obtained for the FM case are often used [2, 9] to calculate the kinetic energy of charge carriers in antiferromagnetic (AF) structures and to construct phase diagrams for doped manganites. Such calculations are not justified, because they ignore the increase in the number of nonequivalent atoms in the unit cell (which leads to a higher order secular equation) as one goes from the FM to the AF case. Thus, it is necessary to calculate $E(\mathbf{k})$ for different AF structures with allowance for the e_g-level degeneracy, the Jahn–Teller (JT) lattice distortions, and the possible charge ordering in order to carry out a correct theoretical analysis of the total energy and the orbital, charge, and spin ordering in the oxides under study.

2. CALCULATION METHOD

This study is dedicated to calculating an $E(\mathbf{k})$ spectrum that takes into account the orbital degeneracy of the e_g electrons in manganites for different types of magnetic (canted antiferromagnetic) ordering in the system. We assume, as in the majority of recent papers, that the spin of a charge carrier is always oriented along the local manganese ion spin formed by the three t_{2g} electrons. Several basic types of magnetic ordering of the manganese sublattice in perovskites have been observed experimentally: type **A** is AF ordering of the neighboring (100) FM planes, which is observed in the

$LaMnO_3$ compound ($\theta_{ij} = \theta_z = \pi$); type **G** is AF ordering of the nearest neighbors ($CaMnO_3$, $\theta_{ij} = \pi$); type **C** is AF ordering in the (100) plane ($\theta_{ij} = \theta_{xy} = \pi$); and type **F** is FM ordering ($\theta_{ij} = 0$). In the case of canted ferromagnetic ordering, the angle $\theta_{ij} \neq \pi$. In **A**, **G**, and **C** magnetic ordering, the perovskite unit cell contains two nonequivalent manganese atoms. In order to calculate the energy spectrum in the tight-binding approximation with allowance for the degeneracy of the e_g level, one should diagonalize the Hamiltonian matrix constructed in terms of eight basis Bloch functions. In the case when both angles θ_{xy} and θ_z are simultaneously nonzero, one should use at least twelve combinations of Bloch functions. It is clear that the energy spectrum of AF structures (especially, of the **G** type) cannot be approximated (as was done in [2]) by the spectrum of the FM state with two hopping integrals dependent on θ_{xy} and θ_z.

In the framework of the infinitively strong intraatomic Hund exchange approximation (where the intraatomic energy is much greater than the hopping integral, $JS \gg t$), we can limit our consideration to 4 × 4 matrices and obtain analytical expressions for the dispersion relations. However, we will consider the general case, where JS is comparable to t [$JS \approx (3–5)t$]. The Hamiltonian of the system is taken to be the double-exchange Hamiltonian:

$$H_{\mathrm{DE}} = \sum_{i\alpha\sigma} \varepsilon_{i\alpha\sigma} d^{+}_{i\alpha\sigma} d_{i\alpha\sigma} + \sum_{ij\alpha\beta\sigma'\sigma} t^{\sigma\sigma'}_{ij\alpha\beta}\left(\frac{\theta_{ij}}{2}\right) d^{+}_{i\alpha\sigma} d_{j\beta\sigma'} + \frac{U}{2}\sum_{i\sigma} n_{i\sigma} n_{i-\sigma}, \tag{1}$$

where

$$t^{\sigma\sigma'}_{ij\alpha\beta}\left(\frac{\theta_{ij}}{2}\right) = \begin{cases} t_{\alpha\beta}\cos\left(\dfrac{\theta_{ij}}{2}\right), & \sigma = \sigma' \\ \pm t_{\alpha\beta}\sin\left(\dfrac{\theta_{ij}}{2}\right), & \sigma \neq \sigma', \end{cases}$$

i and j are the atom indices, α and β are the atomic orbitals $|z^2\rangle$ and $|x^2 - y^2\rangle$, $\varepsilon_{i\alpha\sigma}$ is the energy of the degenerate d level of the α-type Mn^{3+} ion ($\alpha = 1, 2$), σ is the spin index, θ_{ij} is the angle between the local magnetic moments $\mathbf{S}$ ($S = 3/2$) of the neighboring Mn^{4+} ions, and $t^{\sigma\sigma'}_{ij\alpha\beta}$ is the hopping integral between the degenerate orbitals of nearest neighbors. The value of the hopping integral depends on the hopping direction; in the Cartesian coordinate system x, y, and z, the hopping integral is expressed in the matrix form as follows:

$$t_{ij\alpha\beta} \equiv t^{\alpha\beta}_{ij} = -t\begin{pmatrix} \frac{1}{4} & \frac{-\sqrt{3}}{4} \\ \frac{-\sqrt{3}}{4} & \frac{3}{4} \end{pmatrix} \text{ along the } x \text{ axis;}$$
$$-t\begin{pmatrix} \frac{1}{4} & \frac{\sqrt{3}}{4} \\ \frac{\sqrt{3}}{4} & \frac{3}{4} \end{pmatrix} \text{ along the } y \text{ axis;} \tag{2}$$
$$-t\begin{pmatrix} 1 & 0 \\ 0 & 0 \end{pmatrix} \text{ along the } z \text{ axis.}$$

Here,

$$\alpha, \beta = |1\rangle = |z^2\rangle, \quad |2\rangle = |x^2 - y^2\rangle, \quad t = \frac{V^2_{pd\sigma}}{E_d - E_p}.$$

The Hamiltonian matrix for the canted antiferromagnetic structures is conveniently written as

$$H(\mathbf{k}) = \begin{pmatrix} H_1(\mathbf{k}) & H_{12}(\mathbf{k}) \\ \tilde{H}^{*}_{12}(\mathbf{k}) & H_2(\mathbf{k}) \end{pmatrix}, \tag{3}$$

where the matrices H_1 and H_2 describe the interaction between orbitals of the same type, while the matrix H_{12} describes the interaction between degenerate orbitals of different types. The explicit form of the matrices H_i for different magnetic structures is given by the formulas presented in [7]. For example, for the **G**-type structure, we have

$$H_i(\mathbf{k}) = \begin{pmatrix} E'_{di} - JS & 0 & t_i(\mathbf{k})\cos\frac{\theta}{2} & t_i(\mathbf{k})\sin\frac{\theta}{2} \\ 0 & E'_{di} + J(S+1) & -t_i(\mathbf{k})\sin\frac{\theta}{2} & t_i(\mathbf{k})\cos\frac{\theta}{2} \\ t_i(\mathbf{k})\cos\frac{\theta}{2} & -t_i(\mathbf{k})\sin\frac{\theta}{2} & E'_{di} - JS & 0 \\ t_i(\mathbf{k})\sin\frac{\theta}{2} & t_i(\mathbf{k})\cos\frac{\theta}{2} & 0 & E'_{di} + J(S+1) \end{pmatrix}, \tag{4}$$

where $t_1(\mathbf{k}) = -\frac{1}{2}t(\cos k_x + \cos k_y) - 2t\cos k_z$, $t_2(\mathbf{k}) = -\frac{3}{2}t(\cos k_x + \cos k_y)$, $t = \frac{V^2_{pd\sigma}}{\Delta}$, and $\Delta = E_d - E_p$. Here, $E'_{di} = E_{di} + U\langle n_{-\sigma}\rangle$ is the energy of the manganese ion e_g levels, E_p is the energy of the oxygen p level, and t is the effective transfer integral between the orbitals of the nearest neighbor manganese ions calculated in the second-order perturbation theory with respect to the Koster–Slater transfer integral $V_{pd\sigma}$ between the manganese e_g orbital and the p orbital of its nearest neighbor oxygen ion. The parameter t for manganites is positive, because, according to numerical calculations using the cluster method [10], the E_p level lies below the E_{di} levels. Since only the transfer between the $|z^2\rangle$-type orbitals is possible along the z axis, the matrix $H_{12}(\mathbf{k})$ depends only on the perpendicular component of the wave vector $\mathbf{k}_\perp$ and has the form

$$H_{12}(\mathbf{k}_\perp) = \begin{pmatrix} 0 & 0 & t_{12}(\mathbf{k}_\perp)\cos\frac{\theta}{2} & t_{12}(\mathbf{k}_\perp)\sin\frac{\theta}{2} \\ 0 & 0 & -t_{12}(\mathbf{k}_\perp)\sin\frac{\theta}{2} & t_{12}(\mathbf{k}_\perp)\cos\frac{\theta}{2} \\ t_{12}(\mathbf{k}_\perp)\cos\frac{\theta}{2} & -t_{12}(\mathbf{k}_\perp)\sin\frac{\theta}{2} & 0 & 0 \\ t_{12}(\mathbf{k}_\perp)\sin\frac{\theta}{2} & t_{12}(\mathbf{k}_\perp)\cos\frac{\theta}{2} & 0 & 0 \end{pmatrix}, \tag{5}$$

where

$$t_{12}(\mathbf{k}_\perp) = \frac{\sqrt{3}}{2}t(\cos k_x - \cos k_y).$$

For the **A**-type structure, we obtain

$$H_i(\mathbf{k}) = \begin{pmatrix} \mathscr{E} - JS & 0 & t_i(\mathbf{k}_z)\cos\frac{\theta}{2} & t_i(\mathbf{k}_z)\sin\frac{\theta}{2} \\ 0 & \mathscr{E} + J(S+1) & -t_i(\mathbf{k}_z)\sin\frac{\theta}{2} & t_i(\mathbf{k}_z)\cos\frac{\theta}{2} \\ t_i(\mathbf{k}_z)\cos\frac{\theta}{2} & -t_i(\mathbf{k}_z)\sin\frac{\theta}{2} & \mathscr{E} - JS & 0 \\ t_i(\mathbf{k}_z)\sin\frac{\theta}{2} & t_i(\mathbf{k}_z)\cos\frac{\theta}{2} & 0 & \mathscr{E} + J(S+1) \end{pmatrix}, \tag{6}$$

where $E'_{di} + t_i(\mathbf{k}_\perp) = \mathscr{E}$, $t_1(k_z) = -2t\cos k_z$, $t_2(k_z) \equiv 0$, $t_1(\mathbf{k}_\perp) = -\frac{1}{2}t(\cos k_x + \cos k_y)$, and $t_2(\mathbf{k}_\perp) = -\frac{3}{2}t(\cos k_x + \cos k_y)$.

In Eqs. (4)–(6), it is assumed that index 1 corresponds to the d orbital of the $|z^2\rangle$ type and index 2 corresponds to the $|x^2 - y^2\rangle$ orbital. It follows from Eq. (6) that the matrix $H_2(\mathbf{k})$ is diagonal for the **A**-type structure. It is obvious that in this case, the matrix $H_{12}(\mathbf{k})$ is also diagonal, $H_{mn}(\mathbf{k}_\perp) = t_{12}(\mathbf{k}_\perp)\delta_{mn}$ (m, n = 1–4).

For the **C**-type structure, we have

$$H_i(\mathbf{k}) = \begin{pmatrix} \bar{\mathscr{E}} - JS & 0 & t_i(\mathbf{k}_\perp)\cos\frac{\theta}{2} & t_i(\mathbf{k}_\perp)\sin\frac{\theta}{2} \\ 0 & \bar{\mathscr{E}} + J(S+1) & -t_i(\mathbf{k}_\perp)\sin\frac{\theta}{2} & t_i(\mathbf{k}_\perp)\cos\frac{\theta}{2} \\ t_i(\mathbf{k}_\perp)\cos\frac{\theta}{2} & -t_i(\mathbf{k}_\perp)\sin\frac{\theta}{2} & \bar{\mathscr{E}} - JS & 0 \\ t_i(\mathbf{k}_\perp)\sin\frac{\theta}{2} & t_i(\mathbf{k}_\perp)\cos\frac{\theta}{2} & 0 & \bar{\mathscr{E}} + J(S+1) \end{pmatrix}, \tag{7}$$

where $E'_{di} + t_i(\mathbf{k}_z) = \bar{\mathscr{E}}$. The matrix $H_{12}(\mathbf{k}) = H_{12}(\mathbf{k}_\perp)$ is identical to the corresponding matrix for the **G**-type structure.

3. RESULTS AND DISCUSSION

The dispersion curves for different canted antiferromagnetic structures were calculated using Eqs. (3)–(7) both with and without regard for the static JT distortions of the perfect cubic perovskite structure. Because of these distortions, the transfer integral has different values along different directions and the E_{d1} and E_{d2} levels are split. The distance dependence of the transfer integrals (the parameter $V_{pd\sigma}$), which was determined in accordance with Harrison's suggested methods [11], virtually does not affect the calculated dispersion curves. The most important effect of the JT distortions is the e_g-level splitting. When a certain critical value of this splitting is attained, an insulating band gap appears in the lower degenerate band of the **A**-type ($LaMnO_3$) magnetic structure. If the JT effect is not taken into account and, therefore, the e_g level is degenerate, then the **A** structure will always be a metal (even without doping): this contradicts numerous experimental data. For the **G** structure, the band gap arises for considerably smaller amounts of the JT distortions. For perfect structures ($\theta = \pi$), all bands are twofold degenerate. In this case, one can easily derive analytical expressions for the $E(\mathbf{k})$ dispersion relation for some separate points and symmetry lines in the Brillouin zone (BZ). In the general case, it is easier to carry out numerical diagonalization for the eighth-order secular equation for arbitrary values of the angle θ and the wave vector $\mathbf{k}$ in the BZ of an orthorhombic lattice. Because the orthorhombic distortions are small and only the manganese sublattice can be considered, we carried out all calculations for the BZ of the cubic lattice in the standard notation used in [8].

It is convenient to perform numerical calculations of $E(\mathbf{k})$ in units of t. Specific values of this parameter for $LaMnO_3$ lie within the range from a value of 0.1–0.15 eV [12] (obtained in the framework of the band formalism of the density functional) to a value of ≈0.30 eV [10] (found for the $[La_4Mn_2O_{11}]^{4-}$ cluster in

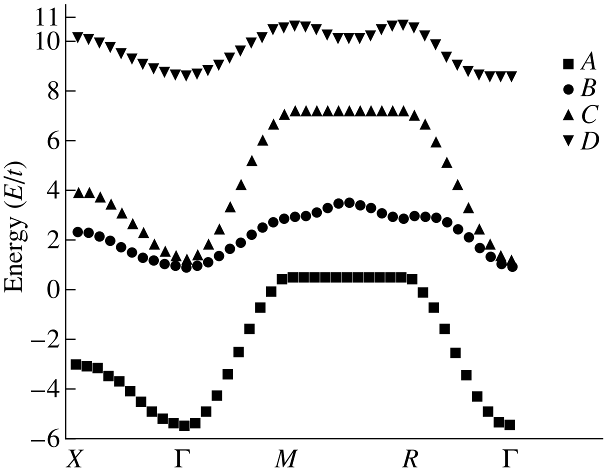

Fig. 1. Energy spectrum of the **A**-type antiferromagnetic structure for the main symmetry directions in the Brillouin zone calculated for the parameters $\theta = \pi$, $J = 1.67t$, $E_{d1} = 5t$, and $E_{d2} = 0$. All bands (A, B, C, D) are twofold degenerate.

the framework of the density-functional formalism). According to cluster calculations, the e_g-level splitting in the crystalline field is $E_{d1} - E_{d2} = 0.3$–0.5 eV [10], while it follows from the optical data [13] that $E_{d1} - E_{d2} = 1$ eV. The parameter $J \approx 0.25$ eV was obtained as a result of calculating the Mn^{3+} ion electronic band structure in the Hartree–Fock approximation using the well-known RAINE program complex [14]. This parameter was determined for $S = 3/2$ from the equation $J(2S + 1) = E_{\mathrm{tot}}[\mathrm{Mn}^3(S = 2)] - E_{\mathrm{tot}}[\mathrm{Mn}^{3+}(S = 1)] \approx 0.97$ eV, where E_{tot} is the total energy of the Mn^{3+} ion in the corresponding spin state. The atomic evaluation almost coincides with the value obtained in the band calculations [12], where the energy difference is approximately equal to 0.9 eV.

Figure 1 presents the spectrum of the **A**-type AF structure calculated for the following values of parameters: $\theta = \pi$, $J = 1.67t$, $E_{d1} = 5t$, $E_{d2} = 0$, and $S = 3/2$. This spectrum has the same shape as the spectrum calculated in [12] in the vicinity of the Fermi level within the local density approximation (LDA). There are two electrons per unit cell in the **A**-type structure at hand. These electrons completely fill the lower twofold-degenerate A band formed by the type 2 orbitals. When the JT distortions are not taking into account, this band overlaps with the upper band B (of type 1); therefore, the compound is a metal. A band gap arises in the spectrum only in the case when the JT distortions are sufficiently large for the amount of splitting of the d level to exceed a certain critical value $E_{d1} - E_{d2} \geq 5t$. An analogous situation was also considered in [12]. The value of the indirect band gap is $E_g \approx t \approx 0.1$–$0.3$ eV, while the direct band gap is $2.5t$. The bottom of the upper empty band is located at the $\Gamma(0, 0, 0)$ point, while the top of the lower band is on the $M(1/2, 1/2, 0)$–$R(1/2, 1/2, 1/2)$ line. This leads to the appearance of a peak in the density of states near the corresponding energy. As the splitting of the degenerate level is increased, the B and C bands (of type 2), having different spin directions, can overlap.

The spectrum of the canted **A**-type antiferromagnetic structure calculated for the angle $\theta = 0.8\pi$ is presented in Fig. 2. It should be noted that the A and B, as well as E and F, bands of type 2 remain twofold degenerate along the BZ symmetry directions in Fig. 2. Only the bands of type 1 (C, D, G, H) are split. Complete band splitting occurs at arbitrary no-symmetry points of the BZ. However, according to the calculations, this splitting is insignificant. For example, the splitting of the lower band in the Γ–X direction is approximately

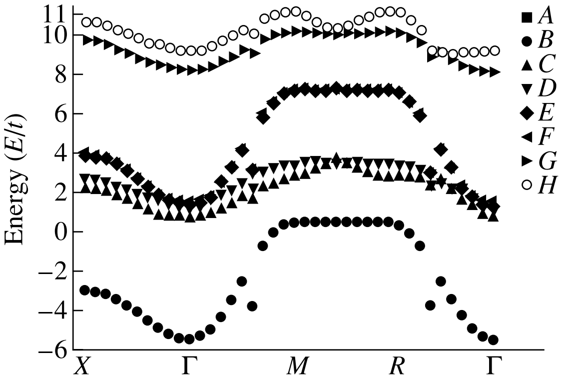

Fig. 2. Energy spectrum of the canted **A**-type antiferromagnetic structure calculated for $\theta = 0.8\pi$, $J = 1.67t$, $E_{d1} = 5t$, and $E_{d2} = 0$. Bands A, B and E, F correspond to the $|x^2 - y^2\rangle$ orbitals and almost coincide in given symmetry direction. Therefore, only six bands are distinguished in this figure.

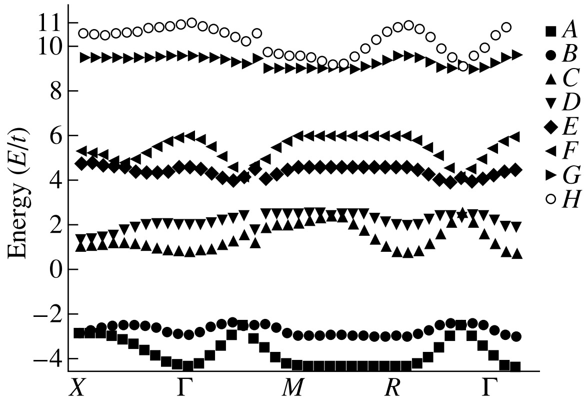

Fig. 3. Energy spectrum of the canted **G**-type antiferromagnetic structure calculated for the same values of parameters as in Fig. 2. For this magnetic structure, the bands are degenerate only at separate points of the Brillouin zone. The spectrum of the **C**-type antiferromagnetic structure is similar in shape to this one.

equal to $0.05t$; it is not shown in Fig. 2. However, overlapping of the *C*, *D* (type 1) and *E*, *F* (type 2) bands with different spin directions is noticeable in Fig. 2.

The calculated spectrum of the canted **G** structure for the same values of parameters as those in Fig. 2 is presented in Fig. 3. Here, the degeneracy occurs only at separate points on symmetry lines of the BZ. The essential feature of this spectrum is very strong narrowing of the lower bands of the **G** structure. It is clear from Figs. 2 and 3 that, for the same parameters, the total width of these bands (empty for $CaMnO_3$) is approximately 4 times smaller than the corresponding value for the spectrum of the **A** structure.

The spectrum of the canted **C** structure was calculated in an analogous manner. Since this spectrum is similar in form and location to the **G**-structure spectrum, we do not present it in this paper. The **C**-structure spectrum for symmetry lines of the BZ can be easily calculated analytically for $\theta = \pi$.

4. CONCLUSIONS

Thus, as follows from the standard DE model, the behavior of the $La_{1-x}Ca_xMnO_3$-type systems for small x and for $x \approx 1$ should be similar (electron–hole symmetry). The experiments show that the *p*-type and *n*-type compounds behave in an absolutely different manner. Thus, for $x < 0.5$, a metallic FM state usually occurs, while for $x > 0.5$, we have an insulating phase. The results of this study allow one to give a qualitative explanation of the experiment. It follows from the numerical calculations that the mobility of charge carriers (electrons) in a doped $CaMnO_3$ (the **G** structure) will be lower than the mobility of holes in a doped $LaMnO_3$ (the **A**-type structure). Therefore, there is no electron–hole symmetry in the properties of $La_{1-x}Ca_xMnO_3$. Such a symmetry will occur if, in the initial electron spectrum, the shape of isoenergetic surfaces for holes in the vicinity of the top of the valence band is identical to the shape of the isoenergetic surfaces for electrons in the vicinity of the bottom of the conduction band. The calculations carried out in this work show that such a situation is impossible for all basic types of the magnetic structures considered. The electron–hole symmetry has also not been observed experimentally (e.g., in numerous phase diagrams of manganites, see [1]).

The results of calculations of the magnetic phase diagram for manganites on the basis of the electronic band structure calculated in this paper will be published at a later date.

ACKNOWLEDGMENTS

This study was supported by the Russian Foundation for Basic Research, projects nos. 00-02-16729 and 00-02-81205 Bel2000-a.

REFERENCES

1. *Colossal Magnetoresistance, Charge Ordering and Related Properties of Manganese Oxides*, Ed. by C. N. R. Rao and B. Raveau (World Scientific, Singapore, 1998).
2. J. van den Brink and D. Khomskii, Phys. Rev. Lett. **82**, 1016 (1999).
3. T. Mizokava, D. I. Khomskii, and G. A. Sawatzky, Phys. Rev. B **63**, 024403 (2001).
4. P. W. Anderson and H. Hasegawa, Phys. Rev. **100**, 675 (1955).
5. E. Muller-Hartmann and E. Dagotto, Phys. Rev. B **54**, R6819 (1996).
6. K. Kubo and N. Ohata, J. Phys. Soc. Jpn. **33**, 21 (1972).
7. S. M. Dunaevskiĭ, Fiz. Tverd. Tela (St. Petersburg) **41** (12), 2179 (1999) [Phys. Solid State **41**, 2000 (1999)].
8. H. Shiba, R. Shina, and A. Takahashi, J. Phys. Soc. Jpn. **66**, 941 (1997).
9. G. Venketeswara Pai, Phys. Rev. B **63**, 064431 (2001).
10. J. W. Liu, Z. Zeng, Q. Q. Zheng, and H. Q. Lin, Phys. Rev. B **60**, 12968 (1999).
11. W. A. Harrison, *Electronic Structure and the Properties of Solids: The Physics of the Chemical Bond* (Freeman, San Francisco, 1980; Mir, Moscow, 1983), Vol. 1.
12. S. Satpathy, Z. S. Popović, and F. R. Vukajlović, Phys. Rev. Lett. **76**, 960 (1996).
13. M. Quijada, J. Černe, J. R. Simpson, *et al.*, Phys. Rev. B **58**, 16093 (1998).
14. I. M. Band and M. B. Trzhaskovskaya, At. Data Nucl. Data Tables **35**, 3 (1986).

Translated by A. Sonin

Physics of the Solid State, Vol. 43, No. 12, 2001, pp. 2262–2266. Translated from Fizika Tverdogo Tela, Vol. 43, No. 12, 2001, pp. 2171–2174.
Original Russian Text Copyright © 2001 by Isupov.

MAGNETISM AND FERROELECTRICITY

Phase Coexistence in Lead Zirconate Titanate Solid Solutions

V. A. Isupov

Ioffe Physicotechnical Institute, Russian Academy of Sciences,
Politekhnicheskaya ul. 26, St. Petersburg, 194021 Russia

Received March 20, 2001

Abstract—This paper discusses the phenomena observed in the vicinity of the morphotropic phase boundary in Pb($Ti_{1-x}Zr_x$)O_3 (PZT) solid solutions. The location of the boundary between the stable tetragonal ferroelectric phase and the stable rhombohedral ferroelectric phase is calculated, and an analytical expression for determining the concentration range of the possible coexistence of these phases is derived. According to the numerical estimates, the concentration range can be as much as 20 mol % lead zirconate. However, reliable experimental data in support of these estimates are as yet unavailable. *© 2001 MAIK “Nauka/Interperiodica”.*

1. INTRODUCTION

Polycrystalline Pb($Ti_{1-x}Zr_x$)O_3 (PZT) solid solutions, which are also referred to as PZT piezoelectric ceramics, have attracted considerable attention of many researchers [1]. PZT ceramic materials are of great practical importance owing to their extensive use in hydroacoustic devices, microphones, force sensors, acceleration transducers, etc. The reason for this is that the most important properties inherent in these materials are revealed in the composition regions adjacent to the morphotropic phase boundary (MPB), i.e., the regions lying along the nearly vertical interface in the phase diagram of the solid solutions. In the phase diagram of the Pb($Ti_{1-x}Zr_x$)O_3 system, the morphotropic phase boundary corresponds to the composition $x = x_{\mathrm{MPB}} = 0.52$, which separates the region of the stable tetragonal ferroelectric phase (the *T* phase) from the region of the stable rhombohedral ferroelectric phase (the *R* phase). In this situation, the morphotropic phase boundary corresponds not to the conventional phase transition observed under variations in temperature (which is a controllable parameter in our case) but to the phase transition induced by changes in the concentration of components (in the studied sample, this parameter remains constant and, hence, cannot be controlled). However, as was shown earlier in [2], the phase transition under investigation can also be controlled through various external factors.

In Pb($Ti_{1-x}Zr_x$)O_3 solid solutions, the phase transition from the *T* phase to the *R* phase can only be considered a first-order transition. This implies that, under hypothetical conditions when the concentration of components in the sample can be varied at a constant temperature, there should occur a concentration hysteresis in the phase transition range. However, since the concentration of components in the sample remains virtually unchanged, the morphotropic phase boundary in the phase diagram of PZT solid solutions represents a certain extended region of the possible coexistence of the *T* and *R* phases. Under the assumption that the thermodynamic potentials of the *T* and *R* phases (which are designated as G_T and G_R, respectively) are equal to each other at a concentration $x = x_e$, the *T* phase is stable and the *R* phase is metastable at $x < x_e$ and, conversely, the *T* phase is metastable and the *R* phase is stable at $x > x_e$. Note that the stable and metastable phases can coexist over a rather wide range of concentrations. This range is specified by the boundaries of the metastable phase regions.

The concentration range of the possible coexistence of the *T* and *R* phases in PZT piezoelectric ceramics has been a subject of much controversy (see, for example, [3–9]). In the present work, an attempt was made to calculate this range in terms of thermodynamics.

2. CALCULATION TECHNIQUE

In our calculations, we use an expansion of the thermodynamic potential *G* into a power series in the form proposed by Kholodenko [10], that is,

$$\begin{aligned} G = {} & G_0 + AP^2 + \frac{B_1}{2}P^4 + B_2(P_x^2P_y^2 + P_y^2P_z^2 + P_z^2P_x^2) \\ & + \frac{C_1}{3}P^6 + C_2[P_x^4(P_y^2 + P_z^2) + P_y^4(P_z^2 + P_x^2) \\ & + P_z^4(P_x^2 + P_y^2)] + C_3P_x^2P_y^2P_z^2. \end{aligned} \tag{1}$$

This expansion of the thermodynamic potential is somewhat different from the form used by Devonshire [11]:

$$\begin{aligned} G &= G_0 + \alpha P^2 + \frac{\beta_1}{2}(P_x^4 + P_y^4 + P_z^4) \\ &+ \beta_2(P_x^2P_y^2 + P_y^2P_z^2 + P_z^2P_x^2) + \frac{\gamma_1}{3}(P_x^6 + P_y^6 + P_z^6) \\ &+ \gamma_2[P_x^4(P_y^2 + P_z^2) + P_y^4(P_z^2 + P_x^2) + P_z^4(P_x^2 + P_y^2)] \\ &+ \gamma_3 P_x^2P_y^2P_z^2. \end{aligned} \tag{1a}$$

These forms of the expansion are equivalent to each other and are related by the expressions

$$\begin{gathered} \beta_1 = B_1, \quad \gamma_1 = C_1, \quad \beta_2 = B_1 + B_2, \\ \gamma_2 = C_1 + C_2, \quad \gamma_3 = C_3 + 2C_1. \end{gathered} \tag{1b}$$

The condition for stability of the tetragonal ferroelectric phase can be written in the form [10]

$$B_2 + C_2P_0^2 = D_1 > 0, \tag{2a}$$

whereas the rhombohedral ferroelectric phase is stable under the condition

$$B_2 + \frac{1}{3}C_3P_0^2 = D_2 < 0, \tag{2b}$$

where P_0 is the spontaneous polarization.

As is seen from the figure, the morphotropic phase boundary can exist under conditions when the coefficient B_2 is positive at $x = 0$, decreases, passes through zero at $x = x_0$, and becomes negative [12]. In this case, the terms $C_2P_0^2$ and $(C_3/3)P_0^2$ should be relatively small. Hence, conditions (2a) and (2b) are satisfied in the vicinity of the point $x = x_0$. It should be noted that, as follows from relationship (1b), the condition $B_2 = 0$ for the Devonshire form of the expansion of the thermodynamic potential G [described by relationship (1a)] corresponds to the condition $\beta_2 = \beta_1$. This is in close agreement with the result obtained in more recent thermodynamic works dealing with the Devonshire expansion of the thermodynamic potential G (see, for example, [13]).

For simplicity, it is reasonable to assume that the B_2 coefficient depends linearly on the concentration of the components:

$$B_2 = B_2(0)\frac{x_0 - x}{x_0} = B_2(0)y, \tag{3}$$

where $B_2(0)$ corresponds to the B_2 coefficient at $x = 0$. It can easily be shown that, under the conditions $C_2 > 0$ and $C_3 < 0$, the concentration range of the possible coexistence of the T and R phases is bounded by the points $x = x_R$ and $x = x_T$ and includes the point $x = x_0$ (i.e., $x_R < x_0 < x_T$).

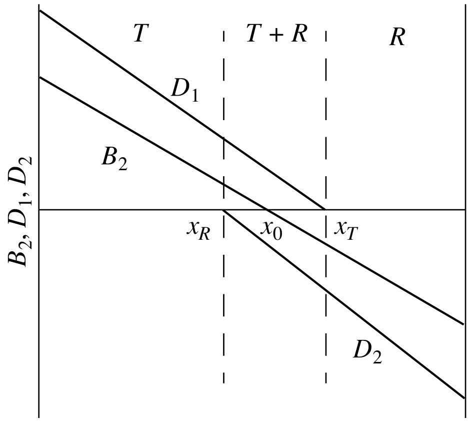

Dependences of the coefficients B_2, D_1, and D_2 for the $Pb(Ti_{1-x}Zr_x)O_3$ solid solutions on the concentration x.

Now, we determine the concentration $x = x_e$ at which the thermodynamic potentials of the T and R phases are equal to each other. According to Kholodenko [10], the thermodynamic potentials of the T and R phases can be represented by the relationships

$$G_T = G_0 + AP_{0T}^2 + \frac{B_1}{2}P_{0T}^4 + \frac{C_1}{3}P_{0T}^6, \tag{4a}$$

$$\begin{aligned} G_R &= G_0 + AP_{0R}^2 + \frac{1}{2}\left(B_1 + \frac{2}{3}B_2\right)P_{0R}^4 \\ &+ \frac{1}{3}\left(C_1 + \frac{2}{3}C_2 + \frac{1}{9}C_3\right)P_{0R}^6 \\ &= G_0 + AP_{0R}^2 + \frac{1}{2}B_0P_{0R}^4 + \frac{1}{3}C_0P_{0R}^6. \end{aligned} \tag{4b}$$

At $x = x_e$, the equality $G_T = G_R$ holds throughout the entire morphotropic phase boundary. For simplicity, we consider only the portion of the morphotropic phase boundary that corresponds to the line of its intersection with the line at $A = 0$.

The spontaneous polarizations of the T and R phases can be written as

$$P_{0T}^2 = -\frac{B_1}{2C_1} - \frac{1}{2C_1}\sqrt{B_1^2 - 4AC_1}, \tag{5a}$$

$$P_{0R}^2 = -\frac{B_0}{2C_0} - \frac{1}{2C_1}\sqrt{B_0^2 - 4AC_0}. \tag{5b}$$

However, taking into account that

$$B_0 = B_1 + \frac{2}{3}B_2, \quad C_0 = C_1 + \frac{2}{3}C_2 + \frac{1}{9}C_3, \tag{5c}$$

the spontaneous polarizations of the T and R phases for the line at $A = 0$ can be represented in the following form:

$$P_{0T}^2 = -\frac{B_1}{C_1}, \quad P_{0R}^2 = -\frac{B_0}{C_0} = -\frac{B_1 + \frac{2}{3}B_2}{C_1 + \frac{2}{3}C_2 + \frac{1}{9}C_3}. \tag{6}$$

By substituting the spontaneous polarizations P_{0T}^2 and P_{0R}^2 into the equality $G_R = G_T$ under the assumption that $A = 0$, we obtain

$$\frac{B_1^3}{C_1^2} = \frac{B_0^3}{C_0^2}. \tag{7}$$

Next, from expression (3) under the assumption that $x = x_e$, we derive the cubic equation

$$\begin{aligned} B_2^3(0)y^3 + \frac{9}{2}B_1B_2^2(0)y^2 + \frac{27}{4}B_1^2B_2(0)y \\ + \frac{27}{8}B_1^3\left(1 - \frac{C_0^2}{C_1^2}\right) = 0. \end{aligned} \tag{8}$$

This equation can easily be solved to give the relationship

$$y = \frac{3}{2}\frac{B_1}{B_2(0)}\left[\left(\frac{C_0}{C_1}\right)^{2/3} - 1\right]. \tag{9}$$

Consequently, we obtain

$$x_e = x_0\left[1 - \frac{3}{2}\frac{B_1}{B_2(0)}\left(\frac{C_0^{2/3}}{C_1^{2./3}} - 1\right)\right]. \tag{10}$$

Now, we use inequalities (2a) and (2b) to determine the concentration range of the possible coexistence of the T and R phases. It is evident that the T phase exists at $x < x_T$ (see figure). In further considerations, we also restrict ourselves to the simple case of the line at $A = 0$ when relationships (6) are satisfied. At $x = x_T$, we have the equality $B_2 + C_2P_{0T}^2 = 0$. Substitution of relationships (3) and (6) into this equality leads to the expression

$$x_T = x_0\left[1 - \frac{B_1C_2}{B_2(0)C_1}\right]. \tag{11a}$$

Since the R phase can exist at $x > x_R$, we obtain the following expression in a similar manner:

$$x_R = x_0\left[1 - \frac{B_1C_3}{3B_2(0)\left(C_1 + \frac{2}{3}C_2 - \frac{1}{9}C_3\right)}\right]. \tag{11b}$$

Therefore, the concentration range of the possible coexistence of the T and R phases is determined from the formula

$$\xi = x_T - x_R = -\frac{B_1}{B_2(0)}\left[\frac{C_2}{C_1} + \frac{C_3}{3\left(C_1 + \frac{2}{3}C_2 - \frac{1}{9}C_3\right)}\right]. \tag{12}$$

Note that the derived expressions are valid for both the vertical and tilt phase boundaries; however, we are interested here in the morphotropic (nearly vertical) phase boundary.

3. RESULTS AND DISCUSSION

All the coefficients in the expansion of the thermodynamic potential G are independent of the temperature (except for the coefficient A) and the concentration x (except for B_2). Hence, we can perform our calculations with the coefficients obtained by Haun *et al.* [14] for $PbTiO_3$. After recalculation of these coefficients according to formulas (1b), we obtained the following values: $B_1 = -14.5 \times 10^{-8}$ $m^5/(C\ F)$, $B_2(0) = 22.0 \times 10^{-8}$ $m^5/(C\ F)$, $C_1 = 7.8 \times 10^{-8}$ $m^9/(C^4\ F)$, $C_2 = -1.7 \times 10^{-8}$ $m^9/(C^4\ F)$, and $C_3 = -16 \times 10^{-8}$ $m^9/(C^4\ F)$. According to the data obtained in [14], the concentration x_0 is equal to 0.35. This value substantially differs from the experimentally found concentration that corresponds to the morphotropic phase boundary (as was already mentioned, $x_{MPB} = 0.52$).

From expressions (10)–(12), we have $x_e = 0.23$, $x_T = 0.30$, $x_R = 0.10$, and $\xi = 0.20$.

Thus, the calculated concentration range of the possible coexistence of the T and R phases is rather wide and equal to 20 mol % lead zirconate. Unfortunately, the results of the above numerical calculations are not reliable, because the initial coefficients reported in [14] cannot be considered trustworthy. For example, the calculation gives $x_e = 0.23$, which is considerably less than the values of $x_0 = 0.35$ taken from [14] and $x_{MPB} = 0.52$.

It seems likely that the main source of error in [14] is associated with the assumption that the ferroelectric phase transition from the cubic phase to the R phase is a second-order phase transition. It is clear that the errors in determination of the magnitude and sign of the B_1 coefficient (which is negative upon first-order phase transitions and positive upon second-order transitions) entail errors in determination of all the other coefficients in the expansion of the G potential.

According to Clarke and Glazer [15] and Roleder [16], the tricritical point is observed in the $Pb(Ti_{1-x}Zr_x)O_3$ system at a value of $(1 - x) = 0.06$–0.07. In this system, the ferroelectric phase transition from the cubic phase to the R phase with an increase in the value of $(1 - x)$ exhibits certain indications of a second-order phase transition: the spontaneous polarization jump is absent and the Curie–Weiss temperature (Θ) becomes equal to a temperature corresponding to the maximum permittivity ($T_{\max}$). However, the spontaneous polarization jump is also absent upon the first-order phase transition provided this transition is smeared (i.e., in relaxor ferroelectrics). As the degree of smearing of the phase transition increases, the Curie–Weiss temperature Θ [which is usually determined from the dependence $1/\varepsilon(T)$] approaches the $T_{\max}$ temperature, reaches its value, and can even exceed $T_{\max}$ at a high degree of smearing [17]. This can be explained by the fact that the linear dependence $1/\varepsilon(T)$ becomes quadratic at a certain degree of smearing of the phase transition, which is frequently ignored by researchers. It should be noted that a certain degree of smearing of the ferroelectric phase transition is also observed in the $Pb(Ti,Zr)O_3$ system [1]. Handerek and Ujma [18] demonstrated that the temperature hysteresis of the ferroelectric phase transition in the concentration range close to $(1 - x) = 0.06$ becomes more pronounced with an increase in the value of $(1 - x)$. This phenomenon cannot be observed for a second-order transition between the ferroelectric phases. Therefore, these findings also cast doubt on the validity of the assumption made in [14] that the ferroelectric phase transition from the cubic phase to the *R* phase is a second-order phase transition.

Let us now consider, in greater detail, the specific features observed in the concentration range of the possible coexistence of the *T* and *R* phases. As follows from the definition given above, it is in this range of concentrations that the *T* and *R* phases can exist and coexist in stable and metastable states. The metastable phases can be stabilized both under internal mechanical stresses and in response to local electric fields. In principle, no phase coexistence can occur in the absence of these stabilizing factors. In this situation, only the stable phases exist and the ceramic material occurs in a single-phase state, except for a narrow range of concentrations in the vicinity of x_e. However, the single-phase ceramic material whose composition corresponds to the concentration range of the possible coexistence of the *T* and *R* phases does not necessarily remain single-phase through time. It should be kept in mind that the PZT ceramic material is fairly sensitive to environmental influences (as was predicted in my earlier works [19–21]) and undergoes transformations with time.

There is considerable experimental evidence that the phase composition and the mean concentration of components in the coexisting *T* and *R* phases change under the action of strong external electric fields and mechanical stresses (see, for example, [22–25]). (A plausible explanation for the observed change in the content of components in the *T* and *R* phases was given in [26].) A change in the phase composition of the surface layer of samples was observed even in the course of grinding [27]. Kakegawa *et al.* [6, 28] revealed that the concentration of the *T* and *R* phases substantially varies with time even during conventional storage of polarized samples. From the aforesaid, it is clear that the concentration range of the possible phase coexistence in PZT ceramic materials (and in other piezoelectric ceramics that correspond to solid solutions with a morphotropic phase boundary) is of great practical importance. This range can, in essence, be identified with the region of the morphotropic phase boundary. The above calculation in terms of thermodynamics has made it possible to obtain analytical expressions for determining the concentration range of the possible coexistence of the *T* and *R* phases and the concentration x_e, which separates the region of the stable *T* phase from the region of the stable *R* phase. Unfortunately, the numerical estimates obtained for these important characteristics of solid solutions in the $Pb(Ti_{1-x}Zr_x)O_3$ system are not reliable, because the exact values of coefficients in the power series expansion of the thermodynamic potential for these solid solutions are as yet unknown. In this respect, the determination of these coefficients is an urgent problem.

Moreover, it remains unclear whether the coexistence of the *T* and *R* phases in grains of piezoelectric ceramics is favorable for increasing the permittivity and other piezoelectric characteristics of real piezoelectric elements. There exist different interpretations of this problem. However, analysis of these variants does not enter into the scope of the present paper and will be performed in a separate work.

REFERENCES

1. B. Jaffe, W. R. Cook, and H. Jaffe, *Piezoelectric Ceramics* (Academic, New York, 1971; Mir, Moscow, 1974).
2. V. A. Isupov, in *Ferroelectrics and Related Materials*, Ed. by G. A. Smolenskii (Gordon and Breach, New York, 1983); V. A. Isupov, in *The Physics of Ferroelectric Phenomena* (Nauka, Leningrad, 1985), Chap. 15.
3. V. A. Freĭmanis, Ya. Ya. Kruchan, *et al.*, Neorg. Mater. **16** (6), 1044 (1980).
4. K. Kakegawa, J. Mohri, T. Takahashi, *et al.*, Solid State Commun. **24** (11), 769 (1977).
5. Y. Abe, K. Kakegawa, and Y. Sasaki, Solid State Commun. **72** (11), 1071 (1989).
6. K. Kakegawa *et al.*, J. Am. Ceram. Soc. **78** (4), 1071 (1995).
7. Y. Ishibashi and M. Iwata, Jpn. J. Appl. Phys., Part 2 **37** (8B), L985 (1998).
8. S. K. Mishra, D. Pandy, and A. P. Singh, Appl. Phys. Lett. **69** (12), 1707 (1996).
9. T. Yamamoto, Jpn. J. Appl. Phys. **37** (11), 6041 (1998).
10. L. P. Kholodenko, *Thermodynamic Theory of Ferroelectrics of the Barium Titanate Type* (Zinatne, Riga, 1971).
11. A. F. Devonshire, Philos. Mag. **40**, 1040 (1949); Philos. Mag. **42**, 1065 (1951).
12. V. A. Isupov, Fiz. Tverd. Tela (Leningrad) **12** (5), 1380 (1970) [Sov. Phys. Solid State **12**, 1084 (1970)].
13. L. Benguigui, Solid State Commun. **11** (6), 825 (1972).

14. M. J. Haun, E. Furman, S. J. Jang, and L. E. Cross, Ferroelectrics **99**, 13 (1989); M. J. Haun, E. Furman, M. A. McKinstry, and L. E. Cross, Ferroelectrics **99**, 27 (1989); M. J. Haun, Z. Q. Zhuang, E. Furman, *et al.*, Ferroelectrics **99**, 45 (1989); M. J. Haun, E. Furman, T. R. Halemane, and L. E. Cross, Ferroelectrics **99**, 55 (1989); M. J. Haun, E. Furman, S. J. Jang, and L. E. Cross, Ferroelectrics **99**, 63 (1989).
15. R. Clarke and M. Glazer, Ferroelectrics **14** (1/2), 695 (1976).
16. K. Roleder, Ferroelectr. Lett. Sect. **2** (2), 63 (1984).
17. V. A. Isupov, to be published.
18. J. Handerek and Z. Ujma, Acta Phys. Pol. A **51** (1), 87 (1977).
19. V. A. Isupov, Fiz. Tverd. Tela (Leningrad) **10** (4), 1244 (1968) [Sov. Phys. Solid State **10**, 989 (1968)].
20. V. A. Isupov, Diélektr. Poluprovodn. **19**, 3 (1981).
21. V. A. Isupov, in *Ferroelectrics under External Influences* (LDNTP, Leningrad, 1981), p. 50.
22. V. Saley *et al.*, Ferroelectrics **22**, 805 (1978).
23. A. Amin, R. E. Newnham, and L. E. Cross, Phys. Rev. B **34** (3), 1595 (1986).
24. A. V. Turik, Kristallografiya **26** (1), 171 (1981) [Sov. Phys. Crystallogr. **26**, 94 (1981)].
25. S. Stotz, Ferroelectrics **76** (1/2), 123 (1987).
26. V. A. Isupov, Fiz. Tverd. Tela (Leningrad) **22** (1), 172 (1980) [Sov. Phys. Solid State **22**, 98 (1980)].
27. C. Cheon and S. Kim, Ferroelectrics **110**, 227 (1990).
28. K. Kakegawa *et al.*, J. Am. Ceram. Soc. **65** (10), 515 (1982).

Translated by O. Borovik-Romanova

Physics of the Solid State, Vol. 43, No. 12, 2001, pp. 2267–2275. Translated from Fizika Tverdogo Tela, Vol. 43, No. 12, 2001, pp. 2175–2183.
Original Russian Text Copyright © 2001 by Boĭkov, Claeson.

MAGNETISM AND FERROELECTRICITY

Dielectric Permittivity Dynamics of $Ba_{1-x}Sr_xTiO_3$ Epitaxial Films ($x = 0.75$): Microstructure and Depolarization Effects

Yu. A. Boĭkov* and T. Claeson**

**Ioffe Physicotechnical Institute, Russian Academy of Sciences, Politekhnicheskaya ul. 26, St. Petersburg, 194021 Russia*
***Chalmers Technical University, Göteborg, S-41296 Sweden*

Received May 7, 2001

Abstract—Trilayer epitaxial heterostructures including metal oxide electrodes ($SrRuO_3$, 200 nm) and a sandwiched dielectric layer ($Ba_{0.25}Sr_{0.75}TiO_3$, 700 nm) were grown by laser ablation on (001)$LaAlO_3$ substrates. The maximum permittivity of the $Ba_{0.25}Sr_{0.75}TiO_3$ layer ($\varepsilon'/\varepsilon_0 \approx 3700$) was obtained at $T_M = 160$ K and an external electric field $E \approx 10^6$ V/m. The $\varepsilon'(T)$ dependence for the $Ba_{0.25}Sr_{0.75}TiO_3$ layer in the paraelectric phase is well fitted by the Curie–Weiss relation, with the Curie constant and the Weiss temperature differing only insignificantly from the corresponding bulk values. The change in the permittivity of the $Ba_{0.25}Sr_{0.75}TiO_3$ layer induced by the application of a ±2.5 V bias voltage to the electrodes reached as high as 85%. The electric-field dependence of the polarization retained clearly pronounced saturated hysteresis loops up to temperatures 10–15 K above T_M. *© 2001 MAIK “Nauka/Interperiodica”.*

1. INTRODUCTION

There is a wealth of published information on the dielectric parameters of single crystals and bulk ceramic samples of $BaTiO_3$ (BTO) and $SrTiO_3$ (STO), as well as of their solid solutions [1–3]. The large magnitudes of the real part of the permittivity ε' of the paraelectric phase and of the remanent polarization P_r at temperatures below the Curie point T_C make $Ba_{1-x}Sr_xTiO_3$ a promising material for use in RAM and ferroelectric memory cells [4]. The essentially nonlinear response of ε' to an external electric field E and the strong dependence of P_r on temperature permit one to use $Ba_{1-x}Sr_xTiO_3$ in tunable microwave devices (filters, phase shifters, and delay lines [5]) and IR sensors [6].

Microelectronics and microwave technology applications require thin $Ba_{1-x}Sr_xTiO_3$ films that alternate with conducting layers to be used as electrodes. However, the properties of thin $Ba_{1-x}Sr_xTiO_3$ films incorporated in a multilayer epitaxial heterostructure are substantially inferior to those of bulk samples. In particular, these films are characterized by small P_r and ε', combined with a weak dependence of ε' on E and a large loss tangent $\tan\delta$. The main reasons for the degradation of the $Ba_{1-x}Sr_xTiO_3$ thin films are believed to be (1) deviations from stoichiometry in the bulk of the film due to an uncontrollable loss of volatile components in the course of deposition and growth, (2) the high density of structural defects caused by the low mobility of the particles adsorbed on the surface of the growing ferroelectric layer, (3) the strong internal electric field originating from the difference between the work function of the electrode material and the electron affinity of the ferroelectric layer, (4) the formation of a layer with a distorted microstructure and a low ε' at the ferroelectric–electrode interface, and (5) the high mechanical stresses caused by the lattice misfit and differences in the thermal linear expansion coefficients between $Ba_{1-x}Sr_xTiO_3$ and the substrate material.

We established earlier that when thin films of the $SrRuO_3$ metal oxide (SRO) are used as electrodes, the strontium titanate layer in the SRO/STO/SRO epitaxial heterostructure possesses a high-perfection structure and the interfaces affect its parameters only insignificantly [7]. This work demonstrates the possibility of forming an SRO/$Ba_{0.25}Sr_{0.75}TiO_3$/SRO (SRO/BSTO/SRO) heterostructure with a *c*-oriented intermediate layer (the *c* axis is perpendicular to the substrate plane) and studies the dielectric parameters of this layer in the para- and ferroelectric phases.

2. EXPERIMENT

The SRO/BSTO/SRO trilayer heterostructures were grown by laser ablation (COMPex-100 KrF excimer laser, $\lambda = 248$ nm, $\tau = 30$ ns) on a (001)$LaAlO_3$ (LAO) sublattice. The laser radiation density on the surface of the SRO and BSTO ceramic targets during their ablation was 1.5 J/cm^2, and the oxygen pressure in the growth chamber was maintained at 0.4 mbar. The top and bottom 200-nm-thick metal oxide electrodes were grown at $T_S = 740$°C; the intermediate ferroelectric layer, at $T_S = 825$°C.

The phase composition and structure of the layers in the trilayer heterostructures grown were studied using x-ray diffraction (Philips X’pert MRD, $\omega/2\theta$ and ϕ scanning, rocking curves). To determine the BSTO layer lattice parameters in the substrate plane ($a_{\|}$) and along its normal ($a_\perp$), the $\omega/2\theta$ scans were made with the substrate fixed such that either (101)LAO or (001)LAO was normal to the plane containing the incident and reflected x-ray beams. To estimate the average grain size d_E and the effective unit-cell strain in the ferroelectric layer, the first four Bragg peaks due to BSTO were measured with a (220)Ge and a plane graphite monochromator in the first and second orders, respectively.

The surface morphology of the ferroelectric films grown on SRO/LAO was studied with an atomic force microscope (AFM) (NanoScope-IIIa, tapping mode). The images were obtained in both the height- and phase-relief modes.

The method employed to prepare plane-parallel capacitors based on the grown SRO/BSTO/SRO heterostructures was described in [7].

The capacitance C and the dielectric loss tangent $\tan\delta$ of our capacitor structures were measured with an hp 4263A LCR meter (ac measuring voltage V_{AC} = 50 mV, f = 1–100 kHz). The C and $\tan\delta$ were measured with a dc bias V_b (up to ±2.5 V) applied to the electrodes, as well as without it. The real (ε') and imaginary (ε'') parts of the permittivity of the ferroelectric layer were calculated using the relations $\varepsilon' = Cd/S$ and $\varepsilon'' = \varepsilon' \tan\delta$, where d = 700 nm is the ferroelectric layer thickness and $S = 400\ \mu\text{m}^2$ is the area of the top electrode in the capacitor structure (the SRO layer grown on LAO served as a common electrode for the SRO/BSTO/SRO film capacitors). The voltage V_b was assumed positive when the plus was applied to the top electrode.

3. EXPERIMENTAL RESULTS AND DISCUSSION

The available data on the growth of multilayer systems including thin STO, BTO, (Ba,Sr)TiO_3, and SRO layers [7–9] suggest the absence of a detectable chemical interaction between BSTO and the metal oxide at the T_S temperatures covered in this work. The lattice parameters of bulk BSTO and SRO crystals (a_{BSTO} = 3.925 Å [10], a_{SRO} = 3.923 Å [11]), as well as the thermal linear expansion coefficients β ($\beta_{BSTO} \approx 11 \times 10^{-6}\ \text{K}^{-1}$, calculated as a weighted mean of the corresponding parameters of the STO and BTO, $\beta_{SRO} \approx 11 \times 10^{-6}\ \text{K}^{-1}$ [12]) are similar in magnitude. The above factors favor the formation of sharp SRO/BSTO interfaces in the metal oxide–ferroelectric–metal oxide trilayer heterostructure. Because $\sqrt{S} \gg d$, the contribution of edge effects to the capacitance and $\tan\delta$ of the SRO/BSTO/SRO plane-parallel capacitor structures formed is small. We shall first discuss the data obtained by us on the structure of the films thus grown; after, the temperature and field dependences of the dielectric parameters will be discussed.

3.1. The Microstructure and Morphology of the BSTO Film Surface

The x-ray diffractograms indicate the BSTO layer to be in epitaxial relation to the SRO/LAO surface (Figs. 1a, 1b). Because the BSTO and SRO lattice parameters differ very little, the x-ray reflections from the top and bottom electrodes made of strontium ruthenate overlap with the much stronger reflections due to the ferroelectric layer. The overlap of the SRO and BSTO reflections in the x-ray diffractograms obtained with the (220)Ge monochromator resulted in a distortion of the (00n)BSTO peaks on the larger 2θ angle side. The x-ray ϕ scans of the (111)BSTO and (111)SRO reflections had four equidistant peaks each (the corresponding data are given in [13]). The unit-cell parameter of the BSTO layer in the direction perpendicular to the substrate plane, $a_\perp$ = 3.945 Å, was derived from the value of 2θ for the (004)BSTO reflection in the x-ray scan displayed in Fig. 1a. The unit-cell parameter of the ferroelectric layer in the substrate plane, $a_\parallel$ = 3.924 Å, was calculated from the relation $1/d_{(n0n)} = [(n/a_\perp)^2 + (n/a_\parallel)^2]^{1/2}$. To determine the interplanar distance $d_{(303)}$, we used the value of 2θ for the (303)BSTO peak in the x-ray scan shown in Fig. 1b. The considerable difference between the measured unit-cell parameters $a_\perp$ and $a_\parallel$ of the BSTO layer is accounted for by the compressive mechanical stresses acting in the substrate plane. The effective unit cell parameter of the BSTO layer, $a_{eff} = (a_\perp a_\parallel^2)^{1/3}$ = 3.931 Å, is substantially larger than that for the corresponding bulk crystals [10]. One of the main reasons for the usually increased a_{eff} in (Ba,Sr)TiO_3 epitaxial films is their high oxygen vacancy density [14]. The low mobility of the particles adsorbed on the surface of a growing film gives rise to defect formation on the cation sublattice of the BSTO layer, which, in turn, is accompanied by oxygen loss.

The inset to Fig. 1b displays a rocking curve (Cu$K_{\alpha1}$, $\omega/2\theta$) for the x-ray (200)BSTO reflection. The rocking-curve width at half maximum is several times smaller than that reported in [9] for (Ba,Sr)TiO_3 epitaxial films. The half-width obtained (≈0.26°) is, however, 25% larger than the corresponding figures for a BSTO layer grown on SRO/LSATO [15]. In contrast to LAO, LSATO [$(LaAlO_3)_{0.3}$ + $(Sr_2TaAlO_6)_{0.7}$] does not undergo phase transformations within the 20–825°C range and its lattice is better matched to those of SRO and BSTO.

Atomic-force microscope images of the free surface of BSTO films grown on SRO/LAO indicate them to consist of crystallites 30–100 nm in size (Fig. 2). Note that the micrographs obtained for the BSTO layer in the height- and phase-relief modes were practically identical. The images of the ferroelectric layer surface clearly reveal a system of characteristic depressions decorating the crystallite boundaries. Decoration of crystallite boundaries in a ferroelectric film minimizes the free energy of the vapor phase–growing film–substrate sys-

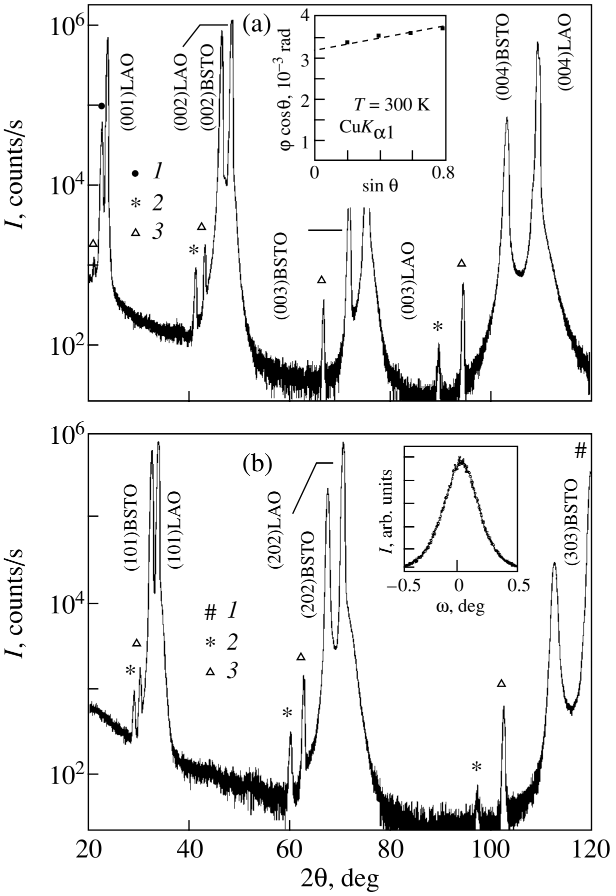

Fig. 1. (a) X-ray diffractogram (CuK_α, ω/2θ scan) of a SRO/BSTO/SRO/LAO heterostructure obtained for the case where the plane containing the incident and reflected x-ray beams is perpendicular to (001)LAO: (*1*) (001)BSTO peak; (*2, 3*) CuK_β peaks due to the BSTO layer and the substrate, respectively; the inset shows the dependence of the x-ray peak half-width φ on θ in an ω/2θ scan; the (00*n*)BSTO peaks were measured with monochromatic x-ray radiation. (b) X-ray diffractogram for the same heterostructure obtained for the case where the plane containing the incident and reflected x-ray beams is orthogonal to (101)LAO: (*1*) (303)LAO peak, (*2, 3*) CuK_β peaks due to the BSTO layer and the substrate, respectively; the inset shows a rocking curve (Cu$K_{\alpha 1}$, ω/2θ) obtained for the (200)BSTO peak of the (001)SRO || (001)BSTO || (001)SRO || (001)LAO heterostructure.

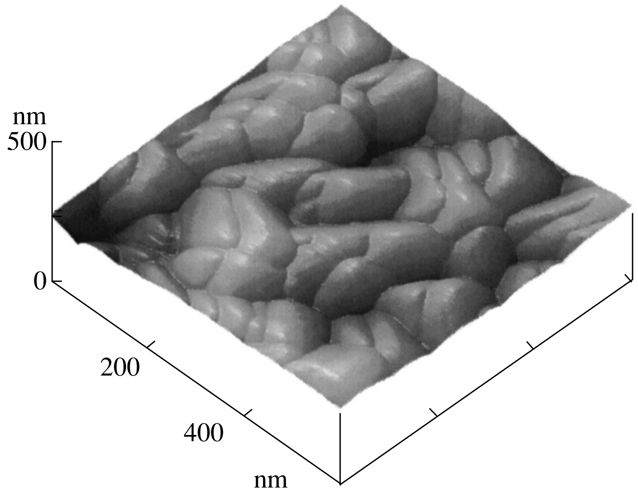

Fig. 2. Atomic-force microscope image of the free surface of a BSTO layer grown on (001)SRO || (001))LAO. The image was obtained in the height-relief mode. The crystallite boundaries in the ferroelectric layer are decorated by characteristic depressions. The phase-relief mode images did not reveal any features which would imply a complex structure of the crystallites.

tem. The thin layers near the crystallite boundaries possess excess free energy. The crystallites are distinctly oriented relative to the normal to the substrate plane, and their azimuthal orientation, as follows from the ϕ scans obtained for the (111)BSTO reflection, does not exceed 0.1°. The phase-relief micrographs of the surface of the $Ba_{0.75}Sr_{0.25}TiO_3$ films, which were in the ferroelectric phase at 300 K, revealed features attesting to a complex structure of the crystallites [13].

In order to estimate the effective size of the crystallites d_E and the relative deformation of the unit cell $\Delta a_\perp/a_\perp$ in a BSTO layer grown on (001)SRO || (001)LAO, we used the dependence of the (00*n*)BSTO peak half-width φ on θ in the x-ray (ω/2θ) scan of the SRO/BSTO/SRO heterostructure (the first four peaks of the BSTO layer were measured with high-precision x-ray optics). The data on the φ vs. θ dependence are given in the inset to Fig. 1a. The procedure employed to determine d_E and $\Delta a_\perp/a_\perp$ is described in [13, 16]. The x-ray data show that d_E and $\Delta a_\perp/a_\perp$ for the grown BSTO films are 38 nm and 4×10^{-4}, respectively. The observed difference between the estimates of the crystallite dimensions derived from x-ray data and obtained with AFM appears only natural, considering that the crystallite size may increase with increasing film thickness. The competing grain growth becomes particularly clearly pronounced for ferroelectric layer thicknesses of less than 200 nm. The value of $\Delta a_\perp/a_\perp$ obtained for the BSTO layer is in accordance with the corresponding data available in the literature on *c*- and *a*-oriented (Ba,Sr)TiO_3 thin epitaxial layers (in the latter case, the *c* axis is parallel to the substrate plane) [13, 15]. The main factors responsible for the variation of interplanar distances in a BSTO layer are nonuniform mechanical stresses and randomly located structural defects, primarily oxygen vacancies.

The compressive in-plane mechanical stresses favor the orientation of the polar axis of the BSTO film along the normal to the substrate plane. In the case of a trilayer SRO/BSTO/SRO heterostructure grown on (001)LAO, the pattern of mechanical stresses in the BSTO layer is governed by both the differences in the lattice parameters between BSTO, SRO, and LAO and the difference between the BSTO and LAO thermal linear expansion coefficients. The unit-cell parameter of the pseudocubic LAO (a_1 = 3.79 Å) is substantially smaller than those of BSTO and SRO, which favors generation of compressive in-plane mechanical stresses in the ferroelectric layer. The difference between the thermal linear expansion coefficients of the BSTO and LAO ($\beta = 9.2 \times 10^{-6}$ K^{-1} [17]) is conducive to the formation of in-plane tensile mechanical stresses in the substrate.

3.2. Temperature Dependence of the BSTO Layer Polarization

Systematic data on the temperature dependence of the remanent polarization in (Ba,Sr)TiO_3 epitaxial films are practically nonexistent. The values quoted in [6, 18] for P_r in thin (Ba,Sr)TiO_3 ceramic layers are substantially lower than those for bulk crystals. Deviations from stoichiometry, size effects, depolarization electric fields, and mechanical stresses can considerably affect the electric-field dependence of the polarization in a (Ba,Sr)TiO_3 film.

Figure 3 presents the polarization of a BSTO layer $P(E)$ as a function of the electric field measured at a frequency of f = 50 kHz at different temperatures. For $T >$ 250 K, P increased practically linearly with E; the insignificant decrease in dP/dE at electric field strengths $E > 5 \times 10^6$ V/m was due to dielectric saturation. For 250 > T > 200 K, the measured $P(E)$ relation did not exhibit any hysteresis; however, sharp variations of dP/dE were observed to occur as E was reduced from -2×10^6 to -4×10^6 V/m. The peak in the $dP(E)/dE$ relation observed in the above-mentioned electric-field range is due to substantial dielectric nonlinearity of the BSTO paraelectric phase in weak electric fields at temperatures close to T_C.

The $P(E)$ curves measured for T < 175 K clearly reveal saturated hysteresis loops. The loops were shifted toward negative electric fields relative to the E = 0 point, and the absolute values of P for positive E were substantially smaller than those obtained at the corresponding negative values of E. The presence of remanent polarization in the BSTO layer above T_C for bulk crystals ($T_C \approx 150$ K [3]) implies that, in the bulk of the BSTO layer, there are microregions (apparently, isolated crystallites) that transfer to the ferroelectric phase at a higher temperature. The presence of remanent polarization in thin BTO films was detected at temperatures exceeding the T_C for single-crystal barium titanate by nearly 200 K [19].

The noticeable asymmetry of the hysteresis loops observed in the measured electric-field dependences of the polarization in the BSTO ferroelectric layer is a consequence of depolarization effects [20, 21]. As already mentioned, the grown BSTO layers were clearly c oriented; i.e., the polarization vector was perpendicular to the substrate plane (inset to Fig. 3). In these conditions, the polarization in a thin ferroelectric

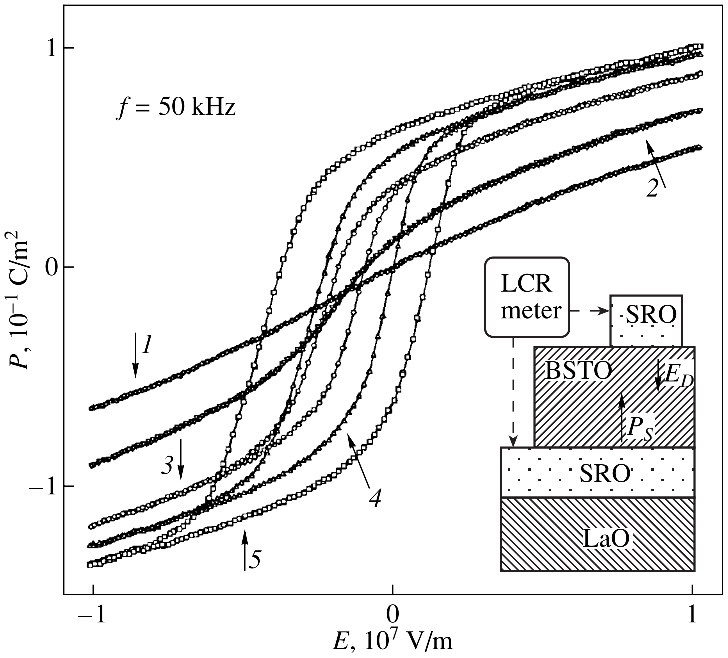

Fig. 3. Plots of polarization P vs. electric field E measured on a BSTO layer at different temperatures T: (*1*) 250, (*2*) 200, (*3*) 140, (*4*) 100, and (*5*) 40 K. The $P(E)$ curves remained practically unchanged under variation of the frequency in the 10–100 kHz range. The inset shows a schematic of the plane-parallel SRO/BSTO/SRO capacitor structure used to study the dielectric parameters of the BSTO layer.

layer depends substantially on the degree of compensation of the polarization charge by the charge of the opposite sign on the electrode at the interface. Because of the relatively high concentration of structural defects (oxygen vacancies), the conductivity of the top electrode in the SRO/(Ba,Sr)TiO_3/SRO trilayer heterostructure is, as a rule, considerably lower than that of the electrode grown on the surface of a single-crystal substrate [7, 8]. The charge induced at the upper boundary of the ferroelectric by its spontaneous polarization is incompletely compensated by the charge of opposite sign on the metal oxide electrode and generates a depolarization electric field E_D in the BSTO layer. This field is directed from the top to the bottom electrode, i.e., in opposition to the spontaneous polarization vector P_S. When a positive bias is applied to the top electrode, the electron concentration in the metal oxide film near the corresponding interface decreases, which weakens the polarization charge compensation, thereby increasing the depolarization field in the ferroelectric layer. If V_b is of the opposite polarity, the electron concentration in the SRO top electrode near the electrode–ferroelectric interface increases and the effect of the depolarization electric field weakens. The substantially larger polarization in the BSTO layer for $E < 0$ than in the $E > 0$ case (Fig. 3) can be explained as being due to the lower depolarization field strength at a negative bias. At temperatures below the phase transition point, the BSTO layer consists of ferroelectric domains separated by 180° domain walls. The separation of the BSTO layer into domains weakens the effect of the depolarization field on the polarization while not suppressing it completely, because the electron concentrations in the top and bottom SRO layers are different [21]. The domain structure in the BSTO layers studied here differs considerably from that in *a*-oriented (Ba,Sr)TiO_3 ferroelectric layers acted upon by in-plane tensile mechanical stresses [13].

The hysteresis loops observed in the $P(E)$ curves were used to determine the temperature dependences of the remanent polarization P_r and the coercive field E_C in a BSTO layer (Fig. 4). Within the 160–80 K range, we observed an approximately linear growth of the remanent polarization in the ferroelectric layer with decreasing temperature; however, for $T < 80$ K, the dependence of P_r on T became weaker and revealed a clear indication of saturation. The pattern of the measured $P_r(T)$ relation agrees well with the data obtained for a *c*-oriented BSTO layer in the SRO/BSTO/SRO/LSATO heterostructure [13]. At the same time, the absolute values of remanent polarization in a BSTO layer grown on SRO/LSATO and possessing a more perfect structure are, on the average, 20% larger than those for the ferroelectric layer studied in this work. Similar to P_r, the magnitude of E_C in the BSTO layer increased with decreasing temperature; however, there was no sign of saturation for $T < 80$ K. Comparison with the data presented in [6, 18] permits one to conclude that both the P_r and the maximum values of dP_r/dT in epitaxial BSTO films are considerably higher and E_C is a few times smaller than their respective values for ceramic (Ba,Sr)TiO_3 films.

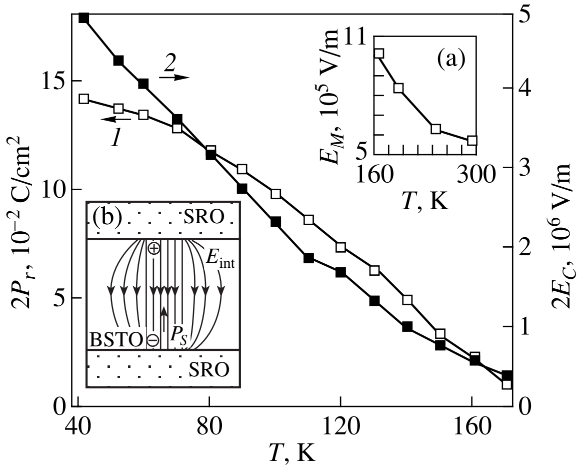

Fig. 4. Temperature dependences of (*1*) remanent polarization P_r and (*2*) coercive field E_C of the BSTO layer in a SRO/BSTO/SRO heterostructure ($f = 50$ kHz). Inset (a) shows the temperature dependence of E_M for the BSTO layer in a (001)SRO || (001)BSTO || (001)SRO heterostructure ($f = 100$ kHz). The electric field due to incomplete compensation of the polarization charge by electrons at the interface in the top layer of the metal oxide penetrates into adjacent crystallites in the BSTO layer that have no spontaneous polarization (see inset (b)).

3.3. Temperature and Field Dependences of ε' *of the BSTO Layer*

The temperature behavior of ε' of the BSTO layer depended strongly on the magnitude and polarity of the bias voltage applied to the metal oxide electrodes. To understand the ε'(E, T) dynamics better, a family of ε'(T) curves for various fixed values of V_b were measured in the range from –2.5 to +2.5 V (Fig. 5). The weak response of ε' to an electric field observed at $T = 300$ K is only natural, as the phase transition in bulk crystals of this solid solution occurs at a substantially lower temperature [3]. The dependence of ε' on the electric field became stronger with decreasing temperature. The maximum value $\varepsilon'_M \approx 3700\varepsilon_0$ was obtained at $T_M \approx 160$ K and $V_b = -0.7$ V. The approximately twofold increase in ε'(160 K) observed as V_b is reduced from 0 to –0.7 V (Fig. 5) indicates the presence of an internal electric field in the BSTO layer.

The internal electric field in a dielectric layer placed between two metal electrodes is associated, as a rule, with the difference between the work function W of the electrode material and the electron affinity χ of the sandwiched dielectric material [22, 23]. Surface states may affect the height of the potential barrier at the inter-

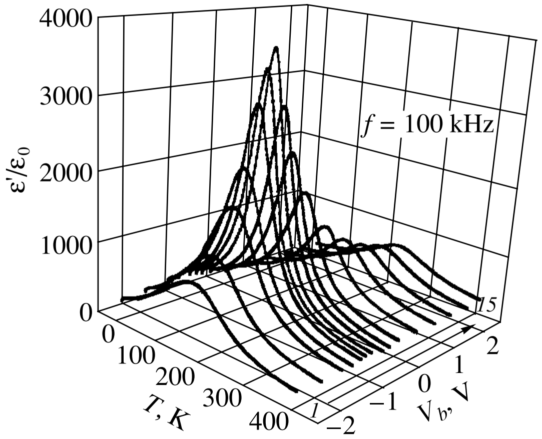

Fig. 5. Dependence of the real part ε' of the permittivity of the BSTO layer on temperature T (10–400 K) and bias voltage V_b (–2.5 to +2.5 V) applied to the metal-oxide electrodes. The maximum value $\varepsilon' \approx 3700\varepsilon_0$ was obtained at T_M = 160 K and V_b = –0.7 V. V_b: (1) –2.5, (*2*) –2, (*3*) –1.7, (*4*) –1.5, (*5*) –1.3, (*6*) –1.0, (*7*) –0.7, (*8*) –0.5, (*9*) –0.3, (*10*) 0, (*11*) 0.5, (*12*) 1.0, (*13*) 1.5, (*14*) 2.0, and (*15*) 2.5 V.

face $\varphi_b = W - \chi$ while not changing its type. In the case of a nonlinear dielectric, the internal electric field shifts the position of the maximum in the $C(E)$ relation for the capacitor structure with respect to the $E = 0$ point. In the case where both electrodes are of the same metal and the intermediate layer is in the paraelectric phase, the internal electric field strength is, as a rule, low and depends only weakly on temperature.

As follows from the data presented in Fig. 6, the maximum in the $\varepsilon'(E)$ relation for the BSTO layer is shifted toward negative values of E, the magnitude of this shift (E_M) with respect to $E = 0$ increasing strongly with decreasing temperature within the 300–165-K range [inset *a* to Fig. 4]. At these temperatures, most of the BSTO layer volume is in the paraelectric phase. The increase in E_M with decreasing temperature in the above temperature range can be traced to the formation of spontaneous polarization in individual crystallites in the bulk of the BSTO layer. The quantity of such crystallites and their spontaneous polarization increase with decreasing temperature. The depolarization electric field caused by the incomplete compensation of the polarization charge by electrons in the top SRO electrode also penetrates into the adjoining crystallites of the intermediate layer, where $P_S = 0$ (inset *b* to Fig. 4). This is the main reason for the emergence of an electric field directed from the top to the bottom electrode in the BSTO layer, which is primarily in the paraelectric phase at T > 160 K. The internal electric field started to increase at temperatures slightly below room temperature (inset *a* to Fig. 4). This shows that microscopic inclusions of the ferroelectric phase in the BSTO films under study started to nucleate at temperatures exceed-

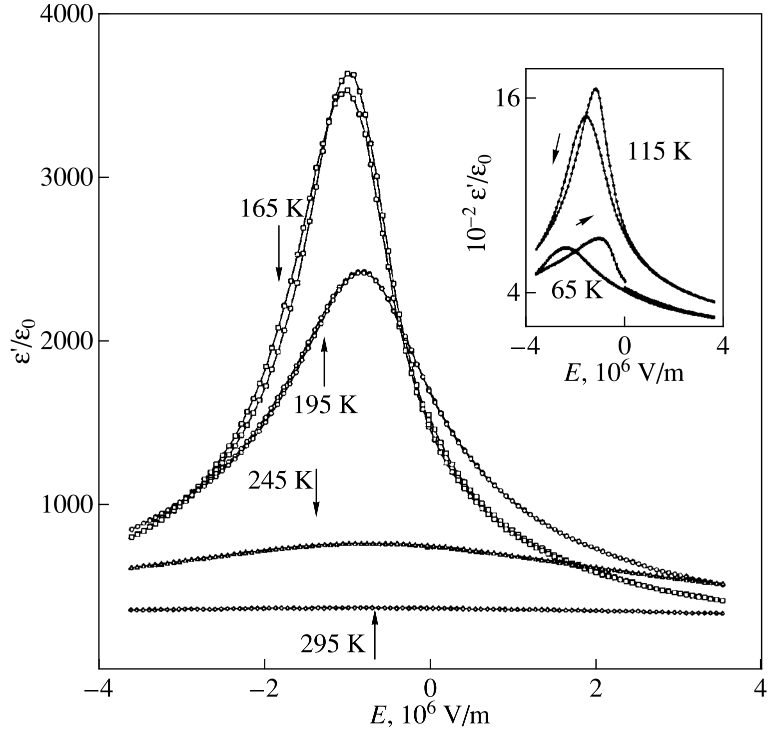

Fig. 6. Dependence of the real part ε' of the permittivity of the BSTO layer on electric field $E = V_b/d$ measured at $T > T_M$. The temperatures are specified on the curves; f = 100 kHz. Inset: $\varepsilon'(E)$ curves obtained for $T < T_M$.

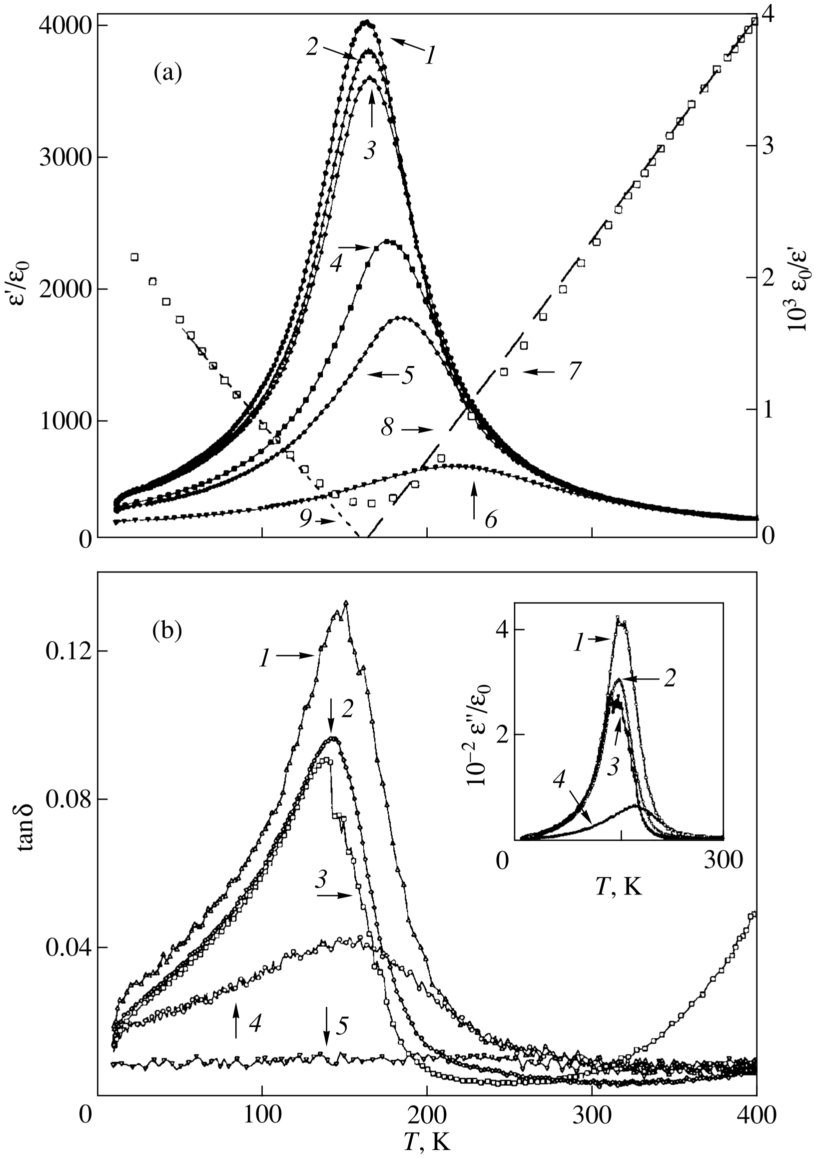

Fig. 7. (a) Temperature dependences of (*1*–*6*) $\varepsilon'/\varepsilon_0$ and (*7*) $\varepsilon_0/\varepsilon'$ for the BSTO layer in a SRO/BSTO/SRO heterostructure measured at frequencies f of (*1*) 1, (*2*) 10, and (*3*–*7*) 100 kHz and bias V_b of (*1*–*3*, *7*) –0.7, (*4*) –0.3, (*5*) 0, and (*6*) +2.5 V; (*8*, *9*) tangents to the $\varepsilon_0/\varepsilon'(T)$ curves drawn at $T = 350$ and 120 K, respectively. (b) Temperature dependences of $\tan\delta$ for the BSTO layer in the same heterostructure measured at f equal to (*1*, *4*, *5*) 100, (*2*) 10, and (*3*) 1 kHz and various V_b, (*1*–*3*) –0.7, (*4*) 0, and (*5*) +2.5 V. Inset: temperature dependences of the imaginary part of the permittivity for the BSTO layer measured at f equal to (*1*, *4*) 100, (*2*) 10, and (*3*) 1 kHz and V_b equal to (*1*–*3*) –0.7 and (*4*) 0 V.

ing T_M (at which the phase transformation occurred in the bulk of the film) by approximately 100 K.

The $\varepsilon'(E)$ curves measured at temperatures above 180 K were anhysteretic. A weakly pronounced hysteresis was observed in the field dependence of ε' obtained at $T = 165$ K (Fig. 6). As the temperature was lowered still further ($T < 165$ K), the asymmetry of the $\varepsilon'(E)$ relation increased and the hysteresis became more clearly seen (inset to Fig. 6). Both the onset of hysteresis in the $\varepsilon'(E)$ relation and the maximum in the $\varepsilon'(T)$ dependence (at $V_b = -0.7$ V) are evidence of the nucleation of the ferroelectric phase at $T \approx 160$ K in the BSTO layer (or, at least, in most of its volume).

For $T > 200$ K and $V_b = -0.7$ V, the $\varepsilon'(T)$ relation can be well fitted by the Curie–Weiss law:

$$\varepsilon_0/\varepsilon' = C_0^{-1}(T - T_0) \quad (1)$$

with the Weiss temperature $T_0 = 160$ K and the Curie constant $C_0 = 0.62 \times 10^5$ K. The values $T_0 = 150$ K and $C_0 = 0.8 \times 10^5$ K were derived in [3] from data on the temperature dependence of ε' for bulk ceramic BSTO samples. The small difference between C_0 and T_0 obtained on bulk samples and their respective values for a BSTO layer can be partially accounted for by the fact that the external field $E = -0.7$ V/d compensates the internal electric field only within a narrow temperature range near T_M; note also that this compensation is only partial because of structural defects present in the bulk of the ferroelectric layer and of the roughness of the ferroelectric–electrode interface in the SRO/BSTO/SRO trilayer heterostructure. The increase in T_M in the BSTO layer compared to the bulk crystal data can be likewise due to the increase in the effective lattice parameter of the BSTO layer [24].

As follows from the data presented in Fig. 7a, the real part of the permittivity decreased and the maximum in the $\varepsilon'(T)/\varepsilon_0$ dependence measured at 100 kHz became more diffuse and shifted toward higher temperatures when V_b increased from –0.7 to +2.5 V. The decrease in ε' in an electric field is due to dielectric saturation, and the shift of the maximum in the $\varepsilon'(T)$ dependence toward higher temperatures agrees well with the data on the effect of an electric field on the phase transition temperature in bulk $BaTiO_3$ crystals [25].

According to [26], the $\varepsilon'(T)$ dependence for a ferroelectric in the vicinity of a (second-order) phase transition can be extrapolated for $T < T_C$ using the relation

$$\varepsilon_0/\varepsilon' = -2C_0^{-1}(T - T_0). \qquad (2)$$

As follows from the data in Fig. 7a, the experimental $\varepsilon_0/\varepsilon'(T)$ relation obtained at $V_b = -0.7$ V and $T < T_M$ can be well fitted by Eq. (2) with a coefficient $-1.1C_0^{-1}$. Possible reasons for the decrease in this coefficient for an epitaxial BSTO layer were analyzed in [15].

When the BSTO layer was in the paraelectric phase, ε' virtually did not depend on frequency (f = 1–100 kHz) (Fig. 7a). The largest difference, of approximately 7%, between the values of ε' at 1 and 100 kHz was observed near T_M. It is only natural to relate the dispersion of ε' found for $T < T_M$ to relaxation of the ferroelectric domain walls. Adjacent ferroelectric domains in the BSTO layer, in which the spontaneous polarization vectors are oppositely directed, are separated by 180° domain walls. The contribution of oscillations of the 180° domain walls (DWs) to the permittivity of bulk BTO crystals was analyzed in [27, 28]. According to [28], DW displacement should give rise to relaxation-type features in the $\varepsilon'(f)$ relation. The resonant frequency at which the contribution of DWs to ε' is maximum depends on their effective mass, which is determined by the domain size and the magnitude of P_S.

Unlike the 90° DWs, 180° walls are not displaced by moderate electric fields [29]. The low mobility of the 180° DWs compared to 90° DWs is assigned to the small thickness of the former and to the fairly high barrier interfering with the wall displacement in the direction perpendicular to the polarization vector [29].

3.4. Dielectric Loss Tangent and ε" for a BSTO Layer

Similar to ε', the maximum values of ε" and $\tan\delta$ for the BSTO layer were obtained at a constant bias of –0.7 V (Fig. 7b and the inset to it). The maxima in the measured $\varepsilon''(T)$ and $\tan\delta(T)$ relations were, however, shifted by 10–15 K toward lower temperatures relative to T_M. These maxima are related to the oscillations of the ferroelectric DWs acted upon by the applied ac voltage V_{AC}. At $V_b = 0$, the presence of an internal electric field, whose strength is substantially higher than V_{AC}/d, accounts for the weak effect of measuring voltage on the DW structure in the BSTO layer. This is the reason for the presence of the diffuse maximum in the measured $\tan\delta(T)$ and $\varepsilon''(T)$ curves (curves *4* in Fig. 7b and the inset to it). When E_{int} is compensated by an external electric field ($V_b = -0.7$ V) and the coercive field is low ($T \approx T_M$, Fig. 4), the measuring ac voltage considerably affects the ferroelectric domain structure in the BSTO layer, which manifests itself in a sharp increase in $\tan\delta$ and ε". With the electrodes biased positively, the external and internal electric fields were added, which reduces the DW contribution to $\tan\delta$ (curve *5* in Fig. 7b).

Unlike ε', the $\tan\delta$ and ε" of the BSTO layer decreased in magnitude within the 10–300-K range with a frequency decrease from 100 to 1 kHz (Fig. 7b). In terms of the Debye approximation, the observed variations of ε' and ε" with decreasing frequency imply that the characteristic relaxation time of the process associated with DW motion in the BSTO layer is shorter than $1/2\pi f$. A comprehensive analysis of the contribution of relaxation processes to ε' and ε" for the $(Ba,Sr)TiO_3$ layer can be found in [13].

The growth of $\tan\delta$ observed to occur at $f = 1$ kHz with increasing temperature for $T > 250$ K is caused by the fairly high conductivity σ of the BSTO layer in the direction perpendicular to the substrate plane. The contribution of σ to $\tan\delta$ in the ferroelectric layer can be written as $\tan\delta = (\varepsilon'' + \sigma/\omega)/\varepsilon'$. As shown in [30], the dependence of the BSTO layer conductivity on temperature and electric field is associated with carrier ejection from the traps connected with oxygen vacancies.

4. CONCLUSIONS

The results obtained in this work can be summed up as follows. When using lanthanum aluminate as the substrate, the polar axis in the $Ba_{0.25}Sr_{0.75}TiO_3$ ferroelectric layer sandwiched between two $SrRuO_3$ metal-oxide epitaxial films is oriented perpendicular to

(001)$LaAlO_3$. The nucleation of single ferroelectric domains in the bulk of the *c*-oriented $Ba_{0.25}Sr_{0.75}TiO_3$ layer in the $SrRuO_3/Ba_{0.25}Sr_{0.75}TiO_3/SrRuO_3$ epitaxial heterostructure begins at temperatures a few tens of degrees above the Curie temperature for bulk single crystals. The formation of microscopic inclusions of the ferroelectric phase in the $Ba_{0.25}Sr_{0.75}TiO_3$ layer is accompanied by an increase in the internal electric field in adjacent crystallites having no spontaneous polarization. Due to a uniform distribution of the dielectric parameters and a high perfection of the microstructure of the grown $Ba_{0.25}Sr_{0.75}TiO_3$ layers, it is possible to compensate the internal electric field to a considerable extent by applying an external bias. Under maximum compensation of the internal electric field, the temperature dependence of the permittivity of the $Ba_{0.25}Sr_{0.75}TiO_3$ layer can be well fitted by the Curie–Weiss relation.

ACKNOWLEDGMENTS

This study was carried out in the framework of scientific cooperation between the Russian and Swedish Royal Academies of Science. This work was partially supported by the Russian Foundation for Basic Research, project no. 99-02-18022.

REFERENCES

1. R. C. Neville, B. Hoeneisen, and C. A. Mead, J. Appl. Phys. **43**, 2124 (1972).
2. G. A. Samara, Phys. Rev. **151**, 378 (1966).
3. A. D. Hilton and B. W. Ricketts, J. Phys. D **29**, 1321 (1966).
4. C. S. Hwang, Mater. Sci. Eng. B **B56**, 178 (1998).
5. J. P. Hong and J. S. Lee, Appl. Phys. Lett. **68**, 3034 (1966).
6. J.-G. Cheng, X.-J. Meng, J. Tang, *et al.*, Appl. Phys. Lett. **75**, 3402 (1999).
7. Yu. A. Boikov and T. Claeson, Physica C (Amsterdam) **336**, 300 (2000).
8. Yu. A. Boikov and T. Claeson, J. Appl. Phys. **89** (9), 5053 (2001).
9. S. Y. Hou, J. Kwo, R. K. Watts, *et al.*, Appl. Phys. Lett. **67**, 1387 (1995).
10. A. von Hippel, Rev. Mod. Phys. **22**, 221 (1950).
11. J. C. Jiang, W. Tian, X. Dan, *et al.*, Mater. Sci. Eng. B **B56**, 152 (1998).
12. J.-P. Maria, H. L. McKinstry, and S. Trolier-McKinstry, Appl. Phys. Lett. **76**, 3382 (2000).
13. Yu. A. Boikov and T. Claeson, submitted to Appl. Phys. Lett.
14. D. Fuchs, M. Adam, P. Schweiss, *et al.*, J. Appl. Phys. **88**, 1844 (2000).
15. Yu. A. Boikov and T. Claeson, submitted to Physica B (Amsterdam).
16. E. D. Specht, R. E. Clausing, and L. Heatherly, J. Mater. Res. **5**, 2351 (1990).
17. C. Zuccaro, M. Winter, N. Klein, and K. Urban, J. Appl. Phys. **82**, 5695 (1997).
18. H. B. Sharma, H. N. K. Sarma, and A. Mansingh, J. Appl. Phys. **85**, 341 (1999).
19. Y. Yoneda, T. Okabe, K. Sakaue, *et al.*, J. Appl. Phys. **83**, 2458 (1998).
20. P. Wurfel and I. P. Batra, Phys. Rev. B **8**, 5126 (1973).
21. I. P. Batra, P. Wurfel, and B. D. Silverman, Phys. Rev. B **8**, 3257 (1973).
22. Yu. A. Boikov, Z. G. Ivanov, A. Kiselev, *et al.*, J. Appl. Phys. **78**, 4591 (1995).
23. S. Saha and S. B. Krupanidhi, Mater. Sci. Eng. B **B57**, 135 (1999).
24. W. J. Merz, Phys. Rev. **77**, 52 (1950).
25. W. J. Merz, Phys. Rev. **91**, 513 (1953).
26. C. Kittel, *Introduction to Solid State Physics*, 7th ed. (Wiley, New York, 1996).
27. C. Kittel, Phys. Rev. **83**, 458 (1951).
28. D. G. Sannikov, Zh. Éksp. Teor. Fiz. **41** (1), 133 (1962) [Sov. Phys. JETP **14**, 98 (1962)].
29. N. A. Pertsev and G. Arlt, Ferroelectrics **132**, 27 (1992).
30. Yu. A. Boikov and T. Claeson, Supercond. Sci. Technol. **12**, 654 (1999).

Translated by G. Skrebtsov

Physics of the Solid State, Vol. 43, No. 12, 2001, pp. 2276–2279. Translated from Fizika Tverdogo Tela, Vol. 43, No. 12, 2001, pp. 2184–2187.

Effect of an Organic Dye on the Ferroelectric Phase Transition in KH_2PO_4 (KDP)

I. V. Shnaĭdshteĭn*, B. A. Strukov*, S. V. Grabovskiĭ*, T. V. Pavlovskaya*, and L. Carman**

**Moscow State University, Vorob'evy gory, Moscow, 119899 Russia*

***Lawrence Livermore National Laboratory, University of California, Livermore, CA 94550, USA*

Received May 8, 2001

Abstract—This paper reports on the first measurement of the dielectric permittivity and heat capacity of a KDP crystal doped by Chicago Sky Blue organic dye within a temperature interval including the ferroelectric phase transition at $T_c = 122$ K. Similar measurements were made on a pure KDP crystal under the same conditions for the sake of comparison. The heat capacities of the pure and doped crystals were shown to differ substantially within an interval 1 K wide in the vicinity of T_c, where an anomaly in the heat capacity of the doped crystal was observed to wash out without producing any change in the temperature position of its maximum. The doping reduces the permittivity in the polar phase markedly. The observed effects are associated with the influence of nonisomorphic defects on the ferroelectric phase transition in a piezoelectric crystal. *© 2001 MAIK "Nauka/Interperiodica".*

1. INTRODUCTION

It is known that at $T_c \approx 122$ K, the KH_2PO_4 crystal (KDP) undergoes a phase transition from the tetragonal $(\bar{4}2m)$ to the orthorhombic (*mm*2) phase, which gives rise to the generation of spontaneous polarization directed along the *c* axis of the tetragonal phase. Most of the properties of KDP near the phase transition are satisfactorily described in terms of Landau's theory with a thermodynamic potential of the type

$$\Phi = \Phi_0 + \frac{1}{2}\alpha(T - T_c)P^2 + \frac{1}{4}\beta P^4 + \frac{1}{6}\gamma P^6 + \frac{1}{8}\zeta P^8 - EP, \qquad (1)$$

where Φ_0 is the part of the thermodynamic potential not associated with the transition, P is the polarization along the c axis, E is the external electric field, $\alpha = 4.0 \times 10^{-3}$ K^{-1}, $\beta = -1.3 \times 10^{-11}$ esu, $\gamma = 3 \times 10^{-19}$ esu, and $\zeta = 3 \times 10^{-17}$ esu. The magnitudes of the coefficients suggest that these crystals undergo a first-order phase transition very close to the tricritical point; the value of the critical electric field E_c lies in the interval from 100 to 300 V/cm [1].

The closeness of the phase transition in KDP to the tricritical point, combined with the piezoelectric activity of the crystal for $T > T_c$, results in a substantial narrowing of the region wherein critical fluctuations affect the phase transition [2]. This makes the KDP crystal a promising subject for use in studying the effect of impurities on structural phase transitions, because it obviates the need for separating the fluctuation and defect-induced contributions to the measured properties.

It has recently been shown that the molecules of Chicago Sky Blue (CSB) and Amaranth organic dyes are capable of entering the KDP crystal lattice and color the pyramidal growth sectors selectively, which implies a peculiar effect of "recognition" of certain faces of a growing crystal by large organic molecules [3, 4]. Interestingly, such molecules are nonisomorphic to the KDP molecules; hence, their anisotropic incorporation into a piezoelectric inorganic host matrix should give rise to considerable local strains and the associated electric polarization in the crystal. Thus, the molecules of organic dyes make it possible to study the influence of strong defects [5] on phase transitions in KDP.

2. EXPERIMENTAL TECHNIQUE

This communication reports on a comparative study of the temperature dependences of the permittivity and heat capacity of a KDP crystal doped with a CSB dye (KDP + CSB), whose molecular structure is given in [3], and of nominally pure KDP. In both cases, the samples were cut from pyramidal growth sectors of the crystals.

The KDP + CSB crystal was seed grown from a solution containing 1.7×10^{-2} mg CSB/g KDP in accordance with the method described in [6]. The solution was prepared at 33°C. The CSB molecules started to incorporate into the pyramidal sectors of the growing crystal at 27.7°C. After the crystal grew to a size of $\approx 5 \times 5 \times 6$ cm, cracks formed on its surface.

The CSB concentration in the crystal was deduced by comparing (with an HP 8452A spectrophotometer) the absorption spectrum of the aqueous solution of a sample cut from the crystal with the absorption spectra of solutions with known KDP and dye concentrations.

Comparison of the spectra permits the conclusion that the colored sectors of the crystal contain 1.4–2 dye molecules per 10^5 KDP molecules.

The permittivity was measured under cooling from room to liquid-nitrogen temperature at a cooling rate of 0.25 K/min far from T_c and at 0.1 K/min in the vicinity of T_c. The samples used were 8 × 5 × 1 mm plates with the plate plane oriented perpendicular to the polar axis. Silver paste was applied to the faces parallel to this plane.

The heat capacity of two samples (pure and colored KDP) was measured in the 82- to 162-K temperature interval using adiabatic calorimetry. The samples were cylinders, 8 mm in diameter and 12 mm high, prepared without any regard for the relative orientation to the crystallographic axes. The measurements were carried out under constant heating power in steps ranging from 1 K (far from T_c) to 0.02 K (near T_c) with an accuracy of 0.5%.

3. EXPERIMENTAL RESULTS

Figure 1 shows the temperature dependences of the permittivity of the pure and colored KDP crystals obtained at 10 kHz. For $T > T_0 + 4$K, the values of ε_c of the colored crystal lie systematically slightly above those for the pure crystal; by contrast, in the polar phase, ε_c of the colored crystal is considerably smaller than that of the pure crystal. The relations plotted in Fig. 1 are in qualitative agreement with those obtained in [7] for ε_c of KDP crystals differing in quality.

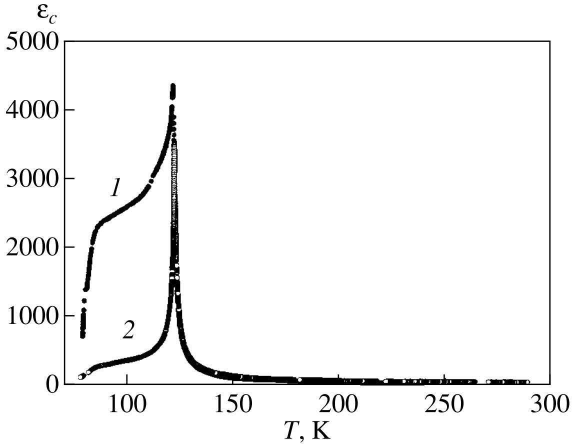

Fig. 1. Temperature dependences of the dielectric permittivity of (*1*) pure and (*2*) colored KDP crystals.

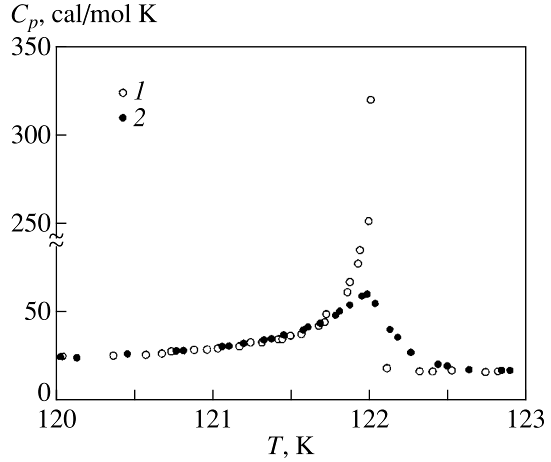

Fig. 2. Temperature dependences of the heat capacity of (*1*) pure and (*2*) colored KDP crystals.

The temperature dependences of the heat capacity of the pure and colored KDP crystals are presented in Fig. 2. The heat capacity of both crystals is seen to be the same, except in a narrow interval in the vicinity of the phase transition. A comparison of our data for pure KDP with the results quoted in [8, 9] revealed that the heat capacity of our crystal is in full agreement with data from previous measurements. Because the heat capacity quoted in the above-mentioned papers is given in cal/mol K, our data are also presented in these units.

As seen from Fig. 2, the heat capacity reaches a maximum at $T = 122.00 \pm 0.03$ K for both the pure and colored crystals; in the latter case, the maximum heat capacity is equal to 61.4 cal/mol K and the phase transition is slightly diffuse. The heat capacity of the pure crystal reached very high peak values (~10^3 cal/mol K), which corresponds to latent heat liberation in a first-order phase transition; therefore, within a 0.1-K wide interval immediately above the peak position, the heat capacity of the pure crystal was not determined; for the colored crystal, there is no such limitation.

Comparison of the results in Fig. 2 with the data on the behavior of the KDP heat capacity in an external electric field [1] shows that the temperature dependence of the heat capacity of the colored crystal is similar to that of KDP in an external electric field higher than the critical level, the only difference being that the maximum of the heat capacity is not shifted toward high temperatures.

4. DISCUSSION OF RESULTS

To perform a quantitative analysis of the data obtained, the temperature dependence of the background heat capacity, C_{lat}, was constructed within a broad temperature region in the form

$$C_{\text{lat}} = C_0 D\left(\frac{\Theta_0}{T}\right) + C_1 E\left(\frac{\Theta_1}{T}\right) + C_2 E\left(\frac{\Theta_2}{T}\right), \qquad (2)$$

where D is the Debye function, E is the Einstein function, $\Theta_0 = 197$ K, $\Theta_1 = 319$ K, $\Theta_2 = 1210$ K, $C_0 = 9.72$ cal/mol K, $C_1 = 12.22$ cal/mol K, and $C_2 =$

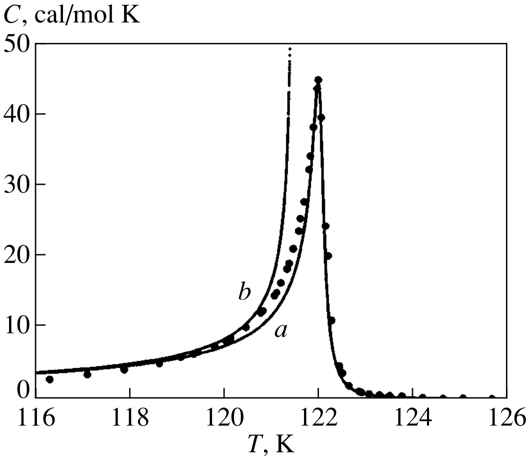

Fig. 3. Temperature dependences of the excess heat capacity of the colored KDP crystal. Curves *a* and *b* were constructed using Eq. (1): (*a*) $E \uparrow\uparrow P_s$ and (*b*) $E \uparrow\downarrow P_s$.

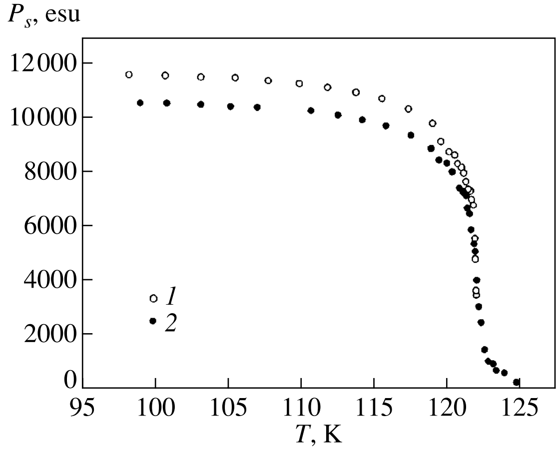

Fig. 4. Polarization of (*1*) pure and (*2*) colored KDP crystals as calculated from Eq. (3) using the experimental heat capacity data.

24.93 cal/mol K. The background heat capacity was derived using experimental data from [8].

Figure 3 plots the temperature dependence of the heat capacity of the colored crystal after subtraction of the background heat capacity given by Eq. (2). Presented in the same figure are the values of the heat capacity calculated assuming Landau's thermodynamic potential in the form of (1) [curve *a*] to be applicable to the description of the behavior of KDP in the vicinity of the phase transition. We believe that the subtracted background heat capacity corresponds to the term Φ_0 in Eq. (1); E was varied from 1.0 to 7.0 esu, and T_c was varied within the interval 121.60–122.00 K, because, according to [5], the phase transition temperature in a crystal with defects should be shifted toward low temperatures. The best fit to the experimental data was obtained at $E = 5.7$ esu (1.71 kV/cm) and $T_c = 121.68$ K. We readily see that above T_c, the experimental data correspond to a phase transition in an external electric field; in other words, the effect of the CSB impurity on the ferroelectric phase transition in KDP is similar to that of polarized defects [5].

However, examination of Fig. 2 also suggests that the area bounded by the heat capacity curve of the pure crystal is larger than that of the colored one. Because the spontaneous polarization is related to the heat capacity through

$$P_s = \sqrt{\frac{2}{\alpha}\int_{\infty}^{T}\frac{C - C_{\text{lat}}}{T}dT}, \qquad (3)$$

this implies that the spontaneous polarization of the colored crystal in the polar phase is smaller than that of the pure crystal. As seen from the corresponding temperature dependences of P_s shown in Fig. 4, the phase transition in the colored crystal is diffuse and its P_s is noticeably smaller (by approximately 8%). The latter is obviously at odds with the conventional effect of a bias field on the spontaneous polarization of a crystal. However, the situation considered in [10] was that of a uniaxial ferroelectric crystal undergoing a phase transition in an external electric field and residing in a metastable state characterized by a polarization directed opposite to the field. Figure 3 presents the values of the heat capacity calculated for this situation (curve *b*) for the same parameters of the thermodynamic potential (1) as those used for curve *a*. We readily see that within the 118- to 121-K interval, curve *b* satisfactorily fits the experimental data.

This apparently means that the bias electric field associated with defects can be oriented opposite to, rather than along, the direction of spontaneous polarization in the polar phase, thus realizing the metastable state predicted in [10], which turns out to be sufficiently stable due to the presence of strong polar defects.

Note that the diffuseness of the phase transition in a colored crystal is also accompanied by features in the temperature dependence of the permittivity ε_c. The degree of diffuseness is characterized by the value of E derived from thermal measurements and can be estimated from Fig. 5, which plots the temperature dependence of the inverse permittivity ε_c^{-1} of the colored crystal together with the corresponding relation calculated from the thermodynamic potential (1) for the values of E and T_0 extracted from heat capacity data. One readily sees that for $T \geq T_c$, the values obtained are in satisfactory agreement with the experiment. For $T < T_c$, no such agreement exists; this is accounted for by a large domain contribution to the dielectric permittivity of KDP. One also sees that incorporation of the impurity markedly reduces the domain contribution to ε_c (Fig. 1). This effect was also observed earlier in studies

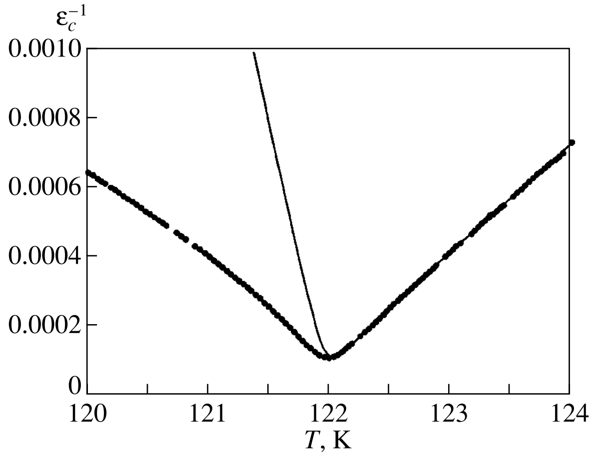

Fig. 5. Temperature dependence of inverse permittivity ε_c^{-1} of the KDP + CSB crystal. The thin line plots the relation calculated using Eq. (1).

on KDP crystals with defects [7] and was assigned to the pinning of domain walls by impurity inclusions.

The data obtained permit some assumptions concerning the mechanism of the effect of the CSB impurity on the phase transition in KDP to be made.

The incorporation of large organic dye molecules into the structure of the KDP crystal was discussed in [3, 4], where the important role of the stereochemical affinity between the impurity and the host matrix was considered. In our case, direct comparison of the parameters of the CSB molecule and its SO_3^- terminal groups, which are believed to be capable of occupying the PO_4^- positions in KDP, would be difficult due to the lack of accurate information on the interatomic distances in the dye molecule. It may, however, be conjectured that these rigid molecules locally distort the lattice in the nonpolar phase to produce local strains and the corresponding polarization due to the piezoelectric effect. Because of the long-range character of the elastic and Coulomb forces, the presence of strained polarized regions becomes manifest, for $T > T_c$, as a macroscopic electric field bias; below T_c, these regions may become appropriately oriented domains. In these conditions, the impurity reduces the average spontaneous polarization in the polar phase if one assumes that the magnitude of P_s near the impurity molecule is determined by the local lattice distortion arising in the nonpolar phase and reaches its normal value only at sufficiently large distances from this region. Such a situation can be considered to be a manifestation of the macroscopic bias electric field being directed opposite to the spontaneous polarization and reducing its average value; this is exactly what is observed in our experiment.

ACKNOWLEDGMENTS

The authors are indebted to L.N. Rashkovich and N.P. Zaĭtseva for their interest in the work.

This study was supported by the Russian Foundation for Basic Research, project no. 99-22-16319.

REFERENCES

1. E. Sandvold and K. Fossheim, J. Phys. C **19**, 1481 (1986).
2. A. P. Levanyuk and A. A. Sobyanin, Pis'ma Zh. Éksp. Teor. Fiz. **11**, 540 (1970) [JETP Lett. **11**, 371 (1970)].
3. J. A. Subramony, S. N. Jang, and B. Kahr, Ferroelectrics **191**, 293 (1997).
4. B. Kahr and R. W. Gurney, Preprint (2000).
5. A. P. Levanyuk, V. V. Osipov, A. S. Sigov, and A. A. Sobyanin, Zh. Éksp. Teor. Fiz. **76**, 345 (1979) [Sov. Phys. JETP **49**, 176 (1979)].
6. N. Zaitseva, L. Carman, I. Smolsky, *et al.*, J. Cryst. Growth **204**, 512 (1999).
7. E. Nakamura and K. Kuramoto, J. Phys. Soc. Jpn. **57**, 2182 (1988).
8. C. C. Stephenson and J. G. Hooley, J. Am. Chem. Soc. **66**, 1397 (1944).
9. B. A. Strukov, M. Amin, and V. A. Kopchik, Phys. Status Solidi **27**, 741 (1968).
10. G. Dukek and G. Falk, Z. Phys. **240**, 93 (1970).

Translated by G. Skrebtsov

Physics of the Solid State, Vol. 43, No. 12, 2001, pp. 2280–2283. Translated from Fizika Tverdogo Tela, Vol. 43, No. 12, 2001, pp. 2188–2191.
Original Russian Text Copyright © 2001 by Dudnik, Duda, Kushnerov.

MAGNETISM AND FERROELECTRICITY

Second-Order Ferroic Properties of a $Pb_5Ge_3O_{11}$ Uniaxial Ferroelectric

E. F. Dudnik, V. M. Duda, and A. I. Kushnerov
Dnepropetrovsk National University, Dnepropetrovsk, 49050 Ukraine
e-mail: elf@ff.dsu.dp.ua

Received April 11, 2001

Abstract—The ferrobielastic properties (ferroic properties of the second order) earlier theoretically predicted for lead germanate uniaxial ferroelectric crystals are justified experimentally. It is demonstrated that single-domain samples are formed upon cooling to temperatures below the Curie point under uniaxial mechanical stresses corresponding to a combination of mechanical stresses $\sigma_{11}\sigma_{13}$ or $\sigma_{22}\sigma_{23}$. The macroscopic mechanism of this phenomenon is considered. © *2001 MAIK “Nauka/Interperiodica”.*

1. INTRODUCTION

It is well known that a second-order ferroic is considered to be a crystal that can exist in two or more orientational states and transform from one state into another under the action of a combination of two forces (fields) applied in certain crystallographic directions [1, 2]. In terms of symmetry, the second-order ferroic properties can manifest themselves in first-order ferroic crystals. Earlier [3–7], we investigated the ferroelastic–ferroelectric properties of ferroelectric materials. The symmetry analysis demonstrated that the majority of ferroelectric phase transitions should also be ferrobielastic phase transitions; consequently, the domains in these ferroelectric–ferrobielastic materials should be switched by an electric field and under the action of a combination of two simultaneously applied mechanical stresses. Uniaxial ferroelectrics that do not exhibit ferroelastic properties can serve as objects of investigation into the ferrobielastic properties of ferroelectric crystals. The most suitable objects are the $Pb_5Ge_3O_{11}$ lead germanate crystals, in which, unlike other uniaxial ferroelectrics, the domain structure can be observed directly through a polarizing microscope.

The ferroelectric phase transition $\bar{6} \longrightarrow 3$ in a lead germanate crystal can lead to the formation of two orientational states $S1$ and $S2$, which represent 180° domains differing in the sign of optical activity. By symmetry, this transition should be ferroelastic–ferroelectric and ferrobielastic simultaneously, because new components of the tensor of piezoelectric coefficients d and components of the tensor of elastic compliance coefficients s spontaneously appear upon the transition. The tensors of the spontaneous piezoelectric and elastic coefficients for the orientational state $S1$ have the following form:

$$\begin{pmatrix} 0 & 0 & 0 & d_{14} & d_{15} & 0 \\ 0 & 0 & 0 & d_{15} & -d_{14} & 0 \\ d_{31} & d_{31} & d_{33} & 0 & 0 & 0 \end{pmatrix}, \tag{1}$$

$$\begin{pmatrix} 0 & 0 & 0 & s_{14} & -s_{25} & 0 \\ & 0 & 0 & -s_{14} & s_{25} & 0 \\ & & 0 & 0 & 0 & 0 \\ & & & 0 & 0 & 2s_{25} \\ & & & & 0 & 2s_{14} \\ & & & & & 0 \end{pmatrix}. \tag{2}$$

The relevant tensors for the orientational state $S2$ can be obtained by multiplying tensors (1) and (2) by –1.

By using these tensors and writing the expansion of the thermodynamic potential Φ for each of the domains, we determine the difference in energies $\Delta\Phi$ that appears under the action of external electric fields and mechanical stresses:

$$\begin{aligned} \Delta\Phi = {} & -2P_3E_3 - 4d_{123}E_1\sigma_{23} - 4d_{113}E_1\sigma_{13} - 4d_{113}E_2\sigma_{23} \\ & + 4d_{123}E_2\sigma_{13} - 2d_{311}E_3\sigma_{11} - 2d_{311}E_3\sigma_{22} - 2d_{333}E_3\sigma_{33} \\ & - 4s^E_{1123}\sigma_{11}\sigma_{23} + 4s^E_{2213}\sigma_{11}\sigma_{13} + 4s^E_{1123}\sigma_{22}\sigma_{23} \\ & - 4s^E_{2213}\sigma_{22}\sigma_{13} - 8s^E_{2213}\sigma_{23}\sigma_{12} - 8s^E_{1123}\sigma_{13}\sigma_{12}\ldots, \end{aligned} \tag{3}$$

where P_3 are the components of the spontaneous polarization vector, d_{ikl} are the spontaneous piezoelectric coefficients, and s^E_{ijkl} are the spontaneous coefficients of the elastic compliance measured in a constant electric field E.

It follows from expression (3) that when the crystal is subjected to an electric field E_3 and mechanical stress through any combination of the electric field and mechanical stress $E_1\sigma_{23}$, $E_1\sigma_{13}$, $E_2\sigma_{23}$, $E_2\sigma_{13}$, $E_3\sigma_{11}$, $E_3\sigma_{22}$, and $E_3\sigma_{33}$, or a combination of two mechanical stresses $\sigma_{11}\sigma_{23}$, $\sigma_{11}\sigma_{13}$, $\sigma_{22}\sigma_{23}$, $\sigma_{22}\sigma_{13}$, $\sigma_{23}\sigma_{12}$, and $\sigma_{13}\sigma_{12}$, there arises a difference between the energies of the two orientational states *S*1 and *S*2. Note that, upon transition to the lowest-energy state, the crystal should become single-domain on the macroscopic level.

In this work, we experimentally investigated the possibility of forming a single-domain state in lead germanate crystals due to their ferrobielastic properties through combinations of mechanical stresses $\sigma_{11}\sigma_{13}$ and $\sigma_{22}\sigma_{23}$.

2. EXPERIMENTAL PROCEDURE

In his experiments on ferrobielastic switching in quartz crystals, Aizu [1] used uniaxial mechanical stresses applied along the [011] direction at an angle of 45° to the *Z* axis, because, in this case, the stress tensor of the crystal contains nonzero components σ_{22}, σ_{23}, σ_{32}, and σ_{33} and it is this combination of the stresses σ_{22} and σ_{23} that provides domain switching.

In the present work, we used the same principle of obtaining combinations of two mechanical stresses to investigate the ferrobielastic properties of lead germanate. Let us consider this principle in more detail.

It is assumed that a crystal is subjected to homogeneous mechanical stress along the direction specified by an arbitrary unit vector **l**. Let σ be the magnitude of this mechanical stress. The stress tensor components of the crystal can be represented in the form [8]

$$\sigma_{ij} = l_i l_j \sigma \quad (i, j = 1, 2, 3), \tag{4}$$

where l_i and l_j are the components of vector **l**. Hence, the stress tensor takes the form

$$(\sigma_{ij}) = \begin{pmatrix} l_1^2\sigma & l_1 l_2\sigma & l_1 l_3\sigma \\ l_2 l_1\sigma & l_2^2\sigma & l_2 l_3\sigma \\ l_3 l_1\sigma & l_3 l_2\sigma & l_3^2\sigma \end{pmatrix}. \tag{5}$$

By varying the direction of application of the uniaxial mechanical stress σ, we can change the form of the stress tensor, thus producing different stress combinations.

We investigated the ferrobielastic properties of a lead germanate crystal subjected to the mechanical stress combinations $\sigma_{11}\sigma_{13}$ and $\sigma_{22}\sigma_{23}$. In this case, the uniaxial mechanical stresses σ should be directed at an angle α to the *Z* axis in the *XZ* and *YZ* planes, respectively, and their magnitudes can be determined from the following relationships:

$$\sigma_{11}\sigma_{13} = (\cos^3\alpha\sin\alpha)\sigma^2, \tag{6}$$

$$\sigma_{22}\sigma_{23} = (\cos^3\alpha\sin\alpha)\sigma^2. \tag{7}$$

Under these conditions, the maximum effect is achieved when $\alpha = 60°$ and $\sigma_{11}\sigma_{13} = \sigma_{22}\sigma_{23} \approx 0.325\sigma^2$.

In our experiments, we used lead germanate single crystals grown by the Czochralski method. Plates ~3 mm thick were cut out normally to the ferroelectric axis *Z* of the crystal. For observations of 180° domains through a polarizing microscope, the plates were polished and cut into rectangular bars with facets perpendicular to the *X* and *Y* crystallographic directions (*X*- and *Y*-cuts, respectively). In order to obtain the facets perpendicular to the direction of uniaxial mechanical compression producing the required combinations of mechanical stresses $\sigma_{11}\sigma_{13}$ or $\sigma_{22}\sigma_{23}$, we worked out the oblique *X*- and *Y*-cuts in such a way that the normals to their surfaces made angles of 60° with the *Z* axis, as determined above. Earlier experiments on ferrobielastic domain switching in quartz crystals demonstrated that, at room temperature, the uniaxial mechanical compressive stresses required for domain switching are rather strong (~5×10^8 Pa [1, 9]). For this reason, we studied the ferrobielastic properties of $Pb_5Ge_3O_{11}$ crystals upon their cooling to temperatures below the Curie point (450 K).

A specially designed holder made it possible to apply uniaxial mechanical compressive stresses and electric fields to the sample and to carry out its heating and cooling to a required temperature at a given rate. Before each experiment, the sample fastened in the crystal holder was annealed at $T \sim 600$ K. Then, the sample was subjected to an electric field or uniaxial compressive stress (~5×10^7 Pa) and cooled to a temperature below the Curie point. After cooling to room temperature, the external actions were eliminated, the sample was withdrawn from the crystal holder, and its domain structure was examined with a polarizing microscope.

Thin lead foil tightly rolled onto the sample facets with transformer oil was used as an electrode. If needed, the foil could be easily removed without injuring the polished crystal surface.

3. RESULTS AND DISCUSSION

Upon cooling the samples of $Pb_5Ge_3O_{11}$ crystals through the Curie point without applying external actions, there arises a polydomain structure characteristic of the majority of ferroelectrics. This structure consists of a large number of very small antiparallel domains. According to Shur *et al.* [10], the width of these domains for lead germanate crystals is approximately equal to $(2–3) \times 10^{-6}$ m. Such small domains are optically indistinguishable through a polarizing microscope. After applying the electric field E_3 during the cooling, the examination of the *Z*-cut at room temperature indicates that a single-domain structure is formed in the crystal due to its ferroelectric properties. Depending on the direction of the applied electric field without variation in the sample orientation, the lead

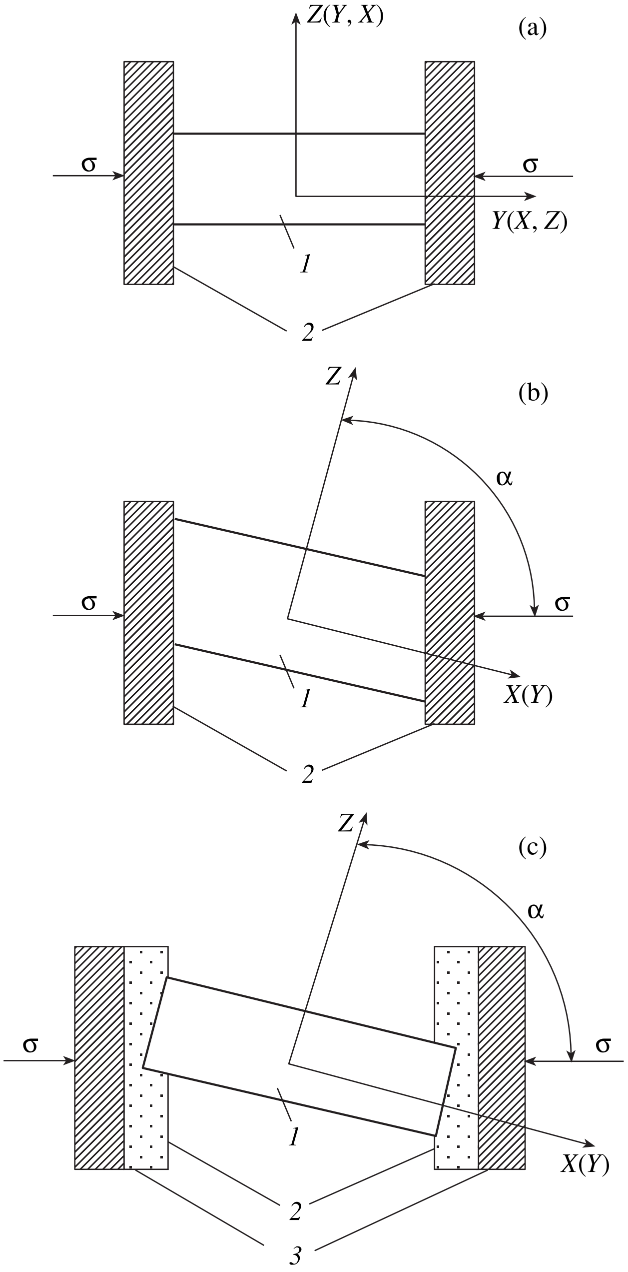

Fig. 1. Different geometries of experiments with lead germanate single-crystal samples: (a) application of uniaxial compressive stresses σ_{22} (σ_{11} or σ_{33}), (b) oblique cuts for producing equivalent combinations of mechanical stresses $\sigma_{11}\sigma_{13}$ ($\sigma_{22}\sigma_{23}$), and (c) *X*- or *Y*-cuts at an angle α to the direction of compression. Designations: (*1*) crystal, (*2*) compressing surfaces, and (*3*) Teflon spacers.

germanate crystal can appear to be light or dark, provided the angle between the polarization planes of the analyzer and polarizer is $\gamma = 90° \pm \rho d$, where d is the sample thickness and ρ is the specific optical rotation. This behavior is a result of the different signs of ρ for domains with different orientations of vector $\mathbf{P}_s$.

Optical observations of the *X*-, *Y*-, and *Z*-cuts of samples subjected to uniaxial mechanical compressive stresses σ_{11}, σ_{22}, and σ_{33} (the geometry of the experiment is shown in Fig. 1a) demonstrated that, after cooling through the Curie point, these samples had a polydomain structure at room temperature. This indicates that the domain structure of lead germanate is unaffected by the applied mechanical stresses.

A different situation occurs with oblique cuts (their preparation was described above). Examination of the samples with oblique cuts (the geometry shown in Fig. 1b) through a polarizing microscope revealed that, after cooling below the phase transition point, the samples at $T = 20°$C are in a single-domain state. This suggests that the effect of the mechanical stress combinations $\sigma_{11}\sigma_{13}$ and $\sigma_{22}\sigma_{23}$ is equivalent to the action of the electric field along the ferroelectric axis *Z*. The same inference follows from the phenomenological consideration and counts in favor of the ferrobielastic properties of lead germanate crystals.

The drawback of the above geometry of the experiment is that the change in sign of mechanical stress combinations becomes impossible in the absence of mechanical tensile stresses. For this reason, samples with *X*- and *Y*-cuts were also used in our experiments. In order to obtain the required combinations of mechanical stresses $\sigma_{11}\sigma_{13}$ or $\sigma_{22}\sigma_{23}$, the samples were adjusted in the crystal holder in such a manner that the *Z* axis made an angle of 60° with the direction of application of the uniaxial mechanical stresses (the geometry of the experiment is shown in Fig. 1c). Moreover, possible inhomogeneous mechanical stresses were suppressed with Teflon spacers 2 mm thick mounted between the compressing surfaces of the crystal holder. This technique made it possible to change over from the angle α to –α, thus reversing the sign of the mechanical stress combinations to obtain $-\sigma_{11}\sigma_{13}$ and $-\sigma_{22}\sigma_{23}$ without applying mechanical tensile stress to the sample. The experiments demonstrated that, even with a slightly simplified technique, the change from the angle α to –α during cooling of the crystal to a temperature below the Curie point results in the formation of a single-domain state but with the opposite direction of $\mathbf{P}_s$ (observations were carried out for a constant orientation of the crystal with respect to the microscope).

These observations of the formation of a single-domain structure were also confirmed by measuring the piezoelectric response of lead germanate crystals in the direction of the polar axis. The piezoelectric response was examined using a superposition of the mechanical compressive stress σ_{33} and its subsequent rapid removal with the measurement of the electric charge thus induced (the static method of measuring the piezoelectric modulus). For the $Pb_5Ge_3O_{11}$ crystals, which were cooled below the Curie point without external actions or under the action of mechanical stresses σ_{11}, σ_{22}, and σ_{33}, the piezoelectric response was found to be insignificant. This indicates a certain unipolarity of the crystals, which can be caused by growth defects. At the same time, the samples cooled in an electric field E_3 or under the action of mechanical stress combinations $\sigma_{11}\sigma_{13}$ and $\sigma_{22}\sigma_{23}$ exhibited a substantial piezoelectric response (exceeding the response in the preceding case by more than one order of magnitude). In the latter case, the response sign reversed with the change in sign of the external action applied above the Curie point.

The experiments performed revealed that, at a temperature far below the Curie point, no ferrobielastic domain switching occurs in the $Pb_5Ge_3O_1$ samples in the case when the mechanical stress combinations $\sigma_{11}\sigma_{13}$ and $\sigma_{22}\sigma_{23}$ are less than or equal to 8×10^{14} Pa^2. However, already at a temperature of 448 K (2 K below T_c), prolonged (~60 min) action of the mechanical stress combinations $\sigma_{11}\sigma_{13} = \sigma_{22}\sigma_{23} = 18 \times 10^{14}$ Pa^2 brings about the formation of large single-domain regions in the form of strips, which is not characteristic of conventional ferroelectric domains in $Pb_5Ge_3O_{11}$.

As a first approximation, the macroscopic mechanism of ferrobielastic switching in $Pb_5Ge_3O_{11}$ crystals can be represented in the following form. One of the mechanical stresses entering into the combination $\sigma_{11}\sigma_{13}$ or $\sigma_{22}\sigma_{23}$ gives rise to strains in the crystal that have different signs for different 180° domains in accordance with the signs of the elastic compliance coefficients. The second component of the mechanical stress induces switching of these domains, as is the case in ferroelastics. It seems likely that the domain switching through the mechanical stress combinations $\sigma_{11}\sigma_{23}$, $\sigma_{22}\sigma_{13}$, $\sigma_{23}\sigma_{12}$, and $\sigma_{13}\sigma_{12}$ should occur in a similar manner.

4. CONCLUSION

The above results have demonstrated that the $Pb_5Ge_3O_{11}$ ferroelectric crystals possess ferrobielastic properties which, in particular, can be used for the formation of a single-domain structure in lead germanate single crystals without application of an electric field.

ACKNOWLEDGMENTS

We are grateful to V.G. Linnik for supplying the high-quality single crystals $Pb_5Ge_3O_{11}$ used in our experiments.

REFERENCES

1. K. Aizu, J. Phys. Soc. Jpn. **34** (1), 121 (1973).
2. R. E. Newnham and L. E. Cross, Mater. Res. Bull. **9**, 1021 (1974).
3. E. F. Dudnik, V. M. Duda, and A. I. Kushnerov, Fiz. Tverd. Tela (St. Petersburg) **39** (9), 1634 (1997) [Phys. Solid State **39**, 1457 (1997)].
4. E. F. Dudnik, V. M. Duda, and A. I. Kushnerov, Ukr. Fiz. Zh. **43** (2), 243 (1998).
5. E. F. Dudnik, A. I. Kushnerov, and V. M. Duda, Mater. Res. Innovations **2** (5), 309 (1999).
6. E. F. Dudnik, V. M. Duda, and A. I. Kushnerov, Ukr. Fiz. Zh. **44** (10), 1277 (1999).
7. E. F. Dudnik, V. M. Duda, and A. I. Kushnerov, Fiz. Tverd. Tela (St. Petersburg) **42** (1), 133 (2000) [Phys. Solid State **42**, 139 (2000)].
8. M. A. Akivis and V. V. Gol'dberg, *Tensor Calculus* (Nauka, Moscow, 1969).
9. G. D. Mansfel'd, R. Besson, and P. Guzzo, Fiz. Tverd. Tela (St. Petersburg) **39** (2), 290 (1997) [Phys. Solid State **39**, 254 (1997)].
10. V. Ya. Shur, A. L. Gruverman, V. V. Letuchev, *et al.*, Ferroelectrics **98**, 341 (1989).

Translated by O. Moskalev

Physics of the Solid State, Vol. 43, No. 12, 2001, pp. 2284–2289. Translated from Fizika Tverdogo Tela, Vol. 43, No. 12, 2001, pp. 2192–2197.
Original Russian Text Copyright © 2001 by Evteev, Kosilov, Milenin.

Phase and Structural Transformations in a Molecular Dynamics Model of Iron under Ultrafast Heating and Cooling

A. V. Evteev, A. T. Kosilov, and A. V. Milenin
Voronezh State Technical University, Moskovskiĭ pr. 14, Voronezh, 394026 Russia
e-mail: mfm@ns1.vstu.ac.ru

Received January 26, 2001; in final form, April 9, 2001

Abstract—It is shown that a system of classical particles considered in a molecular dynamics model with Pak–Doyama pairwise interatomic potential adequately describes not only the various structural states of iron (melt, bcc crystal, metal glass) but also the complex self-organization processes occurring in first- and second-order phase transitions (crystallization and vitrification, respectively). When the temperature is varied at a constant rate of 6.6×10^{11} K/s, crystallization sets in from both the amorphous and the liquid state; at a rate of 1.9×10^{12} K/s, crystallization is observed only in the amorphous state; and when heated at a rate of 4.4×10^{12} K/s, the model amorphous iron transfers to the liquid state without crystallization. The energy of homogeneous formation of a crystal nucleus in the bulk of the amorphous phase of iron is calculated to be ~0.71 eV under the assumption that there is a spectrum of activation energies. *© 2001 MAIK “Nauka/Interperiodica”.*

1. INTRODUCTION

It is known [1] that vitrification of pure metals requires ultrafast quenching rates (~10^{10}–10^{13} K/s) and that the thermal stability of the films thus obtained depends substantially on their thickness. For instance, an iron film 25 Å thick prepared through condensation from the vapor phase on a substrate cooled by liquid helium to ~4.2 K crystallizes at 50–60 K under heating performed at a constant rate of ~5 K/min, while a 150-Å-thick film cannot be obtained in the amorphous state at all [2, 3]. Thus, the limiting cooling rates needed for amorphization can be experimentally attained only in thin films in the initial stages of their formation. Investigation of the structure of such films and of their crystallization and melting under heating is a very complex technical problem.

The study of such systems becomes considerably simpler and the possibilities of gaining information on the structure and its transformations on the atomic level broaden considerably when one invokes computer simulation. Simulations that make use of the molecular dynamics (MD) approach are based on describing the successive motion of atoms in a condensed medium. However, problems also arise here. One of them is associated with the large volume of calculations involved in computer experiments and, as a consequence, with the limited time interval within which the model system is studied. To reduce the real time of the computer experiment, we made use of a well-optimized, highly efficient algorithm developed earlier [4].

Another problem is connected with finding an adequate potential to describe the interaction among atoms of the condensed phase. In the case of iron, the pairwise Pak–Doyama potential [5] proved efficient; this potential was used in the present study.

The computer experiment was aimed at investigating phase transitions between liquid, amorphous, and crystalline iron occurring under ultrafast temperature variation within the interval of 6.6×10^{11} to 4.4×10^{12} K/s.

The results obtained in this work are not restricted to the illustration of first- and second-order phase transitions or to calculations of some thermodynamic parameters. The information obtained on the coordinates of atoms in all stages of their motion in the formation of a new phase provides a basis for the development of a quantitative theory of the nucleation and growth of a new phase and the refinement of macroscopic parameters, which are inherent in the classical theory of nucleation [6].

2. COMPUTER SIMULATION TECHIQUE

The Pak–Doyama empirical pairwise potential is a fourth-degree polynomial [5]:

$$\phi(r) = -0.188917(r-1.82709)^4 + 1.70192(r-2.50849)^2 - 0.198294 \text{ eV}, \quad (1)$$

where r is in Å. The potential cutoff radius (the distance at which the potential and its first derivative vanish smoothly) is $r_c = 3.44$ Å. The parameters of this potential were determined from data on the elastic properties of α-Fe. The simulation of liquid and amorphous iron made with this potential provides good agreement between the calculations and the experimental structural characteristics [7–9].

We first constructed an MD model of liquid iron at $T = 1823$ K with a real density of 7030 kg/m^3 [10]. A bcc lattice was taken as the starting structure. The model contained 2000 atoms in the main cube with periodic boundary conditions. At the initial instant of time, the atoms were imparted velocities according to the Maxwell distribution. The scheme of the MD calculations consisted in numerical integration of the equations of motion with a time step $\Delta t = 1.523 \times 10^{-15}$ s using Verlet's algorithm in the velocity form [11]. The time taken to calculate one step with a Celeron-366 processor was 0.13 s. The melting and relaxation of the system were carried out at the temperature indicated above over 2000 time steps (isothermal conditions). After this, the temperature limitation was removed and thermal equilibrium was established over 4000 time steps at a constant internal energy (adiabatic conditions). Because the density and temperature of the system correspond to liquid iron, the starting configuration, despite the atoms residing at bcc lattice sites, is extremely unstable and the crystal melts in about 10 atomic oscillations ($\sim 600\Delta t$).

The amorphous state was attained through instantaneous quenching [using the static-relaxation (SR) method] of the model melt upon having preliminarily increased its density to 7800 kg/m^3. (Because of the lack of relevant experimental data, the density was chosen from the information available on α-Fe [12], with a 1% correction introduced to account for the amorphization.)

Next, the system was successively heated at three different rates, 6.6×10^{11}, 1.9×10^{12}, and 4.4×10^{12} K/s (the first, second, and third experiments), until complete melting was observed. The cyclic heating procedure consisted in a stepwise increase in temperature of $\Delta T = 20$ K ($T_i = i\Delta T$, where T_i is the environmental temperature in the ith cycle), maintaining this temperature in the system for a time $1000\Delta t$, and subsequent annealing under adiabatic conditions for $19000\Delta t$, $6000\Delta t$, and $2000\Delta t$ in the first, second, and third experiments, respectively. Thus, one cycle lasted $20000\Delta t$, $7000\Delta t$, and $3000\Delta t$ or 3.046×10^{-11}, 1.066×10^{-11}, and 0.457×10^{-11} s, respectively. The thermodynamic characteristics of the system (the temperature T, potential energy U, and the product of pressure multiplied by volume PV) were averaged over the last $16000\Delta t$, $3000\Delta t$, and $1000\Delta t$ in each cycle for the respective temperature variation rates. Note that the temperature T of the system residing under adiabatic conditions and the environmental temperature T_i, strictly speaking, do not coincide. After each cycle, the system was transferred, using the SR method with a constant step of 0.005 Å, to the state with $T = 0$ K to allow the atoms to occupy equilibrium positions in local potential wells. This procedure permitted one to determine the degree of structural relaxation of the model. For statically relaxed models, we also calculated the potential energy U_0 and the product of the pressure by multiplied volume P_0V.

In the first two experiments, the melted system was heated 200 K higher and cooled (quenched) according to the same scheme, with the environmental temperature varied in accordance with the relation $T_i = (2i_{\max} - i)\Delta T$, where $i_{\max}$ is the number of the last heating cycle.

3. RESULTS AND THEIR DISCUSSION

When studied under the conditions of heating at a constant rate of 6.6×10^{11} K/s, the time dependences of T, U, and PV, as well as of U_0 and P_0V, underwent a jump characteristic of a first-order phase transition within the temperature interval 1100–1160 K (Fig. 1).

To establish the structural changes associated with the phase transition, we calculated the atomic radial pair distribution functions (ARPDF) and carried out a statistical–geometric analysis based on the Voronoĭ polyhedra (VP), including the calculation of the angular correlation functions (ACF) describing the distribution of angles between the straight lines passing through the polyhedron center and its two nearest neighbor atoms. The positions of the ARPDF and ACF peaks (Figs. 2, 3, respectively) indicate the formation of a bcc crystalline phase. This is further supported by an

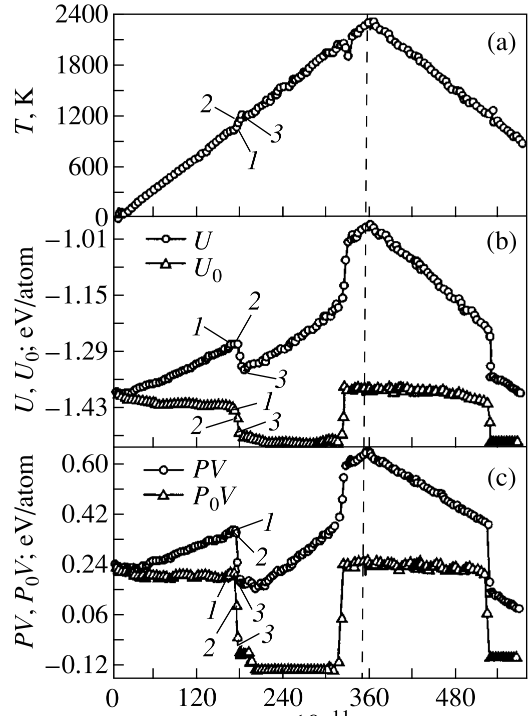

Fig. 1. Time evolution of (a) temperature, (b) potential energy, and (c) product of the pressure multiplied by volume at the running temperature (U, PV) and after static relaxation (U_0, P_0V) of the model iron under heating and cooling at a rate of 6.6×10^{11} K/s (the process starts from the amorphous state). Figures *1*, *2*, and *3* refer to environmental temperatures of 1100, 1120, and 1180 K, respectively. The vertical dashed line separates the heating and cooling runs.

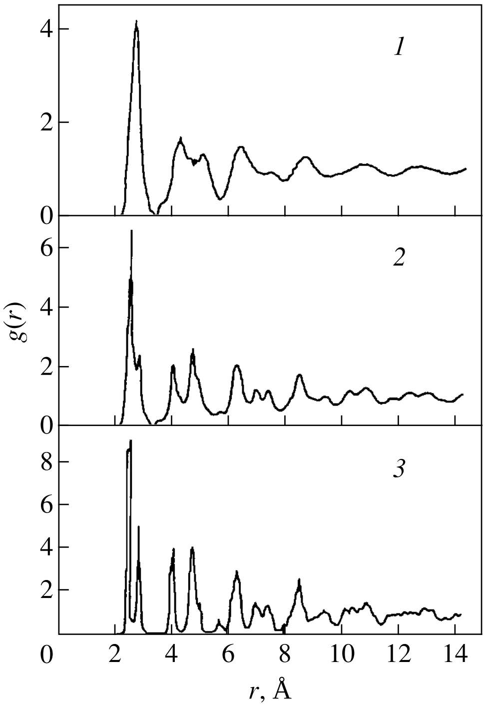

Fig. 2. Atomic radial pair distribution functions in statically relaxed models calculated for environmental temperatures (K) of (*1*) 1100, (*2*) 1120, and (*3*) 1180.

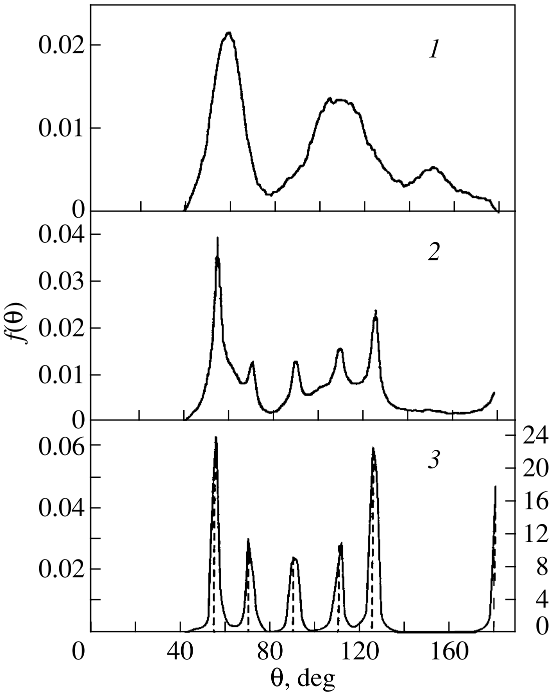

Fig. 3. Angular correlation functions for statically relaxed models calculated for environmental temperatures (K) of (*1*) 1100, (*2*) 1120, and (*3*) 1180. In (*3*), the vertical dashed lines show the distribution of angles in an ideal bcc lattice (right-hand scale).

analysis of the VP-type distribution. Recall that a VP can be described by a set of numbers n_q equal to the number of faces with q sides (n_3–n_4–n_5–…) [13]. After crystallization, the coordination around ~90% of the atoms of the model is characterized by the (0-6-0-8) VP (the cuboctahedron, i.e., the Wigner–Seitz cell of a bcc lattice). Further increase in temperature gives rise to additional ordering of the crystal structure, which ceases at $T \approx 1300$ K. After this, the fraction of the (0-6-0-8) VP atoms can be as high as ~97%. The model iron melted in the temperature interval 2040–2100 K. In the course of the melt cooling run at the same rate, crystallization into a bcc lattice occurred at 1200–1160 K (Fig. 1).

Heat capacity at constant volume for the various structural states of the model iron

Experiment no.	System phase	c_V/k_B	
		heating	cooling
1	Amorphous	3.01 ± 0.02	–
	bcc	3.60 ± 0.04	3.19 ± 0.05
	Melt	4.27 ± 0.02	
2	Amorphous	3.01 ± 0.02	3.16 ± 0.04
	bcc	3.67 ± 0.04	–
	Melt	4.29 ± 0.02	
3	Amorphous	3.01 ± 0.02	–
	Melt	4.39 ± 0.02	–

Increasing the heating rate of the original amorphous-iron model from 6.6×10^{11} to 1.9×10^{12} K/s raises the crystallization temperature (1200–1240 K) by ~100 K and the melting point (2100–2160 K) by ~60 K (Fig. 4). Figure 5 shows the distribution of atoms (after their static relaxation) within an arbitrarily chosen 2.6-Å-thick layer before and after crystallization.

Subsequent cooling of the melt at the same rate did not bring about crystallization; instead, the melt underwent a glass transition. This was indicated by a jump in the heat capacity characteristic of a second-order phase transition (table), which can be determined from the slope of the straight lines approximating the evolution of the potential energy of the system with time (Fig. 4b):

$$c_V = \frac{3}{2}k_B + \left(\frac{\partial U}{\partial T}\right)_V, \qquad (2)$$

where k_B is the Boltzmann constant; $dT \approx \alpha dt$ for the heating and $dT \approx -\alpha dt$ for the cooling (α is the temperature variation rate). Note that Eq. (2) is applicable only above the Debye temperature; for iron, it is valid for $T > 700$ K [9].

As seen from the table, the heat capacity of the melt noticeably exceeds that of the crystalline phase. The

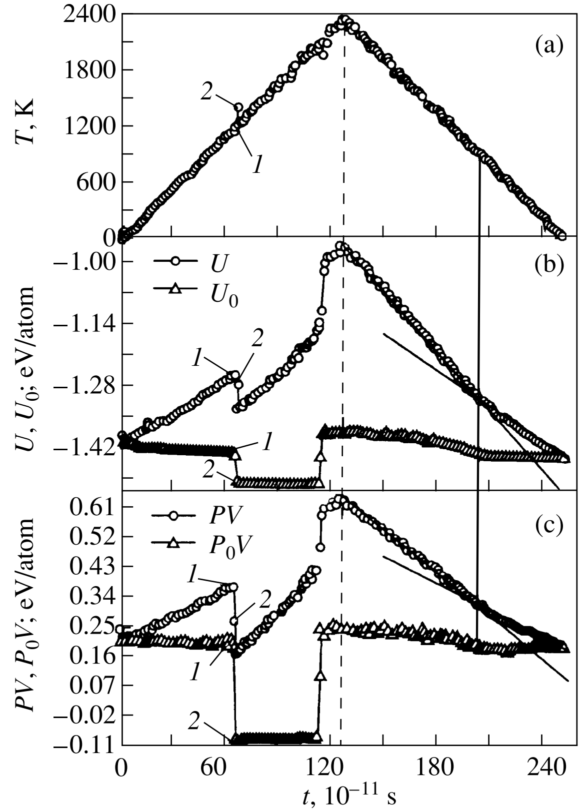

Fig. 4. The evolution of (a) temperature, (b) potential energy, and (c) the product of the pressure multiplied by volume at the running temperature (*U*, *PV*) and after static relaxation (U_0, P_0V) of the model iron under heating and cooling at a rate of 1.9×10^{12} K/s (the process starts from the amorphous state). Figures *1* and *2* refer to environmental temperatures of 1200 and 1240 K, respectively. The vertical dashed line separates the heating and cooling runs.

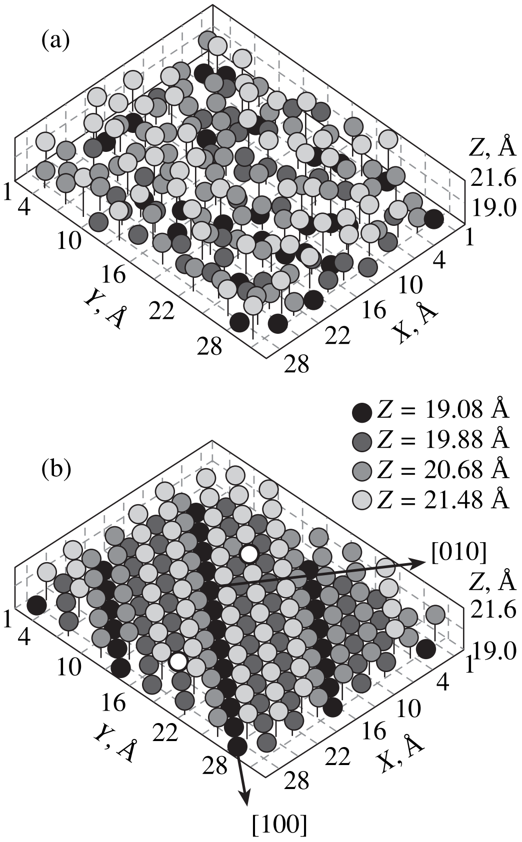

Fig. 5. Atom distribution after static relaxation in an arbitrarily chosen layer 2.6-Å-thick (heating at a rate 1.9×10^{12} K/s): (a) amorphous state, environmental temperature of 1200 K; and (b) crystalline state, environmental temperature of 1240 K. The seven gradations in the atom gray scale code, from black to light gray, identify the variation of the *Z* coordinate from 19 to 21.6 Å with a step $\Delta Z = 2.6/7 \approx 0.37$ Å. The vacant sites in the crystalline phase are encircled in (b).

system does not return to the crystalline phase under cooling, and we assign the change in the slope of the time dependence of the potential energy, which is observed around ~900 K and corresponds to a stepwise decrease in the heat capacity c_V, to the glass transition in the model system. Similar to the heat capacity, the quantity $V(\partial P/\partial T)_V$ also undergoes a jump at the glass transition point (Fig. 4c).

However, during cooling, a crystal nucleus of ~120–130 atoms was formed in the amorphous structure (Fig. 6); its formation started at $T \approx 940$ K with ~30 atoms and became virtually complete at $T \approx 780$ K (Fig. 7). Note that, when crystallization set in throughout the volume of the model iron under heating, more than ~90% of the atoms were (0-6-0-8) VP coordinated.

When the heating rate is further increased to 4.4×10^{12} K/s, amorphous iron transforms into a liquid without passing through the crystalline state, with both c_V and $V(\partial P/\partial T)_V$ undergoing a jump (Figs. 8b, 8c). The time dependences of U_0 and P_0V pass through a minimum ($T \approx 900$–1020 K) without any jumps characteristic of first-order phase transitions (Figs. 8b, 8c). The presence of a minimum in the time dependences of U_0 and P_0V indicates a change in the atom motion from the activated to the activation-free mechanism, the latter being characteristic of atomic diffusion in a liquid.

As follows from an analysis of the data in the table, the values of the heat capacity of the original amorphous phase produced by instantaneous melt quenching, which were calculated for different heating rates (the first, second, and third experiments), coincide well with one another, while being slightly smaller than that of the amorphous phase obtained by cooling the melt at a rate of 1.9×10^{12} K/s. This difference can be assigned to the fact that heating of the original nonequilibrium amorphous phase gives rise to intense structural relaxation, which is indicated by a decrease in the potential energy U_0 of statically relaxed models (Figs. 1b, 4b, 8b), whereas amorphization by melt quenching at a rate of 1.9×10^{12} K/s virtually does not entail any structural relaxation (Fig. 4b). Correcting the temperature dependence of the potential energy *U* in the case of heating of

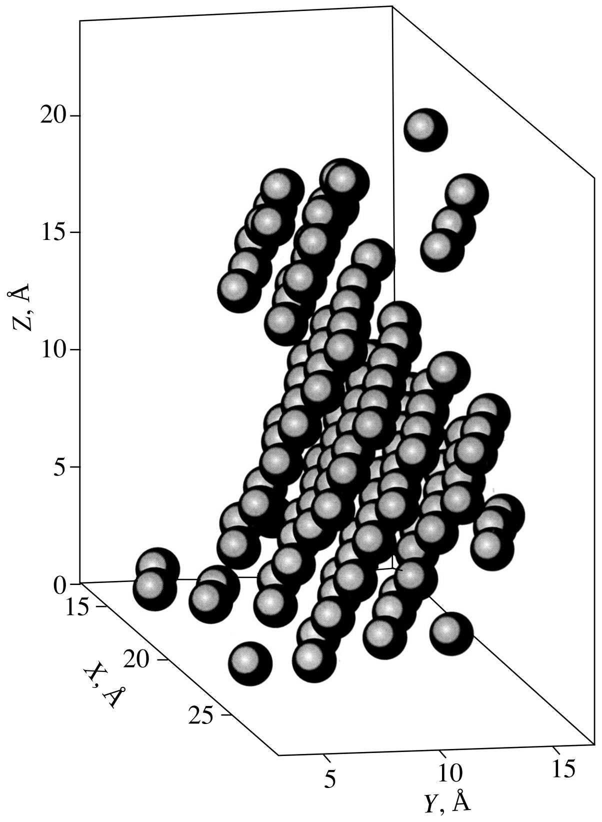

Fig. 6. Atom arrangement in the crystalline nucleus (121 atom) frozen by cooling at a rate of 1.9×10^{12} K/s.

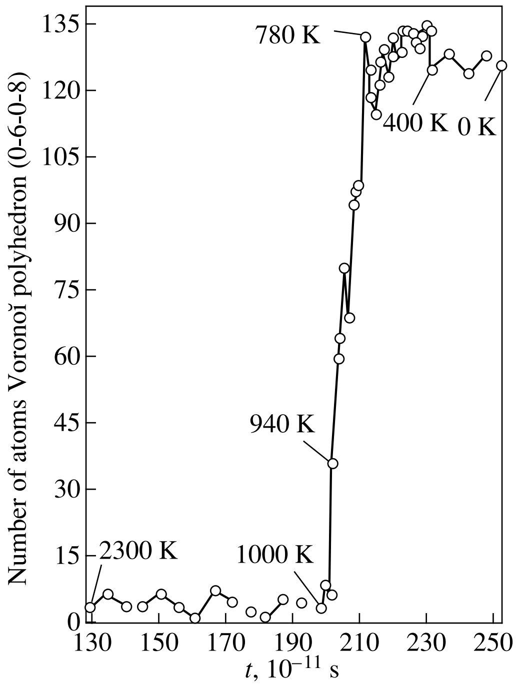

Fig. 7. Variation of the number of atoms with (0-6-0-8) VP in the course of cooling at a rate of 1.9×10^{12} K/s. The figures specify the environmental temperature. The points are spaced at 100 K within the 2300–1000 and 400–0 K intervals, and at 20 K in the 1000–400-K interval. At 940 K, 30 atoms out of 37 are located in one nucleus.

the original amorphous iron model to the magnitude of the thermal effect associated with structural relaxation, which can be estimated from the change in the potential energy U_0 (Figs. 1b, 4b, 8b for the first, second, and third experiments, respectively), increases the heat capacity to the value that is observed for the amorphous phase produced by melt quenching at a rate of 1.9×10^{12} K/s.

The results obtained permitted us to estimate the stability of the iron amorphous state and to determine the activation energy for homogeneous nucleation of a crystal in the volume of the amorphous phase.

Metal glass (MG) produced by ultrafast quenching of a liquid forms a set of unstable (defect) atomic configurations characteristic of the given MG type, which relax through rearrangement with increasing temperature. The process of rearrangement of the structure, which was termed structural relaxation, is characterized by a continuous spectrum of activation energies, whose maximum value corresponds to the energy of formation of a crystalline nucleus.

In this case, the annealing process can be studied using a model involving an activation energy spectrum [14]. Processes involving relaxation centers with distributed activation energies are conventionally analyzed using the rate equation for the reaction:

$$\frac{dn}{dt} = -n\nu \exp\left(-\frac{E}{k_B T}\right), \tag{3}$$

where $n(E, t)$ is the spectral density of relaxation centers with an activation energy E and ν is of the order of the Debye frequency ($\sim 10^{13}$ s^{-1}). By integrating this equation in the case of heating from 0 K at a constant rate α ($T = \alpha t$), one can follow the variation of the spectral density of states with time:

$$n(E, t) = n_0(E) \exp\left[-\nu \int_0^t \exp\left(-\frac{E}{k_B \alpha t}\right) dt\right], \tag{4}$$

where $n_0(E)$ is the energy spectrum of the relaxation centers created in the course of metal glass formation.

According to the principle of superposition, the total concentration of the relaxation centers can be written as

$$N(t) = \int_0^\infty n_0(E) \Theta(E, t) dE, \tag{5}$$

where

$$\Theta(E, t) = \exp\left[-\nu \int_0^t \exp\left(-\frac{E}{k_B \alpha t}\right) dt\right]. \tag{6}$$

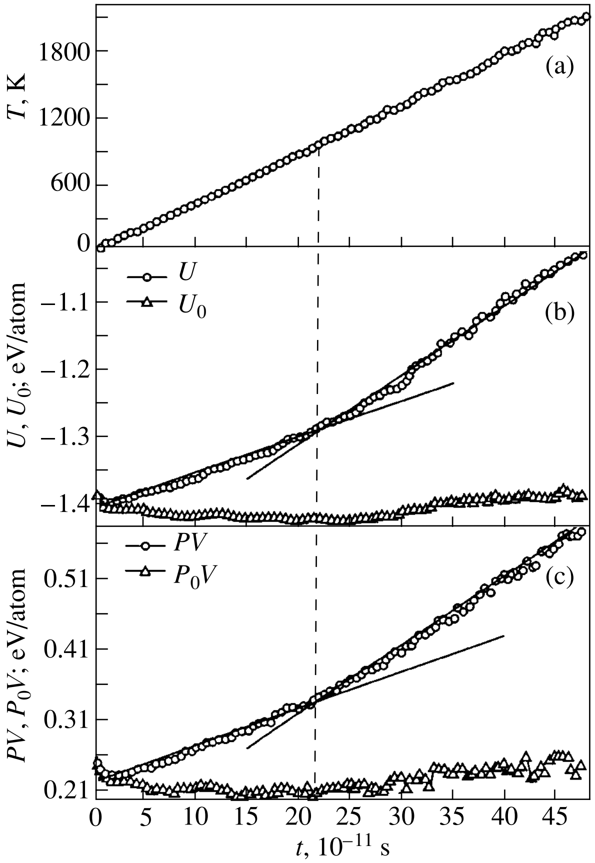

Fig. 8. Time evolution of (a) temperature, (b) potential energy, and (c) the product of the pressure multiplied by volume at the running temperature (U, PV) and after static relaxation (U_0, P_0V) of the model iron under heating at a rate of 4.4×10^{12} K/s (the process starts from the amorphous state).

The quantity $\Theta(E, t)$ is called the characteristic function of linear heating. If the $n_0(E)$ function is smooth enough, i.e., if it varies with E much more slowly than the exponential function $\Theta(E, t)$, the annealing process is determined by the exponential term. In the course of annealing, the $\Theta(E, t)$ curve shifts along the E axis practically without changing its stepwise shape; that is, it rises sharply from zero to unity near the inflection point [15]. The characteristic activation energy E_0 corresponding to the inflection point on the $\Theta(E, t)$ curve and, hence, to the maximum rate of the thermally activated processes can be derived from the condition

$$\frac{\partial^2 \Theta(E, t)}{\partial E^2} = 0. \tag{7}$$

The activation energy E_0 corresponding to this point can be represented as a function of temperature in the form

$$T = \frac{\alpha}{\nu} \frac{\exp(-x)}{x[-Ei(-x)]^2}, \quad E_0 = x k_B T, \tag{8}$$

where

$$-Ei(-x) = \int_x^{\infty} \frac{\exp(-x)}{x} dx \tag{9}$$

is the integral exponent. As seen from the definition of the characteristic energy E_0, practically all atomic configurations with activation energies $E \le E_0$ will have relaxed by the time t.

The calculation performed in terms of the described model has shown that the activation energy of homogeneous formation of a crystalline nucleus in the volume of the iron amorphous phase is 0.72 eV in the first experiment (6.6×10^{11} K/s, 1120 K) and 0.7 eV in the second experiment (1.9×10^{12} K/s, 1220 K).

ACKNOWLEDGMENTS

This study was supported by the “Integration” Program, grant no. A-0032.

REFERENCES

1. K. Suzuki, H. Fujimori, and K. Hashimoto, *Amorphous Metals* (Tokyo, 1982; Metallurgiya, Moscow, 1987), translated from Japanese.
2. T. Ichikawa, Phys. Status Solidi A **19**, 707 (1973).
3. P. K. Leung and J. G. Wright, Philos. Mag. B **30** (5), 995 (1974).
4. A. V. Evteev and A. T. Kosilov, Vestn. Voronezh. Gos. Tekh. Univ., Ser. Materialoved. **1** (4), 4 (1998).
5. H. M. Pak and M. Doyama, J. Fac. Eng., Univ. Tokyo B **30**, 110 (1969).
6. J. W. Christian, *Theory of Transformations in Metals and Alloys* (Pergamon, Oxford, 1975; Mir, Moscow, 1978), Part 1.
7. R. Yamamoto, H. Matsuoka, and M. Doyma, Phys. Status Solidi A **45**, 305 (1978).
8. D. K. Belashchenko, Fiz. Met. Metalloved. **60** (6), 1076 (1985).
9. A. V. Evteev and A. T. Kosilov, Rasplavy, No. 1, 55 (1998).
10. A. A. Vertman and A. M. Samarin, *Properties of Melts of Iron* (Nauka, Moscow, 1969).
11. L. Verlet, Phys. Rev. **159**, 98 (1967).
12. C. J. Smithells, *Metals Reference Book* (Butterworths, London, 1976; Metallurgiya, Moscow, 1980).
13. J. L. Finney, J. Comput. Phys. **32** (1), 137 (1979).
14. W. Primak, Phys. Rev. **100** (6), 167 (1955).
15. V. I. Belyavskiĭ, O. P. Bobrov, A. T. Kosilov, and V. A. Khonik, Fiz. Tverd. Tela (St. Petersburg) **38** (1), 30 (1996) [Phys. Solid State **38**, 16 (1996)].

Translated by G. Skrebtsov

Physics of the Solid State, Vol. 43, No. 12, 2001, pp. 2290–2300. Translated from Fizika Tverdogo Tela, Vol. 43, No. 12, 2001, pp. 2198–2208.
Original Russian Text Copyright © 2001 by Zinenko, Zamkova.

Lattice Dynamics and Statistical Mechanics of the $Fm3m \longrightarrow I4/m$ Structural Phase Transition in Rb_2KInF_6

V. I. Zinenko and N. G. Zamkova
Kirensky Institute of Physics, Siberian Division, Russian Academy of Sciences,
Akademgorodok, Krasnoyarsk, 660036 Russia
e-mail: zvi@iph.krasn.ru

Received May 7, 2001

Abstract—The static and dynamic properties of cubic Rb_2KInF_6 crystals with elpasolite structure are calculated using a nonempirical method. Calculations are performed within a microscopic ionic-crystal model taking into account the deformation and polarization of ions. The deformation parameters of ions are determined by minimizing the total energy of the crystal. The calculated equilibrium lattice parameters agree satisfactorily with the experimental data. It is found that in the cubic phase there are vibrational modes that are unstable everywhere in the Brillouin zone. The eigenvectors of the unstablest mode at the center of the Brillouin zone of the cubic phase are associated with the displacements of F ions and correspond to rotations of InF_6 octahedra. Condensation of this mode leads to a tetragonal distortion of the structure. In order to describe the $Fm3m \longrightarrow I4/m$ phase transition, an effective Hamiltonian is constructed under the assumption that the soft mode whose eigenvector corresponds to octahedron rotation is local and coupled with homogeneous elastic strains. The parameters of the effective Hamiltonian are determined using the calculated crystal energy for the distorted structures due to soft-mode condensation. The thermodynamic properties of the system with this model Hamiltonian are investigated using the Monte Carlo method. The phase transition temperature is calculated to be 550 K, which is twice its experimental value (283 K). The tetragonal phase remains stable down to $T = 0$ K; the effective Hamiltonian used in this paper thus fails to describe the second phase transition (to the monoclinic phase). Thus, the transition to the tetragonal phase occurs for the most part through octahedron rotations; however, additional degrees of freedom, first of all, the displacements of Rb ions, should be included into the effective Hamiltonian in order to describe the transition to the monoclinic phase. *© 2001 MAIK “Nauka/Interperiodica”.*

1. INTRODUCTION

Halides with the elpasolite structure $A_2BB^{3+}X_6$ undergo a wide variety of structural phase transitions associated with lattice instability in the high-symmetry cubic phase. In the lower temperature phases, these compounds show either homogeneous nonpolar distortions of the lattice or distortions that are accompanied by a change in the unit-cell volume of the crystal. In most crystals of this family, structural distortions are associated either with rotations of the octahedra $B^{3+}X_6$ or with a combination of octahedron rotations and *A*-atom displacements.

Instability of the crystal lattice against normal vibrations involving octahedron rotations is likely a characteristic feature of perovskite-like compounds. In most halides and some oxides with perovskite structure, this instability leads to structural phase transitions to a lower symmetry phase, which are accompanied by an increase in the unit-cell volume in comparison with that of the initial cubic phase.

The problem of instability of the perovskite structure against distortions corresponding either to the ferroelectric lattice vibration mode or to octahedron rotations has been discussed in experimental and theoretical studies for several decades. In recent years, many papers have been published in which, using the density-functional method, the electronic band structure and lattice vibration frequencies were calculated and the statistical mechanics of phase transitions for some perovskites were considered. Those calculations have given some insight into the source of crystal lattice instability and the nature of ferroelectricity and antiferroelectricity in oxides with perovskite structure (see, e.g., [1–4]).

For crystals with elpasolite structure, scarcely any calculations of the crystal lattice vibration spectrum exist. At the same time, these crystals have been intensely studied experimentally using various methods and, at the present time, there do exist data on the structures of the low-symmetry phases, physical properties, and the effect of phase transitions on them for many of these crystals (see, e.g., the recent review [5]).

The Rb_2KInF_6 crystal belongs to the elpasolite family; its high-symmetry phase has a cubic crystal structure with one molecule per unit cell (Fig. 1) and belongs to the space group $Fm3m$. As the temperature decreases, Rb_2KInF_6 undergoes two subsequent structural phase transitions: one to a tetragonal phase (space

1063-7834/01/4312-2290$21.00 © 2001 MAIK “Nauka/Interperiodica”

group $I4/m$) with the same unit-cell volume as that in the cubic phase (at T_{c1}= 283 K) and another to a monoclinic phase (space group $P12_1/n1$) with two molecules per unit cell (at T_{c2}= 264 K). Structural studies of the low-symmetry phases of the isomorphic compound Rb_2KScF_6 have revealed [5] that the distortions of the cubic structure in the tetragonal phase are associated, for the most part, with ScF_6 octahedron rotations, which are homogeneous over the entire crystal. The distortions in the lower temperature monoclinic phase are associated with inhomogeneous rotations of ScF_6 octahedra and with displacements of Rb ions from their equilibrium positions in the tetragonal phase. It should be noted that in the series of isomorphic compounds Rb_2KMF_6 (M = Ga, Sc, In, Lu), the phase transition temperature from the cubic phase increases with the size of the trivalent ion M.

Earlier, we calculated the entire lattice vibration spectra of the Rb_2KScF_6 crystal in the unstable cubic and tetragonal phases and the stable monoclinic phase [6] within the Gordon–Kim model generalized by Ivanov and Maksimov [7] to the case of deformable and polarizable ions. Using an effective Hamiltonian in which the coupling constants were calculated without fitting parameters, we described the $Fm3m \longrightarrow I4/m$ phase transition in this compound [8]. The calculated phase transition temperature and the physical properties in the vicinity of the phase transition point were found to agree well with the experimental data.

The objective of this paper is to calculate the equilibrium volume, the entire lattice vibration spectrum, and the high-frequency dielectric constant of Rb_2KInF_6 in the cubic phase from first principles and to determine the parameters of the effective Hamiltonian that describes the $Fm3m \longrightarrow I4/m$ phase transition in this compound. We also investigate the thermodynamic properties of the phase transition using the Monte Carlo (MC) method.

In Section 2, we describe the model and the method for calculating the total energy, the frequencies of normal lattice vibrations, the dynamic charges, and the high-frequency dielectric constant. The results from calculations of the lattice dynamics of the Rb_2KInF_6 crystal are presented in Section 3. In Section 4, we discuss the effective Hamiltonian, which includes the minimum number of degrees of freedom (more specifically, the local mode corresponding to InF_6 octahedron rotations) and homogeneous elastic strains and calculate the parameters of the model Hamiltonian. Some details of the investigation of the thermodynamic behavior of the system with this model Hamiltonian (using the Monte Carlo algorithm), as well as the results of calculations and their discussion, are presented in Section 5.

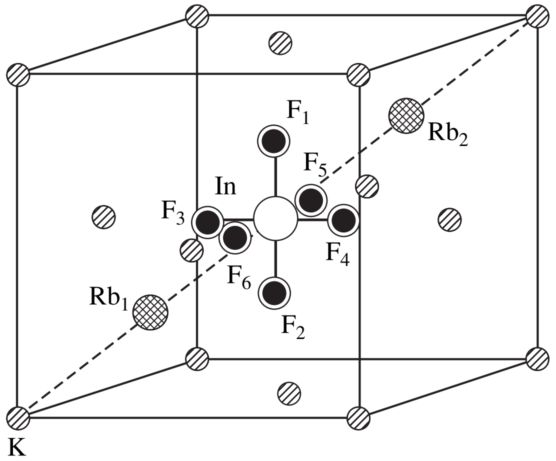

Fig. 1. Crystalline structure of Rb_2KInF_6 in the cubic phase. One molecule and a unit cell of the fcc K lattice are shown. The six Rb ions of the other three molecules are situated at 1/4 and 3/4 lengths of the three other cube body diagonals. The remaining In ions are located at the midpoints of the cube edges. Each In ion is surrounded by six F ions.

2. MODEL AND CALCULATION TECHNIQUE

In order to calculate the lattice vibration spectrum of the $RbKInF_6$ crystal, we use the ionic-crystal model proposed by Ivanov and Maksimov [7]. In this model, the ionic crystal consists of overlapping individual spherically symmetric polarizable ions. The total electronic density of the crystal is written as

$$\rho(\mathbf{r}) = \sum_i \rho_i(\mathbf{r}-\mathbf{R}_i),$$

where summation is carried out over all ions of the crystal. In the density-functional theory, the total crystal energy including only pairwise interaction has the form

$$E_{\mathrm{cr}} = \frac{1}{2}\sum_{i\neq j}\frac{Z_iZ_j}{|\mathbf{R}_i-\mathbf{R}_j|} + \sum_i E_i^{\mathrm{self}}(R_{\mathrm{W}}^i) + \frac{1}{2}\sum_{i\neq j}\Phi_{ij}(R_{\mathrm{W}}^i, R_{\mathrm{W}}^j, |\mathbf{R}_i-\mathbf{R}_j|), \quad (1)$$

where Z_i is the charge of the ith ion,

$$\Phi_{ij}(R_{\mathrm{W}}^i, R_{\mathrm{W}}^j, |\mathbf{R}_i-\mathbf{R}_j|) = E\{\rho_i(\mathbf{r}-\mathbf{R}_i) + \rho_j(\mathbf{r}-\mathbf{R}_j)\} - E\{\rho(\mathbf{r}-\mathbf{R}_i)\} - E\{\rho(\mathbf{r}-\mathbf{R}_j)\}, \quad (2)$$

the energy $E\{\rho\}$ is calculated using the density-functional method and the local approximation to the kinetic and exchange-correlation energies, and $E_i^{\mathrm{self}}(R_{\mathrm{W}}^i)$ is the self-energy of the ion. The electronic density of an individual ion and its self-energy are cal-

Table 1. Calculated and experimental [11] atomic coordinates and lattice parameters

Atom	Position	Occupancy	$a_0 = 8.84$ Å			$a_{\text{exp}} = 9.10$ Å		
			x/a_0	y/a_0	z/a_0	x/a_{exp}	y/a_{exp}	z/a_{exp}
Rb	8*c*	1	0.25	0.25	0.25	0.25	0.25	0.25
K	4*b*	1	0.50	0.50	0.50	0.50	0.50	0.50
In	4*a*	1	0.0	0.0	0.0	0.0	0.0	0.0
F	24*e*	1	0.23	0.0	0.0	0.222	0.0	0.0

culated using the crystal potential as approximated by a charged sphere (the Watson sphere):

$$V(r) = \begin{cases} Z_i^{\text{ion}}/R_{\text{W}} & r < R_{\text{W}} \\ Z_i^{\text{ion}}/r & r > R_{\text{W}}, \end{cases}$$

where R_{W} is the radius of the Watson sphere. The radii R_{W}^i for individual ions are found by minimizing the total energy of the crystal. When calculating the lattice dynamics, the terms describing the changes in energy due to the displacements of ions from their equilibrium positions should be included in the crystal energy in Eq. (2). The dynamic matrix which includes the electronic polarization of the ions and the ionic deformation caused by the crystal field for crystals of arbitrary symmetry in the model used here is written out in [9]. In calculating the lattice vibration frequencies of Rb_2KInF_6 and when classifying the vibrational modes by their symmetry, we use the results of [9].

The Coulomb interaction contribution to the dynamic matrix is calculated using the Ewald method. The ionic parameters are determined using the algorithm developed by Liberman *et al.* [10]. The pairwise interaction energy in Eq. (2) and the ionic polarizability are calculated using the technique developed by Ivanov and Maksimov [7], with the kinetic energy taken in the Thomas–Fermi approximation and with the exchange-correlation energy calculated in the Hedin–Lundqvist approximation. In calculating the derivatives involved in the dynamic matrix, the dependences of the energy on the distances R and the Watson sphere potentials V are approximated by Chebyshev polynomials.

Table 2. Ionic polarizabilities, high-frequency dielectric constants, and dynamic charges

Atom	$\varepsilon_\infty = 1.86$			
	α, Å^3	Z_{xx}	Z_{yy}	Z_{zz}
Rb	1.39	1.24	1.24	1.24
K	0.74	1.17	1.17	1.17
In	0.37	3.02	3.02	3.02
F_1	0.82	–1.03	–1.03	–1.28
F_2	0.82	–1.03	–1.28	–1.03
F_3	0.82	–1.28	–1.03	–1.03

3. LATTICE VIBRATION SPECTRUM

In this section, we present the results of calculations of the equilibrium volume, the dielectric constant, the dynamic charges, and the lattice vibration spectra of the Rb_2KInF_6 crystal in the cubic phase.

The equilibrium lattice parameter and the positions of the atoms in a unit cell were determined by minimizing the total crystal energy as a function of volume. The calculated lattice parameter and coordinates of the ions, as well as their experimental values, are presented in Table 1. It is seen that the calculated values coincide with the experimental values to within 4%. The radii of the Watson spheres for Rb^+, K^+, In^{3+}, and F^- ions found by minimizing the total energy are 2.125, 2.5625, 3.5, and 2.625 a.u., respectively. The calculated values of the polarizabilities of the ions, high-frequency dielectric constant, and dynamic ionic charges of the crystal under study are listed in Table 2.

The calculated dispersion curves of the lattice vibration frequencies of Rb_2KInF_6 in the cubic phase are shown in Fig. 2, and Table 3 lists the limiting vibration frequencies (at $q = 0$) and the frequencies of some Raman-active vibration modes measured in [11]. It can be seen that the calculated limiting frequencies of Raman-active modes are 10–20% lower than the experimental values.

It is also seen from Fig. 2 and Table 3 that there are imaginary vibration frequencies, which is indicative of structural instability of the cubic phase of the crystal. It should be emphasized that unstable modes arise everywhere in the Brillouin zone (BZ) and that their frequencies at symmetry points of the BZ are comparable in absolute value. Since the experimentally observed phase transitions in the Rb_2KInF_6 crystal are associated with instability of vibrational modes at the center and at the boundary point X of the BZ, we will discuss only the vibrational modes at these points. At the center of the BZ, three modes become unstable in the cubic structure. The strongest instability (for which the square of the normal-mode frequency is negative and

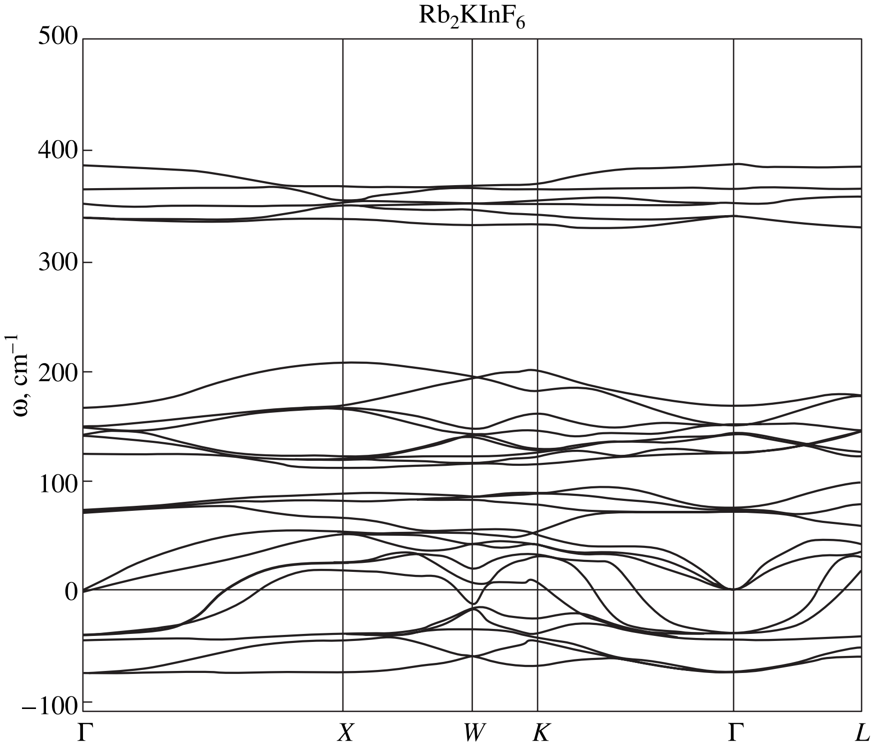

Fig. 2. Dispersion curves of the vibrational modes of the Rb_2KInF_6 crystal in the cubic phase. Negative values correspond to imaginary frequencies.

has a maximum absolute value) is associated with the threefold degenerate T_{1g} mode, in which only four F atoms are displaced from their equilibrium positions [9, 12]. As a result of these displacements, the InF_6 octahedron is rotated as a whole. Another (ferroelectric) unstable mode is the transverse polar mode T_{1u}, in which all atoms in a unit cell are displaced from their equilibrium positions in the cubic phase. However, to our knowledge, ferroelectric phase transitions have not been observed experimentally in halide crystals with elpasolite structure. Finally, the third unstable mode is the threefold degenerate T_{2g} mode. One of the eigenvectors of this mode corresponds to rotation of the InF_6 octahedron about a cube body diagonal and to simultaneous displacements of the Rb atoms situated on this diagonal toward each other. It should be noted that in the vibration spectrum of the crystal under study, there is also a stable mode of the same symmetry, T_{2g} (Table 3).

At point X on the BZ boundary, the strongest lattice instability is associated with the nondegenerate X_2^+ mode, in which the displacements of the four F ions ($F_{3y} = -F_{4y} = F_{5z} = -F_{6z}$) also correspond to rotation of the InF_6 octahedron as a whole. However, the rotations are inhomogeneous over the crystal and condensation of this mode leads to doubling of the unit-cell volume. As indicated in the introduction, when the temperature is decreased, the crystal first undergoes the transition to the tetragonal phase, which is associated with condensation of the soft T_{1g} mode at the center of the BZ.

Table 3. Limiting $q = 0$ vibration frequencies (cm^{-1}) in the cubic phase

ω_i	Cubic phase			
	degeneracy	vibrational mode	frequency	[11]
ω_1	3	T_{1g}	74i	
ω_{2T}	2	T_{1u}	44i	
ω_3	3	T_{2g}	39i	80
ω_4	3	T_{1u}	0	
ω_{2L}	1	T_{1u}	71	
ω_5	3	T_{2u}	74	
ω_{6T}	2	T_{1u}	125	
ω_7	3	T_{2g}	142	210
ω_{6L}	1	T_{1u}	149	
ω_{8T}	2	T_{1u}	149	
ω_{8L}	1	T_{1u}	167	
ω_9	2	E_g	340	380
ω_{11}	1	A_{1g}	365	510
ω_{10T}	2	T_{1u}	352	
ω_{10L}	1	T_{1u}	386	

4. DERIVATION OF THE EFFECTIVE HAMILTONIAN AND CALCULATION OF ITS PARAMETERS

The effective model Hamiltonian in the local-mode approximation [13] has been used in several publications to describe ferroelectric and structural phase transitions in the diatomic compound GeTe [14] and oxides with perovskite structure [1–4]. When deriving the model Hamiltonian, we used the scheme proposed in [3, 4, 14].

In the threefold degenerate T_{1g} vibrational mode at $q = 0$ and the nondegenerate vibrational modes along the lines going through the center of the BZ and one of the points X, Y, or Z on the BZ boundary, only F ions are displaced and their displacements v_k^E in these modes are subject to the relations

$$T_{1g}: \begin{cases} -v_{1y}^F = v_{2y}^F = v_{5z}^F = -v_{6z}^F \\ -v_{1x}^F = v_{2x}^F = -v_{3z}^F = v_{4z}^F \\ -v_{3y}^F = v_{4y}^F = -v_{5x}^F = v_{6x}^F \end{cases}$$

$$X_3: -v_{1y}^F = v_{2y}^F = v_{5z}^F = -v_{6z}^F, \quad (3)$$

$$Y_3: -v_{1x}^F = v_{2x}^F = -v_{3z}^F = v_{4z}^F,$$

$$Z_3: -v_{3y}^F = v_{4y}^F = -v_{5x}^F = v_{6x}^F.$$

These F-ion displacements lead to rotation of the InF_6 octahedron. We derive the model Hamiltonian in the local-mode approximation and take into account only the modes in Eq. (3); the other modes are assumed to be insignificant in the structural transition from the cubic to the tetragonal phase. Thus, for Rb_2KInF_6, a local mode is assumed to have the form

$$S_\alpha = \frac{1}{a_0}\sum_k \xi_{\alpha k} v_k^F, \quad (4)$$

where $\alpha = x, y, z$; v_k^F is the oscillation amplitude of the kth F ion given by Eq. (3); $\xi_{\alpha k}$ are the eigenvectors of a lattice vibrational mode; and $a_0 = 16.71$ a.u. is the lattice parameter in the cubic phase. The vectors ξ are presented in Table 4.

Under the symmetry operations of the high-symmetry cubic phase, the local mode (S_x, S_y, S_z) is transformed as a pseudovector. Thus, in order to construct the effective Hamiltonian that describes the structural phase transition $Fm3m \longrightarrow I4/m$, we proceed as follows. The three-component local mode (pseudovector) is placed at sites of an fcc lattice. For the sake of simplicity, anharmonicity is taken into account in the effective Hamiltonian only through the single-site potential, which contains all second- and fourth-order terms and some anisotropic terms of the sixth order. Pairwise interaction between the local modes at different sites is included only for the nearest and next-to-nearest neighbor sites. The interaction between the local mode and spatially homogeneous elastic strains is also allowed for. Thus, taking into account the transformation properties of the local mode and the fcc lattice under cubic-symmetry operations, the microscopic model Hamiltonian is written as [8]

$$H = \sum_i (H_i^{\text{anh}} + H_i^{SS}) + H^{Se} + H^{ee},$$

$$H_i^{\text{anh}} = B(S_{ix}^4 + S_{iy}^4 + S_{iz}^4) + C(S_{ix}^2 S_{iy}^2 + S_{iy}^2 S_{iz}^2 + S_{iz}^2 S_{ix}^2) + D(S_{ix}^6 + S_{iy}^6 + S_{iz}^6), \quad (5)$$

$$H_i^{SS} = S_{ix}\Bigg[AS_{ix} + a_1 \sum_{\mathbf{d} = (0, \pm1, \pm1)} S_x\left(\mathbf{R}_i + \frac{a_0\mathbf{d}}{2}\right) + a_2 \sum_{\mathbf{d} = \left(\begin{smallmatrix}\pm1, \pm1, 0 \\ \pm1, 0, \pm1\end{smallmatrix}\right)} S_x\left(\mathbf{R}_i + \frac{a_0\mathbf{d}}{2}\right)$$

$$+ a_3 \sum_{\mathbf{d} = (\pm1, 0, \pm1)} (\mathbf{d}\cdot\mathbf{z})(\mathbf{d}\cdot\mathbf{x}) S_z\left(\mathbf{R}_i + \frac{a_0\mathbf{d}}{2}\right) + a_3 \sum_{\mathbf{d} = (\pm1, \pm1, 0)} (\mathbf{d}\cdot\mathbf{y})(\mathbf{d}\cdot\mathbf{x}) S_y\left(\mathbf{R}_i + \frac{a_0\mathbf{d}}{2}\right)\Bigg]$$

$$+ S_{iy}\Bigg[AS_{iy} + a_1 \sum_{\mathbf{d} = (\pm1, 0, \pm1)} S_y\left(\mathbf{R}_i + \frac{a_0\mathbf{d}}{2}\right)$$

Table 4. Eigenvectors of the threefold degenerate vibrational mode T_{1g}

Components	Rb1	Rb2	F1	F2	F3	F4	F5	F6	K	In
ξ_x	000	000	$0-\frac{1}{2}0$	$0\frac{1}{2}0$	000	000	$00\frac{1}{2}$	$00-\frac{1}{2}$	000	000
ξ_y	000	000	$-\frac{1}{2}00$	$\frac{1}{2}00$	$00-\frac{1}{2}$	$00\frac{1}{2}$	000	000	000	000
ξ_z	000	000	000	000	$0-\frac{1}{2}0$	$0\frac{1}{2}0$	$-\frac{1}{2}00$	$\frac{1}{2}00$	000	000

$$+ a_2 \sum_{\mathbf{d} = \left(\begin{smallmatrix}\pm1,\, \pm1,\, 0\\ 0,\, \pm1,\, \pm1\end{smallmatrix}\right)} S_y\left(\mathbf{R}_i + \frac{a_0\mathbf{d}}{2}\right)$$

$$+ a_3 \sum_{\mathbf{d} = (0,\, \pm1,\, \pm1)} (\mathbf{d}\cdot\mathbf{z})(\mathbf{d}\cdot\mathbf{y}) S_z\left(\mathbf{R}_i + \frac{a_0\mathbf{d}}{2}\right)$$

$$+ a_3 \sum_{\mathbf{d} = (\pm1,\, \pm1,\, 0)} (\mathbf{d}\cdot\mathbf{x})(\mathbf{d}\cdot\mathbf{y}) S_x\left(\mathbf{R}_i + \frac{a_0\mathbf{d}}{2}\right)\Bigg]$$

$$+ S_{iz}\Bigg[AS_{iz} + a_1 \sum_{\mathbf{d} = (\pm1,\, \pm1,\, 0)} S_z\left(\mathbf{R}_i + \frac{a_0\mathbf{d}}{2}\right)$$

$$+ a_2 \sum_{\mathbf{d} = \left(\begin{smallmatrix}\pm1,\, 0,\, \pm1\\ 0,\, \pm1,\, \pm1\end{smallmatrix}\right)} S_z\left(\mathbf{R}_i + \frac{a_0\mathbf{d}}{2}\right)$$

$$+ a_3 \sum_{\mathbf{d} = (0,\, \pm1,\, \pm1)} (\mathbf{d}\cdot\mathbf{y})(\mathbf{d}\cdot\mathbf{z}) S_x\left(\mathbf{R}_i + \frac{a_0\mathbf{d}}{2}\right)$$

$$+ a_3 \sum_{\mathbf{d} = (\pm1,\, 0,\, \pm1)} (\mathbf{d}\cdot\mathbf{x})(\mathbf{d}\cdot\mathbf{z}) S_y\left(\mathbf{R}_i + \frac{a_0\mathbf{d}}{2}\right)\Bigg]$$

$$+ S_{ix}\Bigg[b_1 \sum_{\mathbf{d} = (\pm1,\, 0,\, 0)} S_x(\mathbf{R}_i + a_0\mathbf{d})$$

$$+ b_2 \sum_{\mathbf{d} = \left(\begin{smallmatrix}0,\, \pm1,\, 0\\ 0,\, 0,\, \pm1\end{smallmatrix}\right)} S_x(\mathbf{R}_i + a_0\mathbf{d})\Bigg]$$

$$+ S_{iy}\Bigg[b_1 \sum_{\mathbf{d} = (0,\, \pm1,\, 0)} S_y(\mathbf{R}_i + a_0\mathbf{d})$$

$$+ b_2 \sum_{\mathbf{d} = \left(\begin{smallmatrix}\pm1,\, 0,\, 0\\ 0,\, 0,\, \pm1\end{smallmatrix}\right)} S_y(\mathbf{R}_i + a_0\mathbf{d})\Bigg]$$

$$+ S_{iz}\Bigg[b_1 \sum_{\mathbf{d} = (0,\, 0,\, \pm1)} S_z(\mathbf{R}_i + a_0\mathbf{d})$$

$$+ b_2 \sum_{\mathbf{d} = \left(\begin{smallmatrix}\pm1,\, 0,\, 0\\ 0,\, \pm1,\, 0\end{smallmatrix}\right)} S_z(\mathbf{R}_i + a_0\mathbf{d})\Bigg],$$

$$H^{Se} = \sum_i \Bigg\{ g_1(e_1 + e_2 + e_3)(S_{ix}^2 + S_{iy}^2 + S_{iz}^2)$$

$$+ g_2\Big[(e_1 + e_2 - 2e_3)(S_{ix}^2 + S_{iy}^2 - 2S_{iz}^2)$$

$$+ 3(e_1 - e_2)(S_{ix}^2 - S_{iy}^2)\Big]$$

$$+ g_3(e_4S_{iy}S_{iz} + e_5S_{ix}S_{iz} + e_6S_{ix}S_{iy})\Bigg\},$$

$$H^{ee} = C_{11}(e_1^2 + e_2^2 + e_3^2) + C_{12}(e_1e_2 + e_2e_3 + e_3e_1) + C_{44}(e_4^2 + e_5^2 + e_6^2).$$

The elastic strains e_i are written in Voigt notation as

$$e_1 = u_{11}, \quad e_2 = u_{22}, \quad e_3 = u_{33},$$
$$e_4 = 2u_{23}, \quad e_5 = 2u_{13}, \quad e_6 = 2u_{12},$$
$$u_{ij} = (\partial u_i/\partial x_j + \partial u_j/\partial x_i)/2.$$

In order to find the numerical values of the coefficients in the effective Hamiltonian (5), we used the results of calculations of the lattice vibration spectrum and the total crystal energy for some low-symmetry phases whose distortions involve F-ion displacements.

The elastic constants C_{11}, C_{12}, and C_{44} are determined from the calculated small-q dependences of the frequencies of longitudinal and transverse acoustic modes for three symmetry directions: [001], [110], and [111]. The following values are obtained for the elastic constants $C_{ij} = c_{ij}\Omega$ (where Ω is the unit-cell volume) for the Rb_2KInF_6 crystal: $C_{11} = 53.6$ eV, $C_{12} = 11.7$ eV, and $C_{44} = 9.5$ eV. Unfortunately, experimental values of the elastic constants of this crystal are unavailable and we can only compare the calculated constants C_{ij} with their experimental values for the isomorphic compound Rb_2NaHoF_6, which has approximately the same chemical composition as the crystal under study: $C_{11} = 59.5$ eV, $C_{12} = 18.9$ eV, and $C_{44} = 19.2$ eV [15]. It is seen that these values and the respective constants calculated for the Rb_2KInF_6 crystal are of the same order of magnitude.

The coefficients of the second-order terms in Eq. (5) are determined from the total energies E_i of the distorted phases. Table 5 presents the relations between linear combinations of the coefficients in Eq. (5) and the distortion energies $\Delta E_i = E_i - E_0 - E_{\text{anh}}$ (where $E_0 = -356596$ eV), as well as the values of ΔE_i (in eV) calculated from first principles. In this table, E_Γ is the energy of the tetragonally distorted phase in which the rotations of InF_6 octahedra are homogeneous over the crystal and correspond to condensation of one compo-

Table 5. Expressions for the distortion energies $\Delta E_i = E_i - E_0 - E_{\mathrm{anh}}$ of some phases and their values (eV)

ΔE_Γ	$4a_1 + 8a_2 + 2b_1 + 4b_2 + A$	–26.906
ΔE_X	$4a_1 - 8a_2 + 2b_1 + 4b_2 + A$	–26.169
ΔE_L	$-24a_3 - 6b_1 - 12b_2 + 3A$	18.412
ΔE_{zx}	$-4a_1 + 2b_1 + 4b_2 + A$	16.557

Table 6. Calculated phase transition temperatures (K) and the parameters of the effective Hamiltonian (eV)

T_c	550	750	450	350
Single-site parameters				
A	3.087	–15.482	23.490	5.339
B	1.400×10^3	1.577×10^3	1.188×10^3	1.286×10^3
C	2.246×10^3	2.145×10^3	2.415×10^3	2.767×10^3
D	-0.732×10^3	-5.568×10^3	5.567×10^3	16.198×10^3
Intersite parameters				
a_1	–5.386	–3.928	–7.785	–4.969
a_2	–0.046	–0.027	–0.073	0.060
a_3	0.628	0.514	0.849	0.014
b	–1.346	–0.982	–1.948	–1.243
Coupling constants with homogeneous strains				
g_1	39.878	66.420	43.430	29.854
g_2	–15.915	–15.939	–20.672	–18.701

nent of the T_{1g} mode at $q = 0$; E_X is the energy of the tetragonally distorted phase with a doubled unit-cell volume, resulting from condensation of the soft mode X_2^+ at the BZ boundary; and ΔE_L is the difference between the energies of the cubic and the distorted phase in which the octahedra are rotated about a cube body diagonal, which corresponds to the following distribution of the local mode $S_\alpha(\mathbf{R})$:

$$S_x(\mathbf{R}) = S_y(\mathbf{R}) = S_z(\mathbf{R}) = |S|\exp(-i\mathbf{q}_L\mathbf{R}),$$

where $|S|$ is the amplitude of the local mode, $\mathbf{q}_L = \frac{\pi}{a_0}(111)$, and $\mathbf{R}$ is a translation vector of the cubic phase. The amplitude of this local mode is found by minimizing the total energy E_L of the distorted phase. It should be noted that, although this distorted phase cannot result from the condensation of any one phonon mode, the crystal under study has an unstable mode at point L on the BZ boundary in which the displacements of the ions lead to rotation of the octahedron and to a small distortion in it [9]. We also calculated the total energy E_{zx} of the distorted phase in which the $\mathrm{InF_6}$ octahedron is rotated about the [001] axis and the unit cell is doubled along the [100] axis, which corresponds to an $S_\alpha(\mathbf{R})$ distribution of the form

$$S_z(\mathbf{R}) = |S|\exp(-i\mathbf{q}_X\mathbf{R}), \quad S_x = S_y = 0,$$

where $\mathbf{q}_X = \frac{2\pi}{a_0}(100)$. This distorted structure cannot be due to the condensation of a phonon mode. Since the other homogeneously distorted structures in which the unit cell is doubled and the octahedra are rotated do not lead to new relations between linear combinations of the coefficients, we failed to divide the combination $4a_1 + 2b_1 + 4b_2 + A$ into individual terms. For this reason, we assumed that the constants b_1 and b_2, which characterize the interaction with the next-to-nearest neighbors in Eq. (5), have the same value and are four times less than the interaction constant with the nearest neighbors a_1; that is, $b_1 = b_2 = b = a_1/4$. This assumption is consistent with our calculations of the thermodynamic properties of the system with Hamiltonian (5) (see below), according to which these properties (calculated with the value of a_1 determined previously) are scarcely affected by the values of b_1 and b_2; at least, for three values of $b/a_1 = 1/4$, 1/2, and 3/4, the results of numerical simulations differ from one another only slightly.

The coefficients B, C, and D of the anharmonic terms in the single-site potential are determined from the dependences of the total energy of the clamped crystal (whose lattice parameter is the same as that in the cubic phase, $a_0 = 16.71$ a.u.) on the rotation angle of the $\mathrm{InF_6}$ octahedron about the [001] ($S_x = S_y = 0$, $S_z = |S|$), [110] ($S_x = S_y = |S|$, $S_z = 0$), and [111] axes ($S_x = S_y = S_z = |S|$). These dependences are shown in Fig. 3, and the values of the coefficients B, C, and D determined using the least square method are listed in Table 6.

Now, we discuss the coupling coefficients between the local mode and homogeneous elastic strains. Since shear strains do not arise in the tetragonal phase during the $Fm3m \longrightarrow I4/m$ phase transition, we did not determine the coefficient g_3 in Eq. (5). The coefficients g_1 and g_2 are found as follows. The total energy of the unclamped crystal is calculated as a function of the rotation angle of the octahedron about the [001] axis and, for a fixed value of the angle, is minimized with respect to the unit-cell parameters and the radii of the Watson spheres of the ions. The angular dependence of the energy is shown in Fig. 3. Then, we subtract the total energy of the clamped crystal, and this energy difference and the elastic constants determined before are used to fit the coefficients g_1 and g_2 using the least square method (Fig. 3). The values of these coefficients are listed in Table 6.

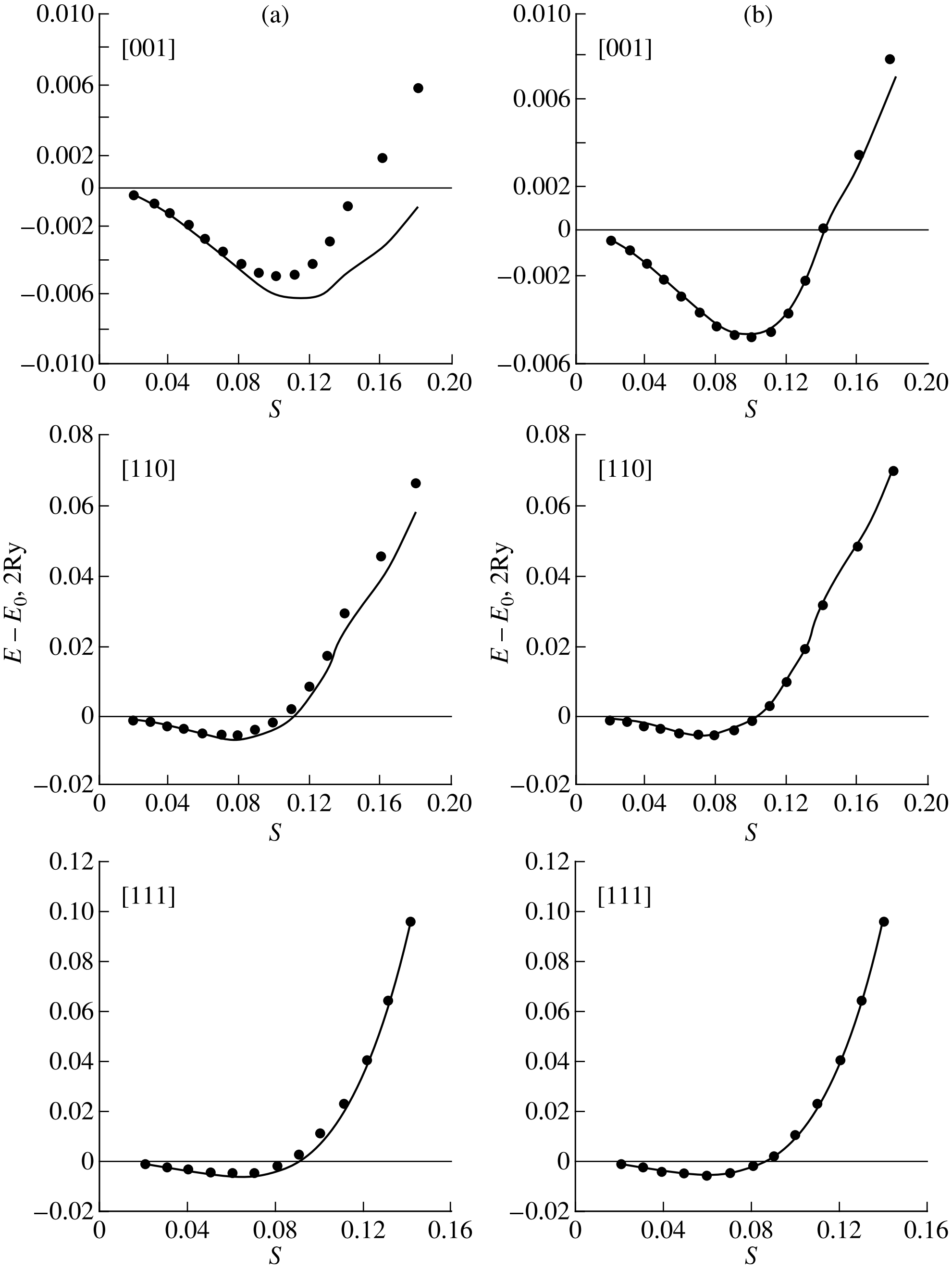

Fig. 3. Total crystal energy (E_0 = –13110.141187 a.u.) as a function of the octahedron rotation angle for (a) the unclamped crystal and (b) the clamped crystal with unit-cell parameters of the cubic phase. Solid curves are calculations, and dots represent the energies obtained from the effective Hamiltonian, whose parameters are fitted using the least square method.

5. INVESTIGATION OF THERMODYNAMIC PROPERTIES AND DISCUSSION OF RESULTS

The effective Hamiltonian derived above is simple but contains many parameters, which hampers calculation of the free energy and other thermodynamic quantities using analytical methods, for example, within the self-consistent-field approximation. Therefore, we investigated the thermodynamic properties of the system with the effective Hamiltonian (5) using the numerical Monte Carlo (MC) method, namely, its classical version with the Metropolis algorithm [16] for an fcc $L \times L \times L$ lattice with periodic boundary conditions. The three-component pseudovector (S_x, S_y, S_z) was placed at each lattice site, and the lattice was subjected to homogeneous strains e_1, e_2, and e_3. We investigated two cases using the MC method: a clamped crystal (i.e., without elastic strains, $e_1 = e_2 = e_3 = 0$) and an unclamped crystal with strains e_1, e_2, and e_3 (their cal-

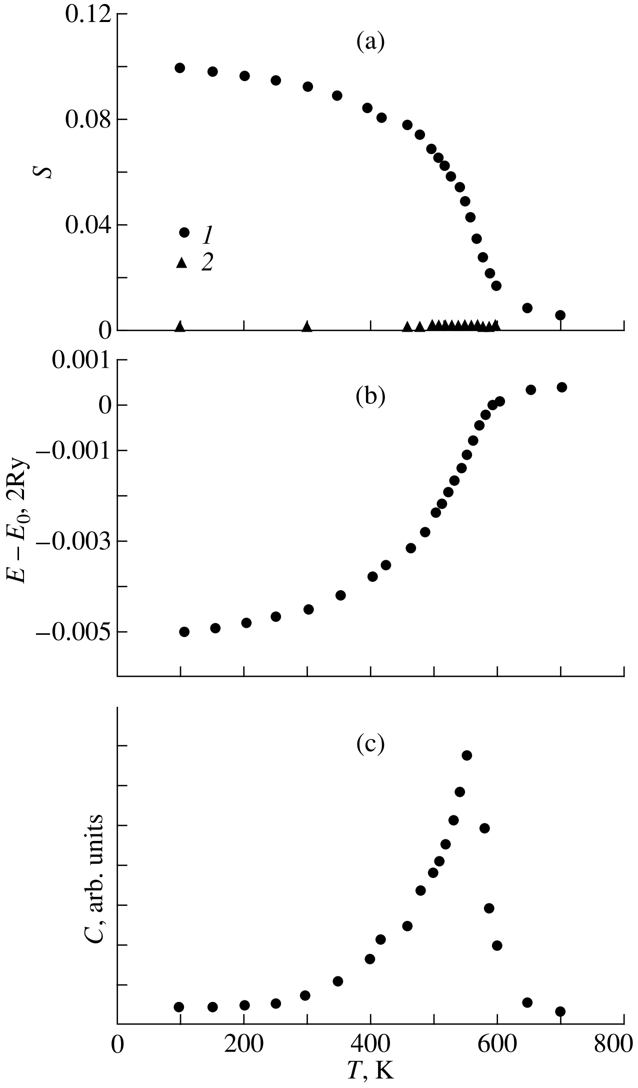

Fig. 4. Temperature dependences, calculated using the MC method, of (a) the order parameter (*1* is S_z, *2* is S_x, S_y), (b) the internal energy, and (c) the heat capacity (in arbitrary units).

culation was included in the MC algorithm). In the former case, in each cycle of the MC procedure, we varied the pseudovector components S_{ix}, S_{iy}, and S_{iz} in a random fashion successively at each lattice site and verified the possibility of each variation. It should be noted here that our calculations of the total energy of distorted phases and numerical simulations of the effective Hamiltonian showed that the energies of distorted phases with unequal pseudovector components $S_x \neq S_y \neq S_z$ were significantly higher than those in the case of equal pseudovector components. Therefore, in order to reduce the computer time required for the MC procedure, we chose only those pseudovectors with the following components: S_z, $S_x = S_y = 0$; $S_z = \pm S_x$, $S_y = 0$; and $S_z = \pm S_x = \pm S_y$.

Since the energy increases sharply in the range above $|S| \sim 0.07$, as seen from Fig. 3, we restricted our calculations to the range [–0.1, 0.1] for the values of the components S_α and their variations. For each value of the temperature, we performed 50000 steps of the MC procedure and the thermodynamic quantities were calculated by averaging over the last 10000 steps in the ordinary way [16].

In the case of the unclamped crystal, after each cycle of the MC procedure described above, we tried to vary each component of the strain tensor. The values of trial variations were chosen randomly and lied in the range [–0.05, 0.05]. For each component, we performed 1000 trials and averaged over them. The averaged strains and the configuration of pseudovectors calculated in a given cycle of the MC procedure were taken as the initial ones for the next cycle.

The calculations were carried out for both high (~1000 K) and low (~50 K) initial temperatures. When the MC procedure was started from high temperatures, we simultaneously treated two initial configurations, corresponding to the high-symmetry cubic phase ($S_x^i = S_y^i = S_z^i = 0$) and to the tetragonally distorted phase ($S_z^i = 0.08$, $S_x^i = S_y^i = 0$). When starting from low temperatures, a configuration corresponding to the tetragonal phase was taken as the initial one. The calculation was carried out for the dimension $L = 10$ (4000 pseudovectors). In order to check the results, we also performed calculations for several temperatures for a larger lattice ($L = 20$, 32000 pseudovectors). The results obtained for the $20 \times 20 \times 20$ lattice differ little from those obtained for the $10 \times 10 \times 10$ lattice; thus, in what follows, we will discuss only the calculations performed for $L = 10$.

The calculated temperature dependences of the pseudovector components S_x^i, S_y^i, and S_z^i and of the internal energy $E - E_0$ (E_0 is the total energy of the crystal in the cubic phase) are shown in Fig. 4. The phase transition temperature was determined as that corresponding to the inflection point in the temperature dependence of the internal energy (Fig. 4b) and to the peak in the temperature dependence of the heat capacity C_V calculated using a standard method [16] (Fig. 4c).

At $T_c = 550$ K, the unclamped crystal undergoes a second-order phase transition to a distorted phase with pseudovectors $S_z^i = S$ and $S_x^i = S_y^i = 0$. Such a tetragonal phase, having the same unit-cell volume as the cubic phase and belonging to the space group *I*4/*m*, was observed experimentally in Rb_2KInF_6 crystals below 283 K [5]. The calculation accuracy of the phase transition temperature is determined by that of the vibration frequencies and of the total energy of the distorted phases. In the approach employed by us, these quantities are calculated to within an accuracy of ~5%. In the case of the clamped crystal (zero strains), the phase transition temperature obtained from the MC calculation data is $T_c = 560$ K, which is ten degrees higher than that for the unclamped crystal.

Figure 5 presents the elastic strains $e_1 = e_2$ and e_3 in the tetragonal phase measured experimentally and from MC calculations. The quantitative agreement between the calculated and experimental values is fairly reasonable, if one takes into account that the values of e_i are very small and that the method according to which we calculated the total crystal energy, vibration frequencies, and the parameters of the model Hamiltonian is poorly accurate.

The phase transition temperature T_c obtained from the MC calculations is nearly twice as large as its experimental value. This discrepancy can be mainly due to the calculated total crystal energy and lattice vibration spectrum, which are not sufficiently accurate in comparison with the first-principles energy-band calculations.

On the other hand, our calculations revealed that the value of the phase transition temperature is very sensitive to the details of the crystal structure in both the high-symmetry cubic phase and the distorted phases. The parameters of the effective Hamiltonian (5) listed in the second column of Table 6 were calculated from the energies of the distorted phases by minimizing the total crystal energy in both the cubic and distorted phases. We also calculated the parameters of the effective Hamiltonian (by following the scheme described above) and performed MC calculations with these parameters for slightly varied crystal structures. The results of these calculations are presented in the last three columns of Table 6: The third column lists the parameters of the Hamiltonian and the calculated phase transition temperature for the case where the F–In distance (between the fluorine and indium ions) in the cubic phase is $0.222a_0$ ($a_0 = 17.08$ a.u. is the lattice parameter in the cubic phase), the fourth column lists the same quantities calculated for a F–In distance equal to $0.24a_0$ ($a_0 = 16.41$ a.u.), and the last column of Table 6 lists the same quantities calculated for the case where the F–In distance ($0.23a_0$, $a_0 = 16.71$ a.u.) corresponds to the minimum of the total energy but, in addition to the F-ion displacements, the Rb ions in the tetragonally distorted phase are also displaced along the cube body diagonal without breaking the tetragonal symmetry. The amount of Rb-ion displacement was taken to be equal to one-third the F-ion displacement. It can be seen from Table 6 that small variations (≈4%) of the ion positions in the crystal structure give rise to significant changes in T_c. However, it should be emphasized once again that the values of the transition temperature from the cubic to the tetragonal phase listed in the last three columns of Table 6 do not correspond to a minimum of the total crystal energy.

According to our MC calculations, the tetragonal phase remains stable down to zero temperature and the other pseudovector components (S_x, S_y) do not appear, which contradicts the experimental observations, according to which another structural phase transition (to the monoclinic phase with unit-cell doubling) occurs in Rb_2KInF_6 crystals at $T_{c2} = 264$ K. Structural studies of the monoclinic phase of the isomorphic Rb_2KScF_6 compound revealed [5] that this phase transition is accompanied by the appearance of another pseudovector component below T_{c2}; this component is inhomogeneous over the crystal and involves displacements of the Rb ions from their equilibrium positions. This suggests that the Rb-ion displacements play a significant part in the stabilization of the monoclinic phase in this crystal and that, therefore, in order to describe the second structural phase transition, not only octahedron rotations but also the vibrational modes that correspond to these degrees of freedom should be included into the model Hamiltonian.

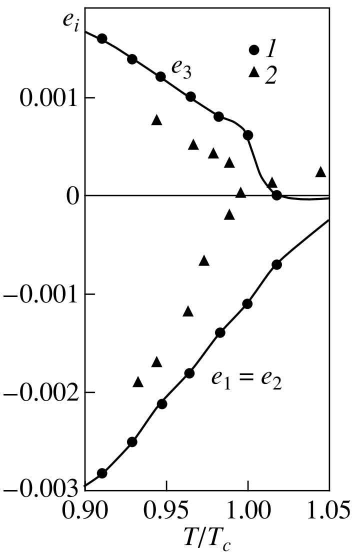

Fig. 5. Temperature dependences of the strain tensor components e_i in the tetragonal phase: (*1*) MC calculations and (*2*) experiment [17].

6. CONCLUSIONS

Thus, in this paper, we calculated the entire spectrum of crystal lattice vibrations and constructed a nonempirical effective Hamiltonian to describe the structural phase transition $Fm3m \longrightarrow I4/m$ in the Rb_2KInF_6 crystal. The parameters of the Hamiltonian were determined by calculating the total energy in an ionic-crystal model taking into account the deformation and polarization of ions. The model Hamiltonian was used in numerical calculations in accordance with the MC method, from which we determined the phase transition temperature from the cubic to the tetragonal phase, $T_c = 550$ K. This calculated temperature is twice as large as the corresponding experimental value. This discrepancy could be mainly due to the insufficiently accurate method used in the calculations. However, according to our calculations, the phase transition temperature is very sensitive to the details of the crystal structure; therefore, the discrepancy between the calculated and experimental values of T_c could be due to the imperfection of the crystals used in the experimental studies.

Nevertheless, from the results obtained in this paper, it is reasonable to infer that the phase transition $Fm3m \longrightarrow I4/m$ in the Rb_2KInF_6 crystal is basically associated with spatially homogeneous rotations of the InF_6 octahedra, whereas the other degrees of freedom affect the mechanism and thermodynamics of this phase transition only slightly.

ACKNOWLEDGMENTS

The authors are grateful to O.V. Ivanov and E.G. Maksimov for permission to employ the computer code for calculating the total crystal energy and ionic polarizability.

This study was supported by the Russian Foundation for Basic Research, project nos. 00-02-17792, 00-15-96790, and the INTAS Foundation, grant no. 97-10-177.

REFERENCES

1. R. D. King-Smith and D. Vanderbilt, Phys. Rev. B **49**, 5828 (1994).
2. K. M. Rabe and U. V. Waghmare, Ferroelectrics **164**, 15 (1995).
3. U. V. Waghmare and K. M. Rabe, Phys. Rev. B **55**, 6161 (1997).
4. D. Vanderbilt and W. Zhong, Ferroelectrics **206** (1–4), 181 (1998); W. Zhong, D. Vanderbilt, and K. M. Rabe, Phys. Rev. B **52**, 6301 (1995).
5. I. N. Flerov, M. V. Gorev, K. S. Aleksandrov, *et al.*, Mater. Sci. Eng., R **24**, 81 (1998).
6. V. I. Zinenko and N. G. Zamkova, Fiz. Tverd. Tela (St. Petersburg) **41**, 1297 (1999) [Phys. Solid State **41**, 1185 (1999)].
7. O. V. Ivanov and E. G. Maksimov, Zh. Éksp. Teor. Fiz. **108**, 1841 (1995) [JETP **81**, 1008 (1995)].
8. V. I. Zinenko and N. G. Zamkova, Zh. Éksp. Teor. Fiz. **118** (2), 359 (2000) [JETP **91**, 314 (2000)].
9. V. I. Zinenko, N. G. Zamkova, and S. N. Sofronova, Zh. Éksp. Teor. Fiz. **114** (5), 1742 (1998) [JETP **87**, 944 (1998)].
10. D. A. Liberman, D. T. Cromer, and J. J. Waber, Comput. Phys. Commun. **2**, 107 (1971).
11. H. Guengard, Ph.D. Thesis (University of Bordeaux, France, 1994).
12. M. Couzi, S. Khairoun, and A. Tressaud, Phys. Status Solidi A **98**, 423 (1986).
13. H. Thomas and K. A. Muller, Phys. Rev. Lett. **21**, 1256 (1968).
14. K. M. Rabe and J. D. Joannopoloulos, Phys. Rev. B **36**, 6631 (1987).
15. P. Selgert, C. Lingner, and B. Luthi, Z. Phys. B **55**, 219 (1984).
16. *Monte Carlo Methods in Statistical Physics*, Ed. by K. Binder (Springer, Berlin, 1979; Mir, Moscow, 1982).
17. I. N. Flerov, M. V. Gorev, S. V. Mel’nikova, *et al.*, Fiz. Tverd. Tela (St. Petersburg) **34**, 3493 (1992) [Sov. Phys. Solid State **34**, 1870 (1992)].

Translated by Yu. Epifanov

Physics of the Solid State, Vol. 43, No. 12, 2001, pp. 2301–2306. Translated from Fizika Tverdogo Tela, Vol. 43, No. 12, 2001, pp. 2209–2213.
Original Russian Text Copyright © 2001 by Flerov, Gorev, Afanas'ev, Ushakova.

**LATTICE DYNAMICS
AND PHASE TRANSITIONS**

Thermodynamic Properties of $(NH_4)_2KGaF_6$ Elpasolite

I. N. Flerov, M. V. Gorev, M. L. Afanas'ev, and T. V. Ushakova

*Kirensky Institute of Physics, Siberian Division, Russian Academy of Sciences,
Akademgorodok, Krasnoyarsk, 660036 Russia*
e-mail: flerov@ksc.krasn.ru

Received April 24, 2001

Abstract—The heat capacity of $(NH_4)_2KGaF_6$ elpasolite is measured in the temperature range from 80 to 350 K. A sequence of three phase transitions at $T_1 = 288.5$ K, $T_2 = 250$ K, and $T_3 = 244.5$ K is revealed, and the thermodynamic characteristics of these transitions are determined. The influence of hydrostatic pressure on the phase transition temperature is investigated. The results obtained are discussed within the model of orientational ordering of NH_4^+ and GaF_6^{3-} ionic groups. © *2001 MAIK “Nauka/Interperiodica”.*

1. INTRODUCTION

Crystals of the elpasolite and cryolite family of the general formula $A_2^+B^+M^{3+}F_6$ (in a cryolite structure, $A^+ \equiv B^+$) have a high-temperature cubic phase and belong to a wide class of ordered perovskites with the space group $Fm\bar{3}m$ ($Z = 4$). Compounds of this family with atomic cations A^+ and B^+ = Na^+, K^+, Rb^+, or Cs^+ ($R_{A^+} > R_{B^+}$) can undergo structural phase transitions upon cooling due to lattice instability with respect to rotational distortions of the crystal framework which consists of vortex-shared octahedra B^+F_6 and $M^{3+}F_6$ [1–3]. The phase transitions occur through the condensation of soft librational modes of octahedral ionic groups.

The presence of NH_4^+ ammonium ions in the structure substantially affects the mechanism of the phase transitions. In elpasolite and cryolite crystal cells, these ions can occupy two nonequivalent positions, namely, 4*b* (inside a halide octahedron) and 8*c* (in a hole between octahedra) positions with coordination numbers of 6 and 12, respectively. In the $(NH_4)_3M^{3+}F_6$ cryolite structure, ammonium ions occupy both positions. For an elpasolite structure, there are two variants: (1) ammonium tetrahedra can be located only in holes between octahedra in the $(NH_4)_2B^+M^{3+}F_6$ compounds and (2) ammonium tetrahedra can occupy only halide octahedra in the $A_2^+NH_4M^{3+}F_6$ compounds.

Among ammonium compounds, the $(NH_4)_3M^{3+}F_6$ cryolites are the best understood. For these compounds, the heat capacity has been carefully measured and the thermodynamic parameters of phase transitions have been reliably determined in a number of works [4–10]. Moreover, the effect of hydrostatic pressure was analyzed in our recent works [9, 10]. The character of the reorientational motion of hydrogen and fluorine was investigated earlier by NMR spectroscopy [4, 11].

In the $(NH_4)_3M^{3+}F_6$ cryolites, as in compounds with atomic cations [2], the phase transition temperature and the sequence of formation of distorted phases essentially depend on the size of the trivalent cation. Earlier, two successive phase transitions were revealed in an ammonium-containing cryolite with $M^{3+} = Al^{3+}$ [4, 12] and one transition from a cubic phase to a triclinic phase was observed in compounds with $M^{3+} = Cr^{3+}$, Ga^{3+}, V^{3+}, and Fe^{3+} [6–8, 13, 14]. It was found that, for compounds with larger-sized trivalent ions ($M^{3+} = Sc^{3+}$ and In^{3+}), the low-temperature triclinic phase is formed upon three phase transitions [8–11, 15].

For the aforementioned cryolites, the total entropy change due to the transition from the cubic to the triclinic phase varies in a narrow range (2.33–2.99)R from crystal to crystal and does not depend on the sequence of phase transitions. The large entropy clearly indicates that ordering processes proceed in the structure. In [7, 8], it was assumed that the phase transitions are associated with orientational ordering of both tetrahedral ammonium and octahedral fluorine ionic groups. Of the above two types of ammonium ions that occupy different crystallographic positions (8*c* and 4*b*), only in the latter case, tetrahedral ions in the cubic phase are disordered over two equivalent orientations according to the symmetry of the occupied position. Fluorine octahedra remain rigid and regular when fluorine atoms in the cubic phase are distributed over the 24*e* or 192*l* positions. In the former case, they occupy a special position on the cell edge. In the latter case, they are distributed over eight positions; i.e., each octahedron is characterized by eight equivalent orientations. Consequently, the entropy change that corresponds to complete ordering of the ionic groups is equal to $R\ln 2 + R\ln 8 = R\ln 16 = 2.77R$. This value is in reasonable agreement with the experimental data for ammonium-containing cryolites.

In the case when ammonium cryolites undergo successive phase transitions, the structural ordering processes occur in two stages [9]. The phase transition from the cubic phase to the monoclinic phase is associated with a partial ordering of octahedra ($\Delta S = R\ln 4$), which results in a forced ordering of ammonium tetrahedra ($\Delta S = R\ln 2$). The octahedra are completely ordered upon the second phase transition between two monoclinic modifications ($\Delta S = R\ln 2$). The third phase transition (to the triclinic phase) is accompanied by an insignificant change in the entropy and is, most likely, a first-order transition between two completely ordered, distorted modifications [9, 16]. The model under consideration is consistent with the NMR data obtained by Sasaki *et al.* [11] for the $(NH_4)_3InF_6$ cryolite. For cryolites with successive phase transitions, the spin-lattice relaxation times of protons (T_{1H}) and fluorine nuclei (T_{1F}) exhibit an anomalous behavior upon phase transition from the cubic phase. However, upon the second phase transition, only the T_{1F} time changes considerably.

It should be noted that, in ammonium elpasolites, an NH_4^+ ion occupies only one of the two possible crystallographic positions (4*b* or 8*c*). This slightly simplifies the problem of elucidating the role of ammonium ions in structural phase transitions and their influence on the motion of fluorine octahedra.

If the model proposed in [8, 9, 16] provides an adequate description of the ordering of structural units upon phase transitions, the $A_2^+NH_4M^{3+}F_6$ elpasolites, like $(NH_4)_3M^{3+}F_6$ cryolites, can undergo phase transitions with ordering of the ammonium tetrahedra and fluorine octahedra. As regards the $(NH_4)_2B^+M^{3+}F_6$ elpasolites, only the fluorine octahedra can be disordered in their cubic structure. In these two cases, the maximum entropy change can be equal to $R\ln 16$ and $R\ln 8$, respectively.

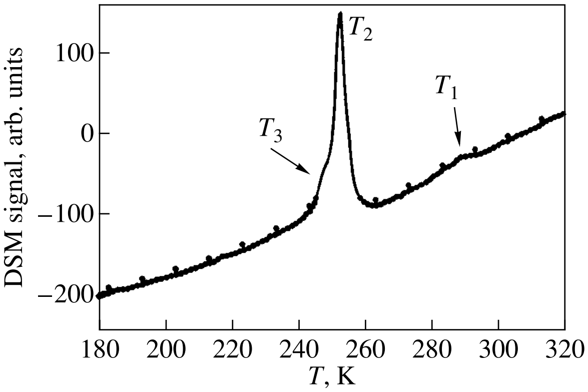

Fig. 1. DSC curve for the $(NH_4)_2KGaF_6$ elpasolite (DSM-2M instrument).

In the present work, we carefully investigated the heat capacity and the *p*–*T* phase diagram for the $(NH_4)_2KGaF_6$ compound over a wide range of temperatures and pressures. The aim of this work was to determine the thermodynamic parameters of phase transitions and to elucidate how the substitution of an atomic cation for ammonium in the crystallographic position 4*b* in the $(NH_4)_2NH_4GaF_6$ cryolite structure affects the thermodynamic properties.

2. SAMPLE PREPARATION AND PRELIMINARY INVESTIGATIONS

The $(NH_4)_2KGaF_6$ compound was prepared using two methods. In the first method, we synthesized this compound from a solution. A solution of $Ga(OH)_3$ in concentrated hydrofluoric acid was evaporated to the onset of crystallization. Then, a saturated solution of an equimolar mixture in hydrofluoric acid on a $2NH_4HF_2 + KHF_2 + Ga(OH)_3$ basis was added to the $Ga(OH)_3$ solution. The resultant solution was allowed to stand in a crystallizer at a temperature of 70°C until fine crystals were formed and was then cooled to room temperature at a rate of 0.5 K/h. As a result, we obtained crystals approximately 0.5 mm^3 in volume.

In the second method, the $(NH_4)_2KGaF_6$ compound was prepared by hydrothermal synthesis. A 35% aqueous solution of HF (in an amount of 20% of the total weight of the initial components) was added to a $2NH_4HF_2 + KHF_2 + GaF_3 \cdot 3H_2O$ mixture in a Teflon vessel. The vessel with the prepared mixture was placed in a high-pressure nickel bomb. The hermetically sealed bomb was held for 48 h at 230°C and then was slowly cooled for 72 h to room temperature. In this manner, we obtained octahedral crystals 30–50 mm^3 in volume.

Analysis of the x-ray diffraction patterns showed that impurities of the initial components and foreign phases are absent in the samples. At room temperature, the $(NH_4)_2KGaF_6$ compound has a cubic symmetry ($Fm\bar{3}m$, $Z = 4$) with the unit cell parameter a_0 = 8.866 Å. According to the chemical formula, ammonium ions occupy the 8*c* positions in the unit cell. No indications of composition disordering of ammonium and potassium ions over the 8*c* and 4*a* positions were found.

Two $(NH_4)_2KGaF_6$ samples prepared using different methods were studied by differential scanning calorimetry (DSC) on a DSM-2M instrument in the temperature range 150–320 K. The experimental data obtained for the sample grown by hydrothermal synthesis are shown in Fig. 1. It can be seen that the heat capacity exhibits two anomalies proportional to the DSM signals at temperatures $T_1 \approx 290$ K and $T_2 \approx 250$ K. Moreover, a small deviation from a smooth decrease in the DSM signal is observed below T_2 in the range of $T_3 \approx 245$ K. In order to make certain that the third anomaly is not accidental and does not depend on the sample preparation procedure, we performed calorimetric measurements with the same instrument for the sample synthesized from the solution. The results of both experiments turned out to be identical: the temperatures of each of the three anomalies in the heat capacity coincided to within 1–2 K, i.e., within the accuracy ensured by the DSM-2M instrument. The enthalpy change upon the phase transition at the T_1 temperature was found to be $\Delta H_1 = 150 \pm 25$ J/mol. Since the difference between the temperatures T_2 and T_3 was small, we succeeded only in determining the total enthalpy change upon two successive transitions: $\Delta H_2 + \Delta H_3 = 3500 \pm 550$ J/mol.

The preliminary polarization-optical investigation of the $(NH_4)_2KGaF_6$ samples prepared by hydrothermal synthesis revealed that twins with a structure typical of tetragonal distortion are formed at temperatures below T_1. Below the T_2 temperature, the pattern of twinning changes and the symmetry becomes lower (most probably, monoclinic). Unfortunately, reliable data on the phase transition at the T_3 temperature are unavailable. Detailed results of optical and structural investigations will be published in a separate paper.

3. HEAT CAPACITY MEASUREMENTS

In order to refine the thermodynamic parameters of the phase transitions under investigation and to reveal possible phase transitions with a small enthalpy (i.e., transitions that cannot be recorded using the DSC method because of its relatively low sensitivity to thermal effects), the temperature dependence of the heat capacity was carefully measured using an adiabatic calorimeter in the temperature range 80–350 K.

For this purpose, a sample (1.46 g) was placed in an indium cell, which was then hermetically sealed in a helium atmosphere. The heat capacity of the cell was determined in a separate experiment. The measurements were carried out upon discrete and continuous heating. In their immediate vicinity, the phase transitions were investigated by the quasi-static thermogram method during heating and cooling at mean rates $|dT/dt| \approx 2.5 \times 10^{-2}$ K/min.

The temperature dependences of the heat capacity of the $(NH_4)_2KGaF_6$ compound over the entire temperature range studied and, in greater detail, at temperatures near 250 K are displayed in Figs. 2a and 2b, respectively.

It can be seen from Fig. 2 that the heat capacity exhibits three anomalies, as is the case in the experiments performed with the DSM-2M instrument. The refined temperatures of the phase transitions are as follows: $T_1 = 288.5 \pm 0.5$ K, $T_2 = 249.3 \pm 0.1$ K, and $T_3 = 244.6 \pm 0.5$ K. The behavior of the heat capacity in the vicinity of the T_1 temperature is characteristic of second-order phase transitions. Thermographic investigations (quasi-static thermogram method) demonstrated that the anomalies observed in the heat capacity at T_2 and T_3 are associated with the first-order phase transformations, which are characterized by the temperature hystereses $\delta T_2 = 1.24 \pm 0.05$ K and $\delta T_3 = 2.06 \pm 0.2$ K.

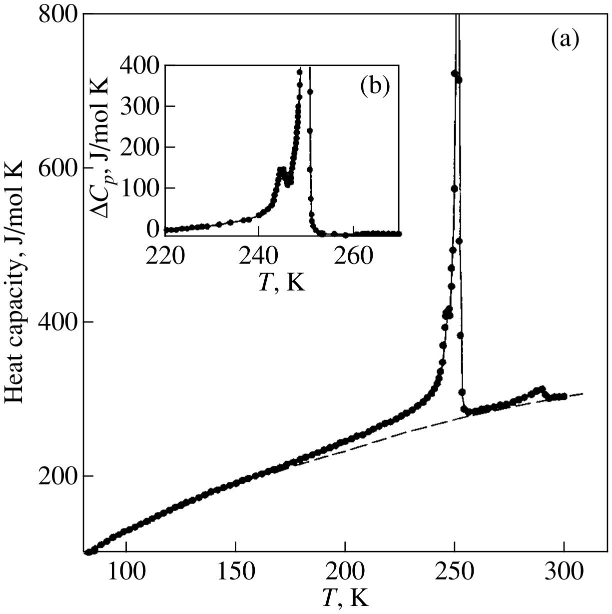

Fig. 2. Temperature dependences of the heat capacity for the $(NH_4)_2KGaF_6$ elpasolite (a) over a wide range of temperatures and (b) in the temperature range of phase transitions at T_2 and T_3. The dashed line shows the lattice heat capacity.

The integrated thermodynamic characteristics of the phase transitions were obtained in the processing of the anomalous component of the heat capacity $\Delta C_p(T) = C_p(T) - C_{\mathrm{lat}}(T)$. The lattice component of the heat capacity $C_{\mathrm{lat}}(T)$ was determined by approximating the experimental data outside the phase transition range ($T < 150$ K and $T > 300$ K) with the use of the Debye and Einstein functions. The temperature dependence of the lattice heat capacity is shown by the dashed line in Fig. 2a. The spread of experimental points about the smoothed dependence in these temperature ranges did not exceed 0.7%. The change in the entropy with temperature was calculated by integrating of the $\Delta C_p(T)/T$ function. The temperature dependence of the excess entropy is depicted in Fig. 3.

The total entropy change for the three phase transitions is equal to 16.0 ± 1.5 J/mol K. The entropy change due to the first phase transition is rather small: $\Delta S_1 = (0.12 \pm 0.01)R$; this value is characteristic of displacive-type transitions. Since the temperatures of the two other transitions are very close to each other, the entropy change attributed to each of these transitions cannot be distinguished. The total entropy change for these transitions is $\Delta S_2 + \Delta S_3 = 1.8R$. This value slightly exceeds the entropy change ($1.68R$) determined by the DSM method.

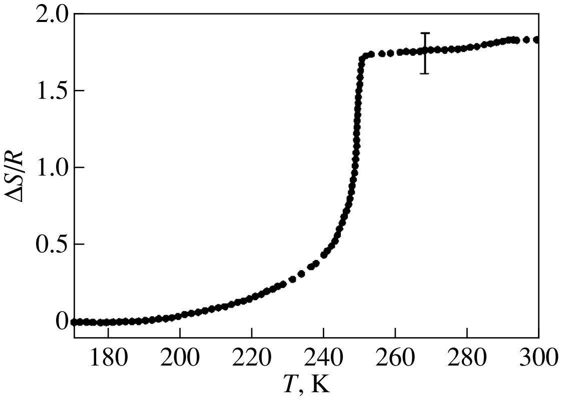

Fig. 3. Temperature dependence of the excess entropy.

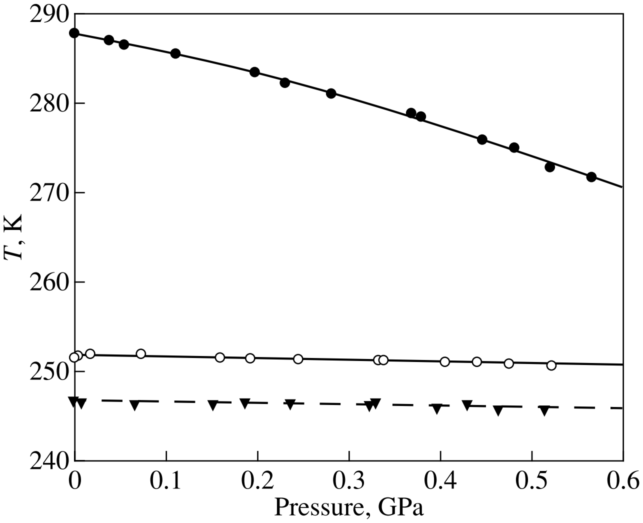

Fig. 4. The *p*–*T* phase diagram for the $(NH_4)_2KGaF_6$ elpasolite.

4. PHASE DIAGRAM

The effect of hydrostatic pressure on the phase transition temperatures was studied with the same sample as was used in the heat capacity measurements. The phase transition temperature and its change with a variation in pressure were determined from a differential thermal analysis (DTA). A copper–germanium thermocouple served as the sensitive element. A quartz reference sample was placed on one junction of the thermocouple, and a small copper cell with the studied compound was placed on the other junction of the thermocouple. The high sensitivity of the thermocouple made it possible to measure reliably even the phase transition at T_1 with a small anomaly in the heat capacity ($\Delta C_p/C_{lat} \approx 6\%$). A pressure as high as 0.6 GPa was produced in a cylinder–piston-type chamber connected to a booster. A mixture of silicone oil and pentane was used as the pressure transferring medium. The pressure in the chamber was measured on a manganin resistance pressure gauge, and the temperature was measured using a copper–constantan thermocouple. The errors of measurements were equal to $\pm 10^{-3}$ GPa and ±0.3 K, respectively. The reliability of the results was checked by measuring the shift in the phase transition temperatures with an increase and a decrease in the hydrostatic pressure.

Figure 4 shows the *p*–*T* phase diagram of the $(NH_4)_2KGaF_6$ elpasolite. It is seen that the stability loss temperature of the cubic phase decreases with an increase in the pressure. It is worth noting that the dependence $T_1(p)$ is obviously nonlinear. The shift in the phase transition temperature dT_1/dp is equal to –18.5 K/GPa at $p = 0$ and reaches a value of –30 K/GPa at $p = 0.5$ GPa. The temperatures of the two other structural transformations also decrease but considerably more slowly: $dT_2/dp = -(2.3 \pm 0.3)$ K/GPa and $dT_3/dp = -(1.4 \pm 0.4)$ K/GPa. It is evident that a further increase in the pressure can lead to the disappearance of the first distorted phase. According to the estimates, this can occur at $p = 1.0$–1.2 GPa.

5. DISCUSSION

The substitution of the K^+ cation for the ammonium ion in the 4*b* position leads to quite a different pattern of phase transitions as compared to that observed in the $(NH_4)_2NH_4GaF_6$ cryolite. Let us consider the $(NH_4)_2KGaF_6$ elpasolite structure in the framework of the model proposed for cryolites in [7–9]. Within this model, fluorine octahedra alone, most probably, fulfill the function of “critical” ions; i.e., they play an active part in the phase transitions. Now, we attempt to either validate or disprove this assumption. In the $(NH_4)_2KGaF_6$ elpasolite, the entropy change upon the phase transition from the cubic phase is small ($\Delta S_1 = 0.1R$) and comparable to the quantity $\Delta S \approx 0.2R$. This entropy change is characteristic of a large number of halide elpasolites (including fluoro-elpasolites) with atomic cations, which undergo phase transitions to the tetragonal phase [2]. According to [2], the entropy change of $0.2R$ is attributed to the rotation of fluorine octahedra through a small angle about one of the fourfold axes of the cubic cell. As was noted above, the preliminary optical investigations also demonstrated that the first distorted phase in the $(NH_4)_2KGaF_6$ elpasolite has a tetragonal symmetry. Therefore, if the transformation at T_1 in the $(NH_4)_2KGaF_6$ elpasolite is also associated with rotations of the octahedra, we can state with assurance that disordering of the fluorine atoms (or fluorine octahedra) is absent in the cubic phase. To put it differently, the change in the character of octahedron motion upon phase transitions at T_2 and T_3 can contribute to the mechanism of structural transformations only through further octahedron rotations with small entropy changes ΔS. On the other hand, close examination of the structure shows that, under the assumption of octahedron disordering in the $Fm\bar{3}m$ phase, the rotation of orientationally disordered octahedra through a small angle cannot provide for the formation of a tetragonal structure with rigid octahedra. Consequently, the considerable entropy change ($\Delta S_2 + \Delta S_3$) most likely corresponds to the ordering of other structural units.

As far as we know, only fragmentary data are available on the properties of crystals belonging to the $(NH_4)_2B^+M^{3+}F_6$ elpasolite family, namely, $(NH_4)_2KAlF_6$ [17], $(NH_4)_2NaFeF_6$ [18], and $(NH_4)_2NaInF_6$ [19].

Hirokawa and Furukawa [17] investigated the $(NH_4)_2KAlF_6$ elpasolite by the DTA technique and revealed two phase transitions at $T_1 = 250$ K and $T_2 = 186$ K. Unfortunately, they did not determine the relevant entropy changes. However, the ratio of areas under the DTA signal anomalies (proportional to the entropy change) indicates that $[\Delta S_2 = \Delta H_2/T_2] \gg [\Delta S_1 = \Delta H_1/T_1]$. In other words, the entropy ratio for the $(NH_4)_2KAlF_6$ elpasolite is identical to that for the $(NH_4)_2KGaF_6$ elpasolite. The inference made in [17] coincides with our opinion that the phase transition at T_1 is a displacive-type transformation and is most likely associated with rotations of fluorine octahedra through a small angle. Reasoning from the NMR data, Hirokawa and Furukawa [17] argued that the second phase transition, which is accompanied by a substantial entropy change, is most probably due to the ordering of ammonium ions. Unlike the $(NH_4)_3M^{3+}F_6$ (M^{3+} = Al and Ga) cryolites, in which the spin-lattice relaxation times of fluorine ions and protons change significantly upon phase transitions [4, 8, 11], the $(NH_4)_2KAlF_6$ elpasolite is characterized by a considerable change only in the T_{1H} time at the T_2 temperature [17].

In the high-temperature cubic phase, the N–H bonds are dynamically disordered and equiprobably directed to three fluorine ions of the same face of an $(AlF_6)^{3-}$ octahedron. In an intermediate phase, ammonium tetrahedra remain disordered but three orientations of each N–H bond become nonequivalent due to the lowering of the symmetry. The correlation time of anion reorientation is very long. This suggests a low probability of dynamic disordering of fluorine octahedra in the intermediate phase. In the low-temperature phase, hydrogen atoms are predominantly bonded to one of three fluorine ions. All the aforementioned features are confirmed by the data on the relaxation times of hydrogen and aluminum and the temperature dependence of the second moment of the H and F NMR spectra [17].

The assumption that the ammonium ions in the 8*c* positions can be orientationally disordered is confirmed by the unusually large temperature parameter of hydrogen atoms in the cubic phase of $(NH_4)_2NaInF_6$ [19], which is appreciably larger than the temperature parameters of the other atoms.

If this disordering of ammonium ions actually occurs in the cubic phase, their complete ordering in the low-temperature phase should be attended by the entropy change $\Delta S = 2R\ln 3 = R\ln 9 = 18.3$ J/mol K. This value exceeds the entropy change observed in the experiment for the $(NH_4)_2KGaF_6$ elpasolite : $\Sigma\Delta S_i = 16$ J/mol K.

6. CONCLUSION

It was demonstrated that the phase transition from the cubic phase in the $(NH_4)_2KGaF_6$ and $(NH_4)_2KAlF_6$ elpasolites is accompanied by a small entropy change. This disagrees with the existing elegant model of structural transformations, which is based only on the orientational ordering of the NH_4^+ (in the 4*b* position) and $M^{3+}F_6^-$ ionic groups [7, 8]. The determination of the actual positions of fluorine and hydrogen atoms calls for further structural investigations. Moreover, when constructing a model of phase transitions in ammonium compounds, the possible softening of rotational vibrational modes of fluorine octahedra should be taken into account.

ACKNOWLEDGMENTS

We are grateful to S.V. Mel'nikova for performing the polarization-optical investigations.

This work was supported by the Russian Foundation for Basic Research (project no. 00-02-16034) and the International Association of Assistance for the promotion of co-operation with scientists from the New Independent States of the former Soviet Union (project INTAS no. 97-10177).

REFERENCES

1. K. S. Aleksandrov and S. V. Misyul', Kristallografiya **26** (5), 1074 (1981) [Sov. Phys. Crystallogr. **26**, 612 (1981)].
2. I. N. Flerov, M. V. Gorev, K. S. Aleksandrov, *et al.*, Mater. Sci. Eng., R **24** (3), 81 (1998).
3. E. G. Steward and H. P. Rooksby, Acta Crystallogr. **6** (1), 49 (1953).
4. K. Moriya, T. Matsuo, H. Suga, and S. Seki, Bull. Chem. Soc. Jpn. **52** (11), 3152 (1979).
5. R. A. Vecher, L. M. Volodkovich, G. S. Petrov, and A. A. Vecher, Thermochim. Acta **87**, 377 (1985).
6. K. Kobayashi, T. Matsuo, and H. Suga, Solid State Commun. **53** (8), 719 (1985).
7. K. Moriya, T. Matsuo, H. Suga, and S. Seki, Bull. Chem. Soc. Jpn. **50** (8), 1920 (1977).
8. A. Tressaud, S. Khairoun, L. Rabardel, *et al.*, Phys. Status Solidi A **96**, 407 (1986).
9. M. V. Gorev, I. N. Flerov, and A. Tressaud, J. Phys.: Condens. Matter **11**, 7493 (1999).

10. I. N. Flerov, M. V. Gorev, and T. V. Ushakova, Fiz. Tverd. Tela (St. Petersburg) **41** (3), 523 (1999) [Phys. Solid State **41**, 468 (1999)].
11. A. Sasaki, Y. Furukawa, and D. Nakamura, Ber. Bunsenges. Phys. Chem. **93**, 1142 (1989).
12. M. Lorient, R. van der Muhll, A. Tressaud, and J. Raves, Solid State Commun. **40**, 847 (1981).
13. S. Morup and N. Thrane, Solid State Commun. **11** (10), 1319 (1972).
14. S. Morup and N. Thrane, Phys. Rev. B **8** (3), 1020 (1973).
15. S. V. Mel'nikova, S. V. Misyul', A. F. Bovina, and M. L. Afanas'ev, Fiz. Tverd. Tela (St. Petersburg) **42** (2), 336 (2000) [Phys. Solid State **42**, 345 (2000)].
16. M. V. Gorev, I. N. Flerov, S. V. Mel'nikova, *et al.*, Izv. Akad. Nauk, Ser. Fiz. **64** (6), 1104 (2000).
17. K. Hirokawa and Y. Furukawa, J. Phys. Chem. Solids **49** (9), 1047 (1988).
18. J. Pebler, E. Herdtweck, W. Massa, and R. Schmidt, *Studies in Inorganic Chemistry* (Elsevier, Amsterdam, 1983), Vol. 3.
19. A. Roliff, D. Trinschek, and M. Jansen, Z. Anorg. Allg. Chem. **621**, 737 (1995).

Translated by O. Borovik-Romanova

Physics of the Solid State, Vol. 43, No. 12, 2001, pp. 2307–2310. Translated from Fizika Tverdogo Tela, Vol. 43, No. 12, 2001, pp. 2214–2217.
Original Russian Text Copyright © 2001 by Vtyurin, Bulou, Krylov, Afanas'ev, Shebanin.

LATTICE DYNAMICS AND PHASE TRANSITIONS

The Cubic-to-Monoclinic Phase Transition in $(NH_4)_3ScF_6$ Cryolite: A Raman Scattering Study

A. N. Vtyurin*, A. Bulou, A. S. Krylov*, M. L. Afanas'ev*, and A. P. Shebanin*****

** Kirensky Institute of Physics, Siberian Division, Russian Academy of Sciences,*
Akademgorodok, Krasnoyarsk, 660036 Russia
e-mail: vtyurin@iph.krasn.ru
*** Université du Maine, Le Mans, Cedex 9, 72085 France*
**** Institute of Geology, Siberian Division, Russian Academy of Sciences,*
ul. Akad. Koptyug 3, Novosibirsk, 630090 Russia

Received May 8, 2001

Abstract—This paper reports on a Raman study of the cubic-to-monoclinic phase transition in $(NH_4)_3ScF_6$ cryolite. We observed sharp anomalies in the frequencies and half-widths of the Raman lines corresponding to internal vibrations of the ScF_6^{3+} ions and to lattice vibrations; no soft lattice mode condensation was revealed. It is concluded that the phase transition studied is related primarily to the orientational ordering of these ions. *© 2001 MAIK "Nauka/Interperiodica".*

1. INTRODUCTION

Cryolites are a family of perovskite-like crystals ($Fm3m$ space group of the undistorted structure, $Z = 4$). They appear to be promising subjects for investigation both as having application potential and as model media for use in studying phase transition (PT) mechanisms [1]. Investigation of the phase transitions occurring in fluorine compounds of this family is usually complicated by their fairly high temperatures; the presence of ammonium ions in the structure reduces the phase transition temperatures [2], thus making them particularly attractive for investigation.

It is presently established that in most ammonium-containing cryolites, phase transitions are associated with orientational motion of the MeF_6^+ and NH_4^+ molecular ions and that the sequence of the phase transformations, their temperatures, and mechanisms vary substantially depending on the radius of the trivalent cation [2]. In the $(NH_4)_3ScF_6$ cryolite, phase transitions were observed to occur in the order $Fm3m$ ($Z = 4$) $\longleftrightarrow$ $P12_1/n1$ ($Z = 2$) $\longleftrightarrow$ $I12/m1$ ($Z = 16$) $\longleftrightarrow$ $I\bar{1}$ ($Z = 16$), with the transition points $T_1 = 330$, $T_2 = 293$, and $T_3 = 243$ K, respectively [2, 3]. The cubic symmetry of the high-temperature phase (shown in Fig. 1) assumes that at least one of the ammonium ion sublattices [denoted by $(NH)_4I$ in Fig. 1] is orientationally disordered (the corresponding ion local symmetry is O_h); it thus appears logical to assume that the observed sequence of the phase transitions (or, at any rate, the first of them) is associated with the ordering of these ions. At the same time, it was pointed out in [2, 3] that the entropy change at the first PT is too large to be accounted for by the ordering of the NH_4^+ ions alone and the possibility of simultaneous orientational ordering of the ScF_6^{3+} sublattice occurring in this transition was suggested. The present work is aimed at establishing the part played by the molecular ions in the mechanism of this transition.

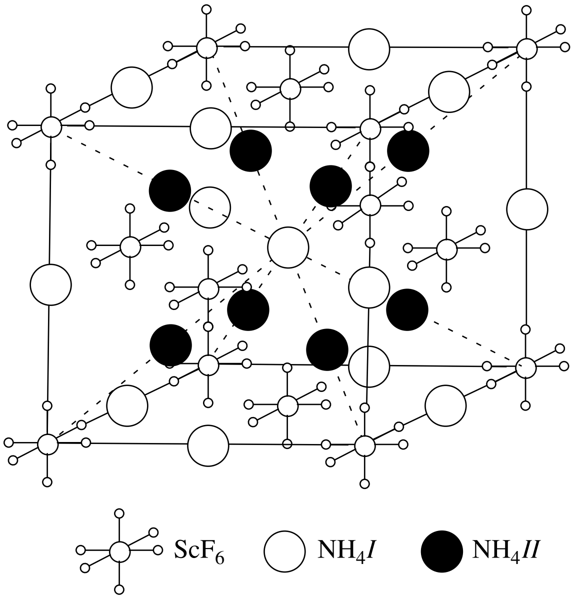

Fig. 1. Structure of the cubic phase of $(NH_4)_3ScF_6$.

1063-7834/01/4312-2307$21.00 © 2001 MAIK "Nauka/Interperiodica"

2. EXPERIMENT

The compound was prepared by reacting equivalent amounts of NH_4F with Sc_2O_3 in HF (10%). Faceted single crystals were grown through slow controlled evaporation of a neutral saturated aqueous solution at 305 K over 8 months. The crystals were thin rectangular plates with well-developed faces (typically measuring 5 × 5 × 0.5 mm); they did not contain defects or inclusions visible under a microscope and were used in spectral measurements without any additional processing. The spectra were obtained on Jobin Ivon U-1000 and T-64000 Raman spectrometers with CCD detector arrays and a set of microattachments. In the latter spectrometer, the high–frequency spectra of the broad bands of internal ion vibrations were measured in a single-monochromator arrangement, while in the region below 1000 cm^{-1}, triple-monochromator arrangement with dispersion subtraction was employed to suppress the elastic-scattering wing as much as possible; the low-frequency cutoff was at 8 cm^{-1}. The spectral slit width was varied from 5 cm^{-1} (at high frequencies) to 1 cm^{-1}, the spectral range of the CCD array cell used in the triple monochromator arrangement was 650/1024 cm^{-1}, and the signal accumulation time was up to 600 s. The excitation was provided by polarized 514.5-nm radiation from a 200-mW Ar$^+$ laser. The phase transition occurring at T_1 = 330 K is essentially first-order, and it is accompanied by considerable spontaneous sample deformation; in this connection, special measures were taken to preclude local heating and defect formation at the laser focal point. The sample temperature determined during spectral measurements was stabilized to within 0.2 K.

3. RESULTS AND DISCUSSION

Because of the earlier conjecture of the ammonium sublattice being possibly involved in the mechanism of the phase transition under study, we first studied the high-frequency part of the Raman spectrum (1200–4500 cm^{-1}), which includes the internal vibrations of these ions. Figure 2 shows the evolution of these spectra with temperature. We readily see that the spectra vary very little in this region; there are no sharp changes in the region of the (first-order) phase transition, and the background, which is apparently associated with the increasing contribution of the well-known strong anharmonicity of the NH_4^+ ion vibrations, grows steadily. The large linewidths, particularly in the 2800–3500 cm^{-1} interval (of the order of hundreds of wavenumbers), which corresponds to the internal valence vibrations of this ion [4], may originate both from strong anharmonicity and from orientational disorder on the ammonium sublattices. The considerable anharmonicity of these modes is also indicated by the intensities of the broad, double-phonon bands near 2500 and 3700 cm^{-1}, which grow with temperature.

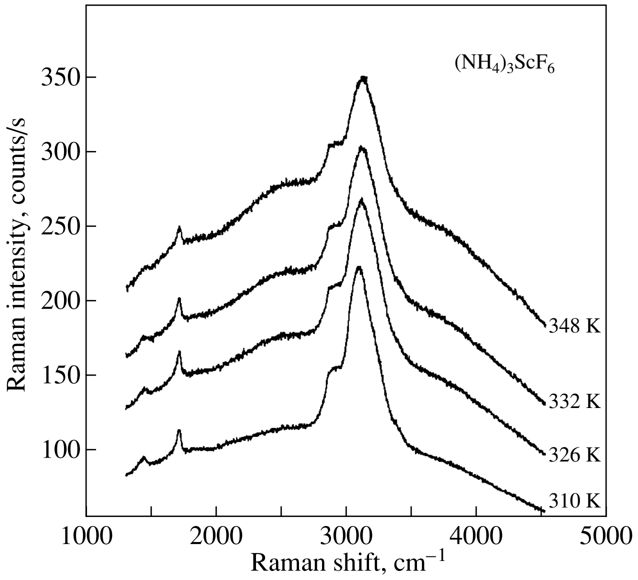

Fig. 2. Spectra of internal ammonium ion vibrations of the $(NH_4)_3ScF_6$ crystal.

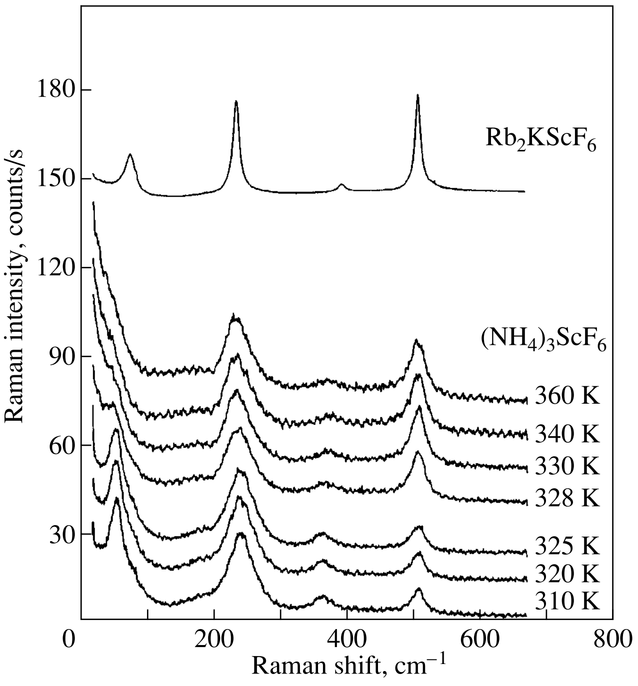

Fig. 3. Transformation of the low-frequency part of the $(NH_4)_3ScF_6$ spectra with temperature. For comparison, a spectrum of the isomorphous cubic phase of Rb_2KScF_6 is shown.

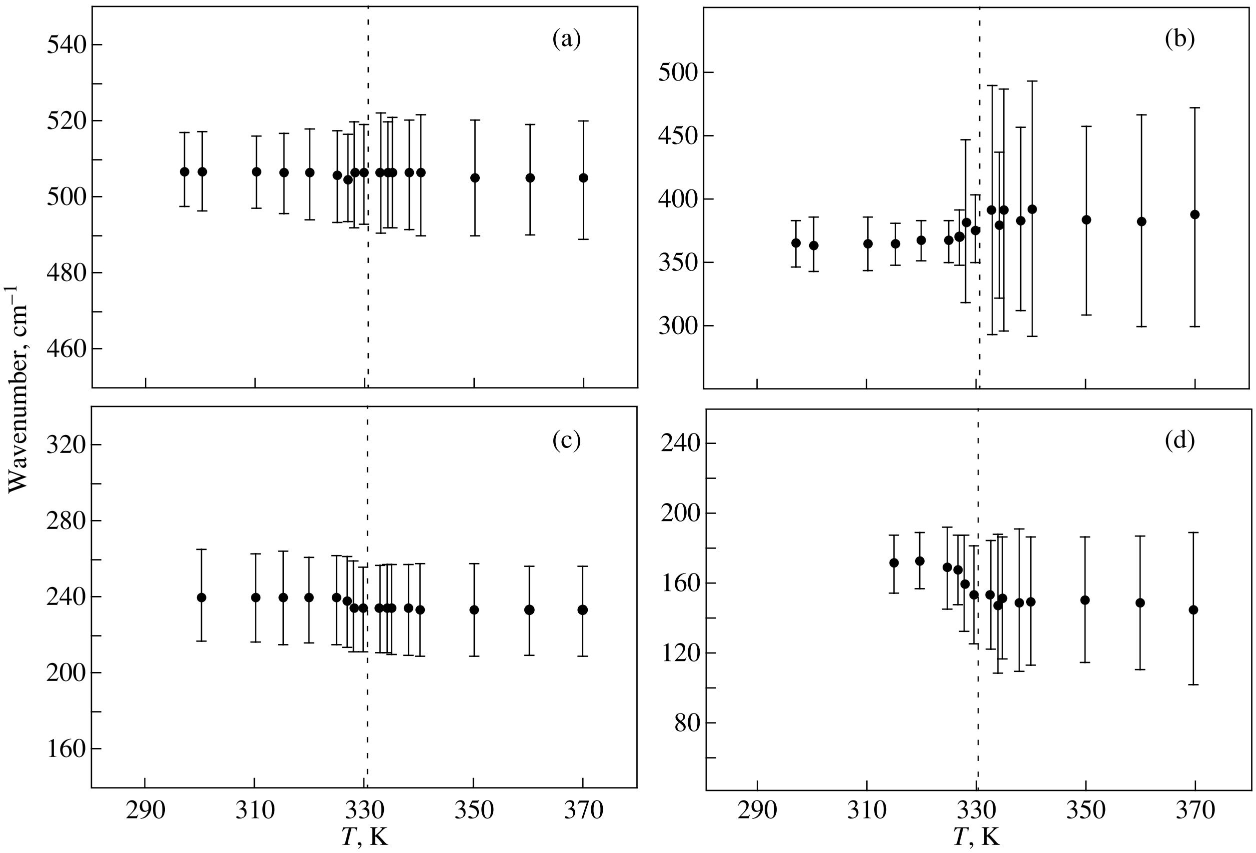

Fig. 4. Temperature dependences of the frequencies and line half-widths (shown by vertical lines) of (a)–(c) the internal ScF_6 ion vibrations and (d) the ammonium sublattice phonon vibration.

The second spectral region studied by us (8–650 cm^{-1} in Fig. 3) includes internal vibrational modes of the ScF_6 molecular ions and lattice vibrations. The octahedral site symmetry in the cubic phase coincides with the free-ion symmetry; thus the selection rules also coincide: the Raman-active free-ion vibration frequencies are $\nu_1(A_{1g})$ = 498 cm^{-1}, $\nu_2(E_g)$ = 390 cm^{-1}, and $\nu_5(F_{2g})$ = 230 cm^{-1} (the frequencies and notation were taken from [4]). The frequencies obtained for the cubic phase are 510, 385, and 240 cm^{-1} (values contained for 360 K), which indicates weak distortion of the ions by the lattice. At the same time, the lines are strongly broadened. For comparison, Fig. 3 also shows an unpolarized room-temperature spectrum of the isomorphous cubic phase of Rb_2KScF_6; one readily sees that the half-widths of the corresponding spectral lines in the crystal under study are a few times larger.

According to the selection rules for the cubic phase (see [5] for a comprehensive analysis), its Raman spectrum should contain one lattice-phonon line corresponding to the translational vibration of one of the ammonium sublattices (with T_d local ion symmetry). This line can be identified with the weak, strongly broadened band peaking near 150 cm^{-1} (360 K). The shift of its frequency compared to the spectrum of Rb_2KScF_6 correlates well with the change in the ion mass. Moreover, one also observes a broad wing of the central peak, which is evidently associated with the strong disorder in the cubic-phase structure.

Lowering the temperature down to the transition point to the monoclinic phase brings about considerable changes in this part of the spectrum. The widths of all lines decrease strongly, which is accompanied by an increase in their frequency (Fig. 4). A new line, seen clearly in Fig. 3, appears against the background of the low-frequency wing.

All these changes occur in a jump, within a 1–2 K interval, with no further modification of the spectrum being observed within the region of existence of the monoclinic phase. This correlates well with the first-order nature of this phase transition, although no noticeable hysteresis effects were revealed.

The strong broadening of the lines corresponding to the internal vibrations of the ScF_6^{3+} ions and to the $(NH)_4$*II* sublattice vibration in the cubic phase implies that they are also disordered. It is apparently the heavier ScF_6^{3+} ions that also primarily govern the nature of the broad low-frequency wing. The strong narrowing and the spectral-line shift to a higher frequency support the conjecture that the transition from the cubic to the monoclinic phase is associated with the ordering processes while the main ordering structural unit is the ScF_6^{3+} ions and, therefore, their internal modes are the most strongly modified. The ordering of the ScF_6^{3+} sublattice makes the potential relief of the structure as a whole more pronounced, and, as a result, the ammonium group vibrations are also modified, although to a lesser extent, whereas the internal vibrations of the ammonium ions remain strongly broadened. The extremely strong broadening of these modes makes it difficult to determine which of the ammonium sublattices is more disordered, however, the substantial change in the parameters of the lattice-phonon line at 150 cm^{-1} suggests that the $(NH)_4$*II* sublattice plays no less a part than the $(NH)_4$*I* sublattice in this transition. Judging from the appreciable widths of the internal vibrations of both ammonium sublattices, these sublattices also remain disordered in the monoclinic phase and their ordering may turn out to be a dominant factor in the mechanisms of lower temperature phase transitions.

ACKNOWLEDGMENTS

The authors express sincere gratitude to K.S. Aleksandrov and I.N. Flerov for the samples and fruitful discussions.

This study was supported by the INTAS Program (grant no. 97-10177), Russian Foundation for Basic Research (project no. 00-02-16034), and Integration Program of the Siberian Division of the RAS.

REFERENCES

1. K. S. Aleksandrov and B. V. Beznosikov, *Perovskite-like Crystals* (Sib. Otd. Ross. Akad. Nauk, Novosibirsk, 1999).
2. S. V. Mel’nikov, S. V. Misyul’, A. F. Bovina, and M. L. Afanas’ev, Fiz. Tverd. Tela (St. Petersburg) **42** (2), 336 (2000) [Phys. Solid State **42**, 345 (2000)].
3. I. N. Flerov, M. V. Gorev, and T. V. Ushakova, Fiz. Tverd. Tela (St. Petersburg) **41** (3), 523 (1999) [Phys. Solid State **41**, 468 (1999)].
4. K. Nakamoto, *Infrared Spectra of Inorganic and Coordination Compounds* (Wiley, New York, 1963; Mir, Moscow, 1966).
5. M. Cousi, S. Khairoun, and A. Tressaud, Phys. Status Solidi A **98** (1), 423 (1986).

Translated by G. Skrebtsov

Physics of the Solid State, Vol. 43, No. 12, 2001, pp. 2311–2312. Translated from Fizika Tverdogo Tela, Vol. 43, No. 12, 2001, pp. 2218–2219.
Original Russian Text Copyright © 2001 by Shmelev, Épshteĭn.

LOW-DIMENSIONAL SYSTEMS AND SURFACE PHYSICS

Plasma Properties of a Quasi-One-Dimensional Ring

G. M. Shmelev* and É. M. Épshteĭn**

** Volgograd State Pedagogical University, Volgograd, 400013 Russia*
e-mail: meglev@fizmat.vspu.ru
*** Institute of Radio Engineering and Electronics, Russian Academy of Sciences (Fryazino Branch),*
pl. Vvedenskogo 1, Fryazino, Moscow oblast, 141190 Russia

Received February 23, 2001

Abstract—The spectrum of plasma oscillations and the frequency of the dielectric relaxation of electrons in a quasi-one-dimensional ring are calculated. The plasmon spectrum is revealed to be equidistant. It is shown that, in contrast to the three-dimensional case, the dielectric relaxation is dispersive and, therefore, the distribution of carriers in quasi-one-dimensional rings can be studied by means of dielectric relaxation spectroscopy. *© 2001 MAIK “Nauka/Interperiodica”.*

The advancements made in the technology of quasi-one-dimensional rings [1, 2] have opened up fresh opportunities for the study and use of mesoscopic conductive systems. It should be noted that most of the investigations of such objects have been devoted to quantum phenomena (see, for example, [3, 4]). However, in [5–8], attention was drawn to the interesting classical properties of quasi-one-dimensional rings. In particular, it was shown that they possess electrodynamic nonlinearity not associated with the nonlinear properties of the material from which the rings are made but with their geometric configuration (geometric nonlinearity).

In the present paper, plasma properties of a quasi-one-dimensional ring are studied in the limiting cases of high and low frequencies corresponding to plasma oscillations and dielectric relaxation, respectively.

Let us consider a quasi-one-dimensional flat ring of radius R and width $d \ll R$. The potential $V(r, \zeta, \varphi, t)$ of the self-consistent field produced by the oscillating electrons in the ring is described by Poisson's equation,

$$\begin{aligned}\frac{\partial^2 V}{\partial r^2} + \frac{1}{r}\frac{\partial V}{\partial r} + \frac{\partial^2 V}{\partial \zeta^2} + \frac{1}{r^2}\frac{\partial^2 V}{\partial \varphi^2}\\ = -4\pi\rho(\varphi, t)\delta(\zeta)\Delta(r-R),\end{aligned} \tag{1}$$

where (r, ζ, φ) are the cylindrical coordinates whose origin is at the center of the ring and $\Delta(r - R)$ is similar to a delta function: it is equal to $1/d$ within a narrow interval $(R - d/2, R + d/2)$ and to zero outside of this interval. The linear charge density in the ring $\rho(\varphi, t)$ satisfies the continuity equation

$$\frac{\partial \rho}{\partial t} + \frac{1}{R}\frac{\partial J}{\partial \varphi} = 0, \tag{2}$$

where the current in the ring $J(\varphi, t)$ is

$$J = \frac{eNv}{2\pi R}. \tag{3}$$

Here, N is the number of electrons in the ring and $v(\varphi, t)$ is the velocity of the electrons in the self-consistent field.

1. For high frequencies ($\omega\tau \gg 1$, where τ is the mean free time), the velocity $v(\varphi, t)$ satisfies the equation of motion

$$\frac{\partial v}{\partial t} = -\frac{e}{mR}\frac{\partial V}{\partial \varphi}. \tag{4}$$

This equation assumes no collisions to occur over the period of plasma oscillations.

Taking the temporal Fourier transform and eliminating the variables ρ, J, and v yields an equation for the Fourier component $\bar{V}(r, \zeta, \varphi, \omega)$:

$$\begin{aligned}\frac{\partial^2 \bar{V}}{\partial r^2} + \frac{1}{r}\frac{\partial \bar{V}}{\partial r} + \frac{\partial^2 \bar{V}}{\partial \zeta^2} + \frac{1}{R^2}\frac{\partial^2 \bar{V}}{\partial \varphi^2}\\ = \frac{2e^2 N}{mR^3\omega^2}\Delta(r-R)\delta(\zeta)\frac{\partial^2 \bar{V}}{\partial \varphi^2}.\end{aligned} \tag{5}$$

We perform Hankel transformation with respect to r and Fourier transformation over ζ and φ:

$$\begin{aligned}\bar{V}(r, \zeta, \varphi, \omega) = \sum_{n=-\infty}^{\infty} e^{in\varphi}\\ \times \int_{-\infty}^{\infty}\frac{dq}{2\pi}e^{iq\zeta}\int_0^{\infty} J_n(kr)kdk\tilde{V}_n(k, q, \omega).\end{aligned} \tag{6}$$

By substituting Eq. (6) into Eq. (5), we can find $\tilde{V}_n(k, q, \omega)$. Taking the inverse Hankel and Fourier transforms and assuming that $r = R$ and $\zeta = 0$, we obtain a dispersion relation for the plasmons in the form

$$\omega^2 = \frac{n^2e^2N}{\pi m R^3}\int_0^\infty Q_{n-\frac{1}{2}}\left(\frac{R^2+\rho^2}{2R\rho}\right)\Delta(R-\rho)d\rho, \\ \approx \frac{n^2e^2N}{\pi m R^3 d}\int_0^d Q_{n-\frac{1}{2}}\left(1+\frac{x^2}{2R^2}\right)dx, \tag{7}$$

where $Q_\nu(x)$ is a Legendre function of the second kind. Taking into account the behavior of this function at $x \longrightarrow 1 + 0$ [9], we obtain the following formula for the plasmon spectrum in the quasi-one-dimensional ring ($R \gg d$):

$$\omega_n^2 = \frac{n^2e^2N}{\pi m R^3}\ln\frac{R}{d} \quad (n = 1, 2, 3\ldots). \tag{8}$$

It follows from Eq. (8) that the plasmon spectrum is equidistant. At $d \longrightarrow 0$, the frequency diverges, which is typical of one-dimensional systems (as is known, this is also the case with a long thin rod); for this reason, it is necessary to introduce a small, but finite, width of the quasi-one-dimensional ring.

At $R \sim 10^{-4}$ cm, $d \sim 10^{-5}$ cm, $m \sim 0.1m_e$, and $N \sim 10^3$ (which corresponds to a two-dimensional electron concentration $n_s \sim 10^{11}$ cm^{-2}), we have $\omega_1 \sim 10^{12}$ s^{-1} for the fundamental plasmon frequency.

2. For low frequencies ($\omega\tau \ll 1$), Eq. (4) is replaced by an equation for viscous motion,

$$v = -\frac{\mu}{R}\frac{\partial V}{\partial \varphi}, \tag{9}$$

where $\mu = e\tau/m$ is the electron mobility.

Carrying out the transformations as above, the dielectric-relaxation frequency is found to be

$$\omega_c = \frac{n^2eN\mu}{\pi R^3}\ln\frac{R}{d}. \tag{10}$$

It follows from Eq. (8) and Eq. (10) that, in the case of the quasi-one-dimensional ring, the dielectric-relaxation frequency ω_c at $\omega\tau \ll 1$ is connected to the frequency of plasma oscillations ω_n at $\omega\tau \gg 1$ through the same formula as that in the bulk material:

$$\omega_c = \omega_n^2\tau. \tag{11}$$

This means that we have an infinite spectrum of relaxation times (frequencies) instead of one Maxwell relaxation time. The physical meaning of this situation is obvious: an arbitrary initial deviation of the concentration of carriers in the ring from a homogeneous distribution can be expanded in terms of the eigenfunctions of the ring (Bessel functions), and different spatial (Bessel) harmonics will correspond to different relaxation times. The relaxation frequency increases as n^2 with increasing harmonic mode number n. Thus, in contrast to the three-dimensional case, the dielectric relaxation is dispersive. Hence, the distribution of carriers in rings can be studied by means of dielectric-relaxation spectroscopy.

ACKNOWLEDGMENTS

The authors are grateful to I.I. Maglevannyĭ for discussions of the results.

This study was supported by the Ministry of Education of the Russian Federation and the Russian Foundation for Basic Research.

REFERENCES

1. A. Lorke, L. J. Luyken, A. O. Govorov, *et al.*, Phys. Rev. Lett. **84** (10), 2223 (2000).
2. N. T. Bagraev, A. D. Buravlev, V. K. Ivanov, *et al.*, Fiz. Tekh. Poluprovodn. (St. Petersburg) **34** (7), 846 (2000) [Semiconductors **34**, 817 (2000)].
3. M. V. Moskalets, Eur. Phys. J. B **7**, 645 (1999).
4. J. Baker, G. Vignale, and A. G. Rojo, Phys. Rev. **60** (12), 8804 (1999).
5. E. M. Epshtein and G. M. Shmelev, Phys. Scr. **61**, 216 (2000).
6. E. M. Epshtein, G. M. Shmelev, and I. I. Maglevanny, J. Phys. A **33**, 6017 (2000).
7. G. M. Shmelev, É. M. Épshteĭn, and G. A. Syrodoev, Zh. Tekh. Fiz. **70** (10), 125 (2000) [Tech. Phys. **45**, 1354 (2000)].
8. E. M. Epshtein, I. I. Maglevanny, and G. M. Shmelev, Phys. Low-Dimens. Struct. **3/4**, 109 (2000).
9. *Heigher Transcendental Functions (Bateman Manuscript Project)*, Ed. by A. Erdelyi (McGraw-Hill, New York, 1953; Nauka, Moscow, 1965), Vol. 1.

Translated by A. Poushnov

Physics of the Solid State, Vol. 43, No. 12, 2001, pp. 2313–2320. Translated from Fizika Tverdogo Tela, Vol. 43, No. 12, 2001, pp. 2220–2227.
Original Russian Text Copyright © 2001 by Bagnich, Konash.

LOW-DIMENSIONAL SYSTEMS AND SURFACE PHYSICS

The Influence of Inhomogeneous Properties of a System on the Percolation Process in Two-Dimensional Space

S. A. Bagnich and A. V. Konash
Institute of Molecular and Atomic Physics, Belarussian Academy of Sciences, Minsk, 220072 Belarus
e-mail: bagnich@imaph.bas-net.by

Received January 23, 2001; in final form, March 27, 2001

Abstract—The percolation process in a two-dimensional inhomogeneous lattice is studied by the Monte Carlo method. The inhomogeneous lattice is simulated by a random distribution of inhomogeneities differing in size and number. The influence of inhomogeneities on the parameters (critical concentration, average number of sites in finite clusters, percolation probability, critical exponents, and fractal dimension of an infinite cluster) characterizing the percolation in the system is analyzed. It is demonstrated that all these parameters essentially depend on the linear size of inhomogeneities and their relative area. *© 2001 MAIK “Nauka/Interperiodica”.*

1. INTRODUCTION

Percolation processes were first considered by Broadbent and Hammersley [1]. These processes can occur in different physical systems. The percolation model was successfully applied to the description of disordered systems (for example, porous media) and related phenomena. Among these are rock fracture, fragmentation [2] and gelation [3, 4], conduction in a random resistance grating [5] and strongly inhomogeneous media [6], and propagation of forest fires [7, 8] and epidemics [9, 10]. This approach made it possible to describe the electronic properties of doped semiconductors [11].

Relying on the percolation theory, Kopelman *et al.* [12, 13] developed a cluster formalism for describing the electronic excitation energy transfer in inhomogeneous systems. This model is based on mathematical functions, such as the percolation probability P_∞ and the average number I_{AV} of sites in a cluster. The dependence of these quantities on the concentration C of sites through which the energy migrates is determined by the scaling relationships [14]

$$I_{\mathrm{AV}} \propto |C/C_c - 1|^{-\gamma}, \qquad (1)$$

$$P_\infty \propto |C/C_c - 1|^{\beta}, \qquad (2)$$

where C_c is the critical concentration of sites and β and γ are the critical exponents, which depend only on the space dimension. Investigations into the transfer of electronic excitation energy in mixed molecular crystals [15, 16] and solid solutions of organic compounds in low-molecular vitrifying solvents [17] have demonstrated that the critical exponents determined experimentally coincide with those obtained within the percolation theory for two-dimensional and three-dimensional spaces, respectively (see table). However, recent studies [18–20] of similar processes in porous matrices revealed a discrepancy between the experimental and theoretical critical exponents. Saha *et al.* [21] also noted that the matrix affects the topology of the energy transfer. In [18–20, 22], this effect was explained in terms of the inhomogeneous properties of porous glasses used as matrices. A microscopic inhomogeneity of porous glass brings about a change in the effective topology of the space in which percolation processes occur. In turn, this can affect the formation and growth of clusters from incorporated molecules.

In this work, we performed the Monte Carlo computer simulation of the percolation process on a square lattice with inhomogeneities differing in size and relative area in order to elucidate the possible effect of these inhomogeneities on the critical concentration C_c, the average number I_{AV} of sites in a cluster, the percola-

Critical exponents for mixed molecular crystals and solid solutions of organic compounds

Critical exponents	Percolation theory		Isotopically mixed molecular crystals	Chemically mixed molecular crystals	Solid solution of benzaldehyde in ethanol	Ethanol solution of benzaldehyde in porous glass
	2*D*	3*D*				
β	0.14	0.41	0.13	0.13	0.41	0.25
γ	2.1	1.6	2.1	2.09	1.7	1.95

tion probability P_∞, and the fractal dimension d_f of an infinite cluster.

2. COMPUTATIONAL TECHNIQUE

We will solve the site percolation problem, because it is the most important from the viewpoint of energy migration in heterogeneous systems. Let us consider a lattice formed by a set of sites and bonds. It is assumed that C is the fraction of sites painted black in a random manner (the sampling was performed by the Monte Carlo method). Any two nearest-neighbor black sites are considered to be connected to each other. An aggregate of black sites connected to one another either directly or through chains of connected black sites is referred to as a cluster. Within the cluster formalism, the dynamics of the initiation of percolation with an increase in C is as follows. At $C = 0$, black clusters are absent in the system. At $C \ll 1$, black clusters consist of a small number of sites: single sites, pairs, triads, etc. However, as the percolation threshold is approached, particular clusters merge together and their average size increases. The average number of sites in finite clusters is defined by the expression

$$I_{\mathrm{AV}} = \frac{\sum_m i_m m^2}{\sum_m i_m m}, \tag{3}$$

where i_m is the number of clusters containing m sites. The analytical dependence of I_{AV} on the fraction C is unknown. Numerical calculations showed that, at $C \longrightarrow C_c - 0$, the quantity I_{AV} goes to infinity [see relationship (1)]. At $C = C_c$, an infinite cluster extending over the whole space arises for the first time. The concentration C_c at which an infinite cluster of black sites is formed corresponds to the percolation threshold. According to [23, 24], the percolation probability is defined as the ratio between the number of sites forming an infinite cluster and the total number of sites in the lattice. In practice, we deal with systems of a finite size. In the numerical simulation, the number of sites contained in the maximum cluster ($m_{\max}$) is calculated and the percolation probability is estimated from the formula

$$P_{\max} = \frac{m_{\max}}{L \times L}, \tag{4}$$

where L is the linear size of the lattice. Extensive simulation and theoretical considerations show that, near $C \longrightarrow C_c + 0$, the percolation probability decreases as the power law (2).

All the results presented in this work were obtained from simulations of the percolation process on a 200 × 200 lattice. Despite the currently available methods of computer reconstruction of Vycor porous glasses (see, for example, [25]), the inhomogeneous system was initially simulated by introducing square inhomogeneities of a specified size into the lattice, as was done by Bujan-Nunez *et al.* [26]. For this purpose, a new lattice with a cell size equal to the linear size of inhomogeneities was constructed on the primary lattice. In the course of Monte Carlo simulation, some of the cells in the new lattice were chosen as inhomogeneities and all the primary lattice sites lying within the chosen inhomogeneities were eliminated from consideration. Note that the computer experiments were performed with inhomogeneous lattice configurations for which the percolation could occur in two mutually perpendicular directions simultaneously. Figure 1 displays variants of the model matrices with inhomogeneities differing in linear size and relative area.

3. RESULTS AND DISCUSSION

First and foremost, we analyzed how the inhomogeneity of the matrix affects the critical concentration. In each case, the value of C_c was determined by two methods. According to Hoshen *et al.* [27], the critical concentration can be determined from the position of the maximum in the dependence of the reduced average number I'_{AV} of sites in clusters on the site concentration C:

$$I'_{\mathrm{AV}} = \frac{\sum_m i_m m^2}{\sum_m i_m m} - \frac{m_{\max}^2}{\sum_m i_m m}. \tag{5}$$

A similar dependence for a clear lattice is depicted in Fig. 2. Note that, in this case, the accuracy of determining the critical concentration is not very high. As can be seen from Fig. 2, the dependence obtained by averaging over 200 realizations exhibits a rather smeared maximum, even though the concentration in the course of the experiment was changed with the step $\Delta C = 0.001$. For this reason, the critical concentration for each realization was taken as the concentration corresponding to the onset of the percolation between opposite sides of the lattice. This approach made it possible to determine the average critical concentration and the frequency of occurrence of a particular critical concentration during the simulation of the percolation in the system. Figure 3 displays a histogram that allows one to judge the probability of an infinite cluster forming at a given concentration of black sites. The critical concentration determined from these data agrees closely with the value obtained using other methods for a square lattice [7, 11, 14, 24]. The introduction of inhomogeneities into the lattice considerably affects the critical concentration: its value increases substantially (Fig. 4). The strongest effect is observed for the smallest inhomogeneities. The increase in the critical concentration in the inhomogeneous matrix can be explained in the following way. In a homogeneous lattice, the shortest path between any two points is a straight line (without regard for the lat-

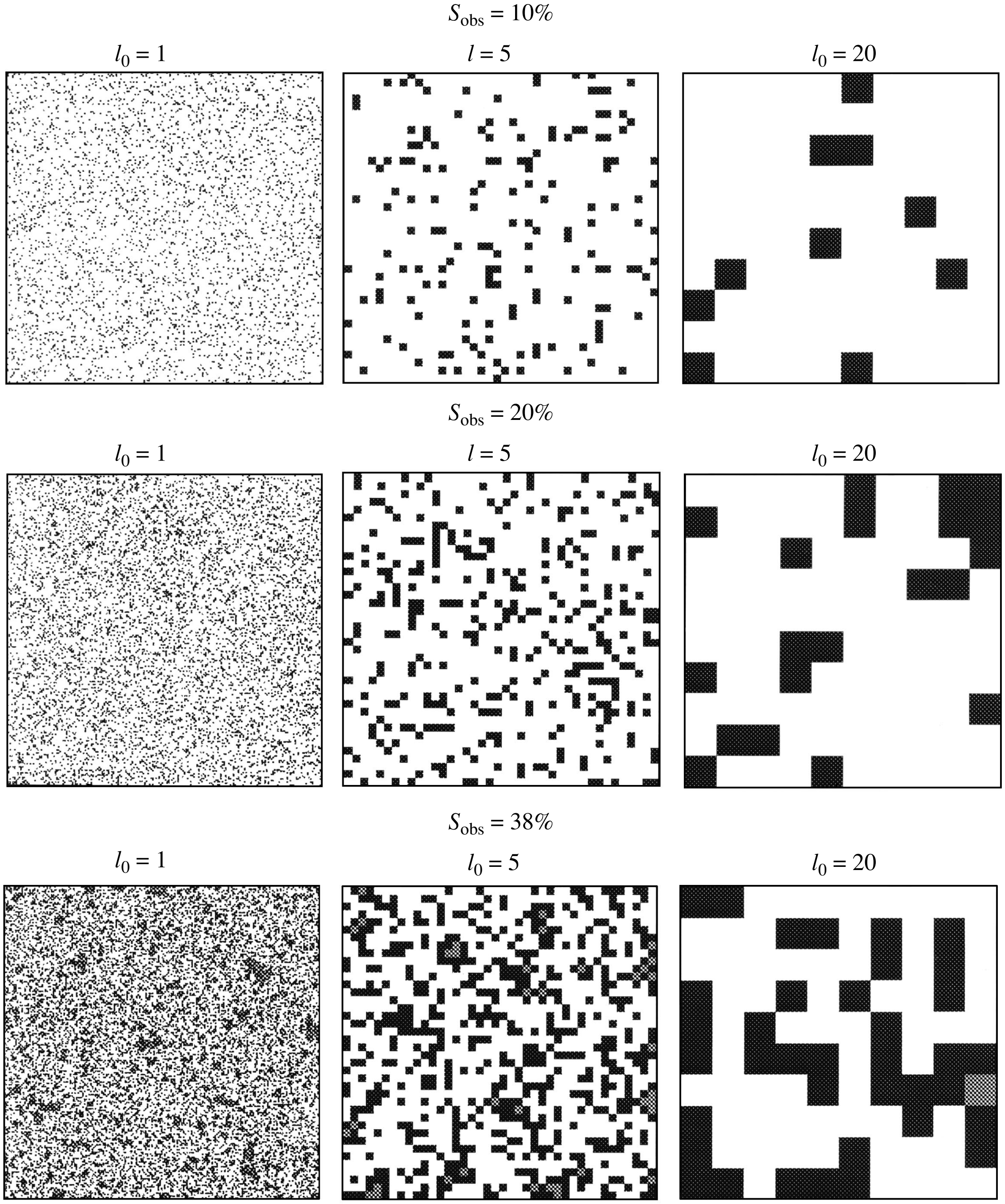

Fig. 1. Variants of matrices with inhomogeneities differing in linear size and relative area.

tice structure on minimum scales). In an inhomogeneous matrix, the shortest path can substantially deviate from a straight line. It is clear that the larger the number of inhomogeneities (or the larger the relative area of inhomogeneities) in the matrix, the longer the shortest path between any two points. Upon introduction of inhomogeneities into the lattice, the total number of accessible sites decreases, whereas the number of black sites required for connecting any two points in the system increases. Consequently, the critical concentration in the inhomogeneous matrix should increase. Recall that, in this case, the critical concentration is equal to the ratio of the number of black sites (this number corresponds to the onset of percolation) to the total number of sites in the system. This effect becomes less pronounced with an increase in the linear size of inhomogeneities, because, at the same relative area, the larger-sized inhomogeneities turn out to be localized in certain

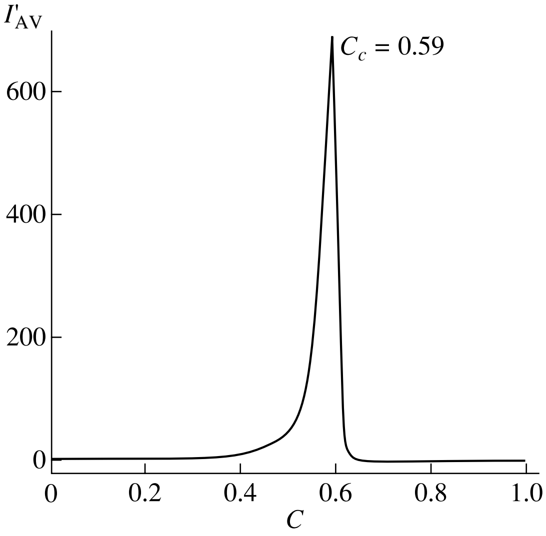

Fig. 2. Dependence of I'_{AV} on the concentration of occupied sites C for a 200 × 200 square lattice. Averaging is performed over 200 realizations.

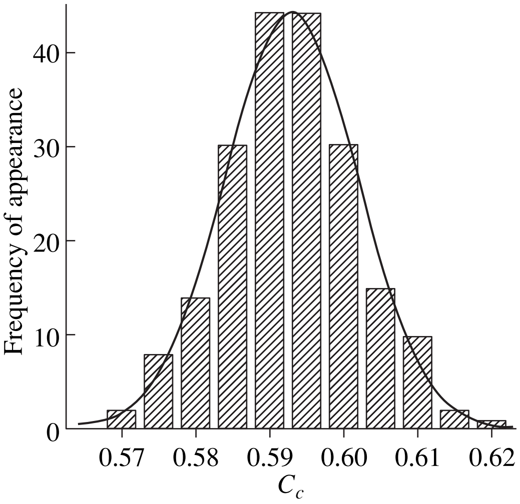

Fig. 3. Probability of a percolation cluster forming as a function of the concentration of occupied sites C_c for the percolation process on the square lattice.

lattice regions. As a result, part of the matrix behaves as a homogeneous lattice. The larger the linear size of inhomogeneities, the greater the fraction of the homogeneous part.

As is known, the behavior of different quantities in the vicinity of the percolation threshold is adequately described by the critical exponents. The critical exponents depend only on the space dimension [14]. However, for each space dimension, there exists a great number of different problems. According to modern concepts, the critical exponents for all problems in a space of the same dimension are identical to one another. The physical reasons for the universality of critical exponents likely lie in the fact that the exponents are determined by the structure of clusters in the vicinity of the percolation threshold. In this case, the geometric properties of clusters play the dominant role, because they manifest themselves at large distances (of the order of the correlation radius). These distances in the vicinity of the percolation threshold are considerably larger than the lattice spacing (in the case of lattice problems). Therefore, the cluster geometry does not depend on the type of lattice used in solving a particular problem. Moreover, a particular problem can be specified not on a periodic lattice but on sites randomly arranged in space; this circumstance will not affect the structure of large-sized clusters. However, the cluster geometry is substantially affected by the space dimension. For these reasons, the critical exponents depend on the dimension of a particular problem rather than on its type.

Therefore, unlike the percolation thresholds, which depend on the type of problem involved, the critical exponents exhibit a certain universality. This leads us to an important conclusion: if the results of a physical experiment are treated within the percolation theory and the microscopic structure is not quite clear, it is necessary, first of all, to compare the critical exponents with the theory, because they depend only on the space dimension.

The dependence of the average number of sites in a cluster on the reduced concentration C/C_c of occupied sites is plotted on the log–log scale in Fig. 5. As is clearly seen, this dependence over a wide range of concentrations is well described by the power law predicted by formula (1). The deviation from the power dependence near the critical concentration is caused by

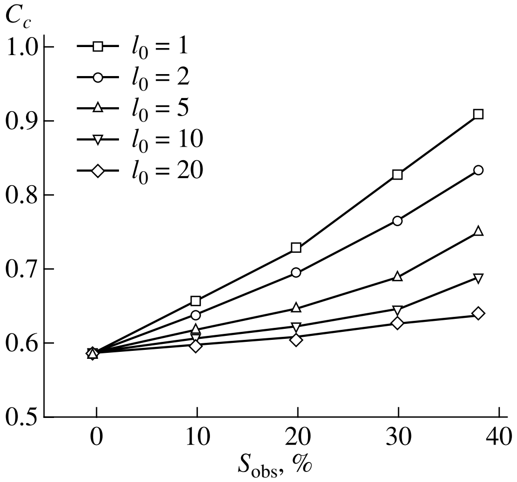

Fig. 4. Dependences of the critical concentration C_c on the inhomogeneity fraction S_{obs} in the matrix at different linear sizes l_0 of inhomogeneities.

the finite sizes of the lattice. In fact, as follows from formula (1), this quantity should increase to infinity at the critical point, which, in principle, is impossible in systems of a finite size. The critical exponent γ determined from this dependence coincides with the value obtained by the same method in [27] and is slightly less than the exponents derived from other techniques [14]. Figure 6 displays the dependences of the critical exponent γ (determined in a similar manner) on the linear size of inhomogeneities at different values of their relative areas. It can be seen that the critical exponent for inhomogeneities with $l_0 = 1$ coincides with the exponent for the homogeneous lattice. As the linear size increases, the critical exponent first increases (to $l_0 = 10$) and then decreases. An increase in the relative area of inhomogeneities in the matrix leads to an increase in the critical exponent γ. The introduction of inhomogeneities into the lattice brings about separation of sites belonging to the same cluster. The critical exponent γ characterizes the cluster growth with an increase in the concentration. The larger the size of inhomogeneities and the larger the relative inhomogeneity area, the higher the concentration at which sites begin to coalesce into clusters and small-sized clusters merge into large-sized clusters. To state this differently, an increase in the average cluster size with an increase in the concentration is more pronounced than that in the system with an homogeneous matrix; in fact, this corresponds to an increase in the critical exponent γ. It is worth noting that all the lattices studied are characterized by a linear dependence similar to that depicted in Fig. 5. The observed decrease in the exponent γ for matrices with inhomogeneities of size $l_0 = 20$ can be explained by the finite sizes of the lattices. As can be seen from Fig. 1, an increase in the inhomogeneity size brings about the transformation of the inhomogeneous matrix into the matrix with a spatially confined structure. This is especially pronounced for lattices with the maximum relative inhomogeneity area used in the computer experiment. Numerical simulation revealed that, for matrices at $l_0 = 20$ and $S_{\text{obs}} =$ 38%, an increase in the lattice size to 400 × 400 is accompanied by an increase in the critical exponent γ to 2.94 (for a 200 × 200 lattice, $\gamma = 2.50$). Note that an increase in the inhomogeneity size to 40 results in a further decrease in the exponent γ.

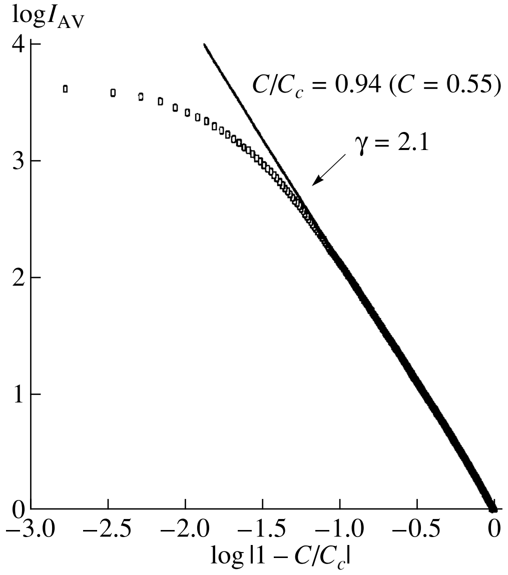

Fig. 5. Dependence of $\log I_{\text{AV}}$ on $\log|1 - C/C_c|$ for the square lattice.

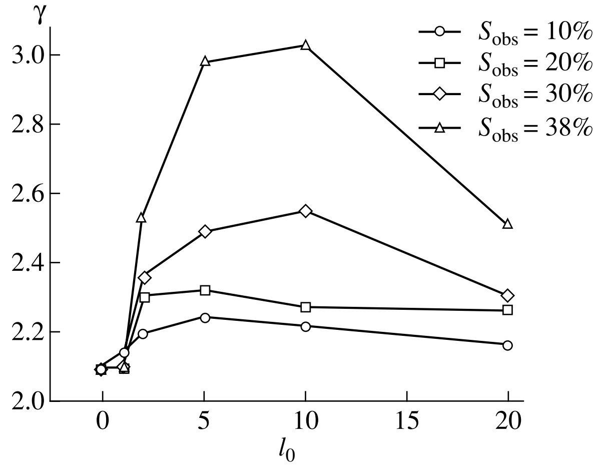

Fig. 6. Dependences of the critical exponent γ on the linear inhomogeneity size l_0 in lattices at different relative inhomogeneity areas S_{obs}.

A more intricate situation arises with dependence of the percolation probability on the concentration of occupied sites. According to formula (2), this dependence on the log–log scale should be represented by a straight line whose slope corresponds to the critical exponent β. Unfortunately, the treatment of our results for the square lattice demonstrated that this dependence does not exhibit a linear behavior with the appropriate slope over the entire range of concentrations ($C > C_c$). Furthermore, analysis of the available data on this problem also showed some disagreement regarding the range of applicability of relationship (2). In particular, Hoshen *et al.* [28] observed the scaling dependence (2) for a 4000 × 4000 triangular lattice only in the ($C - C_c$) concentration range from 10^{-4} to 2×10^{-2}. At higher concentrations, the dependence deviated from linear behavior. In our simulation, the results obtained in this concentration range strongly depend on the finite sizes of the lattice, as is the case with the average number of sites in clusters. Moreover, Hoshen *et al.* [27] observed a linear dependence for a 400 × 400 square lattice in the concentration range from 2×10^{-3} to 7×10^{-2}, even though the slope corresponded to $\beta = 0.19$. Therefore, relationship (2) is valid only in a very narrow concentration range in the vicinity of the percolation threshold. However, reasoning from the results of investigations into the transfer of electronic excitation energy in

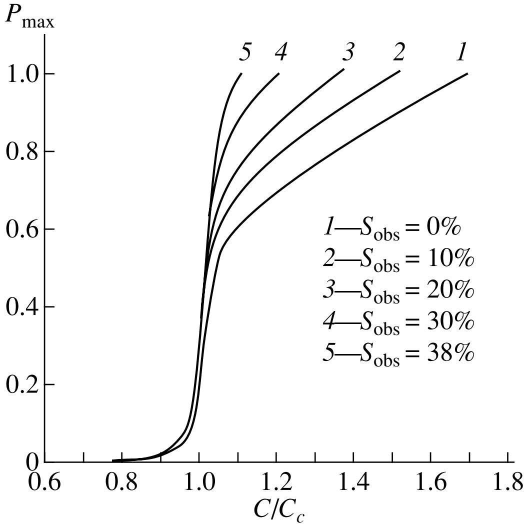

Fig. 7. Dependences of P_{max} on the reduced concentration C/C_c for lattices with inhomogeneities of the linear size $l_0 = 1$ at different inhomogeneity fractions in the matrix.

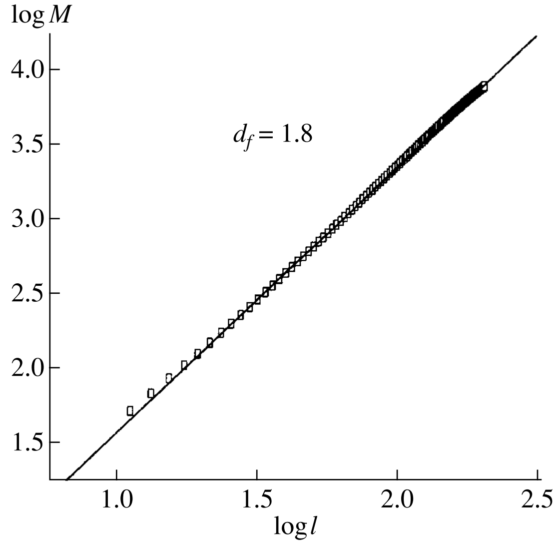

Fig. 8. Dependence of log$M$ on log$l$ for the square lattice free of inhomogeneities.

mixed molecular crystals, Kopelman [13] made the inference that the concentration range of applicability of the critical exponents for energy migration is considerably wider than that for any other critical phenomenon in physics. From the viewpoint of the energy transfer, it is important that the dependence of the probability of trapping an exciton (which is governed by the percolation probability in the range of concentrations higher than the critical concentration [12]) on the reduced concentration C/C_c of activator molecules in the inhomogeneous matrix is steeper than that in the homogeneous matrix [20]. In terms of the critical exponents, this corresponds to a decrease in the exponent β.

Figure 7 depicts the dependences of the percolation probability on the reduced concentration for the lattices with different inhomogeneity fractions. It is clearly seen that the introduction of inhomogeneities into the lattice is attended by a more rapid increase in the percolation probability with an increase in the concentration. The observed effect becomes less pronounced with an increase in the linear size of inhomogeneities. However, our investigations showed that, in any case, the presence of inhomogeneities in the matrix leads to a change in this dependence.

The fractal dimension d_f is a principal characteristic of the infinite cluster at the critical point. Mandelbrot [29, 30] was the first to introduce the notion of a fractal. Subsequently, he specified the tentative concept [31] and defined the fractal as a structure consisting of parts that, in some sense, are similar to a unity [32]. However, until presently, there has been no rigorous and complete definition of fractals. An infinite cluster at the critical point exhibits a statistical self-similarity [24]. The fractal geometry of the infinite cluster and its statistical self-similarity are interrelated. This interrelation leads to the following relationship between the mass and the linear size of the cluster:

$$M = l^{d_f}. \tag{6}$$

Stanley [33] and Sokolov [34] showed that the fractal dimension in virtually all physical problems is defined as the exponent in relationship (6). At present, the fractal dimension is determined using different methods [35]. One of them is the embedded square method proposed in [24]. In essence, this method is as follows. In the object under study, a central point is chosen in a random manner and a series of embedded squares are arranged around this point. The number of sites in each square is counted, and the dependence of the object mass (the number of sites) on the linear square size is constructed. This dependence is used for calculating the fractal dimension. Forrest and Witten [36] proposed to bring the central point into coincidence with the center of gyration of the studied object in order to improve the reproducibility of the results. In our work, we also determined the fractal dimension of the infinite cluster by using the embedded square method. To accomplish this, among all the possible realizations, we chose clusters whose centers of gyration were close to the center of the studied lattice and whose radii of gyration [24] were close to $L/2$. It should be noted that the introduction of this criterion did not affect the statistics obtained for the critical concentration (Fig. 3). The results presented below were obtained by averaging over 300 different clusters. For lattices with large-sized inhomogeneities, additional averaging was performed over 20 configurations of inhomogeneity distribution in these lattices.

The dependence of the cluster mass (the number of sites) on the square size is plotted on the log–log scale

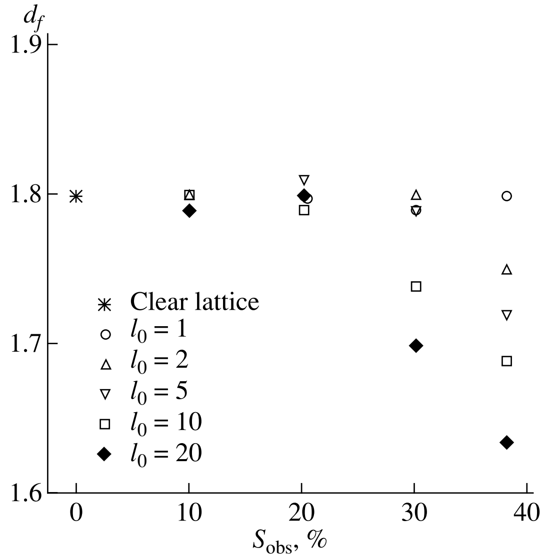

Fig. 9. Dependence of the fractal dimension of a percolation cluster on the inhomogeneity fraction S_{obs} in the matrix at different linear sizes l_0 of inhomogeneities.

in Fig. 8. It is easy to see that the dependence exhibits a linear behavior beginning with square sizes of the order of 20 × 20. The fractal dimension determined from the slope of this dependence is equal to 1.8. This value is slightly less than the exact dimension d_f = 91/48, which was calculated in [7, 14] in terms of the scaling theory. This difference can arise for two reasons. First, as was shown in [35], the fractal dimension determined by the embedded square method is underestimated compared to that obtained by other methods. Second, the underestimated value of d_f can be dictated by finite sizes of the lattice. It is obvious that the percolation cluster on a finite lattice is only a part of an infinite cluster on the infinite lattice for which the exact dimension was deduced. Consequently, particular sites that are not involved in the percolation cluster on the lattice of size L, in actual fact, belong to the infinite cluster, because they are connected to it through bonds lying outside the fragment under consideration. In any case, our prime concern is with the influence of the inhomogeneous properties of the lattice on the fractal dimension rather than in its absolute value. This influence is illustrated by the data shown in Fig. 9. As can be seen, no change in the fractal dimension is observed for lattices with the linear inhomogeneity size l_0 = 1. The value of d_f decreases for lattices with larger-sized inhomogeneities only in the case when their fraction in the system is sufficiently high. The effect is enhanced with an increase in the inhomogeneity size. This behavior can easily be explained with due regard for the fact that the percolation cluster is a strongly porous object. Therefore, when the size of inhomogeneities and their relative area are small, the probability that inhomogeneities occupy these pores is high. As the size of inhomogeneities and their fraction in the matrix increase, they begin to affect the geometry of the percolation cluster and this effect manifests itself in a decrease in its fractal dimension.

4. CONCLUSION

Thus, the results obtained in this work confirm the assumption made earlier (on the basis of available data on the energy transfer in disordered systems, specifically, in matrices with different structures on the microscopic level) that the inhomogeneous properties of matrices substantially affect the percolation process. The introduction of inhomogeneities into the lattice results primarily in an increase in the critical concentration. This effect is enhanced with an increase in the fraction of inhomogeneities in the matrix and a decrease in their linear size. The incorporation of inhomogeneities into the lattice affects both the concentration dependence of the mean number of sites in clusters and the percolation probability. In turn, this leads to a change in the critical exponents and the fractal dimension of the percolation cluster. These changes become more pronounced with an increase in the size of inhomogeneities and their relative area. Since the properties of the percolation cluster are also characterized by other dimensions, it can be assumed that the inhomogeneous properties of the lattices under investigation affect these dimensions.

REFERENCES

1. S. R. Broadbent and J. M. Hammersley, Proc. Cambridge Philos. Soc. **53**, 629 (1957).
2. *Fragmentation Form and Flow in Fractured Media*, Ed. by R. Engelman and Z. Jaeger (A. Hilger, Bristol, 1986).
3. *Proceedings of the International Topical Conference on Kinetics of Aggregation and Gelation, Athens*, Ed. by F. Family and D. P. Landau (North-Holland, Amsterdam, 1984).
4. P. de Gennes, *Scaling Concepts in Polymer Physics* (Cornell Univ. Press, Ithaca, 1979).
5. *Percolation Structures and Processes,* Ed. by G. Deutsher, R. Zallen, and J. Adler (Hilger, Bristol, 1983), Ann. Isr. Phys. Soc., Vol. 5.
6. B. I. Shklovskiĭ and A. L. Éfros, Usp. Fiz. Nauk **117**, 401 (1975) [Sov. Phys. Usp. **18**, 845 (1975)].
7. D. Stauffer, *Introduction to Percolation Theory* (Taylor and Francis, London, 1985).
8. G. Mackay and N. Jan, J. Phys. A **17**, L757 (1984).
9. P. Grassberger, Math. Biosci. **63**, 157 (1983).
10. A. Bunde, H. Herrmann, A. Margolina, and H. E. Stanley, Phys. Rev. Lett. **55**, 653 (1985).
11. B. I. Shklovskiĭ and A. L. Éfros, *Electronic Properties of Doped Semiconductors* (Nauka, Moscow, 1979; Springer-Verlag, New York, 1984).
12. J. Hoshen and R. Kopelman, J. Chem. Phys. **65**, 2817 (1976).

13. R. Kopelman, in *Spectroscopy and Excitation Dynamics in Condensed Molecular Systems*, Ed. by V. M. Agranovich and R. M. Hochstrasser (North-Holland, Amsterdam, 1983; Nauka, Moscow, 1987), p. 61.
14. D. Stuaffer, Phys. Rep. **54**, 1 (1979).
15. D. C. Ahlgren and R. Kopelman, Chem. Phys. **77**, 135 (1981).
16. C. von Borczyskowski and T. Kirski, Ber. Bunsenges. Phys. Chem. **93**, 1377 (1989).
17. S. A. Bagnich, Chem. Phys. **185**, 229 (1994).
18. S. A. Bagnich and P. P. Pershukevich, Fiz. Tverd. Tela (St. Petersburg) **37**, 3655 (1995) [Phys. Solid State **37**, 2013 (1995)].
19. S. A. Bagnich, Opt. Spektrosk. **80**, 769 (1996) [Opt. Spectrosc. **80**, 691 (1996)].
20. S. A. Bagnich, Proc. SPIE **3176**, 212 (1997).
21. D. C. Saha, T. N. Misra, and D. Talukdar, Indian J. Phys. B **69B**, 243 (1995).
22. S. A. Bagnich, Fiz. Tverd. Tela (St. Petersburg) **42**, 1729 (2000) [Phys. Solid State **42**, 1775 (2000)].
23. S. Kirkpatrick, Phys. Rev. Lett. **36**, 69 (1976).
24. J. Feder, *Fractals* (Plenum, New York, 1988; Mir, Moscow, 1991).
25. M. E. Kainourgiakis, E. S. Kikkinides, A. K. Stubos, and N. K. Kanellopoulos, J. Chem. Phys. **111**, 2735 (1999).
26. M. C. Bujan-Nunez, A. Miguel-Fernandez, and M. A. Lopez-Quintela, J. Chem. Phys. **112**, 8495 (2000).
27. J. Hoshen, R. Kopelman, and E. M. Monberg, J. Stat. Phys. **19**, 219 (1978).
28. J. Hoshen, D. Stauffer, G. H. Bishop, *et al.*, J. Phys. A **12**, 1285 (1979).
29. B. B. Mandelbrot, *Fractals: Form, Chance, and Dimension* (Freeman, San Francisco, 1977).
30. B. B. Mandelbrot, *The Fractal Geometry of Nature* (Freeman, New York, 1982).
31. B. B. Mandelbrot, in *Fractals in Physics*, Ed. by L. Pietronero and E. Tosatti (North-Holland, Amsterdam, 1986; Mir, Moscow, 1988), p. 3.
32. B. B. Mandelbrot, Fractals: Encycl. Phys. Technol. **5**, 579 (1987).
33. Y. E. Stanley, J. Stat. Phys. **36**, 843 (1984).
34. I. M. Sokolov, Usp. Fiz. Nauk **150**, 221 (1986) [Sov. Phys. Usp. **29**, 924 (1986)].
35. D. J. Robinson and J. C. Earnshaw, Phys. Rev. A **46**, 2045 (1992).
36. S. R. Forrest and T. A. Witten, J. Phys. A **12**, L109 (1979).

Translated by O. Borovik-Romanova

Physics of the Solid State, Vol. 43, No. 12, 2001, pp. 2321–2327. Translated from Fizika Tverdogo Tela, Vol. 43, No. 12, 2001, pp. 2228–2234.
Original Russian Text Copyright © 2001 by Nelson, Yacobson, Kagan, Gil, Grandjean, Beaumont, Massies, Gibart.

LOW-DIMENSIONAL SYSTEMS AND SURFACE PHYSICS

Electric-Field-Induced Impact Ionization of Excitons in GaN and GaN/AlGaN Quantum Wells

D. K. Nelson*, M. A. Yacobson*, V. D. Kagan*, B. Gil, N. Grandjean***,**
B. Beaumont*, J. Massies***, and P. Gibart*****
** Ioffe Physicotechnical Institute, Russian Academy of Sciences,*
Politekhnicheskaya ul. 26, St. Petersburg, 194021 Russia
*** CNRS-GES, Université de Montpellier II, Montpellier Cedex 5, 34095 France*
**** CNRS-CRHEA, Sophia-Antipolis, Valbonne, 06560 France*

Received April 27, 2001

Abstract—Impact ionization of exciton states in epitaxial GaN films and GaN/AlGaN quantum-well structures was studied. The study was done using an optical method based on the observation of exciton photoluminescence quenching under application of an electric field. It was established that electron scattering on impurities dominates over that from acoustic phonons in electron relaxation in energy and momentum. The mean free path of the hot electrons was estimated. The hot-electron mean free path in GaN/AlGaN quantum wells was found to be an order of magnitude larger than that in epitaxial GaN films, which is due to the electron scattering probability being lower in the two-dimensional case. *© 2001 MAIK “Nauka/Interperiodica”.*

1. INTRODUCTION

The nitrides of Group III elements, which are wide-bandgap semiconductor materials, have been recently receiving considerable attention as having potential application for modern optoelectronic devices operating in the visible and UV region [1]. However, many of the fundamental properties of these materials have not been studied in large enough detail. In particular, the effect of an external electric field on the optical properties of nitrides has thus far been poorly investigated. Until very recently, only a few publications had dealt with the exciton states of the Group-III nitrides in an external electric field [2, 3]. At the same time, such studies appear to be of considerable importance. The radiative recombination via exciton states occurring in these materials coexists in optoelectronic devices with an electric current flowing through the structure. Accordingly, proper understanding of the processes involved in the interaction of charged carriers with excitons in these materials is essential to the physics of semiconductor devices.

This study deals with the phenomenon of impact ionization (or delocalization) of excitons in gallium nitride. The study made use of the optical method based on observation of the quenching of exciton photoluminescence through the application of an electric field. The quenching occurs as a result of the destruction of excitons or exciton–impurity centers by hot carriers, whose energy is increased to the corresponding level by the electric field. The number of such high-energy electrons depends substantially on the mechanisms responsible for the electron relaxation in energy and quasi-momentum. Therefore, studying the quenching effect as a function of the applied electric field may yield information on these mechanisms. The optical method has an advantage in that it permits investigation of the impact ionization of weakly bound states and of states with different ionization energies. The studies were performed on epitaxial GaN films grown by various techniques (ELOG–MOVPE, MOVPE, and MBE). The impact ionization phenomenon was also investigated on MBE-grown GaN/AlGaN quantum-well structures. It was established that electron scattering from impurities in our samples dominates over that from acoustic phonons in hot electron relaxation.

2. EXPERIMENT

The samples studied were nominally undoped epitaxial *n*-type GaN films grown on sapphire substrates. The ELOG sample used in the present investigation was grown by metal-organic vapor-phase epitaxy (MOVPE) in two stages at atmospheric pressure [4]. A mask in the form of a $\langle 10\bar{1}0\rangle$-oriented Si_xN_y grating with strips 3–5 μm wide and a 10-μm period was deposited on the surface of a preliminarily grown GaN film. Next, the growth of the GaN film was resumed and continued to the level where the mask was completely buried. The growth of GaN films and GaN/AlGaN quantum-well structures by molecular-beam epitaxy (MBE) was effected using solid sources of Group III elements and ammonia as the source of nitrogen. The GaN buffer layer 250 Å thick grown at 500°C was annealed at 900°C, after which an epitaxial GaN layer was grown at 800°C (the growth procedure is described in more detail in [5]). The GaN/AlGaN quantum-well

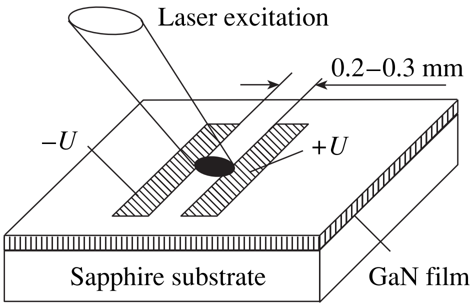

Fig. 1. Schematic of the experiment.

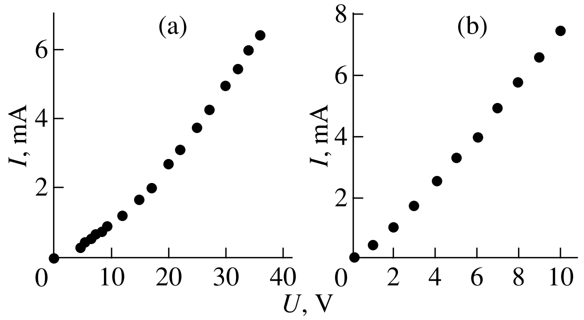

Fig. 2. Current–voltage characteristics of two samples: (a) an epitaxial GaN film and (b) a GaN/AlGaN quantum well 17 MLs wide.

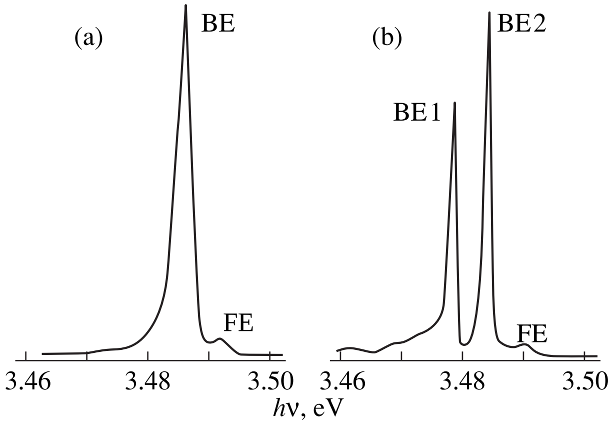

Fig. 3. Exciton luminescence spectra of two different GaN samples. $T = 2$ K.

structures consisted of $Al_{0.09}Ga_{0.91}N$ barriers and GaN quantum wells a few monolayers thick (1 ML = 2.59 Å).

Aluminum Ohmic contacts representing two parallel strips a few millimeters long and separated by a gap 0.2–0.3 mm wide were deposited on the sample surface through vacuum evaporation (Fig. 1). The photoluminescence was excited by the $\lambda = 325$-nm line of a helium–cadmium laser. The laser beam was focused to a spot approximately 0.5 mm in diameter that completely overlapped the electrode gap. The sample was cooled by immersing it in liquid helium. A dc voltage was applied across the structure, with a current of a few milliampers flowing through the sample, which could heat the sample. To ensure the best cooling conditions, liquid helium was pumped out by a fore pump and the measurements were carried out at a temperature ($T = 2$ K) below the λ point, i.e., the temperature below which liquid helium becomes superfluid. In this case, helium wets the sample well and there is no vapor layer between the sample and the cooling agent. If liquid helium is used as a cooling agent above the λ point ($T = 4.2$ K), the vapor layer present hampers heat removal from the sample noticeably, so that even a small current may bring about substantial heating of the sample. It was established in the experiments that the sample heating is very small and does not affect the photoluminescence spectra noticeably. In particular, the quenching of the GaN/AlGaN quantum-well exciton photoluminescence was studied at two temperatures, $T = 2$ and 4.2 K. The plots of the luminescence intensity vs. applied voltage obtained at the two temperatures are practically identical, which implies that there is indeed a field effect.

The current flowing through the sample under applied voltage was measured, and *I–V* characteristics of the samples were constructed. Two of them are displayed in Fig. 2. The *I–V* characteristics of some samples were sufficiently linear. Other samples, however, exhibited a nonlinear section at a low bias, which straightened out at higher voltages. On the whole, we can consider the electric field in a sample to be uniform to a considerable extent, at least at not-too-low voltages.

3. RESULTS

The intense line of the exciton bound to a neutral donor in the region of the $A_{n=1}$ exciton resonance was dominant in the luminescence spectra of our samples. The substantially weaker free-exciton line (FE) was also clearly seen in the spectra. The spectra of some samples exhibited two bound-exciton (BE) lines with different binding energies (BE1 and BE2). The BE1 line can be assigned to the exciton bound to a neutral donor, while we associate the BE2 line with residual magnesium doping [5], which occurs in some samples because of the specific features of the preparation technology employed [6, 7]. Figure 3 displays typical GaN exciton photoluminescence spectra.

When an external voltage was applied to the structure, quenching of the exciton photoluminescence was observed to occur. The behavior of the photoluminescence under an electric field depends on the binding energy of the corresponding exciton state, as can be seen from Fig. 4, which plots the emission line intensity vs. electric field.

One readily sees that the line with the lowest binding energy (BE in Fig. 4a and BE1 in Fig. 4b) suffers the strongest quenching. Simultaneously, at relatively low fields, one observes an intensity enhancement of the emission line corresponding to the state with a higher binding energy. In a stronger electric field, the intensity enhancement is replaced by saturation (for the FE line) or quenching (for the BE2 line).

This effect can be interpreted within the impact ionization model. Hot electrons with a kinetic energy close to the binding energy of the exciton bound to an impurity center (or close to the free-exciton binding energy) destroy the exciton state, which entails quenching of the corresponding emission line. In a relatively weak electric field, this effect can play a noticeable part only for states with a low binding energy. Dissociation of complexes with the lowest binding energy increases the concentration of free excitons, which can undergo radiative recombination or become trapped by deeper centers, thus contributing to the intensity enhancement of the corresponding emission lines. In stronger electric fields, electrons can acquire an energy large enough for them to be capable of breaking up complexes with higher binding energies and the intensities of the corresponding emission lines decrease. Actually, in the region of the electric fields covered, we observed only the quenching of bound-exciton lines with different binding energies (from 4.5 to 12 meV). As for the free-exciton line, we observed only its saturation. To destroy such a strongly bound electron–hole state (its binding energy is approximately 28 meV), much higher electric fields are needed.

A similar effect was also seen to occur in the GaN/AlGaN quantum-well structures. The photoluminescence spectra of these structures consist of a strong localized-exciton line and of a fairly weak phonon replica of it. The exciton localization energy, as estimated from the Stokes shift of the luminescence line, is approximately 20 meV [8]. Application of an external electric field to the sample was observed to result in substantial photoluminescence quenching (Fig. 5), which is due, as in the case of GaN epitaxial films, to exciton delocalization by the field-accelerated electrons.

4. ANALYSIS OF THE EXPERIMENTAL DATA

The number of excitons N in a system obeys the equation

$$\frac{dN}{dt} = -\frac{N}{\tau} + G, \tag{1}$$

where G is the generation rate. The decay probability $(1/\tau)$ of an exciton (or an exciton–impurity complex) being in electric field E is determined by the probability of impact ionization $W(E)$ and the probability of decay $(1/\tau_0)$ due to other radiative and nonradiative processes:

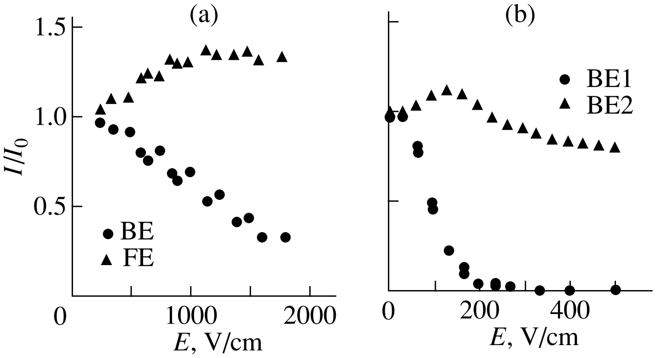

Fig. 4. Relative exciton emission line intensity vs. applied electric field. (a) MOVPE sample with the only bound-exciton line with a binding energy ε_b = 6.5 meV and (b) MBE sample with two bound-exciton lines, with binding energies ε_b = 4.5 and 12 meV.

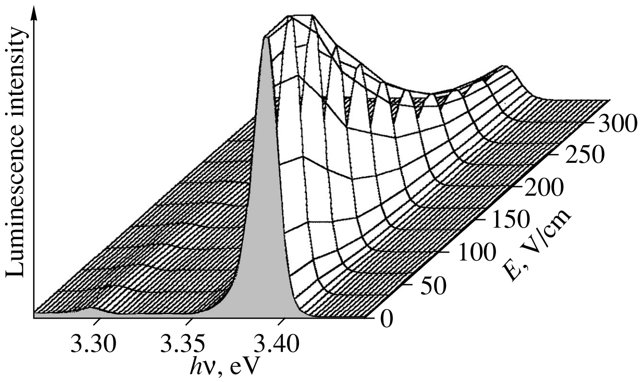

Fig. 5. Photoluminescence spectra of a GaN/AlGaN quantum well vs. applied electric field. Quantum-well width 17 MLs.

$$\frac{1}{\tau} = \frac{1}{\tau_0} + W(E). \tag{2}$$

Because the luminescence intensity $I(E) \sim N(E)$, we obtain the following expression for its steady-state value:

$$I(E) = I(0)[1 + W(E)\tau_0]^{-1}. \tag{3}$$

The impact ionization probability $W(E)$ is given by the integral

$$W(E) = \int_{\varepsilon_i}^{\infty} W_e(\varepsilon)\rho(\varepsilon)f(\varepsilon)d\varepsilon, \tag{4}$$

where $W_e(\varepsilon)$ is the probability of ionization of one exciton, $\rho(\varepsilon)$ is the density of states of the conduction-band electrons, and $f(\varepsilon)$ is the electron energy distribution function. The integration is performed over all energies in excess of the ionization energy ε_i; $W_e(\varepsilon)$ and $\rho(\varepsilon)$ are power-law functions of energy, while $f(\varepsilon)$ depends exponentially on ε at high energies. The energies significant to the integral in Eq. (4) are those close to the ionization threshold ε_i, and the magnitude of the integral is exponentially small. The exponent determines the dependence of W on the electric field E. We will not concern ourselves with the preexponential factor, which is justified in cases where the exponent is large in absolute value. The small value of the exponential is associated with the small number of electrons with energies high enough to ionize the bound state, and our problem consists in calculating this number and, thus, determining the total ionization probability. A rigorous mathematical treatment of the problem is given in [9]; here, we shall restrict ourselves to an analysis applicable to both three- and two-dimensional semiconductors.

The electron momentum distribution function $f_{\mathbf{p}}$ obeys the kinetic equation

$$\begin{aligned} &e\mathbf{E}\frac{\partial f_{\mathbf{p}}}{\partial \mathbf{p}} + \frac{1}{\tau_{\text{im}}(\varepsilon_p)}(f_{\mathbf{p}} - f(\varepsilon_p)) + \frac{2\pi}{\hbar}\sum_{\mathbf{q}}|C_{\mathbf{q}}|^2 \\ &\times[(f_{\mathbf{p}}(N_q+1) - f_{\mathbf{p}-\hbar\mathbf{q}}N_q)\delta(\varepsilon_{\mathbf{p}} - \varepsilon_{\mathbf{p}-\hbar\mathbf{q}} - \hbar\omega_q) \\ &+ (f_{\mathbf{p}}N_q - f_{\mathbf{p}+\hbar\mathbf{q}}(N_q+1))\delta(\varepsilon_{\mathbf{p}} - \varepsilon_{\mathbf{p}+\hbar\mathbf{q}} + \hbar\omega_q)] = 0, \end{aligned} \tag{5}$$

where $\mathbf{p}$ is the momentum of an electron, $\varepsilon_p = \mathbf{p}^2/2m$ is its energy, and m is its effective mass, $\mathbf{q}$ is the wave vector of a phonon, ω_q is its frequency ($\omega_q = sq$, s is the sound velocity), $N_q = \exp(\hbar\omega_q/kT - 1)^{-1}$ is the Planckian distribution function for phonons, $\tau_{\text{im}}(\varepsilon_p)$ is the relaxation time due to electron elastic scattering from lattice defects and impurities, and $C_{\mathbf{q}}$ is the electron–phonon coupling constant. The electron energy distribution function $f(\varepsilon)$ is obtained from $f(\mathbf{p})$ by averaging over all directions of the momentum $\mathbf{p}$. We take into account only the interaction with acoustic or piezoacoustic phonons, because the optical-phonon frequencies in GaN are much higher than the exciton-state ionization energies. As follows from the laws of energy and momentum conservation in electron–phonon collisions, only sufficiently high phonon energies are significant; therefore, the number of phonons at low temperatures is exponentially small, $N_q \approx \exp(-\hbar\omega_q/kT)$, and one can neglect this value compared to unity. The electron relaxation associated with the exciton ionization process is disregarded in Eq. (5), because it is insignificant compared to the relaxation rate due to the interaction of electrons with phonons and impurities.

We transfer now all terms in Eq. (5) to the right-hand side, apply a minus sign, and transform the differential equation (5) into an integral one:

$$\begin{aligned} f_{\mathbf{p}} = \int_0^\infty dt\Bigg\{&\frac{1}{\tau_{\text{im}}(\varepsilon_{\mathbf{p}-e\mathbf{E}t})}f(\varepsilon_{\mathbf{p}-e\mathbf{E}t}) + \frac{2\pi}{\hbar}\sum_{\mathbf{q}}|C_{\mathbf{q}}|^2 \\ &\times[f_{\mathbf{p}-e\mathbf{E}t+\hbar\mathbf{q}}\delta(\varepsilon_{\mathbf{p}-e\mathbf{E}t} - \varepsilon_{\mathbf{p}-e\mathbf{E}t+\hbar\mathbf{q}} + \hbar\omega_q) \\ &+ f_{\mathbf{p}-e\mathbf{E}t-\hbar\mathbf{q}}N_q\delta(\varepsilon_{\mathbf{p}-e\mathbf{E}t} - \varepsilon_{\mathbf{p}-e\mathbf{E}t-\hbar\mathbf{q}} - \hbar\omega_q)] \\ &\times\exp\left[-\int_0^t dt'\left(\frac{1}{\tau_{\text{im}}(\varepsilon_{\mathbf{p}-e\mathbf{E}t})} + \frac{1}{\tau_{\text{ph}}(\varepsilon_{\mathbf{p}-e\mathbf{E}t})}\right)\right]\Bigg\}. \end{aligned} \tag{6}$$

In the elastic approximation, the electron relaxation time due to phonons can be written as

$$\tau_{\text{ph}}^{-1}(\varepsilon_p) = \frac{2\pi}{\hbar}\sum_{\mathbf{q}}|C_{\mathbf{q}}|^2\delta(\varepsilon_{\mathbf{p}} - \varepsilon_{\mathbf{p}-\hbar\mathbf{q}}). \tag{7}$$

The electron mean free path is given by the relations

$$\begin{aligned} l_{\text{ph, im}}(\varepsilon_{\mathbf{p}}) &= \sqrt{\frac{2\varepsilon_{\mathbf{p}}}{m}}\tau_{\text{ph, im}}(\varepsilon_{\mathbf{p}}), \\ \frac{1}{l(\varepsilon)} &= \frac{1}{l_{\text{ph}}(\varepsilon)} + \frac{1}{l_{\text{im}}(\varepsilon)}. \end{aligned} \tag{8}$$

We assume the electric field to be sufficiently strong,

$$\varepsilon_i \gg eEl(\varepsilon_i) \gg kT. \tag{9}$$

As follows from Eq. (6), the electron distribution function at high energies is determined by that at medium thermal energies. We assume that at these energies there exist efficient momentum and energy relaxation mechanisms, such that the distribution function is an equilibrium one. Applying the saddle-point method to the integration of Eq. (6), we obtain

$$f_{\mathbf{p}} = A_{\mathbf{p}}\exp\left[-\frac{\varepsilon_p}{T}\sin^2\vartheta - \cos\vartheta\int_0^{\varepsilon_p}\frac{d\varepsilon'}{eEl(\varepsilon')}\right], \tag{10}$$

where A_p depends more weakly than exponentially on the momentum and θ is the angle between the momentum and the electric field. The function given by Eq. (10) is needle-shaped, extended along the electric-field direction, and falls off rapidly in other directions. Averaging this function over the angles yields the Townsend–Shockley ionization relation:

$$f(\varepsilon) = \exp\left(-\int_0^\varepsilon\frac{d\varepsilon'}{eEl(\varepsilon')}\right). \tag{11}$$

The case of electron scattering dominated by elastic processes, $\tau_{\text{im}}(\varepsilon_p) \ll \tau_{\text{ph}}(\varepsilon_p)$, requires special consideration. It was shown that the electric-field dependence follows different patterns for different electric fields [9]. If the inequalities $kT \ll eE\sqrt{l_{\text{ph}}(\varepsilon_i)l_{\text{im}}(\varepsilon_i)} \ll s\sqrt{2m\varepsilon_i}$

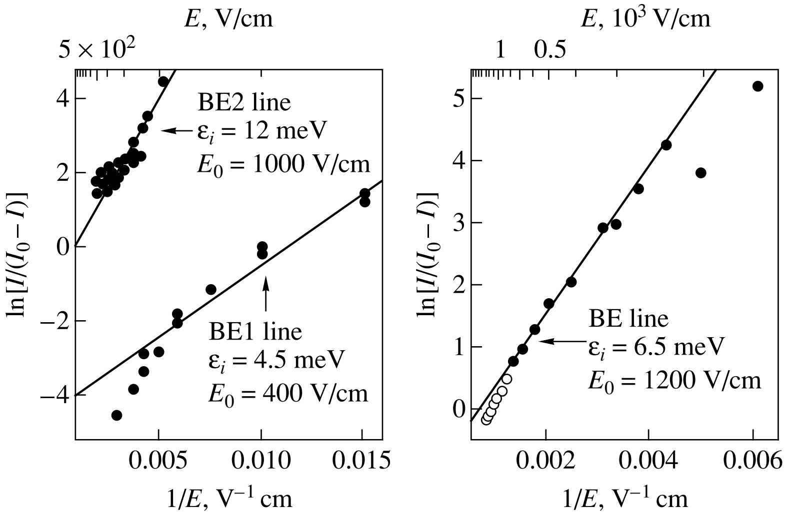

Fig. 6. Bound-exciton luminescence line intensity vs. electric field plots obtained for two different GaN samples. The experimental points are plotted in the $\ln[I/(I_0 - I)] = f(E^{-1})$ vs. E^{-1} coordinates to facilitate comparison with theory. Solid lines are linear approximations.

are met, the Townsend–Shockley dependence is valid:

$$f(\varepsilon) = A\exp\left(-\int_0^{\varepsilon}\frac{\sqrt{3}d\varepsilon'}{eE\sqrt{l_{\mathrm{ph}}(\varepsilon')l_{\mathrm{im}}(\varepsilon')}}\right). \qquad (12)$$

For $kT \ll s\sqrt{2m\varepsilon_i} \ll eE\sqrt{l_{\mathrm{ph}}(\varepsilon_i)l_{\mathrm{im}}(\varepsilon_i)}$, the distribution function is a solution to the hot-electron problem, which yields the Davydov–Wolf ionization relation:

$$f(\varepsilon) = A\exp\left(-\int_0^{\varepsilon}\frac{6d\varepsilon'}{e^2E^2l(\varepsilon')l_{\varepsilon}(\varepsilon')}\right), \qquad (13)$$

$$l_{\varepsilon}(\varepsilon_p) = \frac{\sqrt{2m}}{\varepsilon_p^{3/2}}\pi\sum_q|C_{\mathbf{q}}|^2\omega_q\delta(\varepsilon_{\mathbf{p}} - \varepsilon_{\mathbf{p}-\hbar\mathbf{q}}). \qquad (14)$$

When the electric field increases, one may expect a crossover from Eq. (12) to relation (13). Note that the Davydov–Wolf relation was not observed experimentally. The reason for this probably lies in the fact that an increase in the electric field can give rise to tunneling ionization in addition to impact ionization [10].

Let us analyze the experimental data using the Townsend–Shockley relation, Eq. (12), which we shall recast in the form $W(E) = W_0\exp(-E_0/E)$, with E_0 being a characteristic parameter, and see what information can be extracted from this analysis.

Figure 6 presents the dependence of the GaN photoluminescence intensity on applied electric field plotted as $\ln[I/(I_0 - I)]$ vs. E^{-1}. The experimental points in Fig. 6 are fitted by a straight line for a certain value of parameter E_0. The values of E_0 obtained using this procedure for the GaN samples studied are given in the table.

In pure crystals, the dominant mechanism of electron relaxation at low temperatures should be scattering from piezoacoustic phonons. Estimates made using Eqs. (7), (8), and (11) and the parameters for GaN [11] yield $E_0 = 160$ V/cm for $\varepsilon_i = 6$ meV. This is substantially less than the value $E_0 = 600$ V/cm obtained in our experiment. Furthermore, in the case of electron scattering from piezoacoustic phonons, the parameter E_0 should be proportional to the square root of the ionization energy. However, the data obtained for the MBE samples suggest that $E_0 \sim \varepsilon_i$. These two facts show that the electron relaxation occurs through their scattering not only from piezoacoustic phonons but also from impurity centers, which plays an essential part in our samples. Using Eq. (12), the effective mean free path of hot electrons can be estimated in this case from the expression

$$l_{\mathrm{eff}} = \sqrt{3}\varepsilon_i/eE_0. \qquad (15)$$

The figures obtained in this estimation are listed in the last column of the table. First, the ELOG and MBE samples are seen to yield similar values of the parameter l_{eff}. Second, we can compare these results with the

Experimentally determined values of the parameter E_0 and of the electron mean free path for different GaN samples

Sample, line	ε_i, meV	E_0, V/cm	l_{eff}, 10^{-5} cm
ELOG, line BE1	6.5	600	2
MBE, line BE1	4.5	400	2
MBE, line BE2	12.0	1000	2
MOVPE, line BE	6.0	1500	0.7

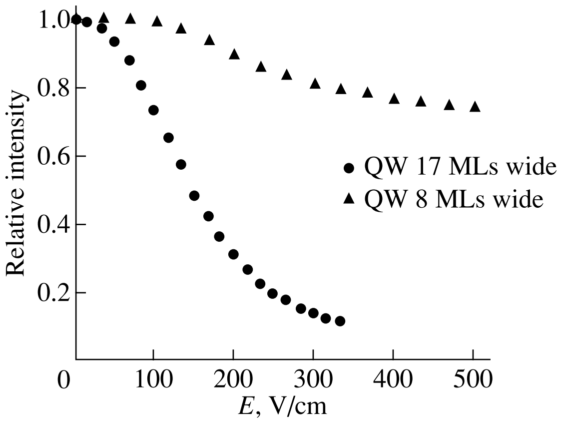

Fig. 7. Luminescence intensity of a GaN/AlGaN quantum well vs. applied electric field plotted for samples with different quantum-well widths.

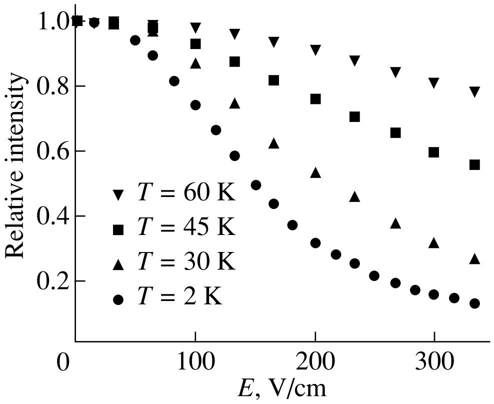

Fig. 8. Luminescence intensity of a GaN/AlGaN quantum well vs. applied electric field plotted for various temperatures. Quantum-well width 17 MLs.

data obtained for CdS crystals [12]. In pure CdS, $l_{\text{eff}} = 10^{-4}$ cm for $\varepsilon_i = 4$ meV. For CdS crystals of a poorer quality, the corresponding value decreased to 5×10^{-6} cm. Thus, the mean free path $l_{\text{eff}} = 2 \times 10^{-5}$ cm obtained in our experiments on three-dimensional GaN samples is not much shorter than that measured in the best cadmium sulfide crystals.

Now, we analyze the data obtained for the GaN/AlGaN quantum-well structures. Figure 7 presents the electric-field dependences of the luminescence intensity for two samples with quantum wells (QW) 17 and 8 monolayers wide, respectively. The quenching effect in the wider QW is seen to be much stronger. The main reason for this is that the exciton lifetime decreases substantially with decreasing QW width [13]. According to Eq. (3), a decrease in τ_0 results in a reduced effect of $W(E)$ on the luminescence intensity.

The linear section of the $\ln[I/(I_0 - I)]$ vs. E^{-1} plot yields for the E_0 parameter values of 350 and 480 V/cm for the QWs 17 and 8 MLs wide, respectively. Accepting $\varepsilon_i = 20$ meV for the exciton localization energy, the mean free paths of hot electrons are obtained to be $l_{\text{eff}} = 1 \times 10^{-4}$cm for the 17-ML QW and 0.7×10^{-4} cm for the 8-ML QW. These values are substantially larger than those for the bulk GaN. When calculating the electron mean free path in a quantum well, one should take into account that, in a scattering event, the electron momentum cannot change in the direction perpendicular to the well plane by more than $\hbar/d$, where d is the well thickness. Therefore, in the two-dimensional case, the electron scattering probability decreases and the mean free paths increase by a factor of $\sqrt{2m\varepsilon_i}\,d/\hbar$. The presence of this factor accounts for the observed difference between the mean free paths of hot electrons in GaN films and GaN/AlGaN quantum wells.

A study was also made of the temperature dependence of the impact ionization coefficient in QWs at temperatures ranging from 2 to 60 K. The quenching effect decreases with increasing temperature (Fig. 8). This can be explained, as with the dependence on the QW width, as being due to the decreased exciton lifetime with increasing temperature. At the same time, analysis of the experimental data using the Townsend–Shockley relation for $W(E)$ did not reveal any temperature dependence of the parameter E_0, which agrees with theory. Thus, the decrease in the impact ionization effect observed in this experiment is completely due to the variation of τ_0 with temperature.

To sum up, we note that, in contrast to a perfect crystal lattice, where electron scattering from piezoacoustic phonons is the dominant mechanism of electron momentum relaxation, this relaxation in undoped GaN epitaxial layers grown by the MOVPE, ELOG, and MBE methods is the result of scattering from impurities. This is evidence of a certain imperfection in the presently available GaN samples. The mean free paths of hot electrons in GaN/AlGaN quantum wells were found to be an order of magnitude larger than those in GaN films, because the electron scattering probability is lower in the two-dimensional case.

ACKNOWLEDGMENTS

The authors owe sincere gratitude to A. Usikov and V. Lundin for providing the MOVPE GaN samples.

This study was partly supported by the Russian Foundation for Basic Research, project no. 00-02-16952.

REFERENCES

1. S. Nakamura and G. Fasol, *The Blue Laser Diode: GaN Based Light Emitters and Lasers* (Springer, Berlin, 1997).

2. F. Binet, J. Y. Duboz, E. Rosencher, *et al.*, Phys. Rev. B **54**, 8116 (1996).
3. D. K. Nelson, V. D. Kagan, E. V. Kalinina, and M. A. Jacobson, J. Lumin. **72–74**, 865 (1997).
4. B. Beaumont, M. Vaille, G. Nataf, *et al.*, MRS Internet J. Nitride Semicond. Res. **3,** 20 (1998).
5. M. Tchounkeu, O. Briot, B. Gil, *et al.*, J. Appl. Phys. **80**, 5352 (1996).
6. M. Leroux, B. Beaumont, N. Grandjean, *et al.*, Mater. Sci. Eng., B **50**, 97 (1997).
7. N. Grandjean, J. Massier, P. Vennéguès, *et al.*, J. Appl. Phys. **83**, 1379 (1998).
8. M. Leroux, N. Grandjean, M. Laügt, *et al.*, Phys. Rev. B **58**, R13371 (1998).
9. V. D. Kagan, Zh. Éksp. Teor. Fiz. **94** (1), 258 (1988) [Sov. Phys. JETP **67**, 145 (1988)].
10. M. A. Jacobson, V. D. Kagan, E. V. Kalinina, *et al.*, in *Proceedings of the 23rd International Conference on the Physics of Semiconductors, Berlin, 1996*, p. 569.
11. http://nina.ecse.rpi.edu/shur/nitride.htm.
12. M. A. Jakobson, V. D. Kagan, R. Katilus, and G. O. Müller, Phys. Status Solidi B **161**, 395 (1990).
13. P. Lefebvre, J. Allègre, B. Gil, *et al.*, Phys. Rev. B **59** (23), 15363 (1999).

Translated by G. Skrebtsov

Physics of the Solid State, Vol. 43, No. 12, 2001, pp. 2328–2335. Translated from Fizika Tverdogo Tela, Vol. 43, No. 12, 2001, pp. 2243–2249.

Dynamic Image Forces near a Semiconductor–Vacuum Interface: The Role of Quantum-Mechanical Corrections

A. I. Voĭtenko and A. M. Gabovich

Institute of Physics, National Academy of Sciences of Ukraine, pr. Nauki 46, Kiev, 03028 Ukraine
e-mail: collphen@iop.kiev.ua

Received February 26, 2001

Abstract—The energy of dynamic image forces acting on a charged particle moving normally to the semiconductor–vacuum interface or in a vacuum gap between two semiconductors is calculated in the framework of the perturbation theory. The dielectric approach allows for spatial and time dispersions of the dielectric functions of electrodes. It is shown that the quantum-mechanical character of the screening should be taken into account. In particular, the dynamic corrections to the static image forces appear to be less than those in the quasi-classical model. The perturbation method used in this work is applicable in wider ranges of external electrostatic fields and particle energies. *© 2001 MAIK “Nauka/Interperiodica”.*

1. INTRODUCTION

The term “image forces” refers to the polarization forces arising in the vicinity of an interface between different media. Within the dielectric formalism [1–4], these forces can be treated in general terms with due regard for the spatial ($\mathbf{k}$) and time (ω) dispersions of the permittivity $\varepsilon_i(\mathbf{k}, \omega)$ [5]. In the classical model, this approach is the most general because it allows for quasiparticle excitations in the problem under consideration (for example, in the case of metals [6]). However, a number of quantum-mechanical effects, in particular, the dissipation associated with the generation of real plasmons [7, 8], excitations of an electron–hole medium [8], or recoil phenomena [7], are beyond the scope of the dielectric approach. It seems likely that, in this case, the Hamiltonian formalism [7] is more adequate.

When calculating the image forces or the potential energy W, the main problem is adequate description of the interface as an inhomogeneity of the system and the reflection of quasiparticles from the interface [4, 9, 10]. The two simplest approximations, namely, the infinite barrier model (i.e., the abrupt interface model) and the model of specular reflection of quasiparticles, allow one to solve analytically the problem in the static limit, so that the final expression for W involves the bulk dielectric functions $\varepsilon_i(\mathbf{k}, \omega = 0)$. The other approximations make allowance for the fact that the interface and scattering of quasiparticles by it can be slightly diffuse; however, in the majority of cases, they lead to numerical results that insignificantly differ for the quantities of interest [11].

At the same time, the infinite barrier and specular reflection models make it possible to investigate a more interesting case of moving charges [3, 7, 8, 11–24]. It was found that, for a metal–vacuum interface, the spatial dispersion of the permittivity (screening) [1, 2, 11, 15], quantum-mechanical recoil [7], and finiteness of the velocity of a projectile [11]—individually and in combination—result in saturation of the W energy at the interface and elimination of the classical divergence.

The static theory of image forces for an abrupt vacuum–semiconductor interface was developed in the specular reflection approximation in our earlier works [1, 2, 16]. The theory generalized to trilayer structures with due regard for dynamic corrections will be presented below.

Huang *et al.* [17] also studied the image forces in metal–vacuum–semiconductor structures. However, these authors considered only the static case in the framework of the Inkson semiclassical model [18] for the dielectric function of a semiconductor. In the present work, we prove that, when solving problems of this type, it is necessary to account for the quantum-mechanical nature of charge carriers in screening media. Within the dielectric approach, this can be done, for example, by introducing the appropriate corrections into the dielectric function of a semiconductor [19]. It should be noted that, owing to the large permittivities of metals, quantum corrections in the case of metal electrodes turn out to be insignificant.

In this work, we restricted our consideration to the case of a vacuum region, even though the image potential profile $W(r)$ (where r is the coordinate reckoned from the interface) could also be obtained in the bulk of the semiconductor ($r < 0$) within the same approach [1, 16]. Generally speaking, the behavior of W inside an electrode is important, for example, in forming surface barriers, and can affect the resulting tunneling currents. However, the screening properties of semiconductors (and, especially, metals) are such that the image potential profile inside a semiconductor reaches a bulk value extremely quickly. As was shown earlier in [17], even the replacement of the exact profile $W(r < 0)$ by this value weakly affects the tunneling characteristics. The vacuum portion of the dependence $W(r > 0)$ depends, to a considerably larger measure, on the parameters of the problem and makes the main contribution to the surface barrier. Hereafter, we will not dwell on this problem, because the investigation of tunneling in semiconductor structures is beyond the scope of the present work. Note also that knowledge of the $W(r > 0)$ profiles near the semiconductor surface is necessary not only for the understanding of electron tunneling but also for adequate description of the charged-particle scattering by this surface and analysis of a number of problems in chemical kinetics.

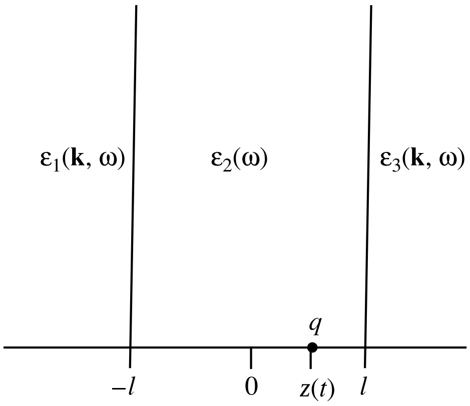

Fig. 1. Charge q moving according to the law $z_0(t)$ across an interlayer of width $2l$ in the trilayer system. The temporal dispersion of the permittivities ε_i is taken into account for all three layers, and the spatial dispersion is allowed only for the outer layers ($i = 1, 3$).

2. THEORY

Let us consider the configuration represented schematically in Fig. 1: a plane-parallel trilayer sandwich with interelectrode spacing $2l$ and charge q moving normally to the interface along the z axis according to the law $z_0(t)$(where t is the time). The temporal dispersion of the permittivities ε_i is taken into account in all three media, whereas the spatial dispersion is allowed for only in the outer layers ($i = 1$ and 3).

The potential energy W of image forces, i.e., the energy of the external charge q in the field with potential V_{ind} of the polarization charges induced in the electrodes, is defined by the relationship

$$W(z_0(t)) = \frac{1}{2}qV_{\text{ind}}[x = y = 0, z_0(t), t]. \qquad (1)$$

In the infinite barrier model with specular reflection from the interface, the appearance of V_{ind} is associated with the formation of the charged planes $(x, y, z = \mp l)$, which coincide with the interfaces [11]. In this case, we completely ignore the "spill" of electrons into the gap between electrodes [10], band bending effects [20], and the possible formation of surface states in the vicinity of the semiconductor [21]. Thus, the outer electrodes are considered homogeneous up to the corresponding interface.

For an arbitrary law $z_0(t)$ of the charge motion in the gap, the general equation for $W[z_0(t)]$ was derived in our earlier works [3, 14]. For nonrelativistic velocities $v \ll c$ (where c is the velocity of light), we developed the general technique of calculating the dynamic (nonadiabatic) corrections $\Delta W[z_0(t)]$ to the energy $W_{\text{st}}[z_0(t)]$ of static image forces in terms of the perturbation theory; i.e., it is assumed that the corrections are small compared to the energy of static image forces. Certainly, the expansions used can appear incorrect, for example, when the contributions from all the instants $t' < t$ are accumulated for a sufficiently long trajectory of a particle. Specifically, if the spatial dispersion is absent, then, at long distances from the interface, the energy W of the charge, which is emitted from a metal into vacuum at a constant rate [11] or under uniform acceleration [22], involves oscillating terms comparable in magnitude to the corresponding asymptotic values in the classical model:

$$W_{\text{cl}}^{\text{met}}[z_0(t)] = -\frac{q^2}{4z_0(t)}. \qquad (2)$$

These terms arise from the excitation of real surface plasmons [11]. However, the inclusion of the plasmon damping leads to a substantial decrease in the oscillation amplitude [23], which appreciably extends the range of applicability of the technique. In any case, the validity of the perturbation solution can be *a posteriori* verified after calculating ΔW and W_{st}.

We will restrict our analysis to the consideration of the nondissipative permittivities ε_i, which, in this case, are the even functions of ω. It is self-evident that we cannot lay claim to the description of the absorption or generation of real plasmons or polar phonons (these processes can be adequately described within the Hamiltonian formalism [7]). Consequently, ΔW takes only real values. The numerical calculations given below demonstrate that, for our purposes, it is sufficient to introduce only the first dynamic correction.

For simplicity, let us consider a vacuum gap with $\varepsilon_2 \equiv 1$. In the given approximation, the energy of static image forces and the dynamic correction have the form [3]

$$\begin{aligned} &W_{\text{st}}[z(t)] \\ &= -\frac{q^2}{2}\int_0^\infty dk_\parallel \frac{\exp(-2k_\parallel l)}{1 - \alpha_1(k_\parallel, 0)\alpha_3(k_\parallel, 0)\exp(-4k_\parallel l)} \\ &\quad \times [\alpha_1(k_\parallel, 0)e^{-2k_\parallel z} + \alpha_3(k_\parallel, 0)e^{2k_\parallel z} \\ &\quad - 2\alpha_1(k_\parallel, 0)\alpha_3(k_\parallel, 0)e^{-2k_\parallel l}], \end{aligned} \qquad (3)$$

$$\begin{aligned}
&\Delta W[z(t)] \\
&= \frac{q^2}{4}\int_0^\infty dk_\parallel \frac{\exp(-2k_\parallel l)}{[1-\alpha_1(k_\parallel,0)\alpha_3(k_\parallel,0)\exp(-4k_\parallel l)]^2} \\
&\times\{k_\parallel(\ddot z + k_\parallel \dot z^2)e^{2k_\parallel z}[\alpha_3''(k_\parallel,0) \\
&+\alpha_1''(k_\parallel,0)\alpha_3^2(k_\parallel,0)e^{-4k_\parallel l}] - k_\parallel(\ddot z - k_\parallel \dot z^2)e^{-2k_\parallel z} \qquad (4) \\
&\times[\alpha_1''(k_\parallel,0)+\alpha_3''(k_\parallel,0)\alpha_1^2(k_\parallel,0)e^{-4k_\parallel l}] \\
&-2k_\parallel^2\dot z^2 e^{-2k_\parallel l}[\alpha_1''(k_\parallel,0)\alpha_3(k_\parallel,0) \\
&+\alpha_3''(k_\parallel,0)\alpha_1(k_\parallel,0)]\}.
\end{aligned}$$

Hereafter, in order to simplify the form of equations, $z(t)$ will be written instead of $z_0(t)$; dots and primes indicate the differentiation with respect to time and frequency, respectively; $k_\parallel = |\mathbf{k}_\parallel|$; the wave vector $\mathbf{k}_\parallel$ is the component (aligned parallel to the interface) of the three-dimensional wave vector $\mathbf{k} = (\mathbf{k}_\parallel, k_z)$;

$$\alpha_i(k_\parallel,\omega) = \frac{\varepsilon_{si}(k_\parallel,\omega)-\varepsilon_2(\omega)}{\varepsilon_{si}(k_\parallel,\omega)+\varepsilon_2(\omega)} \quad (i = 1, 3); \qquad (5)$$

and

$$\varepsilon_{si}(k_\parallel,\omega) = \left[\frac{k_\parallel}{\pi}\int_{-\infty}^{\infty}\frac{dk_z}{\mathbf{k}^2\varepsilon_i(\mathbf{k},\omega)}\right]^{-1} \qquad (6)$$

are the so-called surface dielectric functions in the specular reflection model.

3. PERMITTIVITY OF SEMICONDUCTORS

The permittivity $\varepsilon_L(\mathbf{k}, \omega)$ for isotropic metals was obtained by Lindhard [24] in the framework of the electron gas model with inclusion of the quantum interference of electron waves at the Fermi surface. The well-known difference between the static limit $\varepsilon_L(\mathbf{k}, \omega = 0)$ and the Thomas–Fermi semiclassical screening function

$$\varepsilon_{TF}(\mathbf{k}) = 1 + \frac{\kappa^2}{k^2} \qquad (7)$$

resides in the presence of a weak quantum-mechanical singularity at $k = 2k_F$ (where k is the Thomas–Fermi wave vector and k_F is the Fermi momentum of electrons in the metal) in $\varepsilon_L(\mathbf{k}, 0)$. This singularity leads, in particular, to Friedel oscillations of the electron density and Kohn anomalies in the phonon spectra. At the same time, there is another, frequently overlooked, consequence of the quantum nature of the charge screening: the short-wavelength asymptotics of $\varepsilon_L(\mathbf{k}, 0)$ has the form

$$\lim_{|\mathbf{k}|\to\infty} \varepsilon_L(\mathbf{k}, 0) \approx 1 + \frac{4\kappa^2 k_F^2}{3k^4}. \qquad (8)$$

The fact that expression (8) tends to unity more rapidly compared to the screening function (7) results in a change in the screening of the Coulomb field at short distances.

In intrinsic semiconductors, potential charge carriers are bound and the band gap determines their screening ability. A large number of theoretical investigations of the permittivity $\varepsilon_{semi}(\mathbf{k}, 0)$ in semiconductors have been performed in the random phase approximation [25] within the nearly free electron gas model with due regard for the reflection of electron waves from the Bragg planes [26]. Subsequently, Sharma and Auluck [27] complemented the Penn model [26] and introduced the temporal dispersion. On the other hand, there exists another approach proposed by Resta [28], who solved the linearized variant of the Thomas–Fermi equation for a semiconductor treated as a medium with a finite length of partial screening. All the expressions obtained for the permittivity $\varepsilon_{semi}(\mathbf{k}, \omega)$ in the aforementioned theories are either nonanalytic or cumbersome, even though they were not derived from first principles. It should be noted that the dielectric approach based on the quasi-free electron gas model disregards the possible interband transitions of core (d or f) electrons, which are of crucial importance, for example, in Cu [8]. At the same time, the fast electron probing of semiconductors, such as Si, revealed well-defined plasma oscillations of valence electrons [8, 29]. In any case, the appropriate description of an electron gas (liquid) in the optical range of frequencies ω remains open to question [13].

Inkson [30] proposed a simple interpolation formula for the permittivity $\varepsilon_{semi}(\mathbf{k}, \omega)$, which satisfies the set of basic requirements for the true dielectric function of an intrinsic semiconductor; that is,

$$\varepsilon_I(\mathbf{k},\omega) = 1 + \left(\frac{1}{\varepsilon_0 - 1} + \frac{k^2}{\kappa^2} - \frac{\omega^2}{\omega_p^2}\right)^{-1}, \qquad (9)$$

where ω_p is the plasma frequency of a hypothetical free electron gas with a density identical to that of valence electrons. In the case of strong ionicity ($\varepsilon_0 \longrightarrow \infty$), expression (9) tends to the hydrodynamic limit that describes conducting media. It is worth noting that expression (9), to within the designations, is often used for describing the dielectric function of polar solvents [9].

Unfortunately, despite all of these advantages, the function $\varepsilon_I(\mathbf{k}, \omega)$ does not meet the quantum-mechanical limit (8), even though bound electrons at $|\mathbf{k}| \longrightarrow \infty$ cease to differ from free electrons. In order to improve the behavior of $\varepsilon_I(\mathbf{k}, \omega)$ at large $\mathbf{k}$, we propose the following relationship:

$$\varepsilon_{SU}(\mathbf{k}, \omega) = 1 + \left[\frac{1}{\varepsilon_0 - 1} + \frac{k^2}{\kappa^2}\left(1 + \frac{3k^2}{4k_F^2}\right) - \frac{\omega^2}{\omega_p^2}\right]^{-1}, \quad (10)$$

which, at $\omega = 0$, coincides with the Schulze–Unger static function [16, 19]. Hereafter, function (10) will be also termed the Schulze–Unger function. Both the $\varepsilon_I(\mathbf{k}, \omega)$ and $\varepsilon_{SU}(\mathbf{k}, \omega)$ functions will be used for calculating the energy of image forces near the semiconductor–vacuum interface.

4. THE SEMICONDUCTOR–VACUUM INTERFACE

First, we consider a semiconductor–vacuum interface. The equations for this case can be easily obtained from Eqs. (3) and (4) for the vacuum gap by introducing the distance $r_{\mp}(t) = l \pm z(t)$ to the left (right) interface and passing to the limit $l \longrightarrow \infty$. By virtue of the exponential multipliers, all the terms including α_i and α_i'' for the distant electrode vanish in the equations. Consequently, in this section, we can omit all the indices indicating a particular interface. As a result, the equations become considerably simpler, that is,

$$W_{st}(r) = -\frac{q^2}{2}\int_0^\infty dk_\parallel \alpha(k_\parallel, 0)\exp(-2k_\parallel r), \quad (11)$$

$$\Delta W(r) = \frac{q^2}{4}\int_0^\infty dk_\parallel k_\parallel (k_\parallel \dot{r}^2 - \ddot{r})\alpha''(k_\parallel, 0)\exp(-2k_\parallel r). \quad (12)$$

Now, we analyze the two simplest and, at the same time, most important cases: the motion of a charge with a constant velocity v at a right angle to the interface and the uniformly accelerated motion of a particle under the action of an external field F. All the questions regarding self-consistency problems remain beyond the scope of the present paper.

Within the Inkson approximation (9), we can obtain the far and near asymptotics of Eqs. (11) and (12). Specifically, for the uniformly accelerated motion, when $\kappa r\sqrt{\frac{\varepsilon_0}{\varepsilon_0 - 1}} \ll 1$, we have

$$W_{st}(r) \approx -\frac{q^2\kappa\sqrt{\varepsilon_0(\varepsilon_0 - 1)}}{4}\left\{1 - \frac{\varepsilon_0 - 1}{\sqrt{\varepsilon_0}}\tan^{-1}\frac{1}{\varepsilon_0}\right.$$
$$+ \frac{\kappa r}{\sqrt{\varepsilon_0(\varepsilon_0 - 1)}}\log\left(\gamma\kappa r\sqrt{\frac{\varepsilon_0}{\varepsilon_0 - 1}}\right) \quad (13)$$
$$\left. + \frac{\kappa r}{2\sqrt{\varepsilon_0(\varepsilon_0 - 1)}}\left[\varepsilon_0 - 2 - (\varepsilon_0^2 - 1)\log\frac{\varepsilon_0 + 1}{\varepsilon_0}\right]\right\},$$

$$\Delta W(r) \approx -\frac{q^3\kappa^2 F\varepsilon_0(\varepsilon_0 - 1)}{8m\omega_p^2}\left\{\frac{3}{2\varepsilon_0} - 1\right.$$
$$+ (\varepsilon_0 - 1)\log\frac{\varepsilon_0 + 1}{\varepsilon} + \frac{\kappa r}{\sqrt{\varepsilon_0(\varepsilon_0 - 1)}}\left[5\varepsilon_0^2 - \frac{14}{3}\varepsilon_0\right. \quad (14)$$
$$\left.\left. - 3 - \frac{(\varepsilon_0^2 - 1)(5\varepsilon_0 - 3)}{\sqrt{\varepsilon_0}}\tan^{-1}\frac{1}{\sqrt{\varepsilon_0}}\right]\right\}.$$

It is evident that the static contribution (13) is identical for the uniform and uniformly accelerated motions. At $\kappa r\sqrt{\frac{\varepsilon_0}{\varepsilon_0 - 1}} \gg 1$, we obtain

$$W_{st}(r) \approx -\frac{q^2\alpha_0}{4r}\left[1 - \frac{1}{\kappa r}\frac{\sqrt{\varepsilon_0(\varepsilon_0 - 1)}}{\varepsilon_0 + 1}\right], \quad (15)$$

$$\Delta W(r) \approx \frac{q^3\alpha_0^2 F}{4m\omega_p^2 r^2}. \quad (16)$$

Here,

$$\alpha_0 = \frac{\varepsilon_0 - 1}{\varepsilon_0 + 1}, \quad (17)$$

m is the mass of a particle, and $\gamma = 1.7810\ldots$ is the Euler constant. From the aforesaid, it follows that the energy of static image forces and the dynamic correction reach saturation at the interface due to the spatial dispersion of the permittivity. On the other hand, the usual asymptotics of classical static image forces takes place at long distances. As the ionicity increases, the picture becomes similar to the metallic limit described by the hydrodynamic model [3, 12].

It should be noted that the signs of dynamic corrections for the uniformly accelerated motion are different at long and short distances. The general analysis of different laws of particle motion is given in [3].

The striking, at first glance, similarity between the screening properties (and, hence, the image forces) of media with free and bound charge carriers is in contradiction to the classical viewpoint, which has been widespread to date (see, for example, [31]). According to this viewpoint, bulk screening in an intrinsic semiconductor brings about a decrease in the effective screened charge by a factor of ε_0 (where ε_0 is a constant) at any distance. On the other hand, in the quasi-classical approximation [17, 18, 30], the screened potential has the form

$$V_{semicl}(R) = \frac{q}{\varepsilon_0 R}\left[1 + (\varepsilon_0 - 1)\exp\left(-\kappa R\sqrt{\frac{\varepsilon_0}{\varepsilon_0 - 1}}\right)\right], \quad (18)$$

where R is the distance to the charge; from whence the classical formula $V_{cl}(R) = q/\varepsilon_0 R$ follows at $R \gg \kappa^{-1}$. However, in the immediate vicinity of the charge, we

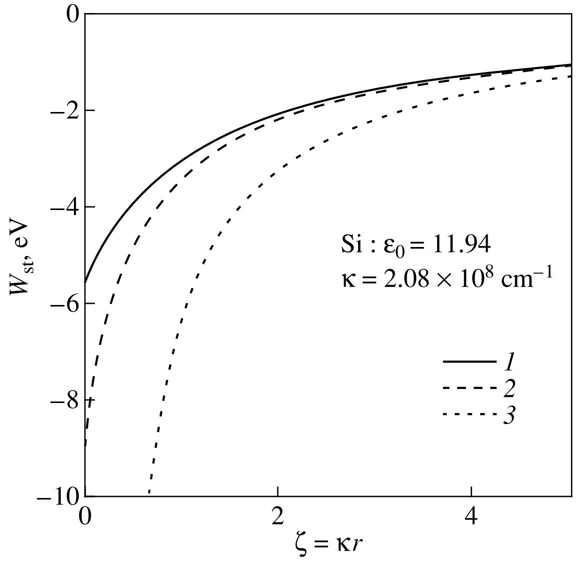

Fig. 2. Profiles of $W_{st}(r)$ near the Si–vacuum interface within the (*1*) Schulze–Unger, (*2*) Inkson, and (*3*) classical models.

have the potential $V_{semicl}(R \longrightarrow 0) \approx q/R$; i.e., it coincides with the Thomas–Fermi near asymptotics. This is not surprising because $\varepsilon_{semi}(\mathbf{k} \longrightarrow \infty, \omega = 0)$ tends to unity rather than to ε_0. At the same time, at high ionicity, the Thomas–Fermi dependence $V_{TF}(R) = (q/R)\exp(-\kappa R)$ for the screening by free electrons can be obtained from the semiclassical formula (18) for semiconductors.

Deng *et al.* [32] studied the impurity states in the GaAs–$Ga_{1-x}Al_xAs$ spherical quantum dots and took into account the spatial dispersion of ε in the coordinate representation. They used the Hermanson model [33] for the dielectric function:

$$\varepsilon^{-1}(R) = \varepsilon_0^{-1} + (1 - \varepsilon_0^{-1})\exp(-R/R_0), \qquad (19)$$

where R_0 is the screening length. It is easy to see that, in this case, the asymptotics of the potential $\tilde{V} = q/\varepsilon(R)$ about the point charge is identical to that of the potential $V_{semicl}(R)$ [relationship (18)].

Returning to our problem, we note that all the quantitative estimates based on formulas (13)–(16) can be confirmed by numerical calculations, which are not presented here for brevity.

As a model semiconductor, we chose Si with the following parameters: $\varepsilon_0 = 11.94$, $\kappa = 2.08 \times 10^8$ cm^{-1}, $k_F = 1.81 \times 10^8$ cm^{-1}, and $\omega_p = 2.6 \times 10^{16}$ s^{-1}. The value of κ corresponds to the hypothetical value when all valence electrons participate in the screening [16]. In what follows, a free electron with the corresponding values of *q* and *m* will be treated as a moving particle. Figure 2 shows the profiles of the static image energy W_{st} in vacuum near the interface with Si in the framework of the Inkson and Schulze–Unger models and in the framework of the classical model represented by the formula

$$W_{cl}^{semi}(r) = -\frac{q^2\alpha_0}{4r}. \qquad (20)$$

A drastic discrepancy between the curves plotted with and without regard for the dependence $\varepsilon_{semi}(\kappa, \omega)$ is observed over the entire range of distances important in the physics and chemistry of surfaces. It becomes clear that the quantum effects in the screening [relationship (8)] substantially affect the dependence $W_{st}(r)$ in the vicinity of the interface: the nonphysical feature $[dW_{st}/dr]_{r \to 0}$ vanishes and the Schulze–Unger profile is more flattened than the Inkson profile. For example, the surface energy $W_{st}^{SU}(0)$ is nearly one-half the energy $W_{st}^{I}(0)$, which indicates that the Inkson model leads to overestimation of this energy.

The inclusion of the quantum effects is even more important in calculating the dynamic corrections $\Delta W(r)$ and the corresponding total profiles of the image energy $W(r)$. The point is that the dynamic correction in our case is appreciably smaller than that in the Inkson model; thus, the range of applicability of our computational scheme [3, 12, 14] is considerably wider. This inference is illustrated in Fig. 3 with the profiles of $W_{st}(r)$ and $W(r)$ for the considered laws of charge motion and different models. In the case of uniform motion, we have the velocity $v = (2E_0/m)^{1/2}$, where E_0 is the kinetic energy of the particle. Consequently, allowance made for the quantum character of the screening in $\varepsilon(\kappa, \omega)$ renders our approach valid virtually over the entire real range of external fields and energies of emitted (incident) particles, whereas the Inkson model results in an excess dynamic renormalization of $W(r)$. Moreover, since the effective parameter of expansion is $\omega_*^2/\omega_p^2 \propto |\Delta W/W_{st}|$ (where ω_* is the characteristic frequency), the image forces are more strongly affected by the behavior of $\varepsilon(\mathbf{k}, \omega)$ at low frequencies ω than by the behavior of $\varepsilon(\mathbf{k}, \omega)$ at frequencies corresponding to the optical range. Therefore, the interband transitions that cannot be described by the semiempirical interpolation formulas (9) and (10) are virtually immaterial [8, 13, 29].

However, this analysis holds true for intrinsic semiconductors with high frequencies ω_p. If the semiconductor is extrinsic with a low density of charge carriers, the corresponding frequency ω_{pi} can be several orders of magnitude lower than the frequency ω_p for valence electrons. In this case, the dynamic effects can play a significant role and the computational scheme used will be valid only at low fields and velocities [3].

5. THE VACUUM GAP BETWEEN SEMICONDUCTORS

Similar calculations were carried out for the energy of image forces in the vacuum gap between two semiconductors (Fig. 1). We will restrict our consideration to the symmetric structure with $\varepsilon_1(\mathbf{k}, \omega) = \varepsilon_3(\mathbf{k}, \omega)$, because, otherwise, the theory would involve additional parameters that do not lead to any conceptually new effects.

Within the Inkson model, we succeeded in deriving asymptotic approximations of the profiles over the entire gap thickness for thin layers with $\delta\sqrt{\frac{\varepsilon_0}{\varepsilon_0 - 1}} \ll 1$ (where $\delta \equiv \kappa l$). In particular,

$$W_{\rm st}(\xi) \approx -\frac{q^2\kappa}{2}\left\{\sqrt{\frac{\varepsilon_0 - 1}{\varepsilon_0}} + \delta\left[\log\left(\gamma\delta\sqrt{\frac{\varepsilon_0}{\varepsilon_0 - 1}}\right) + \frac{\varepsilon_0 - 1}{\varepsilon_0}\left(\log 2 - \frac{1}{2}\right) - \frac{1}{2} + \frac{1}{2}(1 - \xi)\log(1 - \xi) + \frac{1}{2}(1 + \xi)\log(1 + \xi)\right]\right\} \quad (21)$$

and, for example, for the uniformly accelerated motion,

$$\Delta W(\xi) \approx \delta\frac{q^3 F\kappa^2}{12 m\omega_p^2}\sqrt{\frac{\varepsilon_0 - 1}{\varepsilon_0}}\{4 + \xi f(\varepsilon_0)\}, \quad (22)$$

where $\xi = z/l$ (so that $-1 \le \xi \le 1$) and $f(\varepsilon_0)$ is a certain cumbersome smooth function.

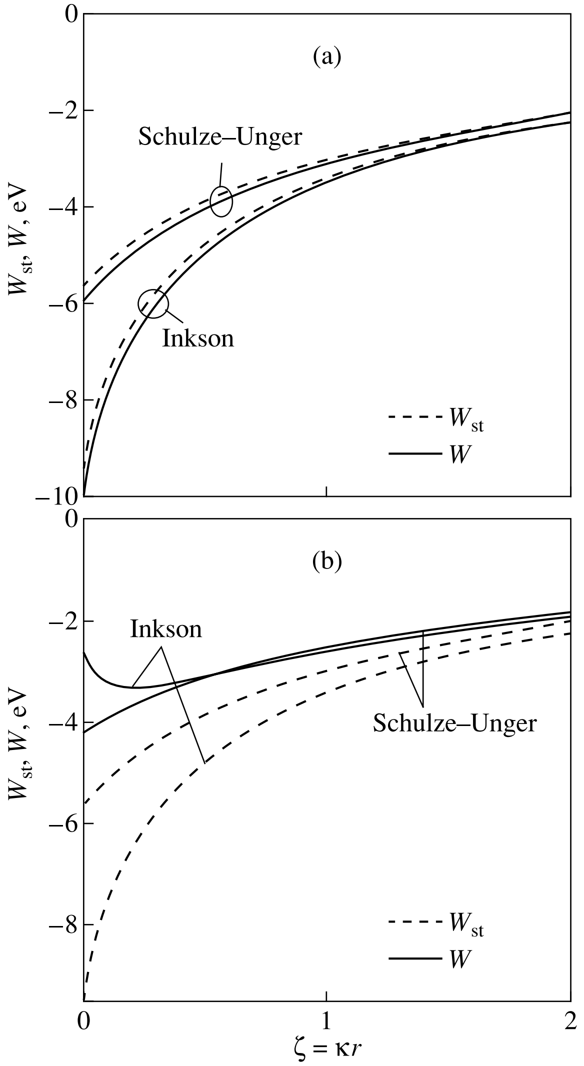

Fig. 3. Energies W of dynamic image forces and their static components $W_{\rm st}$ within different models of the Si semiconductor for (a) uniformly accelerated motion of a charge in the external field $F = 5 \times 10^8$ V/cm and (b) uniform motion of a charge with the kinetic energy $E_0 = 10$ eV.

All the inferences made in the previous section about the necessity of accounting for the quantum nature of the screening refer equally to the gap between the semiconductors. The profiles of $W_{\rm st}(\xi)$ for different models of $\varepsilon(\mathbf{k}, \omega)$ are displayed in Fig. 4. It is easy to see that, as the interlayer width $2l$ decreases, a strong difference between the Inkson and Schulze–Unger dependences is observed not only near the interface but across the whole width of the gap as well. In turn, this considerably affects the tunneling characteristics of similar junctions.

Finally, let us compare the energies W of dynamic image forces and their static components $W_{\rm st}$ for different models of $\varepsilon(\mathbf{k}, \omega)$ and the uniformly accelerated

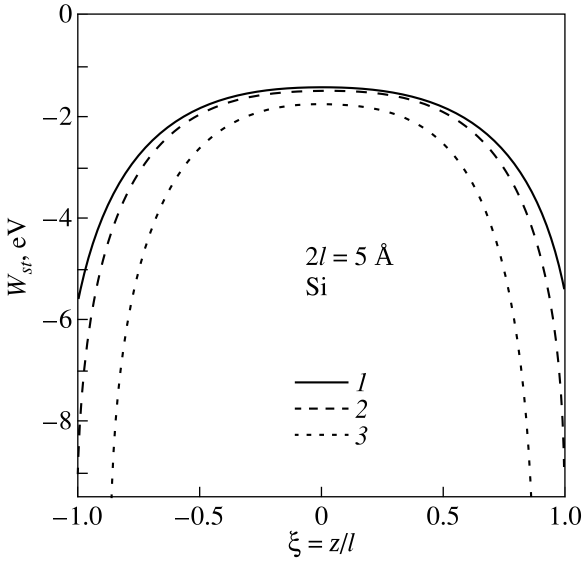

Fig. 4. Dependences $W_{\rm st}(z)$ in the vacuum gap between Si layers within the (*1*) Schulze–Unger, (*2*) Inkson, and (*3*) classical models.

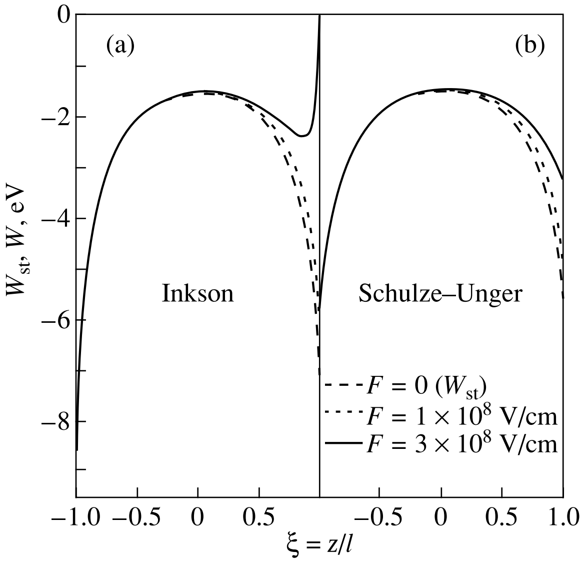

Fig. 5. Energies W of dynamic image forces and their static components W_{st} in the vacuum gap between Si layers ($2l$ = 5 Å) for uniformly accelerated motion of a charge in different external fields F within the (a) Inkson and (b) Schulze–Unger models.

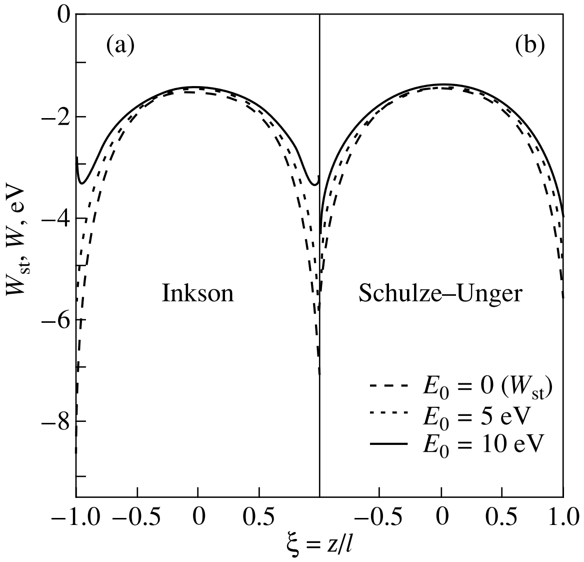

Fig. 6. The same as in Fig. 5 for uniform motion of a charge at different kinetic energies E_0.

(Fig. 5) and uniform (Fig. 6) laws of motion. As before, the nonadiabatic corrections in the framework of the more precise Schulze–Unger approximation appear to be sufficiently small, whereas the Inkson approximation ceases to work well at strong fields F or high kinetic energies of the particle.

What has been said regarding extrinsic semiconductors also remains true. In this respect, we note that the experimental results obtained by Guéret *et al.* [34] can be considered evidence that the dynamic corrections are not small. On the other hand, these results can be a consequence of a decrease in the tunneling barrier (associated with the static image forces) at small l [see expression (21)]. Therefore, it remains unclear whether the dynamic character of the image forces actually manifests itself in the experimental data described in [34].

Thus, the calculations performed demonstrate that the quantum character of the screening in semiconductors at large $\mathbf{k}$ should be adequately taken into account in order to calculate correctly the energy of the dynamic image forces near the semiconductor–vacuum interface. The dynamic corrections turned out to be sufficiently small at reasonable velocities of external charge motion. This justifies the use of the perturbation technique developed in our earlier works. It was found that the image energies $W(z)$ near the vacuum–metal and vacuum–intrinsic semiconductor interfaces do not differ qualitatively. In this case, it is of importance that the screening parameters κ and ω_p for semiconductors are of the same order of magnitude as those for metals [29]. Therefore, unlike the opinion of Krupski [35], the range of applicability of the specular reflection and infinite barrier model for semiconductors is identical to that for metals.

Although the dynamic corrections ΔW are not crucial for intrinsic semiconductors, they can appear to be important for the analysis of interfaces with plasma-like media at low densities of charge carriers. In this case, the ω_p frequencies are low and the dynamic contribution is not a small correction. Therefore, methods more perfect [7] than the perturbation approach should be applied. It is quite possible that the dynamic phenomena were actually observed in semiconductor heterostructures [34].

ACKNOWLEDGMENTS

This work was supported in part by the Ukrainian Foundation for Basic Research.

REFERENCES

1. A. M. Gabovich, L. G. Il’chenko, and É. A. Pashitskiĭ, Fiz. Tverd. Tela (Leningrad) **21**, 1683 (1979) [Sov. Phys. Solid State **21**, 965 (1979)].
2. A. M. Gabovich, L. G. Il’chenko, E. A. Pashitskii, and Yu. A. Romanov, Surf. Sci. **94**, 179 (1980).
3. A. M. Gabovich, V. M. Rozenbaum, and A. I. Voitenko, Surf. Sci. **186**, 523 (1987).
4. F. Bechstedt, R. Enderlein, and D. Reichardt, Phys. Status Solidi B **117**, 261 (1983).
5. V. M. Agranovich and V. L. Ginzburg, *Crystal Optics with Spatial Dispersion and Excitons* (Nauka, Moscow, 1979; Springer-Verlag, New York, 1984).
6. F. J. García de Abajo and P. M. Echenique, Phys. Rev. B **46**, 2663 (1992).

7. J. R. Manson and R. H. Ritchie, Phys. Rev. B **24**, 4867 (1981).
8. R. Núñez, P. M. Echenique, and R. H. Ritchie, J. Phys. C **13**, 4229 (1980).
9. M. A. Vorotyntsev and A. A. Kornyshev, *Electrostatics of Media with Spatial Dispersion* (Nauka, Moscow, 1993).
10. N. D. Lang, in *Theory of the Inhomogeneous Electron Gas (Physics of Solids and Liquids)*, Ed. by S. Lundqvist and N. H. March (Plenum, New York, 1983; Mir, Moscow, 1987), p. 309.
11. J. Heinrichs, Phys. Rev. B **8**, 1346 (1973).
12. A. I. Voĭtenko, A. M. Gabovich, and V. M. Rozenbaum, Zh. Éksp. Teor. Fiz. **87**, 1064 (1984) [Sov. Phys. JETP **60**, 608 (1984)].
13. A. Rivacoba, N. Zabala, and J. Aizpurua, Prog. Surf. Sci. **65**, 1 (2000).
14. A. I. Voĭtenko, A. M. Gabovich, and V. M. Rozenbaum, Fiz. Nizk. Temp. **22**, 86 (1996) [Low Temp. Phys. **22**, 64 (1996)].
15. A. V. Sidyakin, Zh. Éksp. Teor. Fiz. **58**, 573 (1970) [Sov. Phys. JETP **31**, 308 (1970)].
16. A. M. Gabovich and A. I. Voitenko, Phys. Status Solidi B **110**, 407 (1982).
17. Z.-H. Huang, M. Weimer, and R. E. Allen, Phys. Rev. B **48**, 15068 (1993).
18. J. C. Inkson, J. Phys. C **4**, 591 (1971).
19. K.-R. Schulze and K. Unger, Phys. Status Solidi B **66**, 491 (1974).
20. A. G. Milnes and D. L. Feucht, *Heterojunctions and Metal-Semiconductor Junctions* (Academic, New York, 1972; Mir, Moscow, 1975).
21. S. G. Davison and J. D. Levine, Solid State Phys. **25**, 1 (1970).
22. A. M. Gabovich, Fiz. Tverd. Tela (Leningrad) **25**, 1885 (1983) [Sov. Phys. Solid State **25**, 1088 (1983)].
23. A. M. Gabovich, V. M. Rozenbaum, and A. I. Voitenko, Phys. Status Solidi B **214**, 29 (1999).
24. J. Lindhard, K. Dan. Vidensk. Selsk. Mat.-Fys. Medd. **28**, 1 (1954).
25. H. Ehrenreich and M. Cohen, Phys. Rev. **115**, 786 (1959).
26. D. R. Penn, Phys. Rev. **128**, 2093 (1962).
27. A. C. Sharma and S. Auluck, Phys. Rev. B **28**, 965 (1983).
28. R. Resta, Phys. Rev. B **16**, 2717 (1977).
29. D. Pines, *Elementary Excitations in Solids* (Benjamin, New York, 1963; Mir, Moscow, 1965).
30. J. C. Inkson, J. Phys. C **5**, 2599 (1972).
31. M. Krčmar, W. M. Saslow, and M. B. Weimer, Phys. Rev. B **61**, 13821 (2000).
32. Z.-Y. Deng, J.-K. Guo, and T.-R. Lai, Phys. Rev. B **50**, 5736 (1994).
33. J. Hermanson, Phys. Rev. **150**, 660 (1966).
34. P. Guéret, E. Marclay, and H. Meier, Appl. Phys. Lett. **53**, 1617 (1988).
35. J. Krupski, J. Phys.: Condens. Matter **1**, 3009 (1989).

Translated by O. Borovik-Romanova

Physics of the Solid State, Vol. 43, No. 12, 2001, pp. 2336–2343. Translated from Fizika Tverdogo Tela, Vol. 43, No. 12, 2001, pp. 2255–2261.
Original Russian Text Copyright © 2001 by Kibis.

Features of Electron–Phonon Interaction in Nanotubes with Chiral Symmetry Placed in a Magnetic Field

O. V. Kibis
Novosibirsk State Technical University, Novosibirsk, 630092 Russia
e-mail: oleg.kibis@nstu.ru

Received April 16, 2001

Abstract—The interaction of electrons with acoustic phonons is considered in a nanotube with chiral symmetry placed in a magnetic field parallel to the nanotube axis. It is shown that in such a system, the electronic energy spectrum is not invariant under electron wavevector reversal and, therefore, the electron–phonon interaction is different for identical phonons with oppositely directed wavevectors. This phenomenon leads to the occurrence of an electromotive force during spatially homogeneous heating of an electron gas and to the presence of a term quadratic in current in the current–voltage characteristic of a nanotube. *© 2001 MAIK "Nauka/Interperiodica".*

1. INTRODUCTION

Considerable recent attention of theorists and experimentalists has been focused on low-dimensional structures in which the invariance under space inversion and the fundamental invariance under time reversal are simultaneously broken. Such systems are of interest, because the electronic energy spectrum in them is asymmetric:

$$\varepsilon(\mathbf{k}) \neq \varepsilon(-\mathbf{k}), \tag{1}$$

where **k** is the wavevector of an electron. Due to this asymmetry, the electronic properties of these structures become different in opposite directions, which leads to many fundamentally new physical phenomena [1–11]. For example, the electrons interact differently with any elementary excitations (photons, acoustic phonons, etc.) having oppositely directed wavevectors [5–7]. In turn, the asymmetry of the electron–phonon interaction gives rise to new thermodynamic effects; these effects were predicted theoretically in [8–10] and observed experimentally quite recently in two-dimensional structures with an asymmetric quantizing potential [11]. It is also of interest to study systems that are different from two-dimensional structures, i.e., systems in which the electronic energy spectrum exhibits asymmetry of Eq. (1) and the phenomena associated with this asymmetry take place. One of such low-dimensional solid-state systems may be a nanotube with chiral symmetry.

The physical properties of nanotubes with chiral symmetry (which are approximately a nanometer in diameter and in which the atomic arrangement has helical symmetry) became the subject of intense investigations after the first report on the fabrication of carbon nanotubes was published [12]. These are graphite layers rolled into tubes; the manner of rolling is characterized by two crystallographic parameters (n, m) which determine the diameter of the nanotube and its chirality [13–15]. The nanotube has no inversion center because of the helical symmetry of its crystalline structure. In the presence of a magnetic field, the invariance under time reversal is also broken. Therefore, carbon nanotubes with chiral symmetry, when placed in a magnetic field, must exhibit anomalous kinetic effects like those indicated above. In this paper, we theoretically investigate the effects associated with the specific features of electron–phonon interaction in such structures.

2. ASYMMETRY OF THE ELECTRONIC ENERGY SPECTRUM IN THE PRESENCE OF A MAGNETIC FIELD

We use a model [16, 17] in which a nanotube with chiral symmetry is considered as being composed of identical atoms (or atomic unit cells) arranged with a period b along a helical line (figure). It is assumed that the diameter of the helix is $D \gg b$ and its pitch is $d \ll D$; therefore, the length of one turn of the helix is

$$\sqrt{\pi^2 D^2 + d^2} = N_0 b,$$

where

$$N_0 \gg 1$$

is the number of atoms on one turn. The nanotube is placed in a magnetic field **H** directed along the axis of the helix. If the magnetic field is fairly weak, it will affect the magnitude of the wave function of an electron in an individual atom insignificantly and only the phase of the wave function will be varied in going from one atom to another. In this case, in the tight-binding approximation, the Hamiltonian of an electron in the nanotube is given by

$$\hat{\mathcal{H}} = \sum_n (|n\rangle\langle n|\mathcal{H}|n\rangle\langle n| + |n\rangle\langle n|\mathcal{H}|n+1\rangle\langle n+1| + |n\rangle\langle n|\mathcal{H}|n-1\rangle\langle n-1| + |n\rangle\langle n|\mathcal{H}|n+N_0\rangle \times \langle n+N_0| + |n\rangle\langle n|\mathcal{H}|n-N_0\rangle\langle n-N_0|), \tag{2}$$

where $|n\rangle$ is the electronic state in which the electron is near an atom with index n (the atoms are enumerated along the helical line, $n = \ldots, -1, 0, 1, \ldots$) and $\langle n|\mathcal{H}|n\rangle = \varepsilon_0$ is the energy of an electron in an isolated atom. The matrix elements of the Hamiltonian that determine the transition amplitude of an electron from atom n to its four nearest neighbors $n \pm 1$ and $n \pm N_0$ have the form

$$\langle n|\mathcal{H}|n\pm 1\rangle = -A(l_{n,n\pm 1})\exp(i\varphi_{n\pm 1}),$$

$$\langle n|\mathcal{H}|n\pm N_0\rangle = -A(l_{n,n\pm N_0})\exp(i\varphi_{n\pm N_0}).$$

Here, $-A(l_{n,m})$ is the real overlap integral of the wave functions of atoms n and m in a zero magnetic field (it depends on the distance $l_{n,m}$ between these atoms) and the phase shifts due to the magnetic field are given by

$$\varphi_{n\pm N_0} = \frac{e}{\hbar c}\int_n^{n\pm N_0} \mathbf{A}_H(\mathbf{r}')d\mathbf{r}', \tag{3}$$

$$\varphi_{n\pm 1} = \frac{e}{\hbar c}\int_n^{n\pm 1} \mathbf{A}_H(\mathbf{r}')d\mathbf{r}', \tag{4}$$

where $\mathbf{A}_H(\mathbf{r})$ is the vector potential of the magnetic field and e is the magnitude of the electronic charge. Integration in Eq. (3) is performed over the linear segment connecting atoms n and $n \pm N_0$ in adjacent turns, and integration in Eq. (4) is performed over the linear segment connecting atoms n and $n \pm 1$. Taking the vector potential in the axially symmetrical gauge

$$\mathbf{A}_H = \frac{1}{2}[\mathbf{H}\times\mathbf{r}],$$

we obtain from the general equations (3) and (4)

$$\varphi_{n\pm N_0} = 0,$$

$$\varphi_{n\pm 1} = \pm 2\pi\frac{\nu(H)}{N_0},$$

where

$$\nu(H) = \frac{\pi D^2 eH}{4ch}$$

is the number of quanta hc/e in the magnetic flux through the nanotube cross section.

First, let us consider the case where there are no phonons in the nanotube and, therefore, the interatomic distances $l_{n,m}$ are time-independent; that is, $l_{n,n\pm 1} = b$ and $l_{n,n\pm N_0} = d$ at any instant. In this case, the Hamiltonian (2) takes the form

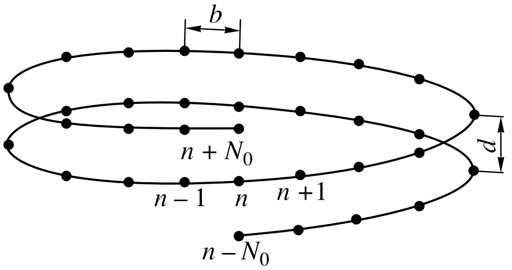

Fragment of the nanotube composed of atoms arranged along a helical line (schematic).

$$\hat{\mathcal{H}}_0 = \sum_n (|n\rangle\varepsilon_0\langle n| - |n\rangle A(b)\exp(i\varphi_{n+1})\langle n+1| - |n\rangle A(b)\exp(i\varphi_{n-1})\langle n-1| - |n\rangle A(d)\langle n+N_0| - |n\rangle A(d)\langle n-N_0|). \tag{5}$$

The eigenfunctions of this Hamiltonian are

$$\psi_k = \sum_n C_n(k)|n\rangle, \tag{6}$$

where the probability amplitude of an electron being near atom n is

$$C_n(k) = \frac{1}{\sqrt{N}}\exp(inkb)\exp[-i\varepsilon(k)t/\hbar], \tag{7}$$

k is the wavenumber of the electron characterizing its motion along the helical line, N is the total number of atoms in the nanotube, and the energy of an electron in the nanotube is

$$\varepsilon(k) = \varepsilon_0 - 2A(b)\cos\left(kb + 2\pi\frac{\nu(H)}{N_0}\right) - 2A(d)\cos(N_0 kb). \tag{8}$$

It follows from Eq. (8) that the energy spectrum of electrons in the nanotube is a periodic function of the magnetic field. If the magnetic field is such that

$$\frac{\nu(H)}{N_0} \neq z \quad (z = 0, 1, 2, 3, \ldots),$$

then we have an asymmetric energy spectrum as in Eq. (1).

Before proceeding to an analysis of the effects associated with the asymmetric spectrum in Eq. (1), we adapt our model to the specific case of carbon nanotubes with a weak chirality of the (n, 1) type, where $n \gg 1$. In such nanotubes, the interatomic distances are $b \approx d$ and, hence, for the overlap integrals of the atomic wave functions, we have $A(b) \approx A(d)$. Therefore, in our calculations in what follows, we put

$$b = d = a, \quad A(b) = A(d) = A(a),$$

where $a \sim 10^{-8}$ cm is the characteristic spatial period of the crystalline structure of the nanotube and $A(a) \sim 1$ eV is the typical value of an overlap integral. In what follows, we restrict our analysis to the case of weak magnetic fields for which

$$\frac{\nu(H)}{N_0} \ll 1 \tag{9}$$

and the electrons are assumed to be in states close to the minimum of the energy band in Eq. (8) situated at the point $k = 0$ in the absence of a magnetic field. Taking the energy at the minimum as zero, the electronic energy spectrum in Eq. (8) near this minimum in the presence of a magnetic field can be written as

$$\varepsilon_k = \frac{\hbar^2(k-k_H)^2}{2m}, \tag{10}$$

where the shift of the bottom of the conduction band due to the magnetic field is

$$k_H = -\frac{2\pi}{aN_0^3}\nu(H)$$

and the effective electronic mass equals

$$m = \frac{\hbar^2}{2A(a)N_0^2a^2}.$$

3. SPATIAL ASYMMETRY OF ELECTRON–PHONON INTERACTION

In the nanotube under study, acoustic waves propagating along the helical line are characterized by the wavenumber q. Let us consider the interaction of electrons with longitudinal acoustic phonons (which cause the atoms to be displaced from their equilibrium positions along the helical line) and transverse acoustic phonons (with atomic displacements perpendicular to the helical line) in the case of an asymmetric energy spectrum (1).

In a longitudinal acoustic wave, the coordinate x_n of atom n along the helical line is given by

$$x_n = na + \tilde{x}_n, \tag{11}$$

where the atomic displacement from the equilibrium position is

$$\tilde{x}_n = \sum_{q_l} u_{q_l}\exp(inq_la)\exp[-i\omega(q_l)t],$$

q_l is the wavenumber of a longitudinal phonon, the amplitude of atomic displacements is given by

$$u_{q_l} = \left[\frac{\hbar}{2\omega(q_l)NM}\right]^{1/2},$$

the phonon frequency is

$$\omega(q_l) = v_l|q_l|,$$

v_l is the velocity of the longitudinal acoustic wave, and M is the atomic mass. We substitute Eq. (11) into the overlap integrals and, taking into account that the change in the interatomic distance in the acoustic wave is much smaller than the crystalline-structure period a,

$$\frac{|\tilde{x}_n - \tilde{x}_{n\pm 1}|}{a} \ll 1,$$

we expand the overlap integrals of atomic wave functions $A(l_{n,\,m})$ in a power series in this small parameter and obtain up to first-order terms from Eq. (2):

$$\hat{\mathcal{H}} = \hat{\mathcal{H}}_0 + \sum_{q_l}\hat{\mathcal{H}}_{q_l}. \tag{12}$$

Here, $\hat{\mathcal{H}}_{q_l}$ is the interaction Hamiltonian between an electron and a longitudinal phonon with wavenumber q_l, which is given by

$$\begin{aligned}\hat{\mathcal{H}}_{q_l} = \sum_n (|n\rangle\langle n|\mathcal{H}_{q_l}|n+1\rangle\langle n+1| \\ + |n\rangle\langle n|\mathcal{H}_{q_l}|n-1\rangle\langle n-1|),\end{aligned} \tag{13}$$

where the matrix elements are

$$\begin{aligned}\langle n|\mathcal{H}_{q_l}|n+1\rangle &= (\Xi/a)u_{q_l}\exp[-i\omega(q_l)t]\exp(inq_la) \\ &\times \exp(i\varphi_{n+1})[\exp(iq_la)-1], \\ \langle n|\mathcal{H}_{q_l}|n-1\rangle &= (\Xi/a)u_{q_l}\exp[-i\omega(q_l)t]\exp(inq_la) \\ &\times \exp(i\varphi_{n-1})[1-\exp(-iq_la)],\end{aligned}$$

and the deformation-potential constant for the nanotube is

$$\Xi = -a\frac{dA(l)}{dl}\bigg|_{l=a}.$$

The probability of a phonon with q_l being absorbed by electrons is given by the well-known quantum-mechanical relation

$$\begin{aligned}W_a(q_l) = \frac{f_{\mathrm{BE}}(q_l)}{\hbar^2}\sum_k\sum_{k'}|\langle\psi_{k'}|\hat{\mathcal{H}}_{q_l}|\psi_k\rangle|^2 \\ \times f_{\mathrm{FD}}(\varepsilon_k)[1-f_{\mathrm{FD}}(\varepsilon_{k'})],\end{aligned} \tag{14}$$

where $f_{\mathrm{BE}}(q)$ is the Bose–Einstein distribution function for a phonon with wavenumber q, $f_{\mathrm{FD}}(\varepsilon)$ is the Fermi–Dirac distribution function for an electron with energy ε, and $\langle\psi_{k'}|\hat{\mathcal{H}}_{q_l}|\psi_k\rangle$ is the matrix element of the electron–phonon interaction corresponding to the transition of an electron from state k to state k' due to absorption of a phonon with q_l. Inserting the explicit expressions (6) and (7) for the wave function and Eq. (13) for the electron–phonon interaction Hamiltonian into this matrix element, we obtain

$$\begin{aligned}\langle\psi_{k'}|\hat{\mathcal{H}}_{q_l}|\psi_k\rangle &= i\left(\frac{2\pi}{a}\right)^2\left(\frac{\Xi\hbar}{N}\right)\left(\frac{2\hbar}{\omega(q_l)NM}\right)^{1/2} \\ &\times\delta(\varepsilon_k+\hbar\omega(q_l)-\varepsilon_{k'})\delta(k+q_l-k') \\ &\times\left[\sin\left([q_l+k]a+2\pi\frac{\nu(H)}{N_0}\right)\right. \\ &\left.-\sin\left(ka+2\pi\frac{\nu(H)}{N_0}\right)\right].\end{aligned} \qquad (15)$$

Substituting Eq. (10) into Eqs. (14) and (15), we find the longitudinal-phonon absorption probability per unit time per unit length of the helical line to the first order in the magnetic-field strength:

$$w_a(q_l) = w_{a0}(q_l)\left[1-\frac{4\pi amv_l}{\hbar N_0}\frac{q_l}{|q_l|}\nu(H)\right], \qquad (16)$$

where

$$\begin{aligned}w_{a0}(q_l) &= \left(\frac{4\Xi^2m}{\hbar^2v_lMN}\right)f_{\mathrm{FD}}\left(\frac{\hbar^2}{2m}\left[\frac{mv_l}{\hbar}-\frac{|q_l|}{2}\right]^2\right) \\ &\times\left[1-f_{\mathrm{FD}}\left(\frac{\hbar^2}{2m}\left[\frac{mv_l}{\hbar}+\frac{|q_l|}{2}\right]^2\right)\right]f_{\mathrm{BE}}(q_l)\end{aligned} \qquad (17)$$

is the probability of phonon absorption in a zero magnetic field.

In a similar way, the probability that a longitudinal phonon with wavenumber q_l will be emitted is found to be

$$w_e(q_l) = w_{e0}(q_l)\left[1-\frac{4\pi amv_l}{\hbar N_0}\frac{q_l}{|q_l|}\nu(H)\right], \qquad (18)$$

where

$$\begin{aligned}w_{e0}(q_l) &= \left(\frac{4\Xi^2m}{\hbar^2v_lMN}\right)f_{\mathrm{FD}}\left(\frac{\hbar^2}{2m}\left[\frac{mv_l}{\hbar}+\frac{|q_l|}{2}\right]^2\right) \\ &\times\left[1-f_{\mathrm{FD}}\left(\frac{\hbar^2}{2m}\left[\frac{mv_l}{\hbar}-\frac{|q_l|}{2}\right]^2\right)\right][f_{\mathrm{BE}}(q_l)+1]\end{aligned} \qquad (19)$$

is the phonon emission probability in a zero magnetic field.

The interaction of electrons with transverse acoustic phonons is treated in the same manner as in the case of longitudinal phonons, the only difference being that one should take into account the fact that transverse phonons change the distance between atoms situated in different turns of the helix. In a transverse acoustic wave, the coordinate z_n of atom n along the axis of the helix is given by

$$z_n = na+\tilde{z}_n, \qquad (20)$$

where the atomic displacement from the equilibrium position is

$$\tilde{z}_n = \sum_{q_t}u_{q_t}\exp(inq_ta)\exp[-i\omega(q_t)t],$$

q_t is the wavenumber of a transverse phonon, the amplitude of atomic displacements is given by

$$u_{q_t} = \left[\frac{\hbar}{2\omega(q_t)NM}\right]^{1/2},$$

the transverse-phonon frequency is

$$\omega(q_t) = v_t|q_t|,$$

and v_t is the velocity of the transverse acoustic wave. We substitute Eq. (20) into the overlap integrals, and, taking into account that the change in the interatomic distance in the acoustic wave is much smaller than the pitch of the helix,

$$\frac{|\tilde{z}_n-\tilde{z}_{n\pm1}|}{a} \ll 1,$$

we expand the overlap integrals of atomic wave functions $A(l_{n,m})$ in a power series in this small parameter and obtain up to first-order terms from Eq. (2):

$$\hat{\mathcal{H}} = \hat{\mathcal{H}}_0+\sum_{q_t}\hat{\mathcal{H}}_{q_t}. \qquad (21)$$

Here, $\hat{\mathcal{H}}_{q_t}$ is the interaction Hamiltonian between an electron and a transverse phonon with wavevector q_t, which is given by

$$\begin{aligned}\hat{\mathcal{H}}_{q_t} &= \sum_n(|n\rangle\langle n|\mathcal{H}_{q_t}|n+N_0\rangle\langle n+N_0| \\ &+|n\rangle\langle n|\mathcal{H}_{q_t}|n-N_0\rangle\langle n-N_0|),\end{aligned} \qquad (22)$$

where the matrix elements are

$$\begin{aligned}\langle n|\hat{\mathcal{H}}_{q_t}|n+N_0\rangle &= (\Xi/a)u_{q_t}\exp[-i\omega(q_t)t] \\ &\times\exp(inq_ta)[\exp(iN_0q_ta)-1], \\ \langle n|\mathcal{H}_{q_t}|n-N_0\rangle &= (\Xi/a)u_{q_t}\exp[-i\omega(q_t)t] \\ &\times\exp(inq_ta)[1-\exp(-iN_0q_ta)].\end{aligned}$$

The probability of a transverse phonon being absorbed by electrons is

$$W_a(q_t) = \frac{f_{\mathrm{BE}}(q_t)}{\hbar^2}\sum_k\sum_{k'}\left|\langle\psi_{k'}|\hat{\mathcal{H}}_{q_t}|\psi_k\rangle\right|^2 \times f_{\mathrm{FD}}(\varepsilon_k)[1 - f_{\mathrm{FD}}(\varepsilon_{k'})], \tag{23}$$

where the matrix element of the electron–phonon interaction, corresponding to the transition of an electron from state k to state k' due to absorption of a phonon with q_t, is

$$\begin{aligned}\langle\psi_{k'}|\hat{\mathcal{H}}_{q_t}|\psi_k\rangle &= i\left(\frac{2\pi}{a}\right)^2\left(\frac{\Xi\hbar}{N}\right)\left(\frac{2\hbar}{\omega(q_t)NM}\right)^{1/2}\\ &\times\delta(\varepsilon_k + \hbar\omega(q_t) - \varepsilon_{k'})\delta(k + q_t - k')\\ &\times[\sin(N_0[q_t + k]a) - \sin(N_0ka)].\end{aligned} \tag{24}$$

Substituting Eq. (10) into Eqs. (23) and (24), we find the transverse-phonon absorption probability per unit time per unit length of the helical line to the first order in the magnetic-field strength:

$$w_a(q_t) = w_{a0}(q_t)\left[1 + \frac{4\pi am v_t}{\hbar N_0}\frac{q_t}{|q_t|}\nu(H)\right], \tag{25}$$

where

$$\begin{aligned}w_{a0}(q_t) &= \left(\frac{4\Xi^2 mN_0^2}{\hbar^2 v_t MN}\right)f_{\mathrm{FD}}\left(\frac{\hbar^2}{2m}\left[\frac{mv_t}{\hbar} - \frac{|q_t|}{2}\right]^2\right)\\ &\times\left[1 - f_{\mathrm{FD}}\left(\frac{\hbar^2}{2m}\left[\frac{mv_t}{\hbar} + \frac{|q_t|}{2}\right]^2\right)\right]f_{\mathrm{BE}}(q_t)\end{aligned} \tag{26}$$

is the transverse-phonon absorption probability in a zero magnetic field.

In a similar way, the transverse-phonon emission probability is found to be

$$w_e(q_t) = w_{e0}(q_t)\left[1 + \frac{4\pi am v_t}{\hbar N_0}\frac{q_t}{|q_t|}\nu(H)\right], \tag{27}$$

where

$$\begin{aligned}w_{e0}(q_t) &= \left(\frac{4\Xi^2 mN_0^2}{\hbar^2 v_t MN}\right)f_{\mathrm{FD}}\left(\frac{\hbar^2}{2m}\left[\frac{mv_t}{\hbar} + \frac{|q_t|}{2}\right]^2\right)\\ &\times\left[1 - f_{\mathrm{FD}}\left(\frac{\hbar^2}{2m}\left[\frac{mv_t}{\hbar} - \frac{|q_t|}{2}\right]^2\right)\right][f_{\mathrm{BE}}(q_t) + 1]\end{aligned} \tag{28}$$

is the transverse-phonon emission probability in a zero magnetic field.

From Eq. (16), (18), (25), and (27), it is immediately obvious that the electron–phonon interaction is spatially asymmetric: the interaction probabilities between an electron and identical phonons with oppositely directed wavevectors are different.

4. THE OCCURRENCE OF AN ELECTROMOTIVE FORCE DURING SPATIALLY HOMOGENEOUS HEATING OF AN ELECTRON GAS

Now, we discuss the interaction between the electron and phonon subsystems during spatially homogeneous heating. In this case, the subsystems are in a nonequilibrium state. The energy distribution of phonons is described by the Bose–Einstein function

$$f_{\mathrm{BE}}(q) = \left[\exp\left(\frac{\hbar\omega(q)}{k_{\mathrm{B}}T}\right) - 1\right]^{-1},$$

where T is the temperature of the crystal lattice, whereas the energy distribution of electrons is described by the Fermi–Dirac function

$$f_{\mathrm{FD}}(\varepsilon) = \left[\exp\left(\frac{\varepsilon - \varepsilon_{\mathrm{F}}}{k_{\mathrm{B}}T_e}\right) + 1\right]^{-1},$$

where T_e is the electronic temperature. At $T_e < T$, heat transfer occurs from the phonon subsystem to the electronic subsystem and phonons are absorbed by electrons. At $T_e > T$, conversely, heat is transferred from electrons to the phonon subsystem, which is accompanied by phonon emission. Since the electron–phonon interaction probability is different for phonons with oppositely directed wavevectors, the heat transfer is accompanied by a change in the total momentum of the electronic subsystem, which gives rise to the occurrence of an electromotive force (emf) at $T_e \neq T$. This phenomenon is a manifestation of the universal law [7] stating that an emf is induced in any electronic system with an asymmetric energy spectrum, as in Eq. (1), when subjected to an isotropic perturbation. In the case under consideration, the isotropic perturbation is spatially homogeneous heating.

Now, we consider the relatively low temperatures at which umklapp scattering due to electron–phonon interaction is negligible (the wave vectors remain within the first Brillouin zone). In this case, the average force exerted on an electron by the phonon subsystem is

$$\begin{aligned}F &= \frac{\hbar}{n_L}\sum_{q_l} q_l[w_a(q_l) - w_e(q_l)]\\ &+ \frac{\hbar}{n_L}\sum_{q_t} q_t[w_a(q_t) - w_e(q_t)],\end{aligned} \tag{29}$$

where n_L is the electron concentration per unit length of the helical line. Therefore, the electric field of extraneous forces is

$$E^* = -\frac{F}{e} \tag{30}$$

and the emf induced in the nanotube is

$$\mathcal{E} = \int_{-L/2}^{L/2} E^* dx, \tag{31}$$

where $L = Na$ is the length of the helical line. It follows from Eqs. (29)–(31) that the emf of interest can be written as

$$\begin{aligned}\mathcal{E} &= \frac{\hbar L}{n_L e}\sum_{q_l} q_l[w_e(q_l) - w_a(q_l)] \\ &+ \frac{\hbar L}{n_L e}\sum_{q_t} q_t[w_e(q_t) - w_a(q_t)].\end{aligned} \tag{32}$$

Using Eqs. (16)–(19) and (25)–(28) for the electron–phonon interaction probabilities, we find that

$$\frac{w_a(q_t)}{w_a(q_l)} \sim \frac{w_e(q_t)}{w_e(q_l)} \sim N_0^2 \gg 1;$$

therefore, the emf given by Eq. (32) is basically due to the interaction with transverse phonons. We will neglect the interaction of electrons with longitudinal phonons in Eq. (32) and substitute this expression into Eqs. (25)–(28). By transforming the sum over phonon states into an integral over the phonon wavenumber, one can obtain from Eq. (32)

$$\begin{aligned}\mathcal{E} &= \left(\frac{4\Xi ma}{\hbar}\right)^2\left(\frac{LN_0}{Men_L}\right)\nu(H) \\ &\times \int_0^\infty dq_t q_t \left\{\left[1 - f_{\rm FD}\left(\frac{\hbar^2}{2m}\left[\frac{mv_t}{\hbar} - \frac{|q_t|}{2}\right]^2\right)\right]\right. \\ &\times f_{\rm FD}\left(\frac{\hbar^2}{2m}\left[\frac{mv_t}{\hbar} + \frac{|q_t|}{2}\right]^2\right)[f_{\rm BE}(q_t) + 1] \\ &- \left[1 - f_{\rm FD}\left(\frac{\hbar^2}{2m}\left[\frac{mv_t}{\hbar} + \frac{|q_t|}{2}\right]^2\right)\right] \\ &\left.\times f_{\rm FD}\left(\frac{\hbar^2}{2m}\left[\frac{mv_t}{\hbar} - \frac{|q_t|}{2}\right]^2\right) f_{\rm BE}(q_t)\right\}.\end{aligned} \tag{33}$$

We will treat the electron–phonon interaction as a quasi-elastic process, which is justified if

$$\frac{mv_t^2}{k_{\rm B}T_e} \ll 1,$$

and, in addition, we will assume that the electron gas is highly heated,

$$\frac{T}{T_e} \ll 1.$$

Under these conditions, Eq. (33) takes a simple form,

$$\begin{aligned}\mathcal{E} &= \left(\frac{4\Xi ma}{\hbar}\right)^2\left(\frac{LN_0}{Men_L}\right)\nu(H) \\ &\times \int_0^\infty dq_t q_t\left[1 - f_{\rm FD}\left(\frac{\hbar^2 q_t^2}{8m}\right)\right] f_{\rm FD}\left(\frac{\hbar^2 q_t^2}{8m}\right).\end{aligned} \tag{34}$$

The integral in Eq. (34) can be easily expressed as elementary functions, and we obtain a final expression for the emf,

$$\begin{aligned}\mathcal{E} &= \left(\frac{8\Xi ma}{\hbar^2}\right)^2\left(\frac{LN_0 mk_{\rm B}T_e}{Men_L}\right)\nu(H) \\ &\times \left[1 + \exp\left(-\frac{\varepsilon_{\rm F}}{k_{\rm B}T_e}\right)\right]^{-1}.\end{aligned} \tag{35}$$

In the case of a degenerate electron gas, we have

$$\exp\left(-\frac{\varepsilon_{\rm F}}{k_{\rm B}T_e}\right) \ll 1$$

and, therefore, the emf in Eq. (35) is a linear function of temperature:

$$\mathcal{E} = \left(\frac{8\Xi ma}{\hbar^2}\right)^2\left(\frac{LN_0 mk_{\rm B}T_e}{Men_L}\right)\nu(H). \tag{36}$$

If the electron gas is nondegenerate, that is,

$$\exp\left(-\frac{\varepsilon_{\rm F}}{k_{\rm B}T_e}\right) \gg 1,$$

$$n_L = \sqrt{\frac{mk_{\rm B}T_e}{2\hbar^2\pi}}\exp\left(\frac{\varepsilon_{\rm F}}{k_{\rm B}T_e}\right),$$

then the emf in Eq. (35) varies as the square root of the temperature:

$$\mathcal{E} = \left(\frac{8\Xi ma}{\hbar^2}\right)^2\left(\frac{LN_0\hbar}{Me}\right)\nu(H)\sqrt{2\pi mk_{\rm B}T_e}. \tag{37}$$

For carbon nanotubes of diameter $D \sim 10^{-9}$ m, magnetic fields $H \sim 10^4$ G, and electronic temperatures $T_e \sim 10^2$ K, we obtain from Eq. (37)

$$\frac{\mathcal{E}}{L} \sim 10^{-4} \text{ V/cm}.$$

5. THE EFFECT OF ASYMMETRIC ELECTRON–PHONON INTERACTION ON THE CURRENT–VOLTAGE CHARACTERISTIC OF THE NANOTUBE

The electronic subsystem can be easily heated with respect to the crystal lattice, and an emf $\mathcal{E}$ can be induced by Joule heating. Therefore, an electric current J flowing through a carbon nanotube placed in an external magnetic field will induce an emf $\mathcal{E}$, which will cause a change in the current–voltage characteristic of the nanotube. In order to analyze the effect of the electron–phonon interaction on the current–voltage characteristic, one must derive a relation between J and $\mathcal{E}$.

The energy per unit time, J^2R, is transferred from the power source to the electron subsystem and then to the crystal lattice through phonon emission. Therefore, the energy balance equation for the electron and phonon subsystems has the form

$$J^2R = L\sum_{q_l}\hbar\omega(q_l)[w_e(q_l) - w_a(q_l)] + L\sum_{q_t}\hbar\omega(q_t)[w_e(q_t) - w_a(q_t)], \tag{38}$$

where R is the electrical resistance of the nanotube. From the analysis performed above, it follows that the electrons interact predominantly with transverse phonons and, therefore, their interaction with longitudinal phonons can be neglected in Eq. (38). Substituting Eq. (38) into Eqs. (25)–(28) for the electron–transverse-phonon interaction probabilities and transforming the sum over phonon states into an integral over the phonon wavenumber, we obtain

$$\begin{aligned} J^2R &= \left(\frac{4\Xi^2 m N_0^2 La}{\hbar\pi M}\right) \\ &\times\int_0^\infty dq_t q_t\left\{\left[1 - f_{\mathrm{FD}}\left(\frac{\hbar^2}{2m}\left[\frac{mv_t}{\hbar} - \frac{|q_t|}{2}\right]^2\right)\right]\right. \\ &\times f_{\mathrm{FD}}\left(\frac{\hbar^2}{2m}\left[\frac{mv_t}{\hbar} + \frac{|q_t|}{2}\right]^2\right)[f_{\mathrm{BE}}(q_t) + 1] \\ &- \left[1 - f_{\mathrm{FD}}\left(\frac{\hbar^2}{2m}\left[\frac{mv_t}{\hbar} + \frac{|q_t|}{2}\right]^2\right)\right] \\ &\left.\times f_{\mathrm{FD}}\left(\frac{\hbar^2}{2m}\left[\frac{mv_t}{\hbar} - \frac{|q_t|}{2}\right]^2\right)f_{\mathrm{BE}}(q_t)\right\}. \end{aligned} \tag{39}$$

It is seen that the integral in Eq. (39) is the same as that in Eq. (33). Therefore, by combining Eqs. (33) and (39), one easily obtains the relation between $\mathcal{E}$ and J:

$$\mathcal{E} = \alpha(H)J^2, \tag{40}$$

where

$$\alpha(H) = \frac{4\pi maR}{\hbar e n_L N_0}\nu(H).$$

The voltage U across the ends of the nanotube carrying current J is the sum of the conventional ohmic term JR and the emf given by Eq. (40). Therefore, the current–voltage characteristic $U(J)$ of the nanotube is given by

$$U(J) = JR + \alpha(H)J^2. \tag{41}$$

It follows from Eq. (41) that, due to the spatial asymmetry of the electron–phonon interaction, a term quadratic in the current appears in the current–voltage characteristic. For $N_0 \approx 5$, $n_L \sim 10^4$ cm^{-1}, $J \sim 10$ nA, and $H \sim 10^5$ G, the term quadratic in the current in Eq. (41) for the voltage is equal to a few tenths of percent of the ohmic term.

6. CONCLUSIONS

Thus, we have shown that the electronic energy spectrum of a nanotube with chiral symmetry becomes asymmetric when the nanotube is placed in a magnetic field directed along its axis. Due to this asymmetry, the electrons interact differently with identical phonons moving in opposite directions. In turn, because of the spatially asymmetric electron–phonon interaction, the energy transfer from the electronic subsystem to the crystal lattice through phonon emission is accompanied by a change in the electronic-subsystem momentum and, therefore, an emf is developed. In particular, the emf can be generated when the electronic subsystem is heated by passing an electric current through the nanotube. The induced emf leads to the appearance of a term quadratic in current in the current–voltage characteristic of the nanotube, because the electronic-subsystem heating is independent of the direction of the current. The value of this quadratic term and the corresponding rectifying effect in the nanotube are controlled by the magnetic field; this is promising for the use of nanotubes as elements of functional electronics.

ACKNOWLEDGMENTS

This study was supported by the Russian Foundation for Basic Research (project nos. 00-02-17987, 00-02-18010), the Ministry of Education of the Russian Federation (project no. E00-3.4-506), and the INTAS Foundation (grant no. 99-1661).

REFERENCES

1. A. A. Gorbatsevich, V. V. Kapaev, and Yu. V. Kopaev, Pis'ma Zh. Éksp. Teor. Fiz. **57** (9), 565 (1993) [JETP Lett. **57**, 580 (1993)].
2. Yu. A. Aleshchenko, I. D. Voronova, S. P. Grishechkina, *et al.*, Pis'ma Zh. Éksp. Teor. Fiz. **58** (5), 377 (1993) [JETP Lett. **58**, 384 (1993)].
3. O. E. Omel'yanovskiĭ, V. I. Tsebro, and V. I. Kadushkin, Pis'ma Zh. Éksp. Teor. Fiz. **63** (3), 197 (1996) [JETP Lett. **63**, 209 (1996)].
4. A. A. Gorbatsevich, V. V. Kapaev, Yu. V. Kopaev, *et al.*, Pis'ma Zh. Éksp. Teor. Fiz. **68** (5), 380 (1998) [JETP Lett. **68**, 404 (1998)].

5. O. V. Kibis, Pis’ma Zh. Éksp. Teor. Fiz. **66** (8), 551 (1997) [JETP Lett. **66**, 588 (1997)].
6. O. V. Kibis, Phys. Lett. A **237**, 292 (1998); **244**, 574 (1998).
7. O. V. Kibis, Physica B (Amsterdam) **256–258**, 449 (1998).
8. O. V. Kibis, Phys. Lett. A **244**, 432 (1998).
9. O. V. Kibis, Zh. Éksp. Teor. Fiz. **115** (3), 959 (1999) [JETP **88**, 527 (1999)].
10. O. V. Kibis, Phys. Low-Dimens. Struct. **9/10**, 143 (1999).
11. A. G. Pogosov, M. V. Budantsev, O. V. Kibis, *et al.*, Phys. Rev. B **61** (23), 15603 (2000).
12. S. Iijima, Nature **354**, 56 (1991).
13. M. S. Dresselhaus, G. Dresselhaus, and P. C. Eklund, *Science of Fullerenes and Carbon Nanotubes* (Academic, San Diego, 1996).
14. A. V. Eletskiĭ, Usp. Fiz. Nauk **167** (9), 945 (1997) [Phys. Usp. **40**, 899 (1997)].
15. L. G. Bulusheva, A. V. Okotrub, D. A. Romanov, and D. Tomanek, Phys. Low-Dimens. Struct. **3/4**, 107 (1998).
16. D. A. Romanov and O. V. Kibis, Phys. Lett. A **178**, 335 (1993).
17. O. V. Kibis and D. A. Romanov, Fiz. Tverd. Tela (St. Petersburg) **37** (1), 129 (1995) [Phys. Solid State **37**, 69 (1995)].

Translated by Yu. Epifanov

Physics of the Solid State, Vol. 43, No. 12, 2001, pp. 2344–2350. Translated from Fizika Tverdogo Tela, Vol. 43, No. 12, 2001, pp. 2262–2268.
Original Russian Text Copyright © 2001 by Kobelev, Nikolaev, Sidorov, Soĭfer.

Temperature Dependence of Elastic Moduli for Solid C_{60}

N. P. Kobelev, R. K. Nikolaev, N. S. Sidorov, and Ya. M. Soĭfer
Institute of Solid-State Physics, Russian Academy of Sciences, Chernogolovka, Moscow oblast, 142432 Russia
e-mail: kobelev@issp.ac.ru

Received April 16, 2001

Abstract—The attenuation and velocity of ultrasonic waves (at a frequency of ~4 MHz) along the ⟨111⟩ and ⟨100⟩ directions in solid C_{60} single-crystal samples are measured in the temperature range 100–300 K. The temperature dependences of the complete set of elastic constants for C_{60} fullerite are determined from the experimental data. It is shown that the specific features in the behavior of the elastic moduli near the orientational phase transition temperature are associated with different contributions of the relaxation processes to the effective elastic moduli. The activation volume and deformation potentials for the ground and excited states of the C_{60} low-temperature phase are evaluated from the results obtained in this work and the data available in the literature. © *2001 MAIK "Nauka/Interperiodica".*

1. INTRODUCTION

The elastic moduli, thermodynamic potential, specific heat, Grüneisen constant, and other parameters are the fundamental characteristics of a solid. The determination of their magnitudes and temperature dependences is essential to the understanding of the specific features in the physical properties of solid C_{60}. Moreover, measurement of the elastic constants can serve as an experimental test of the validity of theories describing intermolecular interaction in fullerite. At present, all elastic constants for the face-centered cubic phase of C_{60} at room temperature are known [1–3]. However, the available data on the temperature dependences of the elastic constants are contradictory. These contradictions can be explained by the fact that the aforementioned dependences were determined from measurements of only one of the elastic constants. It was found that anomalies in the temperature dependences of the elastic moduli of solid C_{60} are observed in two temperature ranges: near the orientational phase transition temperature $T_c = 260$ K and at temperatures in the range from 100 to 220 K (the frequency-dependent range). Moreover, the anomalies observed in the elastic moduli are accompanied by the appearance of the corresponding peaks of the internal friction.

It was shown that the anomalies at T_c are associated with the phase transition. However, Shi *et al.* [4] revealed that the Young's modulus drastically increases (by approximately 8%) at T_c, whereas Hoen *et al.* [5] observed a "softening" of the Young's modulus in the same temperature range. A similar result was obtained by Schranz *et al.* [6]. In this respect, interesting results were obtained in measuring the velocities of both longitudinal and transverse waves in the megahertz frequency range in compact C_{60} samples [7, 8]. It is worth noting that the longitudinal velocity of sound was found to decrease in the phase transition range, whereas only a slight change in the slope of the temperature dependence was observed for the transverse velocity of sound. In [6], the negative jump in the modulus at T_c was attributed to an additional inelastic deformation due to the order parameter relaxation in an elastic field of the acoustic wave. Yan *et al.* [9] assumed that the difference in behavior of the elastic moduli near the orientational phase transition temperature can be associated with the quality of the C_{60} crystals used in the experiments, because measurements with polycrystalline films have revealed that the height of the internal friction peak and the drop in the Young's modulus in the range of T_c increase with a decrease in the grain size.

The anomalies in the behavior of the elastic properties and the sound attenuation at temperatures below T_c (the internal friction peak and the corresponding step in the temperature dependence of the modulus, whose temperatures depend on the frequency of measurements [4–7]) are rather consistently described within the concept of orientational relaxation of molecules. This can be explained by the fact that the rotational degrees of freedom of C_{60} molecules persist below the orientational phase transition temperature [10]. As a result of thermal excitation, molecules in the low-temperature phase can occur in different energy states—the so-called pentagonal (ground) and hexagonal (excited) orientational configurations [11]. This situation was described in the framework of a phenomenological model of double-well orientational potential [11–14], according to which molecules can be in two energy states that differ from each other by the quantity $\Delta U \approx 12$ meV and are separated by the potential barrier $U_0 \approx 0.3$ eV. The deformation field of an acoustic wave stimulates transitions between these energy states. In turn, this causes an additional crystal deformation and leads to the attenuation Q^{-1} and a change in the effective elastic modulus $\Delta C/C$ of the relaxation type, that is,

$$Q^{-1} = R\omega\tau/(1+\omega^2\tau^2), \quad (1)$$

$$\Delta C/C = R/(1+\omega^2\tau^2), \quad (2)$$

where $\tau = \tau_0\exp(U_0/kT)$ is the effective relaxation time, ω is the circular frequency, and R is the relaxation depth. The activation parameters ($U_0 \approx 0.3$ eV and $\tau_0 \sim 10^{-13}$–10^{-14} s) determined from acoustic measurements [4, 6, 7] are in agreement with the results obtained by other techniques [10, 12, 15, 16].

Note that the temperature dependence of the effective relaxation time τ in the framework of the double-well potential model is represented by a more complex relationship,

$$\begin{aligned}\tau &= \exp(U_0/kT)/[2\nu_0 \\ &\times \cosh((\Delta U/2kT) + \ln(\nu_h/\nu_p)/2)].\end{aligned} \quad (3)$$

Here, $\nu_0 = (\nu_h\nu_p)^{1/2}$ and ν_h and ν_p are the frequencies of attempts in the hexagonal and pentagonal configurations, respectively. Hence,

$$\begin{aligned}\tau_0 &= 1/[2\nu_0\cosh((\Delta U/2kT) + \ln(\nu_h/\nu_p)/2)] \\ &= 1/(2\nu_0\cosh(\Delta U^*/2kT)),\end{aligned} \quad (4)$$

where $\Delta U^* = \Delta U + kT\ln(\nu_h/\nu_p)$. Therefore, both τ_0 and the effective difference ΔU^* between the energy levels can depend on the temperature (even without regard for the possible temperature dependences of ΔU, ν_h, and ν_p [14]). However, since the experimental estimates obtained for ΔU at various temperatures by using different methods differ by no more than 30% [6, 11–13, 16] (i.e., ν_h and ν_p cannot differ by more than a factor of 1.5) and the value of $\cosh(\Delta U/2kT)$ in the temperature range 80–260 K also changes by a factor of approximately 1.5, a simplified relationship for τ can be used in the majority of cases.

It should be noted that the lack of information on the temperature dependence of all the elastic moduli for solid C_{60} does not allow one to judge the adequacy of the model for the phenomenon under consideration.

The aim of this work was to determine the temperature dependences of the complete set of elastic moduli for solid C_{60} in the temperature range 100–300 K and to analyze the obtained results in the framework of existing theoretical concepts.

2. EXPERIMENTAL TECHNIQUE

The single crystals of solid C_{60} used for measuring the elastic properties were grown according to the procedure described in our earlier work [2]. In order to obtain samples of larger sizes, the growth time was increased to 24 h. As a result, we succeeded in growing crystals weighing as much as 200–250 mg. Among the grown crystals, the most perfect crystals (i.e., containing no twins and inclusions of other phases) were chosen for preparing the samples used in our measurements. The samples were produced in the form of plates ≈6 × 8 mm in size and 1–3 mm in thickness. The planes of the plates were parallel to the crystallographic planes (111) and (100). One of the sample planes was the growth plane, and the other plane was mechanically ground parallel to the first plane with a parallelism of ≈1 μm/cm. In some samples with the (111) orientation, the second plane was also the growth plane.

The elastic characteristics were determined by the acoustical method. The velocity and attenuation of sound (propagated along the $\langle 111\rangle$ and $\langle 100\rangle$ directions) in the sample were measured in the temperature range 100–300 K by the high-frequency resonance method [17] with the use of longitudinal or transverse ultrasonic vibrations at a frequency of ~4 MHz. The samples were cooled and heated at a rate of ≈1 K/min. The measurements were carried out using lithium niobate piezoelectric transducers with a frequency of 5 MHz. Particular attention was given to the choice of the adhesive used to cement the piezoelectric transducers to the sample, because solid C_{60} has a high thermal expansion coefficient. In the case of longitudinal vibrations, the GKZh-94 adhesive (monoethylsiloxane) turned out to be the most suitable. This adhesive enabled us to perform measurements without breaking acoustic contact over the entire temperature range covered (down to 80–100 K). A silicone vacuum paste could be used as a cement in the range from room temperature to 180–200 K. For transverse waves, we failed to choose a cement that would provide measurements over the entire temperature range. For this reason, different cements were used in different temperature ranges: an epoxy resin or picein in the range from room temperature to 260 K (the phase transition temperature), silicone paste in the range from 270–280 to 180–200 K, and GKZh-94 in the range from 150 to 80–100 K. As a rule, when the minimum cooling temperature of the sample was no lower than the temperature permissible for each type of cement, the acoustical parameters (the attenuation and velocity of sound) measured upon cooling and heating coincided with each other [except in the range near the T_c temperature in which a temperature hysteresis of 3–5 K was observed (Fig. 1)]. Otherwise (if the acoustic contact was retained), the transducers most likely deformed the sample, because a considerable hysteresis (an increase in the attenuation of sound and a decrease in its velocity) occurred upon heating beginning with temperatures near 200 K. Note that the hysteresis was more pronounced for transverse vibrations. After holding at room temperature, the measured quantities relaxed to their initial values within a few hours. The accuracy of determination was equal to approximately 2% for the absolute velocity of sound and 0.0025 ± 0.0001 K^{-1} for the relative change in the velocity in measuring the temperature dependences. The velocity of sound in the same samples at room temperature was additionally controlled by the echo pulse

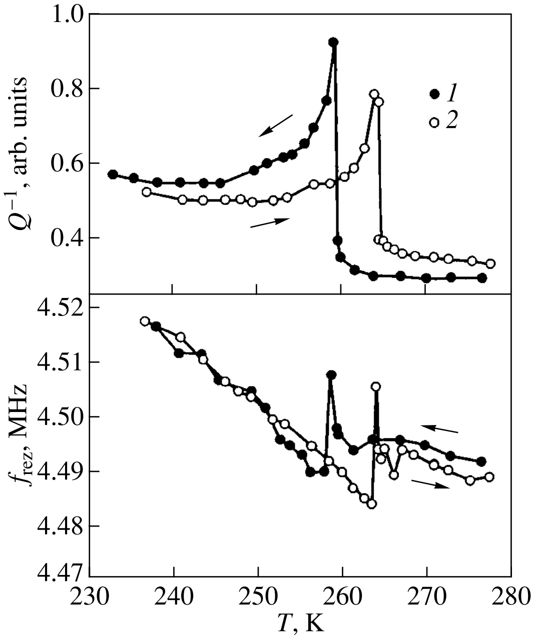

Fig. 1. Temperature dependences of the attenuation and the resonance frequency of a composite transducer near the orientational phase transition temperature upon (*1*) cooling and (*2*) heating of the sample. Longitudinal waves propagate along the ⟨111⟩ direction.

technique [2, 3]. The velocities obtained with the use of both techniques at room temperature, to within the experimental error, coincided with those determined earlier for solid C_{60} [1–3].

3. RESULTS

The experimental temperature dependences of the attenuation Q^{-1} and the velocity V_L of the longitudinal ultrasonic wave along the ⟨111⟩ direction in a solid C_{60} sample are displayed in Figs. 2 and 3. The $Q^{-1}(T)$ dependence is characterized by two peaks of the internal friction (a narrow asymmetric peak in the range of 260 K and a broad peak at 212 K). The $V_L(T)$ dependence shows specific features: a sharper increase (step) in the velocity with a decrease in the temperature in the range 200–225 K and a nonmonotonic anomaly in the range of the orientational phase transition (the velocity jumpwise increases by approximately 1% at ≈259 K, exhibits a dip by ≈1.5% with a minimum near 255–256 K, and steeply increases to temperatures of 235–240 K). For other modes of ultrasonic vibrations (the longitudinal mode along the ⟨100⟩ direction and the transverse mode along the ⟨111⟩ direction), the behavior of $Q^{-1}(T)$ is qualitatively similar, whereas the $V(T)$ dependences differ noticeably (Figs. 4, 5). The velocity V_L of the longitudinal wave along the ⟨100⟩ direction (Fig. 4), as for the wave along the ⟨111⟩ direction, stepwise increases in the temperature range 200–225 K. However, this velocity jumpwise increases (by approximately 2–3%) in the range of the T_c temperature and then increases more smoothly. For the transverse wave (Fig. 5), the V_T anomaly in the range 200–225 K is appreciably less pronounced and the velocity jump at T_c is substantially larger (5–6%).

Figure 6 shows the temperature dependences of the elastic moduli $(C_{11} + 2C_{12} + 4C_{44})/3$, C_{11}, and $(C_{11} - C_{12} + C_{33})/3$. These dependences were obtained from the temperature dependences of the velocities of the corresponding ultrasonic waves with the use of the standard relationship $C = \rho V^2$, where ρ is the density, C is the modulus, and V is the velocity of sound. In order to calculate the other elastic constants, which can also serve for describing crystals with cubic symmetry, the experimental data in Fig. 6 in the temperature range

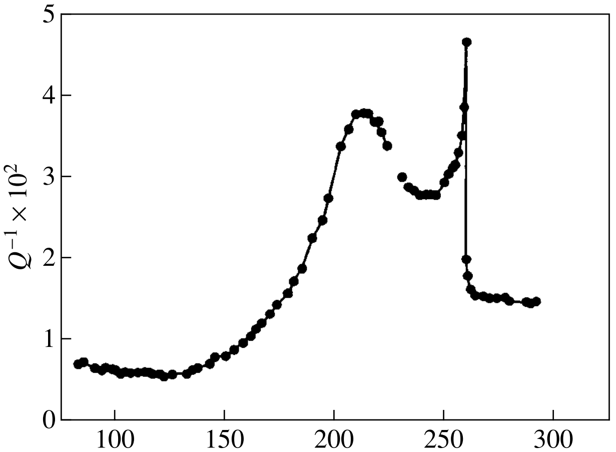

Fig. 2. Temperature dependence of the attenuation of the longitudinal ultrasonic wave propagating along the ⟨111⟩ direction in a solid C_{60} sample upon cooling.

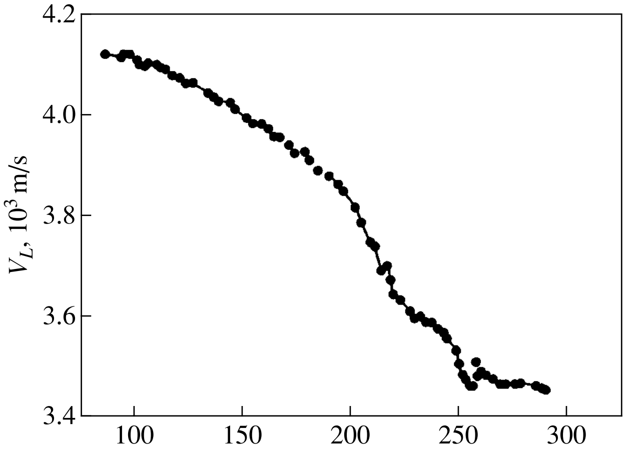

Fig. 3. Temperature dependence of the velocity of the longitudinal ultrasonic wave propagating along the ⟨111⟩ direction upon cooling.

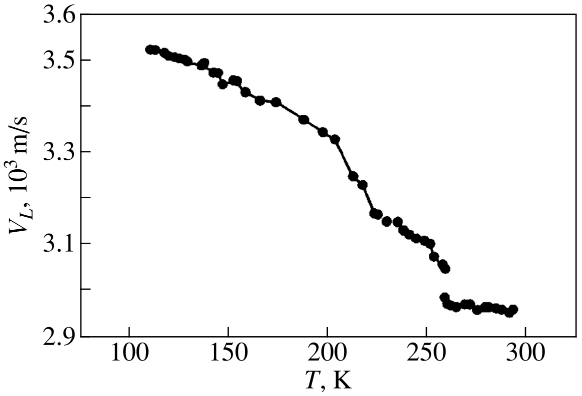

Fig. 4. Temperature dependence of the velocity of the longitudinal ultrasonic wave propagating along the ⟨100⟩ direction upon cooling.

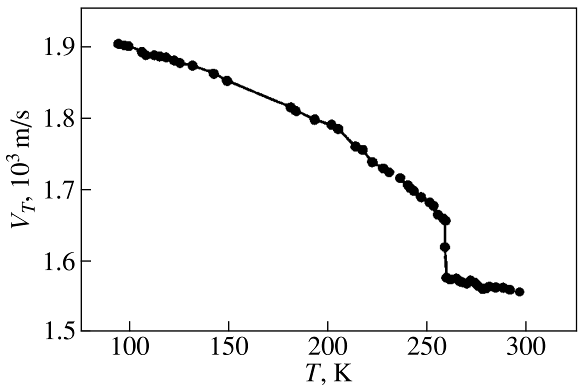

Fig. 5. Temperature dependence of the velocity of the transverse ultrasonic wave propagating along the ⟨111⟩ direction upon cooling.

100–300 K were approximated by nonlinear dependences (solid lines in Fig. 6). By using these dependences and the standard relationships between different elastic moduli, we constructed the temperature dependences of the elastic constants C_{12}, C_{44}, and $C' = (C_{11} - C_{12})/2$ (Fig. 7) and the bulk modulus $K = (C_{11} + 2C_{12})/3$ (Fig. 8).

4. DISCUSSION

It can be seen from Figs. 6–8 that the most significant differences in the temperature dependences of the elastic constants manifest themselves in the temperature range 200–230 K (the different relative heights of the step in the temperature dependences of the moduli) and in the orientational transition range. Note that both a jumpwise increase in the moduli and their softening can be observed in the latter range.

As was noted above, it is assumed that, at temperatures of 200–230 K, the anomalies in the effective elastic moduli measured at megahertz frequencies stem from the relaxation contribution (2) due to the reorientation of C_{60} molecules in the elastic field of the acoustic wave. In the case when the behavior of the “unrelaxed” elastic modulus $C^{(\infty)}$ is approximated by a linear temperature dependence, the temperature dependences of $\Delta C/C = (C^{(\infty)} - C)/C$ are adequately described (to temperatures in the range of 240 K) using expression (2) with the parameters $E_0 = 0.29$ eV and $\tau_0 \approx 0.5 \times 10^{-14}$ s (see, for example, Fig. 8) and the attenuation peak is represented by relationship (1). The specific features in the behavior of the elastic moduli at temperatures near T_c can be explained (as in the case of low-frequency vibrations [6]) by the contribution from the order parameter relaxation in the acoustic wave field to the effective moduli. According to [6], the additional contribution to the free energy due to the interaction between the order parameter η and the strain ε can be expressed as $a\eta^2\varepsilon + b\eta^2\varepsilon^2$. This leads to the appearance of additional terms in the relationship between the elastic modulus C and the frequency and temperature:

$$C(\omega, T) = C^{(\infty)}(\omega, T) - \Delta C_\eta(T)/(1 + \omega^2\tau_\eta^2) + b\eta_0^2(T), \quad (5)$$

where τ_η is the characteristic relaxation time of the order parameter, η_0 is the equilibrium order parameter at a given temperature, $C^{(\infty)}$ is the elastic modulus above T_c, and $\Delta C_\eta(T)$ is the modulus relaxation amplitude proportional to a^2 and dependent on η_0. It follows from formula (5) that, as the temperature decreases

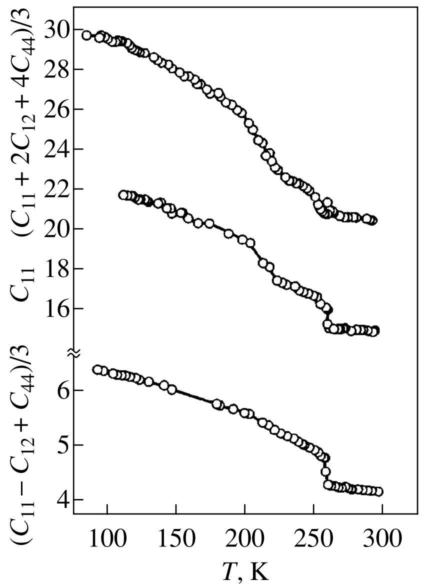

Fig. 6. Temperature dependences of the elastic moduli $C_L(111) = (C_{11} + 2C_{12} + 4C_{44})/3$, $C_L(100) = C_{11}$, and $C_T(111) = (C_{11} - C_{12} + C_{44})/3$ obtained from the temperature dependences of the ultrasonic wave velocities (Figs. 3–5).

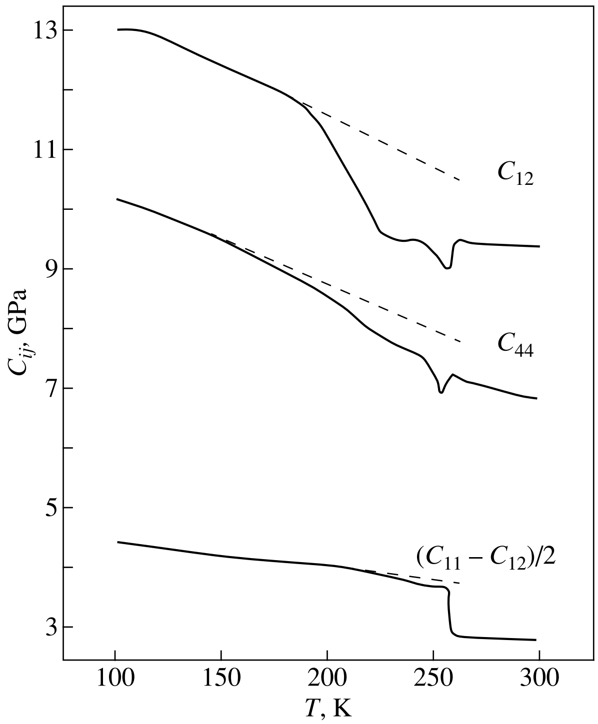

Fig. 7. Temperature dependences of the elastic moduli C_{12}, C_{44}, and $(C_{11} - C_{12})/2$ calculated from the data presented in Fig. 6. Dashed lines correspond to the linear extrapolation of the temperature dependences below 180 K to the range up to the orientational phase transition temperature.

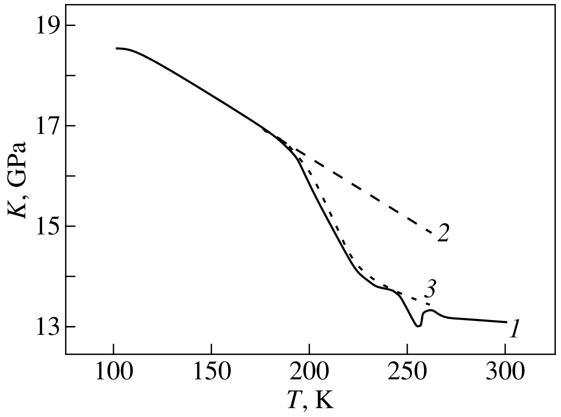

Fig. 8. (*1*) Temperature dependence of the bulk modulus K calculated from the data presented in Fig. 6. (*2*) Linear extrapolation of the low-temperature portion of the temperature dependence to the range up to the orientational phase transition temperature. (*3*) Temperature dependence calculated with inclusion of the relaxation contribution from the reorientation of C_{60} molecules according to formula (2).

below T_c, the elastic modulus should, on the one hand, increase owing to a jump in the order parameter [the third term in formula (5)] and, on the other hand, decrease as a consequence of the contribution from the relaxation component. This decrease depends on the frequency of measurements, because the relaxation time τ_η at temperatures close to T_c sharply increases and the relaxation contribution becomes insignificant. Therefore, the relaxation contribution at a given frequency of measurements nonmonotonically depends on the temperature and decreases at temperatures far from and close to the transition temperature. In this case, the location of an extremum at a given frequency of measurements is determined by the temperature dependences $\Delta C_\eta(T)$ and $\tau_\eta(T)$. Furthermore, since the relaxation contribution caused by the molecular reorientation leads to a decrease in the modulus, the behavior of the elastic modulus near the transition temperature is governed by the competition of three factors: (a) an increase in the modulus due to a jump in the order parameter, (b) a decrease in the modulus owing to molecular reorientation, and (c) a nonmonotonic temperature-dependent decrease associated with the order parameter relaxation. Depending on the relative contributions of these factors (and the frequency of measurements), the temperature dependence of the modulus can be qualitatively different in character, which is actually observed in the experiments.

This situation is clearly illustrated in Figs. 7 and 8 in the temperature dependences of the elastic moduli K, C_{44}, and $C' = (C_{11} - C_{12})/2$ (all the other elastic moduli can be expressed in terms of these three moduli). For the bulk modulus, the modulus jump in the absence of relaxation contributions is approximately 13%, the maximum relaxation depth associated with the molecular reorientation is equal to approximately 10%, and the order parameter relaxation depth is approximately 5%. For the C_{44} modulus, the jump is approximately 11% and the relaxation depths for both processes are equal to approximately 6%. For the C' modulus, the jump at temperatures close to T_c is of the order of 30% and the total contribution from the relaxation processes does not exceed 3% (i.e., in essence, it is within the experimental error of the C' measurement). Now, we consider the theoretical estimates available in the literature for all these contributions to the elastic moduli.

The relaxation depth R_{or}, which is related to the reorientation of C_{60} molecules in the acoustic wave field, was estimated by Natsik and Podol'skiĭ [14] for the bulk modulus within the model of double-well orientational energy potential. In this model, the time change in the concentration of the hexagonal (N_h) and pentagonal ($N_p = N_0 - N_h$, where N_0 is the total number of orientational states per unit volume) states is given by the kinetic equation

$$\partial N_h/\partial t = -N_h/\tau_h + (N_0 - N_h)/\tau_p, \qquad (6)$$

where $\tau_{h,b} = \tau_0 \exp(U_{h,p}/kT)$ stands for the relaxation times, $U_h = U_0 - \Delta U/2 - V_h\varepsilon_{ll}$, $U_p = U_0 + \Delta U/2 - V_p\varepsilon_{ll}$, $V_{h,p}$ is the deformation potential, and $\varepsilon_{ll} = \varepsilon_{11} + \varepsilon_{22} + \varepsilon_{33}$ is the volume strain. By changing over to the relative concentrations of excited states $n = N_h/N_0$, within the approximation linear in ε_{ll}, we obtain

$$\tau_{\mathrm{or}}\partial n/\partial t + n = n_0 + (V_\Delta\varepsilon_{ll}/kT)n_0(1-n_0), \quad (7)$$

where $\tau_{\mathrm{or}} = \tau_0\exp(U_0/kT)/(2\cosh(\Delta U/2kT))$, $n_0 = 1/(1 + \exp(\Delta U/kT))$, and $V_\Delta = V_p - V_h$. The thermodynamic analysis of the elastic and thermal properties of fullerite in terms of the two-level model with inclusion of the orientational transitions [14] demonstrated that the effective complex elastic modulus K at megahertz frequencies can be represented in the form

$$K = K^{(\infty)} - A/(1 - i\omega\tau_{\mathrm{or}}), \quad (8)$$

where $K^{(\infty)}$ is the adiabatic bulk modulus, $A = \gamma(V_\Delta/kT)n_0(1 - n_0)$, $\gamma = -(\partial/\partial\varepsilon_{ll}(\partial F/\partial n)_{T,\varepsilon})_{T,n} \equiv -(\partial/\partial n(\partial F/\partial\varepsilon_{ll})_{T,n})_{T,\varepsilon}$, and F is the free energy density. The quantity γ can also be written as $\gamma = \alpha K^{(0)}$ [14, 16], where $K^{(0)}$ is the isothermal elastic modulus and α is the relative dilatation of the crystal upon transition from the ground state to the excited state. Therefore, in the case of the bulk modulus, the relaxation depth R_{or}, which is related to the reorientation of C_{60} molecules, can be expressed by the formula

$$R_{\mathrm{or}} = \alpha(V_\Delta/kT)(K^{(0)}/K^{(\infty)})n_0(1-n_0). \quad (9)$$

These relationships make it possible to calculate the value of R_{or} from the estimate $\alpha \approx -10^{-2}$ derived in [16, 18] and the estimate $V_\Delta \approx -0.8$ eV obtained by David and Ibberson [19], who proved that the relative densities of the ground and excited states at a temperature of 150 K and a pressure of 190 MPa are identical. At 230 K, we obtain $R_{\mathrm{or}} \approx 0.1$, which is in agreement with the experimental value. The γ quantity can also be represented as $\gamma = V_\Delta/v_0$ (where v_0 is the volume involved in an elementary act of the transition from the ground state to the excited state under pressure). Consequently, we have the estimate $v_0 \approx 10^{-27}$ m^3, which is equal in order of magnitude to the volume occupied by one C_{60} molecule. This confirms the validity of the phenomenological single-particle model of double-well potential [11–13]. By using the pressure dependence of the temperature T_g of the orientational glass transition [20], it is also possible to evaluate the magnitudes of the deformation potentials V_p and V_h [14]. From the quantity $dT_g/dP = 60$ GPa [20], we obtain $V_p \approx 2$ eV and, correspondingly, $V_h \approx 2.8$ eV. (A similar estimate was made by Natsik and Podol'skiĭ [14]; however, they took V_h equal to 2 eV, because it was implicitly assumed that $V_p > V_h$.)

Unfortunately, the relaxation contribution from the order parameter fluctuations (in the deformation field of an acoustic wave) to the elastic moduli was not calculated theoretically. Schranz *et al.* [6] made merely the qualitatively assessment that this contribution can occur in the case of longitudinal acoustic waves [see relationship (5)]. This assessment was based on the results obtained by Lamoen and Mishel [21], who proved that the free energy includes the terms accounting for the interaction between the order parameter and the crystal dilatation. Therefore, the order parameter relaxation can contribute to the bulk modulus and the experimental temperature dependence of the bulk modulus qualitatively agrees with the theoretical curve predicted in this case (see the discussion at the beginning of this section).

The jump in the elastic moduli upon orientational transition in solid C_{60} was calculated by Burgos *et al.* [18] in the framework of a simplified phenomenological model, which disregards the possible orientational transitions in the low-temperature phase of fullerite. According to these calculations, all the elastic constants at the T_c temperature should increase by approximately 30%. Our experimental data correlate in order of magnitude with these estimates.

As regards the relaxation contributions to the shear moduli (for example, the C_{44} modulus) observed in the experiment, the possible effect of shear strains on the frequency of transitions between orientational states or on the order parameter in solid C_{60} has not yet been analyzed theoretically. Natsik and Podol'skiĭ [14] assumed that the relation between the probability of orientational transitions and shear components can be found from a consideration of the torsional strains in the framework of the nonsymmetric theory of elasticity [22]. This is due to the fact that the rotation axis of a particular molecule in the low-temperature phase of fullerite is polar [23, 24] and that the terms proportional to the nonsymmetric part of the strain tensor and to the spatial derivatives of the rotation vector can appear in the expression for the energy barrier to the transition of molecules between orientational states. Another important factor is the formation of orientational domains (crystal regions with an isomorphic structure) in the low-temperature phase of solid C_{60} [13, 25]. The occurrence of these domains implies that the direction and the sign of polarity of the rotation axis of a particular molecule remain unchanged upon translation through the lattice spacing in a statistically significant volume. Under these conditions, the equations of motion take the form characteristic of a micropolar medium [22, 26], which can result in a relaxation-type contribution to the shear wave velocity. According to estimates, the effects comparable in order of magnitude with those experimentally observed can manifest themselves only at very high frequencies (~10^{12} Hz). However, it turns out that, under the same conditions (the occurrence of the polar axis and the formation of domains with an isomorphic structure), the terms related to the symmetric part of the shear strain can be written in the expression for the deformation potential (this problem will be considered in more detail in a separate work). In this case, the relaxation contribution to the shear moduli appears already within the classical theory of elasticity.

In our opinion, the problem of the possible coupling of the shear strains to the order parameter fluctuations can be solved by consistently considering the polarity of the rotation axes of C_{60} molecules and the orientational excitations in the structure of the low-temperature phase of fullerite.

ACKNOWLEDGMENTS

This work was supported by the State Scientific and Technical Program “Topical Directions in the Physics of Condensed Matter: Fullerenes and Atomic Clusters,” complex project no. 2.

REFERENCES

1. N. P. Kobelev, R. K. Nikolaev, Ya. M. Soifer, and S. S. Khasanov, Chem. Phys. Lett. **276**, 263 (1997).
2. N. P. Kobelev, R. K. Nikolaev, Ya. M. Soĭfer, and S. S. Khasanov, Fiz. Tverd. Tela (St. Petersburg) **40** (1), 173 (1998) [Phys. Solid State **40**, 154 (1998)].
3. N. P. Kobelev, Ya. M. Soifer, R. K. Nikolaev, and V. M. Levin, Phys. Status Solidi B **214**, 303 (1999).
4. X. D. Shi, A. R. Kortan, J. M. Williams, *et al.*, Phys. Rev. Lett. **68**, 827 (1992).
5. S. Hoen, N. G. Chopra, R. Mostovoy, *et al.*, Phys. Rev. B **46**, 12737 (1992).
6. W. Schranz, A. Fuith, P. Dolinar, *et al.*, Phys. Rev. Lett. **71**, 1561 (1993).
7. N. P. Kobelev, A. P. Moravskiĭ, Ya. M. Soĭfer, *et al.*, Fiz. Tverd. Tela (St. Petersburg) **36** (9), 2732 (1994) [Phys. Solid State **36**, 1491 (1994)].
8. Ya. M. Soifer and N. P. Kobelev, Mol. Mater. **7**, 267 (1969).
9. F. Yan, M. Gu, and Y. N. Wang, J. Phys. IV **6**, C8-819 (1996).
10. R. Tycko, R. C. Haddon, G. Dabbagh, *et al.*, J. Phys. Chem. **95**, 518 (1991).
11. W. I. F. David, R. M. Ibberson, and T. Matsuo, Proc. R. Soc. London, Ser. A **442**, 129 (1993).
12. R. C. Yu, N. Tea, M. V. Salanon, *et al.*, Phys. Rev. Lett. **68**, 2050 (1992).
13. W. I. F. David, R. M. Ibberson, T. J. S. Dennis, *et al.*, Europhys. Lett. **18**, 219 (1992).
14. V. D. Natsik and A. V. Podol’skiĭ, Fiz. Nizk. Temp. **24**, 689 (1998) [Low Temp. Phys. **24**, 523 (1998)].
15. G. B. Alers, B. Golding, A. R. Kortan, *et al.*, Science **257**, 511 (1992).
16. F. Gugenberger, R. Heid, C. Meingast, *et al.*, Phys. Rev. Lett. **69**, 3774 (1992).
17. N. P. Kobelev and Ya. M. Soĭfer, Fiz. Tverd. Tela (Leningrad) **21** (5), 1362 (1979) [Sov. Phys. Solid State **21**, 787 (1979)].
18. E. Burgos, E. Halas, and H. Bonadeo, Phys. Rev. B **49** (22), 15544 (1994).
19. W. L. F. David and R. M. Ibberson, J. Phys.: Condens. Matter **5**, 7923 (1993).
20. O. Anderson, A. Soldatov, and B. Sundqvist, Phys. Rev. B **54**, 3093 (1996).
21. D. Lamoen and K. H. Mishel, Phys. Rev. B **48** (2), 807 (1993).
22. W. Nowacki, *Theory of Elasticity* (PWN, Warszawa, 1970; Mir, Moscow, 1975), translated from Polish.
23. K. H. Michel, D. Lamoen, and W. I. F. David, Acta Crystallogr. A **51**, 365 (1995).
24. S. Savin, A. B. Harris, and T. Yildirim, Phys. Rev. B **55** (21), 14182 (1997).
25. A. B. Harris and R. Sachidanandam, Phys. Rev. B **46** (8), 4944 (1992).
26. V. I. Erofeev, *Wave Processes in Solid Microstructures* (Moscow Gos. Univ., Moscow, 1999).

Translated by O. Borovik-Romanova